IntechOpen

Ferroelectrics and Their Applications

Edited by Husein Irzaman

FERROELECTRICS AND THEIR APPLICATIONS

Edited by **Husein Irzaman**

Ferroelectrics and Their Applications
http://dx.doi.org/10.5772/intechopen.73075
Edited by Husein Irzaman

Contributors

Alexander Skaliukh, Xianmin Zhang, Liuxia Ruan, Donghai Zhang, Junwei Tong, Jianli Kang, Yufang Chang, Lianqun Zhou, Gaowu Qin, Trong Tue Phan, Rongli Gao, Zhenhua Wang, Oscar Marcelo Suarez, Amarilis Declet, Nelson Sepúlveda Ramos, Xin Chen, Yan Sheng, Wieslaw Krolikowski, Rahul Kambale, Bharat Baraskar, Pravin Sadashiv Kadhane, Ajit James, Tulshidas Darvade, Husein Irzaman, Renan Prasta Jenie

© The Editor(s) and the Author(s) 2018
The rights of the editor(s) and the author(s) have been asserted in accordance with the Copyright, Designs and Patents Act 1988. All rights to the book as a whole are reserved by INTECHOPEN LIMITED. The book as a whole (compilation) cannot be reproduced, distributed or used for commercial or non-commercial purposes without INTECHOPEN LIMITED's written permission. Enquiries concerning the use of the book should be directed to INTECHOPEN LIMITED rights and permissions department (permissions@intechopen.com).
Violations are liable to prosecution under the governing Copyright Law.

Individual chapters of this publication are distributed under the terms of the Creative Commons Attribution 3.0 Unported License which permits commercial use, distribution and reproduction of the individual chapters, provided the original author(s) and source publication are appropriately acknowledged. If so indicated, certain images may not be included under the Creative Commons license. In such cases users will need to obtain permission from the license holder to reproduce the material. More details and guidelines concerning content reuse and adaptation can be foundat http://www.intechopen.com/copyright-policy.html.

Notice

Statements and opinions expressed in the chapters are these of the individual contributors and not necessarily those of the editors or publisher. No responsibility is accepted for the accuracy of information contained in the published chapters. The publisher assumes no responsibility for any damage or injury to persons or property arising out of the use of any materials, instructions, methods or ideas contained in the book.

First published in London, United Kingdom, 2018 by IntechOpen
eBook (PDF) Published by IntechOpen, 2019
IntechOpen is the global imprint of INTECHOPEN LIMITED, registered in England and Wales, registration number: 11086078, The Shard, 25th floor, 32 London Bridge Street
London, SE19SG – United Kingdom
Printed in Croatia

British Library Cataloguing-in-Publication Data
A catalogue record for this book is available from the British Library

Additional hard and PDF copies can be obtained from orders@intechopen.com

Ferroelectrics and Their Applications
Edited by Husein Irzaman

p. cm.

Print ISBN 978-1-78984-013-1

Online ISBN 978-1-78984-014-8

eBook (PDF) ISBN 978-1-83881-714-5

Meet the editor

Dr. Husein Irzaman was born in Jakarta, Indonesia, in 1963. He received the B.S. in Agro-meteorology from Bogor Agricultural University, Indonesia, in 1988, his M.S. degree in Physics from the University of Indonesia in 1998, and his Ph.D. degree in Physics from Bandung Technology University, Bandung, Indonesia, in 2005. Since 1997, he has been a resident lecturer in the Physics Department, Bogor Agricultural University. From 2011, he is Head of the Material Physics Laboratory, Physics Department, Bogor Agricultural University. He is the author of 30 Scopus-indexed journal articles and one book chapter. His research interests include sensors engineering, semiconductor device physics and new material characterization, and ferroelectrics. From 2012, he has been a technical member of the Alternative Energy Division, Ministry of Energy and Mineral Resources, Republic of Indonesia.

Contents

Preface

Ferroelectricity is a symptom of inevitable electrical polarization changes in materials without external electric field interference. Ferroelectricity is a phenomenon exhibited by crystals with a spontaneous polarization and hysteresis effects associated with dielectric changes when an electric field is given.

This book is a compilation of articles provided by kind contributors:

1. Our introductory chapter focuses on ferroelectrics and its aplications.
2. Rongli Gao et al. study transverse photovoltaic effects as a function of sample directions in-plane as well as the angle between the linearly polarized light and the plane of the sample along X and Y directions. A sample was made, tetragonal BiFeO3 film with a thickness of 30 nm, which was grown epitaxially on (001)-oriented LaAlO3 substrate by using pulsed laser deposition (PLD).
3. Xin Chen et al. review the nonlinear optical effects that are bundled with ferroelectric domain walls or whose properties can be significantly enhanced by the presence of domain walls.
4. Alexander Skaliukh presents prevalent mathematical models of irreversible processes in polycrystalline ferroelectric materials when they are subjected to intense electrical and mechanical influences
5. Amarilis Declet-Vega et al. report their studies on mechanical and dielectric properties of biocomposites containing strontium titanate particles.
6. Phan Trong Tue and Yuzuru Takamura contribute their work on lead zirconium titanate films and devices made by a low-temperature solution-based process.
7. Bharat G. Baraskar et al. discuss the strategy to develop superior quality, high-density microstructured BaTiO3 electroceramic material.
8. Liuxia Ruan et al. describe the preparation and device applications of ferroelectric β-PVDF films.

We have been researching ferroelectric materials since 2001, but there is still a blue ocean of ferroelectric applications yet to be elaborated. It is and hopefully always will be a bright future.

We would like to thank IntechOpen and all the contributors. Their support has made this book possible. We also would like to thank all researchers and the institute that has supported our research since 2001.

Dr. Husein Irzaman, M.Sci.
Department of Physics
Faculty of Mathematics and Sciences
Bogor Agricultural University, Indonesia

Section 1

Ferroelectricity

Introductory Chapter: Ferroelectrics Material and Their Applications

Irzaman Husein and Renan Prasta Jenie

Additional information is available at the end of the chapter

http://dx.doi.org/10.5772/intechopen.80643

1. Ferroelectrics material

Ferroelectricity is a symptom of inevitable electrical polarisation changes in materials without external electric field interference. Ferroelectricity is a phenomenon exhibited by crystals with a spontaneous polarisation and hysteresis effects associated with dielectric changes when an electric field is given. Our fascination with ferroelectricity is thanks to a beautiful article by Itskovsky, in which he explains about kinetics of a ferroelectric phase transition in thin ferroelectric layer (film) [1]. We have been researching about ferroelectrics materials since 2001 [2, 3].

There are several materials known for its ferroelectric properties. Barium titanate and barium strontium titanate are the most well known [2–4]. Several others include tantalum oxide, lead zirconium titanate, gallium nitride, lithium tantalate, aluminium, copper oxide and lithium niobate [5–14].

Researchers often introduce dopant to enhance material's ferroelectric characteristics. Lanthanum is one of the most well-known materials to be used as dopant [10, 13, 15–18]. Ferric oxide is also most often used as dopant [8, 19–21]. Other dopants include gallium oxide, tantalum oxide, niobium oxide and manganese [9, 14, 19, 22–24]. Furthermore, we are currently trying to enhance the ferroelectric effects using photonic crystals [25].

When researchers are growing ferroelectric thin films, they have used various concentrations, starting from 0.25 to 2.5 mole [7, 23, 25–28]. Researchers applied the chemical solutions of various substrates: the most often is p-type silicone [3, 11]. n-Type silicone, transparent conductive oxide substrate and corning glass are also known to be used as ferroelectric substrates [2, 24–26]. We ourselves have prepared our ferroelectric materials mostly using chemical solution deposition methods and coupled with spin-coating methods, usually for 30 s, with rotational speed of 2000–8000 rpm [3, 4, 6, 7, 11, 18, 19, 23, 27, 29]. Other preparation methods researchers have used include pulsed laser ablation deposition (PLAD), DC magnetron unbalanced magnetron sputtering (DC UBMS), solid solution methods, plasma-assisted metal-organic chemical vapour deposition (PAMOCVD) and sol-gel method [2, 9, 14, 27, 30, 31].

Researchers usually anneal or heat the ferroelectric samples in furnace. We have tried low temperature in rich oxygen chamber, at 200–280°C [23]. We mostly anneal our ferroelectric samples in atmospheric chamber, at various temperatures from 350 to 950°C [5, 20, 24, 28, 32, 33]. We also have varied the holding duration from 1 to 29 h [3, 7–9, 11, 17, 18, 20, 27, 29, 30, 34, 35]. The resultant ferroelectric crystal shape is either hexagonal, tetragonal, or orthorhombic [6, 9, 12, 13, 36].

To learn more about the nature of our ferroelectrics, researchers have utilised several characterisation devices. They usually start with IV meter or current-voltage photovoltaic measurement and LCR meter [3, 27, 33, 37]. They are also heavily utilising spectrophotometric devices, in an ultraviolet to visible range, visible to near-infrared range and Fourier transformed infrared (FTIR) spectrophotometry [2, 4, 10, 15, 18, 37]. To assess deep inside the ferroelectric crystal structure, researchers have utilised particle size analyser, scanning electron microscopy, atomic force microscopy, dispersive energy X-ray and X-ray diffraction device (XRD) [3, 10, 14, 16, 23]. We are currently working on an implementation of ARIMA methods to enhance FTIR and XRD results [15, 16].

With those measurement devices, researchers could observe the ferroelectric electrical characteristics such as voltage responsivity, electrical insulation/conductivity, energy gap, ellipsometric measurement, value range, accuracy level, sensitivity, hysteresis, dielectric constant, time constant and dielectric loss [2, 3, 6, 7, 10, 11, 18, 20, 36]. The researchers have also measure physical characteristics such as gravimetric calculation, depth measurement, resolution, surface roughness, structural properties and functional groups [4, 10, 23, 36]. Other than those parameters, researchers also have measured spectral and applied characteristics such as refractive index, photonic absorption, pyroelectric characteristics and solar cell efficiency [6, 9, 17, 25, 27, 30, 35].

2. Ferroelectrics material and their applications

Researchers have been developing various forms of sensors with various working principles. The sensor is a simple device, which can measure how much and produce some form of the output of mechanical, electrical and optical output. Today, developmental sensors use computing, communications and connectivity to the web, mobile smart devices and integration clouds added to the sensor capabilities [38]. The development of censorship in the healthcare world was initially widely used in hospitals, but now censorship is widely used by many patients both in public places, individual homes that support their health management. Clarke and Lyons first developed the concept of biosensing in 1962. The concept of glucose biosensor was successfully commercialised in 1975 by the instrument companies Yellow Springs and the American National Standards Institute. Currently, medical industries are massively developing the biosensor as a tool for AIDS testing and home pregnancy, allergy detection. Besides, biosensors are now widely developed for environmental applications such as detection of bacteria, pesticides and heavy metals in water samples [39]. The next sensor development is a MEMS-based sensor. This sensor has a small size accurate, and industries can integrate this sensor into the device ranging from sports hours, electronics, to cars. The U.S Government initiated an accelerated program in the development of MEMS-based sensors in 1990. The technique used was the manufacture of semiconductors, accelerometers (ADXL50) was the first sensor to be sold commercially in 1992 [40]. Currently, the evolution of sensors is strongly influenced by ICT technology, with integration with the microcontroller, wireless communications module and data storage permanently. Industries have supported this technology by the development of sensor systems with a standard architecture. Computing, storage and communication features are used to present multiple sensors with connectivity. The development of the next sensor leads to the sensor connection process to the smartphone or tablet, or connection with the web or cloud storage [40]. So far, we have implemented our ferroelectric technology as automatic switch sensor, infrared sensor, light sensor and temperature sensor, as well as solar or photovoltaic cells, which made for IPB satellite design [5, 7, 11, 18, 19, 27, 32, 36]. There is still a blue ocean of ferroelectric applications yet to be elaborated. It is and hopefully always a bright future.

Acknowledgements

This work is supported by Higher Education Basic Research of Directorate General of Higher Education, Ministry of National Education, The Republic of Indonesia, contract no. 1751/IT3.11/PN/2018 and Postgraduate Research Team of Directorate General of Higher Education, Ministry of National Education, The Republic of Indonesia, contract no. 1548/IT3.11/PN/2018

Author details

Irzaman Husein[1]* and Renan Prasta Jenie[2]

*Address all correspondence to: irzaman@apps.ipb.ac.id

1 Department of Physics, Faculty of Mathematics and Science, Bogor Agricultural University, Bogor, Indonesia

2 Department of Community Nutrition and Physics, Faculty of Human Ecology, Mathematics, and Science, Bogor Agricultural University, Bogor, Indonesia

References

[1] Itskovsky MA. Kinetics of ferroelectric phase transition: Nonlinear pyroelectric effect and ferroelectric solar cell. Japanese Journal of Applied Physics. 1999;**38**(8):4812-4817

[2] Irzaman, Fuad A, Barmawi M. Spectral response of Al/Si photodiodes for IR sensor. In: Proceeding Instrumentation, Measurement, and Communications for the Future, Bandung, Indonesia: Indonesian German Conference (IGC); 2001. pp. 340-342

[3] Irzaman, Sudiana Y, Hikam M, Loeksmanto W, Barmawi M. Analisis struktur kristal dan full width half maximum (Fwhm) dengan metode rietveld (Studi Kasus: Kalsit ($CaCO_3$)). Jurnal Kontribusi Fisika Indonesia. Indonesia: ITB Bandung. 2000;**11**(2):41-48

[4] Mulyadi, Rika W, Sulidah, Irzaman, Hardhienata H. Barium strontium titanate thin film growth with rotational speed variation as a satellite temperature sensor prototype. IOP Conference Series: Earth and Environmental Science. 2017;**54**:012094

[5] Dahrul M, Alatas H, Irzaman. Preparation and optical properties study of CuO thin film as applied solar cell on LAPAN-IPB satellite. Procedia Environmental Sciences. 2016;**33**:661-667

[6] Darmasetiawan H, Irzaman, Nur Indro M, Sukaryo S, Hikam M, Peng Bo N. Optical properties of crystalline Ta_2O_5 thin films. Physica Status Solidi A: Applications and Materials Science. 2002;**193**(1):53-60

[7] Hikam M, Irzaman, Darmasetiawan H, Arifin P, Budiman M, Barmawi M. Pyroelectric properties of lead zirconium titanate ($PbZr_{0.525}Ti_{0.475}O_3$) metal ferroelectric-metal capacitor and its application for IR sensor. Indonesian Journal of Materials Science. 2005;**6**(3):6

[8] Indro MN, Irzaman, Sastri B, Nady L, Syafutra H, Siswadi. Electric and pyroelectric properties of $LiTaO_3$ and $LiFe_2TaO_3$ films. Materials Science and Technology. 2010;**6**:19-22

[9] Irzaman, Darvina Y, Fuad A, Arifin P, Budiman M, Barmawi M. Physical and pyroelectric properties of tantalum-oxide-doped lead zirconium titanate [$Pb_{0.9950}(Zr_{0.525}Ti_{0.465}Ta_{0.010})O_3$] thin films and their application for IR sensors. Physica Status Solidi A: Applications and Materials Science. 2003;**199**(3):416-424

[10] Irzaman, Hardhienata H, Maddu A, Aminullah, Alatas H. The Effects of Lanthanum Dopant on the Structural and Optical Properties of Ferroelectric Thin Films. In: Orjuela JEA, editor. Rare Earth Element [Internet]. InTech; 2017 [cited 2018 Jul 4]. Available from: http://www.intechopen.com/books/rare-earth-element/the-effects-of-lanthanum-dopant-on-the-structural-and-optical-properties-of-ferroelectric-thin-films

[11] Irzaman, Siskandar R, Nabilah N, Aminullah, Yuliarto B, Hamam KA, Husin A. Application of lithium tantalate ($LiTaO_3$) films as light sensor to monitor the light status in the Arduino Uno based energy-saving automatic light prototype and passive infrared sensor. Ferroelectrics. 2018;**524**(1):44-55

[12] Irzaman, Erviansyah R, Syafutra H, Maddu A, dan Siswadi. Studi konduktivitas listrik film tipis $Ba_{0.25}Sr_{0.75}TiO_3$ yang didadah ferium oksida (BFST) menggunakan metode chemical solution deposition. Berkala Fisika. Indonesia: Universaitas Diponegoro. 2010;**13**(1):33-38

[13] Irzaman, Sitompul H, Masitoh, Misbakhusshudur M, Mursyidah. Optical and structural properties of lanthanum doped lithium niobate thin films. Ferroelectrics. 2016;**502**(1):9-18

[14] Mulyanti B, Subagio A, Arsyad FS, Arifin P, Barmawi M, Irzaman, Jusoh SN, Taking S, Jamal Z, Idris MA. Effect of growth temperature and Mn incorporation on GaN: Mn thin films grown by plasma-assisted MOCVD. ITB Journal of Science. 2008;**40**(2):97-108

[15] Aidi MN, Irzaman H. Classification Detection of FTIR and XRD Spectrum on Thin Film of Lithium Tantalate with ARIMA Model on High Level Accuracy [Internet]. Unpublished; 2018 [cited 2018 Jul 4]. Available from: http://rgdoi.net/10.13140/RG.2.2.24872.06403

[16] Aidi MN, Irzaman H. Arima analysis for detecting FTIR and XRD spectral pattern on barium strontium titanate (BST) thin film [Internet]. Unpublished; 2018 [cited 2018 Jul 4]. Available from: http://rgdoi.net/10.13140/RG.2.2.18161.17768

[17] Irzaman, Pebriyanto Y, Apipah ER, Noor I, Alkadri A. Characterization of optical and structural of lanthanum doped $LiTaO_3$ thin films. Integrated Ferroelectrics. 2015;**167**(1):137-145

[18] Mulyadi, Wahyuni R, Hardhienata H, Irzaman. Barium strontium titanate thin film growth with variation of lanthanum dopant compatibility as sensor prototype in the satellite technology. IOP Conference Series: Earth and Environmental Science. 2018;**149**:012069

[19] Dahrul M, Syafutra H, Arif A, Irzaman, Indro MN, Siswadi. Manufactures and characterizations of photodiode thin film barium strontium titanate (BST) doped by niobium and iron as light sensor. In: The 4th Asian Physics Symposium—An International Symposium. AIP Publishing; 2010. pp. 43-46

[20] Irzaman, Heriyanto S, Darmasetiawan H, Hardhienata H, Erviansyah R, Huriawati F, Akhiruddin MH, Arifin P. Electrical properties of photodiode BST thin film doped with ferrium oxide using chemical deposition solution method. Atom Indonesia. 2011;**37**(3):133-138

[21] Novianty I, Yani S, Chahyani R, Athiyah Z, Casnan, Fendi, Serah S, Hartono J, Rofiah N, Syahfutra H, Akhiruddin, Irzaman. Electrical properties Fe_2O_3 doped based $Ba_{0.5}Sr_{0.5}TiO_3$ thin film as light sensor. Indonesian Journal of Materials Science: Special Edition on Materials for Sensor. 2011. p. 9-12

[22] Estrada R, Djohan N, Pasole D, Dahrul M, Kurniawan A, Iskandar J, Hardhienata H, Irzaman. The optical band gap of $LiTaO_3$ and Nb_2O_5-doped $LiTaO_3$ thin films based on Tauc plot method to be applied on satellite. IOP Conference Series: Earth and Environmental Science. 2017;**54**:012092

[23] Irzaman, Darmasetiawan H, Hardhienata H, Hikam M, Arifin P, Jusoh SN, Taking S, Jamal Z, Idris MA. Surface Roughness and Grain Size Characterization of Annealing Temperature Effect For Growth Gallium and Tantalum Doped $Ba_{0.5}Sr_{0.5}TiO_3$ Thin Film. Atom Indonesia. 2009;**35**(1):57-67

[24] Setiawan A, Aminullah, Juansah J, Irzaman. Optical and electrical characterizations of niobium-doped $Ba_{0.25}Sr_{0.75}TiO_3$ (BSNT) on p-type silicon and corning glass substrates and its implementation as photodiode on satellite of LAPAN–IPB. Procedia Environmental Sciences. 2016;**33**:620-625

[25] Nuayi AW, Alatas H, Husein IS, Rahmat M. Enhancement of photon absorption on $Ba_xSr_{1-x}TiO_3$ thin-film semiconductor using photonic crystal. International Journal of Optoelectronics. 2014;**2014**:1-8

[26] Djohan N, Estrada R, Sari D, Dahrul M, Kurniawan A, Iskandar J, Hardhienata H, Irzaman. The effect of annealing temperature variation on the optical properties test of $LiTaO_3$ thin films based on Tauc plot method for satellite technology. IOP Conference Series: Earth and Environmental Science. 2017;**54**:012093

[27] Irzaman, Putra IR, Aminullah, Syafutra H, Alatas H. Development of ferroelectric solar cells of barium strontium titanate ($Ba_xSr_{1-x}TiO_3$) for substituting conventional battery in LAPAN-IPB satellite (LISAT). Procedia Environmental Sciences. 2016;**33**:607-614

[28] Ismangil A, Irmansyah, Irzaman. The diffusion coefficient of lithium tantalite ($LiTaO_3$) with temperature variations on LAPAN-IPB satellite infra-red sensor. Procedia Environmental Sciences. 2016;**33**:668-673

[29] Yogaraksa T, Hikam M, Irzaman. Rietveld analysis of ferroelectric $PbZr_{0.525}Ti_{0.475}O_3$ thin films. Ceramics International. 2004;**30**(7):1483-1485

[30] Irzaman, Syafutra H, Arif A, Alatas H, Hilaluddin MN, Kurniawan A, Iskandar J, Dahrul M, Ismangil A, Yosman D, Aminullah LB, Prasetyo LB, Yusuf A, Kadri TM. Formation of solar cells based on $Ba_{0.5}Sr_{0.5}TiO_3$ (BST) Ferroelectric Thick Film; 2014. AIP Conference Proceedings. 2014;**1586**:24-34

[31] Jamal Z, Idris MS, Irzaman, Barmawi M. Lattice constants analysis of $Ba_xSr_{1-x}TiO_3$ ceramic for x = 0.3; 0.5 and 0.7 by visual basic program. Journal of Nuclear and Related Technology. 2007;**4**:7

[32] Ismangil A, Jenie RP, Irmansyah, Irzaman. Development of lithium tantalate ($LiTaO_3$) for automatic switch on LAPAN-IPB satellite infra-red sensor. Procedia Environmental Sciences. 2015;**24**:329-334

[33] Misbakhusshudur M, Ismangil A, Aminullah, Irmansyah, Irzaman. Phasor diagrams of thin film of $LiTaO_3$ as applied infrared sensors on satellite of LAPAN-IPB. Procedia Environmental Sciences. 2016;**33**:615-619

[34] Iskandar J, Syafutra H, Juansah J, Irzaman. Characterizations of electrical and optical properties on ferroelectric photodiode of barium strontium titanate ($Ba_{0.5}Sr_{0.5}TiO_3$) films based on the annealing time differences and its development as light sensor on satellite technology. Procedia Environmental Sciences. 2015;**24**:324-328

[35] Kurniawan A, Yosman D, Arif A, Juansah J, Irzaman. Development and application of $Ba_{0.5}Sr_{0.5}TiO_3$ (BST) thin film as temperature sensor for satellite technology. Procedia Environmental Sciences. 2015;**24**:335-339

[36] Irzaman, Siskandar R, Aminullah, Irmansyah, Alatas H. Characterization of $Ba_{0.55}Sr_{0.45}TiO_3$ films as light and temperature sensors and its implementation on automatic drying system model. Integrated Ferroelectrics. 2016;**168**(1):130-150

[37] Irzaman, Syafutra H, Rancasa E, Nuayi AW, Rahman TGN, Nuzulia NA, Supu I, Sugianto, Tumimomor F, Surianty, Muzikarno O, Masrur. The effect of Ba/Sr ratio on electrical and optical properties of $Ba_xSr_{(1-x)}TiO_3$ (x = 0.25; 0.35; 0.45; 0.55) thin film semiconductor. Ferroelectrics. 2013;**445**(1):4-17

[38] Fraden J. Handbook of Modern Sensors: Physics, Designs, and Applications. Singapore: Springer; 2010

[39] McGrath MJ, Scanaill CN. Sensing and sensor fundamentals. In: Sensor Technologies. Germany: Springer; 2013. pp. 15-50

[40] Council NR. Expanding the Vision of Sensor Materials. Washington, DC: National Academies Press; 1995

Ferroelectric Photovoltaic Effect

Rongli Gao, Zhenhua Wang, Chunlin Fu, Wei Cai,
Gang Chen and Xiaoling Deng

Additional information is available at the end of the chapter

http://dx.doi.org/10.5772/intechopen.78238

Abstract

Tetragonal $BiFeO_3$ films with the thickness of 30 nm were grown epitaxially on (001) oriented $LaAlO_3$ substrate by using pulsed laser deposition (PLD). The transverse photovoltaic effects were studied as a function of the sample directions in-plane as well as the angle between the linearly polarized light and the plane of the sample along X and Y directions. The absorption onset and the direct band gap are ~2.25 and ~2.52 eV, respectively. The photocurrent depends not only on the sample directions in-plane but also on the angle between the linearly polarized light and the plane of the sample along X and Y directions. The results indicate that the bulk photovoltaic effect together with the depolarization field was ascribed to this phenomenon. Detailed analysis presents that the polarization direction is along [110] direction and this depolarization field induced photocurrent is equal to ~3.53 μA/cm². The BPV induced photocurrent can be approximate described as $Jx \approx 2.23\cos(2\theta)$, such an angular dependence of photocurrent is produced as a consequence of asymmetric microscopic processes of carriers such as excitation and recombination.

Keywords: transverse, photovoltaic effect, depolarization, tetragonal $BiFeO_3$, photocurrent

1. Introduction

Driven by the energy crisis all over the world, more and more researchers have begun to investigate a broad spectrum of candidate materials for thin-film photovoltaic cells as a renewable energy production [1–3]. Among them, ferroelectric photovoltaic effect has been received considerable attention in the past few years because of its potential application in optoelectronics, information storage and energy conversion [4, 5]. However, different mechanisms have been proposed to explain experimental observations in the literature, such as the depolarization field effect [6–8], interface effect [9], domain theories [10], or spin polarization [11]. It is worth mentioning that bulk photovoltaic effect (BPVE) is another primary mechanism, which was discovered in noncentrosymmetric ferroelectrics several decades ago. It is often suggested that different from p-n junction based systems, BPVE does not require an asymmetric interface, especially its photovoltage is not limited by the band gap of the material, which can reach 10^3 V/cm or more and it is called anomalous photovoltaic effect [12–14]. All of the various ferroelectric materials, $BiFeO_3$ (BFO) is of particular interest because of its robust ferroelectricity, room temperature coexistence of ferroelectric and antiferromagnetic orders and the possible magnetoelectric couple effect. More important, the band gap of BFO (~2.7 eV) is smaller than many other ferroelectric materials (more than 3 eV), making it become a more suitable candidate materials for the next generational thin-film photovoltaic cells. Apart from the fundamental research on its ferroelectric properties, the photovoltaic effect of BFO has been reported in ceramics, nanowires, single crystals and highly oriented films [15–17]. However, in all of these studies, BFO is a rhombohedrally distorted perovskite [18] belonging to the $R3c$ space group, each Fe^{3+} center is coordinated by six O^{2-} ions, although the distortion along [111] yields a quasioctahedral arrangement [19]. Since its photovoltaic tensor have a nonzero G_{22} component, photocurrent should exist in the direction perpendicular to the ferroelectric polarization [20]. Recently, first-principles calculations predicted that a metal stable tetragonal (T) phase with a giant axial ratio (~1.27) and an extremely large spontaneous polarization of P ~ 150 μC/cm^2 can be achieved in BFO under a compressive strain [19], which were confirmed by several experiments [21–23]. Besides, the first principles theoretical calculations predict a smaller band gap in tetragonal BFO than in rhombohedral one [19]. Therefore, it is a great importance to research the photovoltaic effects due to its smaller band gap and more larger polarization as well as its special directions. In this letter, we report on photovoltaic devices based on tetragonal BFO thin films that demonstrate bulk photovoltaic effect and represent an interesting alternative material class for study of mechanism of photovoltaic effect and in pursuit of energy related applications.

2. Experimental process

Tetragonal phase $BiFeO_3$ (T-BFO) films of ~30 nm thickness were fabricated epitaxially by pulsed laser deposition (PLD) technique on (001)-oriented $LaAlO_3$. In this experimental process, KrF excimer laser with the wavelength of 248 nm was used for deposition, the deposition frequency is 3 Hz with an energy of about 240 mJ. The substrate was kept at 650°C with 11 Pa of oxygen atmosphere. In the course of deposition, the substrate holder was still rotated with the speed of 360°/min so that the thickness variation of the film can be reduced and the uniform composition of the film can be obtained as much as possible. Followed the deposition, oxygen stoichiometric T-BFO films were in situ annealed in 500 Pa oxygen pressure and cooled slowly down at 5°C/min to room temperatures to avoid the effect of deficient oxygen. Structural characterization was performed using X-ray diffraction (XRD), using M/s Bruker make D8-Discover system. Room temperature transmittance and reflectance spectra were collected by using a Perkin-Elmer Lambda-900 spectrometer (with the energy of 0.41–6.53 eV). For the conductive characteristics measurements, platinum electrodes of 200 μm length and interelectrode distances of 20 μm were fabricated by sputter deposition using conventional photolithography and lift-off technique. The photoelectric effect was measured by illuminating the gap between the electrodes with a $\lambda \approx 405$ nm ($E \approx 3.06$ eV) laser (Newport LQA405-85E) with a maximum power of 80 mW for the illumination, yielding the incident light power density on the sample surface up to 0.8 W/cm^2 and simultaneously measuring the photocurrent using a high-input impedance electrometer (Keithley 6517).

3. Results and discussion

Figure 1(a) shows the results of the X-ray diffraction θ–2θ scans of the T-BFO deposited on (001) LAO substrates. Only peaks corresponding to (00*l*) reflections of BFO and those from the substrate are seen, indicating the epitaxial growth of the films. The out-of-plane lattice parameter *c* calculated from the (00*l*) peaks is estimated to be ~4.67 Å, which is larger than that of rhombohedral BFO reported [14–16]. The larger lattice parameter c of T-BFO means that it is stabilized by a large compressive strain. The reciprocal-space map of BFO films indicates that the in plane parameter of BFO is very close to that of LAO, i.e., a ~ 3.79 Å and the BFO film with an out-of-plane lattice parameter of 4.67 Å were detected, indicating that the film is pure tetragonal-like. This corresponds to c/a ~ 1.27 for BFO in the sample. **Figure 1(b)** shows the topography of the corresponding film. The AFM image reveals a smooth surface morphology with a surface roughness of ~0.5 nm. In order to research the polarization direction, the planar Pt electrodes were patterned on the films to directly measure the in-plane P-E loops.

As shown schematically in **Figure 1(c)**, the edge of the Pt electrode was aligned along the [100] and [110] directions of the substrate, so as to ensure the electric field directions. The applied electric field *E* was determined using $E = V/d$, where *V* is the voltage and *d* is the channel width. **Figure 1(d)** shows the P-E hysteresis loop for the T-BFO films on LAO substrate when *E* is along the [100] and [110] directions, respectively. One can clearly see that hysteresis loop saturation in each direction is evident. The remnant polarization along the [100] and [110] directions are 30 and 37 μC/cm^2, respectively, consistent with previous study [24]. This different polarization in various directions should be attributed to the different polarization component. Besides, the coercive field along [110] is larger than that of [100] directions, this may be that the polarization in the [110] direction is more stable and domains wall pinning effect and grain boundary along different directions. It is noteworthy that the coercive field (E_c) along [110] is asymmetric in positive and negative position, which may be due to a residual strain in the crystal or might be the different internal field in each interface. The in-plane measure structure can be used to investigate the in-plane photovoltaic effect and strain effect of ferroelectric and multiferroic films.

The transmission spectrum of the samples were displayed in **Figure 2(a)**, the direct band gap is extracted by a linear extrapolation of an $(\alpha.E)^2 \sim E$ plot to zero, as shown in inset of **Figure 2(a)**. It is clear that the band gap in tetragonal $BiFeO_3$ is 2.52 eV, which is 0.13 eV smaller than that in rhombohedral $BiFeO_3$ (2.68 eV). This result is mainly consistent with the results from the theoretical calculations [19]. We have performed detailed photoelectric investigations on BFO epitaxial thin films with T-Phase to get a better insight into the actual

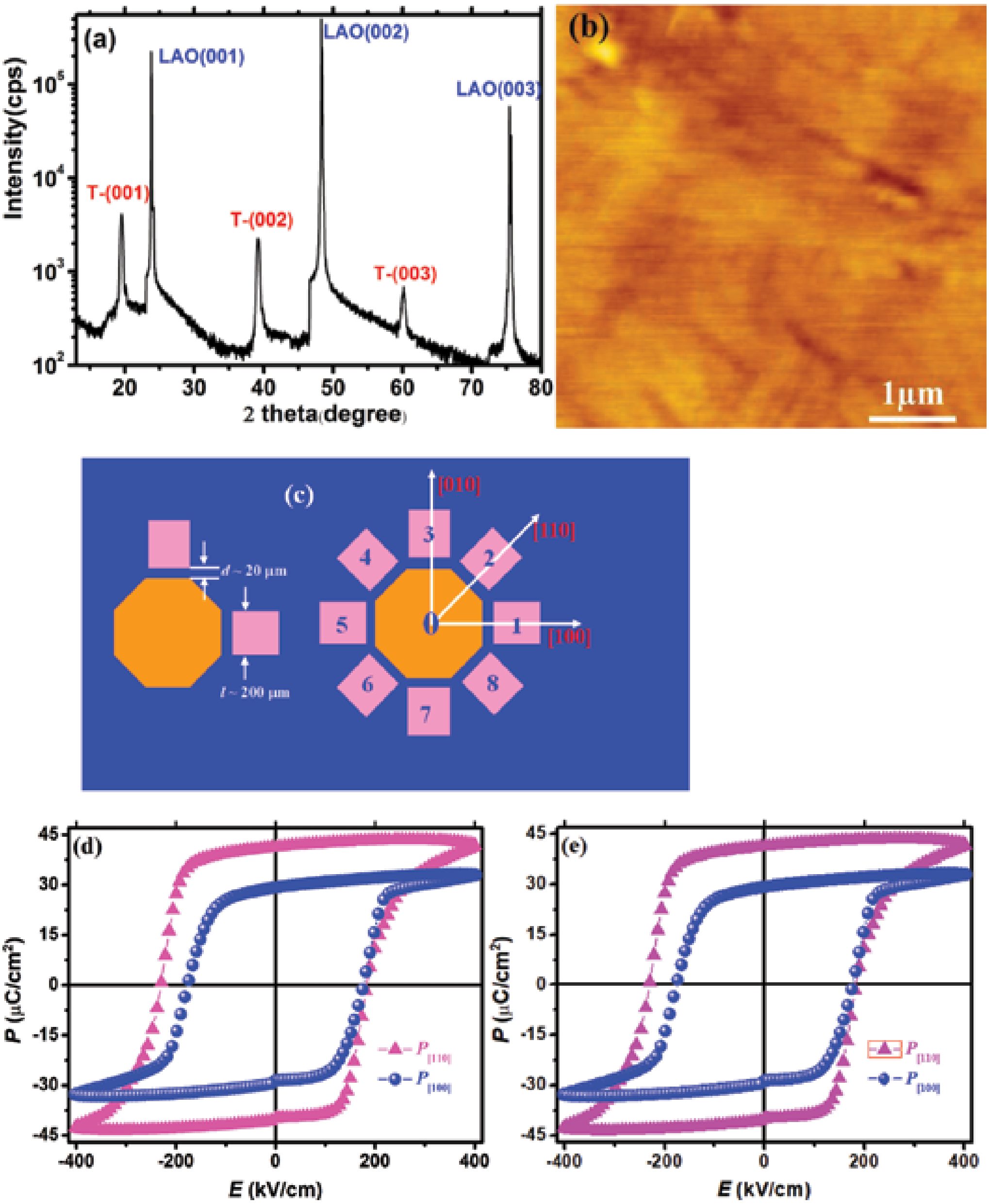

Figure 1. (a) XRD spectrum of tetragonal phase $BiFeO_3$ films grown on $LaAlO_3$ substrate. (b) The topography of the corresponding film by AFM. (c) Schematic illustration of the sample geometry used for the P-E curve measurements. (d) Field-dependent variation of P-E loops of the tetragonal $BiFeO_3$ films grown on $LaAlO_3$, and the applied electric field is along the [100] and [110] direction.

mechanism of ferroelectric photovoltaic effect. Pt in-plane electrodes with a gap of 20 μm were patterned by a standard photolithography process. The *x* axis is along the [100] direction and *y* axes is parallel to the [010] direction while *z* is perpendicular to both the *y* and *x* axes,

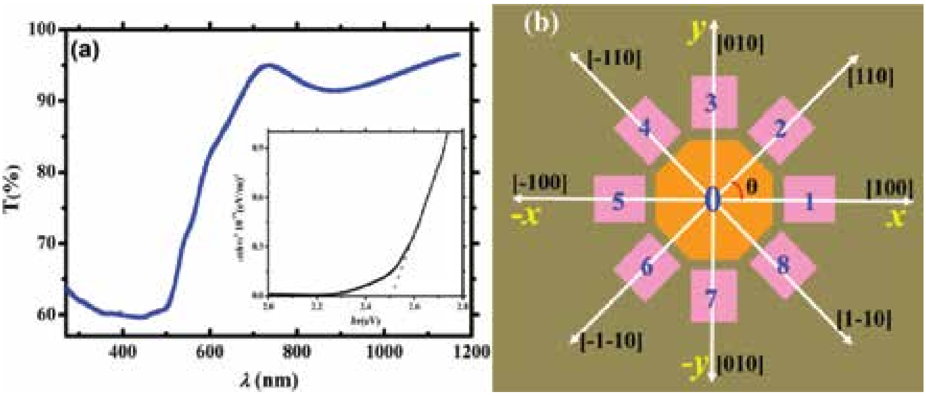

Figure 2. (a) Transmission spectrum of tetragonal BiFeO$_3$ films. Inset shows the direct band gap analysis. (b) Schematic illustration of the sample geometry used for the photocurrent measurements of the epitaxial tetragonal BFO thin film with in-plane electrodes. The angle between the polarizer transmission axis and the x axis is θ.

forming a right-hand coordinate system. The angle between the [100] direction (x axes) and the direction of current (I_{oc}) flow is θ, as shown in **Figure 2(b)**.

To measure the photovoltaic effect of T-BFO films, we illuminated the gap areas between the top Pt electrodes, unwanted light illumination on the surfaces was avoided by covering with black tape. In the process of measuring the photovoltaic effect, the central electrode was connected with the negative side of source meter (Keithley 6517) and the outer electrodes were linked to the positive one. The photocurrent density J was determined using $J = I/(d.t)$, where I is the measured short-circuit current voltage, d is the channel width and t is the film thickness, $J_{[hkl]}$ denotes the current flows along [hkl] direction, as shown in **Figure 2(b)**. **Figure 3(a)** shows time dependence of photocurrent density, showing a good retention of the photovoltaic effect, exhibiting no degradation when it was measured during several on-and-off cycles. The photocurrent density J along [100] direction ($J_{[100]}$ ~ 1.24 μA/cm^2) is always smaller than that of [110] direction ($J_{[110]}$ ~ 2.24 μA/cm^2), this distinct difference may be a result of a larger depolarization field along [110] direction compared with [100] direction due to the larger polarization along [110] direction, as shown in **Figure 1(d)**. From the P-E curves we can find that the polarization along (110) direction is larger than that of (001) and (010) directions, therefore we suppose that the component of polarization in the x-y plane should lie along the (110) direction. It was reported that photocurrent can be tuned by the depolarization field, i.e., different polarization will induce unlike photocurrent. Because the polarization along (110) direction is larger than that of (001) and (010) directions, thus, the depolarization filed along (110) direction is larger than that of (001) and (010) directions and so does the photocurrent. This result presents a evident influence of depolarization field on the transverse photovoltaic effects. To prove this viewpoint, we have reversed the polarization along the [100] and [110] directions to check the polarization dependence of photovoltaic effect. Both the photocurrent along [100] and [110] directions decrease after polarization switching, as shown in **Figure 3(b)**. This decreased photocurrent indicates that the photocurrent is at least composed of two parts, one is the contribution of depolarization field, another one will be discussed later.

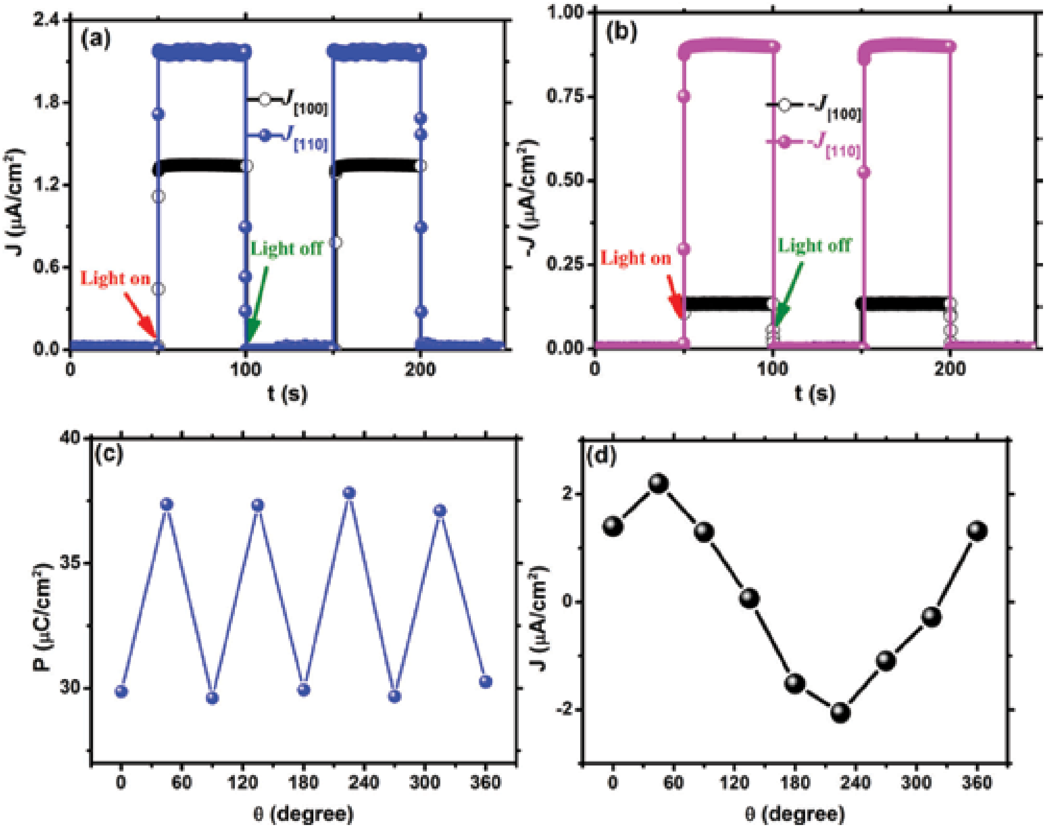

Figure 3. (a) Time dependence of short-circuit photocurrent for the $BiFeO_3$ samples with light on and off along [100] and [110] directions with the film is polarized by positive voltages. The negative electrode connected with point "0", i.e., the central electrode and the positive electrode connected with other points, i.e., the outer electrodes. (b) Time dependence of short-circuit photocurrent for the $BiFeO_3$ samples with light on and off along [100] and [110] directions with the film is polarized by negative voltages. (c) The angular dependence of polarizations. (d) Photocurrent as a function of crystal orientation.

In order to elucidate the crystallographic direction and polarization dependence of photocurrent, we measured the PV current by changing the angle between the [100] direction and the direction of current flow (x direction), i.e., measure the photocurrent and polarization along different directions, as shown in **Figure 3(c)** and **(d)**. We find that both the photocurrent and polarization along different directions show fluctuation behavior, more importantly than all of that, the absolute values of polarization along x and y axes are smaller than in other directions, while the photocurrent is a local maximum (~2.2 μA/cm²) parallel or antiparallel to [110] direction while the minimal value can be obtained when measured along [-110] or [1-10] directions. These results suggest that the different values of photocurrent along different crystallographic direction can be attributed to the inequality depolarization field and the minimum photocurrent occurs when it is perpendicular to the polarization directions. However, we found that the angular dependence of polarizations shows obvious difference from that of photocurrent, indicating that the photocurrent is not entirely decided by polarization, which presents typical bulk effect.

Therefore, our results mentioned above cannot be explained by the depolarization field effect simply. Such a crystallographic direction dependence can be described in the framework of the bulk photovoltaic (BPV) theory, where the photocurrent is produced as a consequence of asymmetric microscopic processes such as excitation and recombination of photon induced electrons and holes [25, 26]. According to this theory, the dependence of the photocurrent on the polarization orientation of incident light can be expressed by a bulk photovoltaic tensor. The BPV effect has been studied extensively, it is assumed that the photocurrent in non-centrosymmetric ferroelectrics materials depends on the orientation of the crystal with respect to the projections of the electric field of the linearly polarized light onto the plane of the sample along *X* and *Y* directions [26], when the light propagating along Z direction, the photocurrent generated along *X* and *Y* directions with can be expressed by [26–28].

$$J_x = -I\beta_{22}\sin 2\theta \text{ and } J_y = I\beta_{22}\cos 2\theta \tag{1}$$

where I, β_{22} and θ are the intensity of light, bulk photovoltaic tensor coefficient and the angle between the plane of the linearly polarized light and *X* direction.

In order to prove the existence of the BPV in our films, we measured the photo current for T-BFO films by changing the angle between the plane of the linearly polarized light and the direction of current flow (*x* direction). The schematic diagram of the experimental configuration was given in **Figure 4(a)**. The photo current was measured with the negative electrode connected with point "0", i.e., the central electrode and the positive electrode connected with outer electrodes. θ is defined as the angle between the linearly polarized light and the plane of the sample along *x* axes, i.e., the [100] direction. The photocurrent densities along and perpendicular [110] direction were measured at different polarizer angles for the samples, which is presented in **Figure 4**. It is clearly that the photocurrent exhibits definitive angular dependency, however, the magnitude and signs of the photocurrent varied with directions, i.e., the photocurrent is relatively smaller and the sign changes with angle when it perpendicular the [110] direction (that is, along [-110] or [1-10] directions), while it is larger and it is always a positive value since it is along [110] and [-1-10] directions. This result demonstrates that excepted for the BPV, other factors such as interfacial barrier, domain walls, depolarization field, as well as a misalignment between the light direction and the sample surface can contribute to the photocurrent. As a consequence, a constant current J_0 should be introduced to Eq. (1), which can be expressed as:

$$J_x = J_{x0} - I\beta_{22}\sin(2\theta + \theta_0) \text{ and } J_y = J_{y0} + I\beta_{22}\cos(2\theta + \theta_0) \tag{2}$$

For the above four directions, the results can be fitted very well to a cosine function. The fitting function is for the four directions as follows: $J_{[-110]} = -2.21\cos(2\theta - 13°)$, $J_{[1-10]} = -2.26\cos(2\theta - 12°)$, $J_{[110]} = -3.23 + 1.97\cos(2\theta - 9°)$, and $J_{[-1-10]} = 3.51 + 2.13\cos(2\theta - 11°)$, respectively. It is worth emphasizing again that the constant current J_0 is near zero for the [-110] and [1-10] directions, i.e., perpendicular the polarization direction ([110] direction), which shows typical bulk photovoltaic effect. However, the constant currents are −3.23 and 3.51 for [110] and [-1-10]

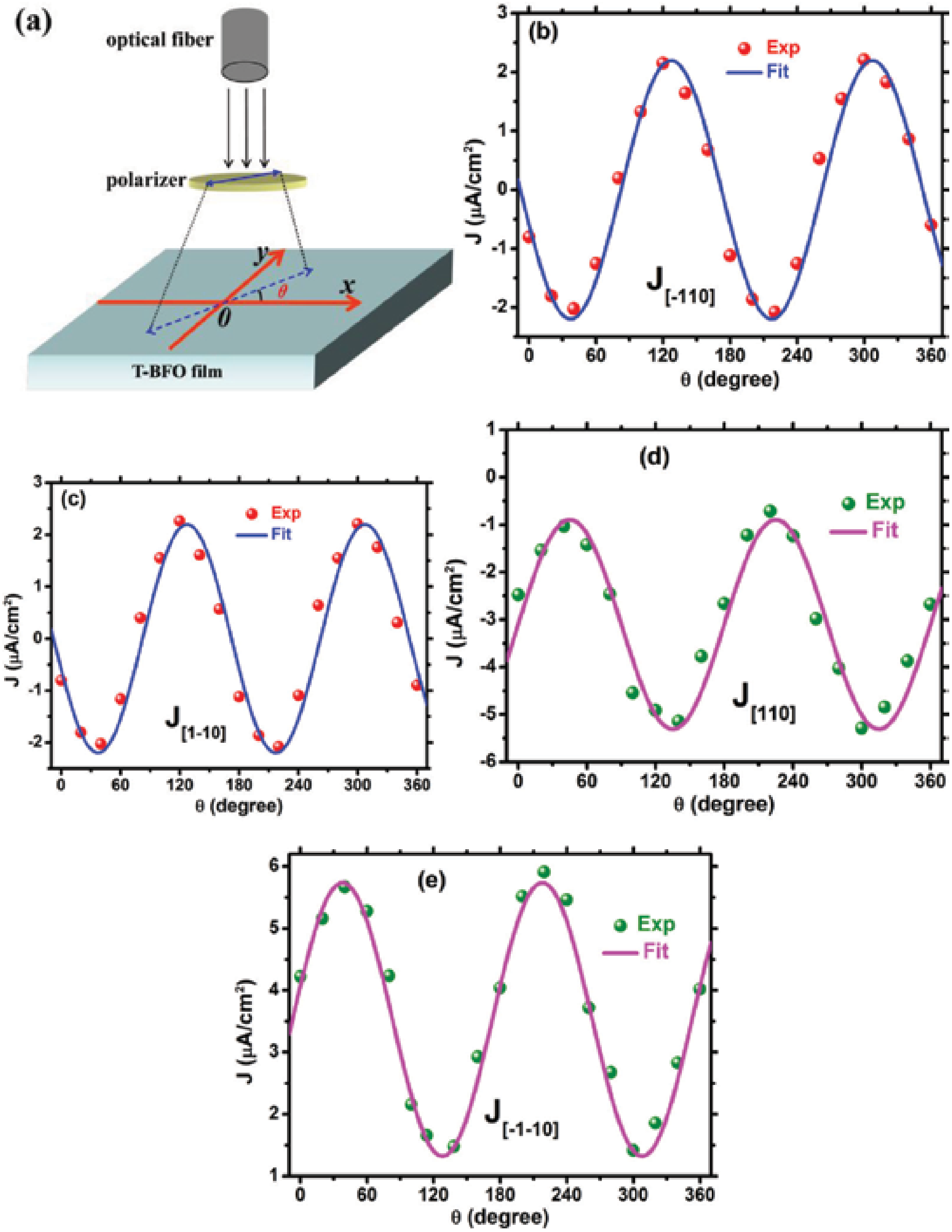

Figure 4. (a) The schematic diagram of the experimental configuration. The photocurrent was measured with the negative electrode connected with the central electrode and the positive electrode connected with the outer electrodes. θ is defined as the angle between the linearly polarized light and the plane of the sample along x axes, i.e., the (100) direction. Photocurrent measured at different angles, with the direction of the current flow along [-110] direction (b), [1-10] direction (c), [110] direction (d) and [-1-10] direction (f). The solid line represents the fit with Eq. (2).

directions, respectively. We argue that this different positive and negative constant current can be attributed to the depolarization field effect, different direction of depolarization field will lead to different photocurrent because the photocurrent is opposite to that of polarization direction according to depolarization theory [13]. Nonetheless, we note that the compensated angle θ is near the same and is very closer to zero, this very small compensated angle may be a result of the misalignment between the light beam direction and the normal to the sample surface while the constant current J_0 parallel to the [110] and [-1-10] directions should have been ascribed to the depolarization or the asymmetry interface barriers between the internal electrode and outer electrode. Combined the results of **Figures 3** and **4** with **Figure 1(e)**, we can deduce that although the polarization direction in the tetragonal phase BFO films lies nearly the (001) direction, a fraction of the component of polarization direction on the sample surface lies along the [110] direction. It should be emphasized that the photocurrent measured perpendicular to [110] direction is perpendicular to the ferroelectric polarization, hence, the results cannot be explained by the depolarization field. Moreover, The use of symmetric in-plane Pt electrodes can exclude the photovoltaic effect from the interfacial energy barriers mostly, and domain walls cannot explain the angular dependence of the photocurrent and thus they can be excluded here.

Therefore, the photovoltaic effect along [-110] and [1-10] directions are both perpendicular to [110] direction, which is a product of BPV, yet it is a total effects combined depolarization and BPV effects when the photocurrent measured parallel to [110] and [-1-10] directions. Based on above analysis, depolarization field induced photocurrent is equal to the constant current J_0 (~3.53 μA/cm^2). The BPV induced photocurrent can be approximate described as $Jx \approx 2.23\cos(2\theta)$, such an angular dependence of photocurrent is produced as a consequence of asymmetric microscopic processes of carriers such as excitation and recombination [5].

4. Conclusions

Tetragonal $BiFeO_3$ films with the thickness of 30 nm were grown epitaxially on (001) oriented $LaAlO_3$ substrate by using pulsed laser deposition (PLD) and the photovoltaic effect of tetragonal $BiFeO_3$ along different crystallographic direction with in plane symmetric electrodes was investigated, the absorption onset and the direct band gap are ~2.25 and ~2.52 eV, respectively. The photocurrent exhibits definitive angular and direction dependency, indicating obvious bulk photovoltaic effect and depolarization field effect. The photocurrent depends not only on the sample directions in-plane but also on the angle between the linearly polarized light and the plane of the sample along X and Y directions. The polarization direction is along [110] direction and the photocurrent induced by this depolarization field is as large as ~3.53 μA/cm^2, while the BPV induced photocurrent can be described as $Jx \approx 2.23\cos(2\theta)$, such an angular dependence of photocurrent is produced as a consequence of asymmetric microscopic processes of carriers such as excitation and recombination. These results indicate that the BPV and depolarization field effect in tetragonal $BiFeO_3$ thin films could be further explored for the next generation of solar photovoltaic applications.

Acknowledgements

This work is supported by the National Natural Science Foundation of China (51402031), the Program for Innovation Teams in University of Chongqing, China (Grant no. CXTDX201601032) and the Natural Science Foundation Project of Chongqing (CSTC2015jcyjA50015).

Author details

Rongli Gao[1,2]*, Zhenhua Wang[1,2], Chunlin Fu[1,2], Wei Cai[1,2], Gang Chen[1,2] and Xiaoling Deng[1,2]

*Address all correspondence to: gaorongli2008@163.com

1 School of Metallurgy and Materials Engineering, Chongqing University of Science and Technology, Chongqing, China

2 Chongqing Key Laboratory of Nano/Micro Composite Materials and Devices
Chongqing, China

References

[1] Ginley D, Green MA, Collins R. Solar energy conversion toward 1 terawatt. MRS Bulletin. 2008;**33**:355

[2] Gur I, Fromer NA, Geier ML, Alivisatos AP. Air-stable all-inorganic nanocrystal solar cells processed from solution. Science. 2005;**310**:462

[3] O'Regan B, Grätzel M. Optical electrochemistry I: Steady-state spectroscopy of conduction-band electrons in a metal oxide semiconductor electrode. Nature London. 1991;**353**:737

[4] Fridkin VM, Popov BN. Anomalous photovoltaic effect in ferroelectrics. Soviet Physics Uspekhi. 1978;**21**:981

[5] Glass AM, von, der Linde D, Negran TJ. High-voltage bulk photovoltaic effect and the photorefractive process in $LiNbO_3$. Applied Physics Letters. 1974;**25**:233

[6] Glass AM, von, der Linde D, Auston DH, Negran TJ. Excited state polarization, bulk photovoltaic effect and the photorefractive effect in electrically polarized media. Journal of Electronic Materials. 1975;**4**:915

[7] Brody PS, Crowne F. Mechanism for the high voltage photovoltaic effect in ceramic ferroelectrics. Journal of Electronic Materials. 1975;**4**:955

[8] Nelson J. The Physics of Solar Cells. London: Imperial College Press; 2003

[9] Gregg BA. Excitonic solar cells. The Journal of Physical Chemistry B. 2003;**107**:4688

[10] Yang SY, Seidel J, Byrnes SJ, Shafer P, Yang C-H, Rossell MD, Yu P, Chu Y-H, Scott JF, Ager JW, III LWM, Ramesh R. Above-bandgap voltages from ferroelectric photovoltaic devices. Nature Nanotechnology. 2010;**5**:143-147

[11] Ganichev SD, Prettl W. Spin photocurrents in quantum wells. Journal of Physics: Condensed Matter. 2003;**15**:R935

[12] Basu SR, Martin LW, Chu Y-H, Gajek M, Ramesh R, Rai RC, Xu X, Musfeldt JL. Photoconductivity in $BiFeO_3$ thin films. Applied Physics Letters. 2008;**92**:091905

[13] Gao RL, Yang HW, Sun JR, Zhao YG, Shen BG. Oxygen vacancies induced switchable and nonswitchable photovoltaic effects in $Ag/Bi_{0.9}La_{0.1}FeO_3/La_{0.7}Sr_{0.3}MnO_3$ sandwiched capacitors. Applied Physics Letters. 2014;**104**:031906

[14] Wang J, Neaton JB, Zheng H, Nagarajan V, Ogale SB, Liu B, Viehland D, Vaithyanathan V, Schlom DG, Waghmare UV, Spaldin NA, Rabe KM, Wuttig M, Ramesh R. Epitaxial BiFeOmultiferroic thin film heterostructures. Science. 2003;**299**:1719

[15] Catalan G, Scott JF. Physics and Applications of Bismuth Ferrite. Advanced Materials. 2009;**21**:2463

[16] Li JF, Wang JL, Wutiig M, Ramesh R, Wang NG, Ruette B, Pyatakov AP, Zvezdin AK, Viehland D. Dramatically enhanced polarization in (001), (101), and (111) BiFeO3 thin films due to epitiaxial-induced transitions. Applied Physics Letters. 2004;**84**:5261

[17] Gao RL, Chen YS, Sun JR, Zhao YG, Li JB, Shen BG. Complex transport behavior accompanying domain switching in $La_{0.1}Bi_{0.9}FeO_3$ sandwiched capacitors. Applied Physics Letters. 2012;**101**:152901

[18] Fischer P, Polomska M, Sosnowska I, Szymanskig M. Temperature dependence of the crystal and magnetic structures of $BiFeO_3$. Journal of Physics C. 1980;**13**:1931

[19] Tütüncü HM, Srivastava GP. Electronic structure and lattice dynamical properties of different tetragonal phases of $BiFeO_3$. Physical Review B. 2008;**78**:235209

[20] Fridkin VM. Bulk photovoltaic effect in noncentrosymmetric crystals. Crystallography Reports. 2001;**46**:654

[21] Ederer C, Spaldin NA. Effect of epitaxial strain on the spontaneous polarization of thin film ferroelectrics. Physical Review Letters. 2005;**95**(25):257601

[22] Cheng CJ, Lu CL, Chen ZH, You L, Chen L, Wang J, Wu T. Thickness-dependent magnetism and spin-glass behaviors in compressively strained $BiFeO_3$ thin films. Applied Physics Letters. 2011;**98**(24):242502

[23] Zhang JX, He Q, Trassin M, Luo W, Yi D, Rossell MD, Yu P, You L, Wang CH, Kuo CY, Heron JT, Hu Z, Zeches RJ, Lin HJ, Tanaka A, Chen CT, Tjeng LH, Chu YH, Ramesh R. Microscopic origin of the giant ferroelectric polarization in tetragonal-like $BiFeO_3$. Physical Review Letters. 2011;**107**(14):147602

[24] Chen ZH, Zou X, Ren W, You L, Huang CW, Yang YR, Yang P, Wang JL. Study of strain effect on in-plane polarization in epitaxial BiFeO3 thin films using planar electrodes. Physical Review B. 2012;**86**:235125

[25] Chen P, Podraza NJ, Xu XS, Melville A, Vlahos E, Gopalan V, Ramesh R, Schlom DG, Musfeldt JL. Optical properties of quasi-tetragonal $BiFeO_3$ thin films. Applied Physics Letters. 2010;**96**:131907

[26] Sturman BI, Fridkin VM. The Photovoltaic and Photorefractive Effects in Noncentrosymmetric Materials. Gordon and Breach Science; 1992

[27] Ji W, Yao K, Liang YC. Evidence of bulk photovoltaic effect and large tensor coefficient in ferroelectric $BiFeO_3$ thin films. Physical Review B. 2011;**84**:094115

[28] Festl HG, Hertel P, Kratzig E, von Baltz R. Investigations of the Photovoltaic Tensor in Doped $LiNbO_3$. Physica Status Solidi (B). 1982;**113**:157-164

Chapter 3

Nonlinear Optical Effects at Ferroelectric Domain Walls

Xin Chen, Wieslaw Krolikowski and Yan Sheng

Additional information is available at the end of the chapter

http://dx.doi.org/10.5772/intechopen.77238

Abstract

Ferroelectric materials tend to form macroscopic domains of electric polarization. These domains have different orientations and coexist in the medium being separated by domain walls. In general, symmetry and structure of ferroelectric domain walls differ from their parent materials and consequently lead to abundant physical properties. In this book chapter, we review the nonlinear optical effects which are bundled with ferroelectric domain walls or whose properties can be significantly enhanced by the presence of domain walls. In particular, we have reviewed Google Scholar articles from 2008 to 2018 using the keywords "nonlinear Čerenkov radiation from ferroelectrics". We show that the spatially steep modulation of the second-order nonlinear optical coefficient across the domain wall leads to strong emission of the Čerenkov second harmonic in bulk materials. This feature also enables an effective nondestructive method for three-dimensional visualization and diagnostics of ferroelectric domain structures with very high resolution and high contrast.

Keywords: ferroelectric domain wall, second harmonic generation, nonlinear Čerenkov radiation, nonlinear diffraction, optical imaging

1. Introduction

The ferroelectric phenomenon was discovered in 1921 by J. Valasek during an investigation of the anomalous dielectric properties of Rochelle salt, $NaKC_4H_4O_6 \cdot 4H_2O$ [1]. During the last few decades, the group of ferroelectric materials has been extended to over 250 pure materials and many more mixed crystal systems. They are intensively investigated because of a wide range of actual and potential applications of ferroelectric in critical fields such as electronics, nonvolatile memories, photonics, photovoltaics, etc. [2–8]. The ferroelectric materials generally consist of small uniform regions in which the spontaneous polarization points to the same direction, called ferroelectric domains. The interfaces separating different domains in a crystal are called domain walls. For example, there are "180° walls" separating domains with oppositely orientated polarizations and "90° walls" separating regions with mutually perpendicular polarizations. The ferroelectric domain walls have symmetry and structure different from their parent materials and consequently possess many various physical properties including huge conductivity and anomalous dielectric responses [4–7].

Lithium niobate ($LiNbO_3$) is a ferroelectric crystal with important photonics applications thanks to its excellent electro-optic, acousto-optic, and nonlinear optical properties. The crystal supports two distinct orientations of the spontaneous polarization along its optical (z) axis, i.e., only 180° domains exist in $LiNbO_3$ crystals. Most importantly for nonlinear optical applications, the ferroelectric domains in $LiNbO_3$ crystal can be periodically aligned by using external stimuli such as external electric field [9] or intense light field [10–13]. The alternative orientations of spontaneous polarization amounts to a spatial modulation of the second-order nonlinear coefficient of the crystal, an essential condition of the so-called quasi-phase-matching (QPM) technique, where the phase mismatch of a nonlinear optical process is compensated by one of the resulting reciprocal lattice vectors induced by the nonlinearity modulation. In the simplest case of second harmonic generation (SHG) in the medium, the quasi-phase-matching condition (which is equivalent to conservation of the momentum of interacting waves) can be expressed as $k_2 - 2k_1 = G$, where k_2 and k_1 represent wave vectors of the second harmonic and fundamental waves, respectively. G is the magnitude of the reciprocal vector of the nonlinearity grating.

It has been recently reported that efficient second-order nonlinear optical effects can also occur in an extreme case where only a single-domain wall was involved [14–16]. In fact the steep change of the second-order (χ^2) nonlinearity across the domain wall gives rise for the appearance of the so-called nonlinear Čerenkov radiation, whose emission angle is defined by the longitudinal phase-matching condition [17]. In case of frequency doubling via the Čerenkov second harmonic generation (ČSHG), the second harmonic signal is observed at the angle θ_C defined as $k_2 \cos\theta_C - 2k_1 = 0$ [see **Figure 1(a)**]. The nonlinear Čerenkov interaction has been intensively investigated recently to fully understand all aspects of this fundamental

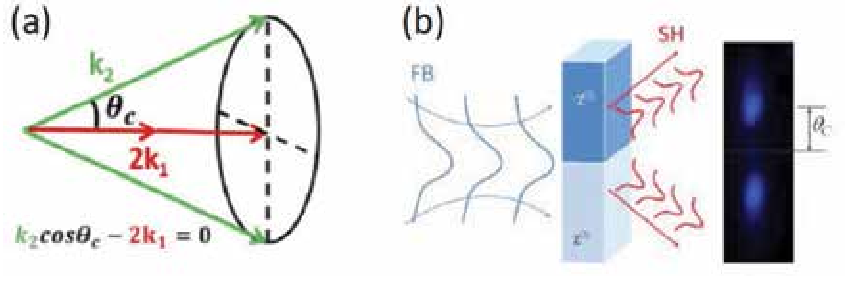

Figure 1. (a) The phase-matching diagram of Čerenkov-type second harmonic generation, where the harmonic emission angle is determined by the longitudinal phase-matching condition, i.e., $k_2 \cos\theta_C - 2k_1 = 0$. (b) Illustration of an experimental observation of the Čerenkov second harmonic generation at a single ferroelectric domain wall. FB, fundamental beam, and SH, second harmonic; represent the second-order nonlinear coefficient of the material [15].

phenomenon and also because of a number of important actual and potential applications in nonlinear optical microscopy [18, 19], ultrashort pulse characterization [20], high harmonic generations [21], and functional materials analysis [22].

In this chapter we review the latest research achievements in both experimental and theoretical studies of the nonlinear Čerenkov interactions that are closely associated with the existence of ferroelectric domain walls. In particular, we discuss two situations, namely, the nonlinear effects arising from a single ferroelectric domain wall and those coming from the multiple domain walls. We solve nonlinear coupled equations for the second harmonic generation and show how the efficiency of these nonlinear interactions depends on the structures of ferroelectric domain patterns and conditions of fundamental wave. These results are important for better understanding of second-order nonlinear optics and inspire optimizing the process for practical applications.

2. Approach and methodology

The authors of this book chapter have been active in the field of nonlinear Čerenkov radiation from domain-engineered ferroelectric crystals for many years. Their latest research outcomes constitute the main body of this review. More details about these research works are available in the authors' publications, which have been correctly cited in the "References." Meanwhile, the authors have also reviewed other research groups' Google Scholar articles on this topic and have included some milestones in this chapter. These research progresses are organized into two categories according to the number of ferroelectric domain walls involved in the interaction, namely, the nonlinear Čerenkov radiations from a single-domain wall and those from multiple walls. In each category, not only experimental research but also theoretical treatment (using, e.g., the standard fast Fourier-transform-based beam propagation method) have been presented.

3. Čerenkov-type second harmonic generation from a single ferroelectric domain wall

The experimental generation of the Čerenkov second harmonic is schematically illustrated in **Figure 1(b)**. The fundamental beam (FB) generally propagates along a ferroelectric domain wall. A pair of beams at doubled frequency, i.e., the second harmonic (SH), is observed in the far field. Their emission angle agrees with that defined by the longitudinal phase-matching condition, i.e., as $\theta_C = \cos^{-1}(2k_1/k_2) = \cos^{-1}(n_1/n_2)$, where n_1 and n_2 are refractive indices of the fundamental and second harmonic waves, respectively. It is clear that the Čerenkov angle depends strongly on material properties. It is worth noting that the efficiency of Čerenkov harmonic generation in a single-domain (homogeneous $\chi^{(2)}$) crystals is low and its experimental observations have been scarce. As we show below, the emission of Čerenkov signal can be strongly enhanced by the presence of ferroelectric domain wall in the beam illuminated area.

For a better understanding of the Čerenkov-type second harmonic generation at a single ferroelectric domain walls, the nonlinear optical interactions from a material system consisting of semi-infinite regions with different quadratic nonlinear responses $\chi^{(2)}$ and $\tilde{\chi}^{(2)}$, as shown in **Figure 2(a)**, are treated both numerically and analytically. We assume the fundamental Gaussian beam (wavelength λ_1 and beam width w) propagates along the boundary separating both media. To avoid any possible influence of the discontinuity in the linear polarization, the refractive index of the system is assumed to be homogenous.

The interaction of the fundamental and second harmonic waves in the nonlinear optical medium is described by the following system of coupled wave equations [23]:

$$\begin{aligned} \frac{\partial E_1}{\partial z} &= \frac{i}{2k_1}\nabla_\perp^2 E_1 - i\frac{\omega_1^2\chi^{(2)}(x)}{k_1c^2}E_1^* E_2 e^{i(k_2-2k_1)z}; \\ \frac{\partial E_2}{\partial z} &= \frac{i}{2k_2}\nabla_\perp^2 E_2 - i\frac{\omega_2^2\chi^{(2)}(x)}{2k_2c^2}E_1^2 e^{i(2k_1-k_2)z}. \end{aligned} \tag{1}$$

In these equations ω_1 and $\omega_2 = 2\omega_1$ are the fundamental and SH frequencies, respectively. We assumed that the field can be decomposed into a superposition of these two frequencies, with stationary envelopes and fast oscillating term:

$$E = E_1(x,z)e^{i(k_1z-\omega_1t)} + E_2(x,z)e^{i(k_2z-\omega_2t)} + c.c. \tag{2}$$

Here only the contributions from the diffraction and the quadratic nonlinearity are included, and no transient behavior or interface enhanced linear and/or nonlinear effects are considered.

We numerically solve the Eq. (1) by using the standard fast-Fourier-transform-based beam propagation method. We use the dispersion data of $LiNbO_3$ crystal [24] in simulations. In **Figure 3**, we depict the far-field SH distributions versus the propagation distance, calculated with the fundamental beam propagating along two types of $\chi^{(2)}$ boundary in nonlinear media. **Figure 3(a)** shows the SHG when the nonlinearity changes its sign across the boundary, i.e., $\chi^{(2)} = -\tilde{\chi}^{(2)} = \chi_0^{(2)}$. The strong emission of Čerenkov SHG is observed around 28.6° for the

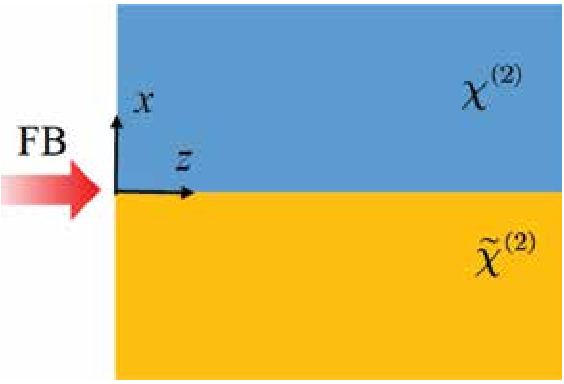

Figure 2. Schematic of the simulation with second harmonic generation in optical media containing two layers of different nonlinear optical responses: $\chi^{(2)}$ and $\tilde{\chi}^{(2)}$.

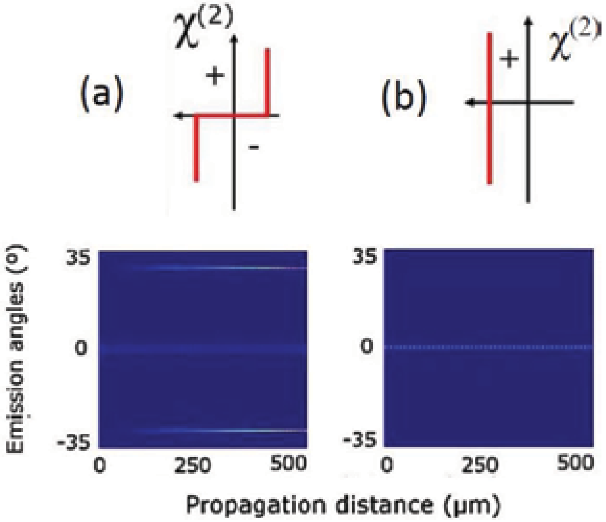

Figure 3. Far-field intensity of the second harmonic generation in composite media with fundamental beam propagating (a) along ferroelectric domain wall and (b) in a homogeneous $\chi^{(2)}$ medium.

fundamental wavelength $\lambda_1 = 1.2\ \ \mu m$, in a good agreement with the calculated Čerenkov angle for the LiNbO$_3$ [24]. It is clearly seen that the Čerenkov signal grows monotonically with the interaction distance, which is a typical feature of the longitudinally phase-matched nonlinear interactions. This simulation represents the experimental generation of nonlinear Čerenkov radiation on a single ferroelectric domain wall, across which the second-order nonlinear coefficient alters its sign. In **Figure 3(b)**, we show the calculated SHG in a homogenous $\chi^{(2)}$ medium, i.e. $\chi^{(2)} = \tilde{\chi}^{(2)} = \chi_0^{(2)}$. In this situation only the phase-mismatched, forward second harmonic signal is present. There is no trace of noncollinear Čerenkov harmonic signal. Compared with results shown in **Figure 3(a)**, we confirm the presence of a sharp spatial variation of the $\chi^{(2)}$ nonlinearity forms a sufficient condition for efficient nonlinear Čerenkov radiation.

The behavior becomes even clearer if we analytically deal with the frequency conversion process assuming the undepleted fundamental beam. In this case from Eq. (1), we can obtain the following formula to describe the strength of the nonlinear Čerenkov signal [15]:

$$E_{SH} \propto z \int_{-\infty}^{+\infty} \chi^{(2)}(x) E_1^2(x,z) e^{ik_c x} dx, \tag{3}$$

in which k_c represents the transverse component of the Čerenkov second harmonic wave vector. According to Eq. (3) the amplitude of the Čerenkov signal is defined by the Fourier transform of the product of nonlinearity distribution function $\chi^{(2)}(x)$ and the spatial distribution of the squared amplitude of the fundamental wave $E_1^2(x,z)$. Eq. (3) takes large value as long as its kernel undergoes a fast spatial variation. There are two ways to satisfy this condition. The first is to employ a spatial variation of the second-order nonlinearity $\chi^{(2)}$ in the transverse direction, e.g., propagating the fundamental wave along a ferroelectric domain wall [as shown in **Figure 3(a)**]. The other is to impose a strong spatial confinement to the fundamental beam, namely, to create a spatially confined $E_1^2(x,z)$. This agrees with the presence of Čerenkov harmonic signal with an assumption of the well-defined rectangular profile of the fundamental beam in [25]. Similar effect was also reported in [26], which shows that a non-diffracting Bessel fundamental beam can lead to nonlinear Čerenkov radiation in a homogeneous crystal.

3.1. Nonlinear diffraction from multiple ferroelectric domain walls

When the fundamental beam is wide enough to cover multiple ferroelectric domain walls, the second harmonic shows more complicated far-field intensity distribution. In fact each domain wall can contribute toward its own Čerenkov second harmonic, and these harmonics will interfere with each other, leading to the so-called nonlinear diffraction [27]. As shown in **Figure 4(a)**, the second harmonic pattern in this case generally consists of two types of spots [15]: (i) peripheral Čerenkov harmonic spots, situated relatively far from the fundamental beam at both sides of the diffraction pattern (top and bottom pairs in the figure), and (ii) central diffraction spots, grouped around the pump position, which is called nonlinear Raman-Nath diffraction, because of its close analogy to the linear Raman-Nath diffraction from a dielectric grating.

In fact Eq. (3) can still be used to calculate the Čerenkov second harmonic from multiple ferroelectric domain walls, except that the $\chi^{(2)}(x)$ is now a periodic function of spatial variable [28]. For 1D periodic domain pattern, the function $\chi^{(2)}(x)$ can be expressed as the following Fourier series:

$$\chi^{(2)}(x) = \sum_{m=0,\pm1,\pm2} g_m e^{imG_0X}. \tag{4}$$

Here $G_0 = 2\pi/\Lambda$ is the primary reciprocal lattice vector (Λ is the modulation period of $\chi^{(2)}$ grating), the coefficients $g_m(m \neq 0) = 2\sin(\pi m D)/\pi m$ and $g_0 = 2D - 1$ with D being the duty cycle defined by the ratio of the length of the positive domains to the period of the $\chi^{(2)}$ structure. Considering a fundamental Gaussian beam, i.e., $E_1(x) = e^{-(x-x_0)^2/a^2}$ (with a being the beam width and x_0 denoting the central position of the beam), the integral in Eq. (3) can be evaluated as

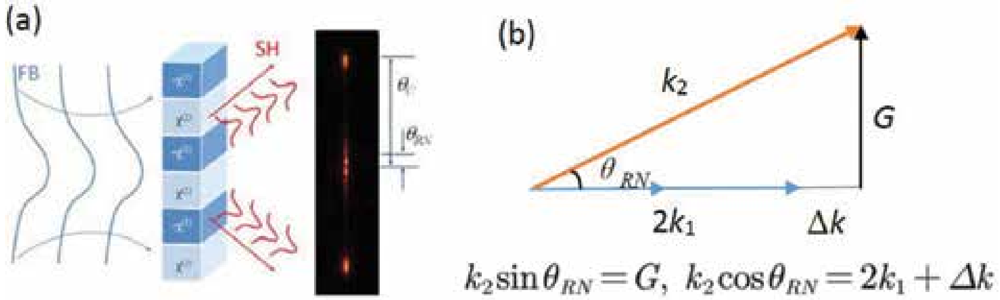

Figure 4. (a) Scheme of Čerenkov SH emission in a 1D periodically poled $LiNbO_3$ crystal. The right inset shows experimentally recorded far-field second harmonic image. The SH spots at small angles (θ_{RN}) represent the Raman-Nath emission, while the spot at bigger angles θ_C is the Čerenkov second harmonics [15]. (b) The phase-matching diagram of the nonlinear Raman-Nath diffraction, which satisfies only the transverse phase-matching condition $k_2\sin\theta_{RN} = G$.

$$\int \chi^{(2)}(x)E_1^2(x)e^{ik_c x}dx = a(\pi/2)^{1/2} \times \sum_{m=0,\pm 1,\pm 2,\ldots} g_m e^{-a^2(mG_0+k_c)^2/8} e^{i(mG_0+k_c)x_0}. \tag{5}$$

According to the definition of the Čerenkov second harmonic generation, the variation of the fundamental wavelength leads to the harmonic emission at different angles, i.e. the spatial frequency k_c in Eq. (5) changes. As a result, the intensity of the Čerenkov second harmonic signal varies as well considering the fact that different k_c corresponds to different Fourier coefficients g_m. In **Figure 5**, we show the wavelength response, i.e., the value $|E_{SH}|^2$ of the Čerenkov SH generated by the fundamental Gaussian wave with different beam widths (*a*). When a wide fundamental beam is used, for instance, $a = 60$ μm, the strength of the Čerenkov signal is very sensitive to the wavelength, showing a series of intensity peaks [see **Figure 5(a)**]. The emission is quite strong at these peak wavelengths (e.g., at $\lambda_1 = 1.108$ μm) but falls dramatically at the others (e.g., at $\lambda_1 = 1.038$ μm). Such a sensitive dependence of the Čerenkov second harmonic intensity on the fundamental wavelength is a typical characteristic of light interference in the case of multiple domain walls. It is very interesting to see that, depending on the value of beam width *a*, the wavelength tuning shows weaker dependence on the wavelength, namely, the less contribution from the interference effect. Finally when the width of the fundamental beam becomes so narrow that it covers only a single-domain wall (e.g., $a = 2$ μm), all second harmonic peaks disappear, and the Čerenkov intensity exhibits monotonic dependence on wavelength.

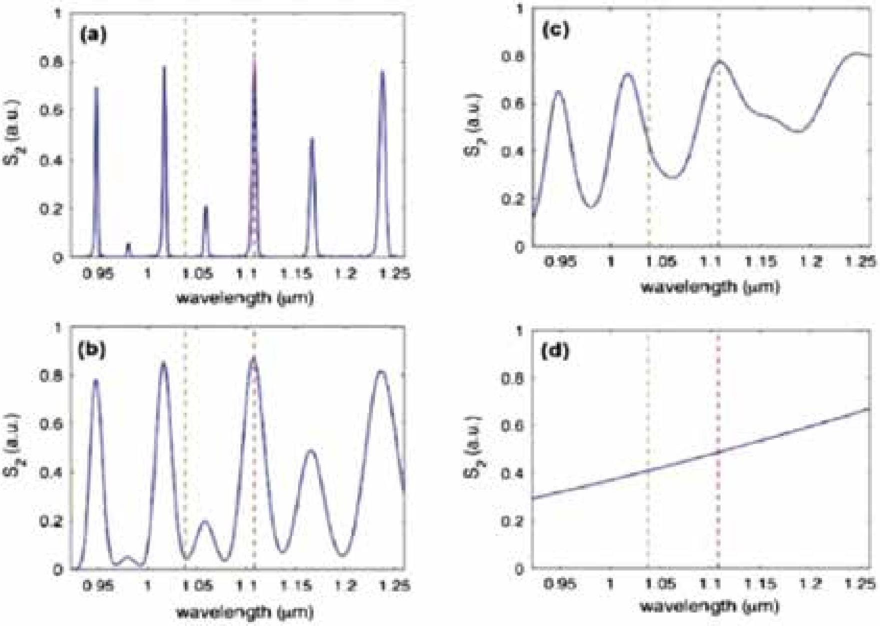

Figure 5. The spectral response of the Čerenkov SHG for different beam widths [28]. From (a) to (d), the beam widths of the fundamental wave are 60, 10, 5, and 2 μm, respectively. The plots are normalized to their individual maximum value.

In contrast to the Čerenkov emission defined by the fulfillment of the longitudinal phase-matching condition, the other group of the second harmonic diffraction spots (central spots located close to the pump in **Figure 4(a)**) only satisfies the transverse phase-matching (TPM) conditions, i.e., $\sin\theta_{RN} = mG_0/k_2$, for the *m*th diffraction order, *m* = 1,2,3… The external angles are then determined as follows:

$$\sin\beta_m = m\lambda_2/\Lambda,\ m = 1, 2, ..., \tag{6}$$

where λ_2 is the SH wavelength. This is a generic condition that holds for any periodic $\chi^{(2)}$ structure and does not depend on its refractive index.

The intensity of the nonlinear Raman-Nath second harmonic diffraction depends strongly on the duty cycle of the $\chi^{(2)}$ grating [29]. In fact the impact of the duty cycle on the nonlinear Raman-Nath diffraction is very similar to that in linear diffraction on dielectric grating. The duty cycle directly determines the Fourier coefficient g_m in Eq. (4), so it will cause the variation of the efficiency of nonlinear Raman-Nath diffraction. The detailed influence of duty cycle on the Raman-Nath diffraction from a periodic ($\Lambda = 9\ \mu m$) ferroelectric domain structure is shown in **Figure 6**. Agreeing quite well with the equation of Fourier coefficient $g_m(m \neq 0) = 2\sin(\pi m D)/\pi m$, the first-order Raman-Nath harmonic diffraction (*m* = 1) takes the maximum intensity at duty cycle *D* = 0.5, while the second-order (*m* = 1) exhibits two equal maxima at *D* = 0.25 and 0.75, respectively.

We consider now the influence of the structure randomness of ferroelectric domain patterns on the Raman-Nath harmonic diffraction. It is well known that the fabrication process of periodic domain patterns in ferroelectric crystals often introduces some degree of randomness in otherwise fully periodic domain structure. For the collinear quasi-phase-matching frequency conversion processes, the randomness generally has a negative impact because it reduces frequency conversion efficiency. The situation becomes more complicated when it comes to the nonlinear Raman-Nath diffraction. As we show in **Figure 7**, the randomness of the domain pattern not only affects the efficiency of nonlinear diffraction but also leads to appearance of

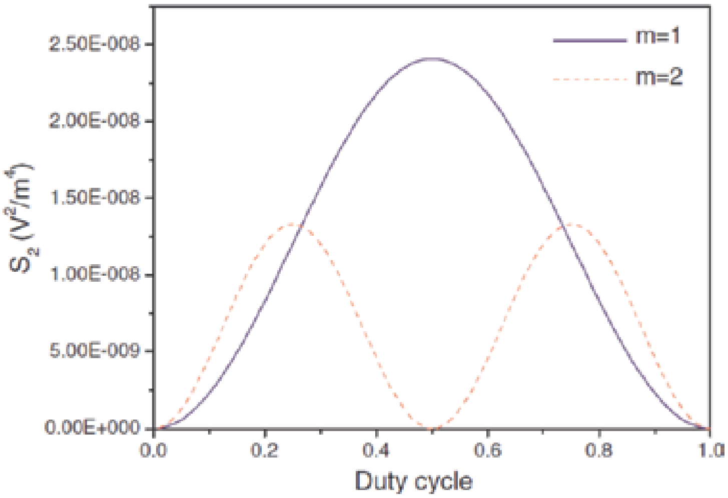

Figure 6. The effect of duty cycle on the strengths of nonlinear Raman-Nath diffraction [29].

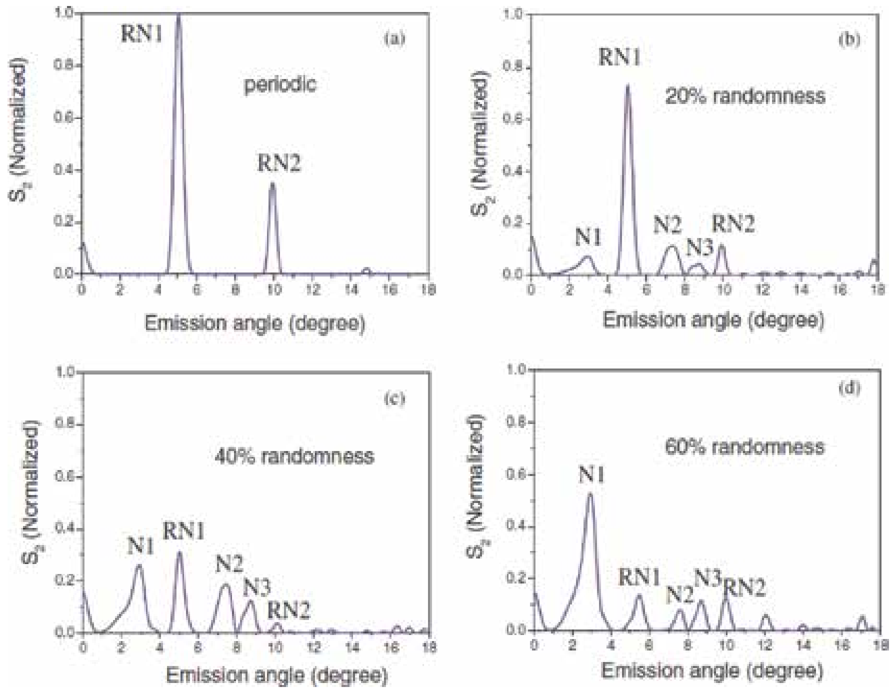

Figure 7. The influence of structure randomness of the ferroelectric domain patterns on the nonlinear Raman-Nath diffraction [29]. We take an average domain period $\Lambda_0 = 9$ m and consider four different degrees of structure randomness ranging from 0 to 60%. All emission strengths are normalized to that of the first-order Raman-Nath diffraction without randomness, namely, RN1 in (a).

new emission peaks. We choose an average period $\Lambda_0 = 9$ μm and consider that the domain width fluctuates randomly around its mean value. We consider four different degrees of randomness. From **Figure 7(a)–(d)**, the randomness degree increases from 0 to 60%, which is defined by $\sigma = \Delta l/\Lambda_0$ with Δl representing the largest dispersion of the ferroelectric domain width. In the figure, we show the normalized harmonic strengths with respect to that of the first-order nonlinear Raman-Nath diffraction without any randomness, namely, $\sigma = 0$. As shown in **Figure 7(a)**, two intensity maxima, which correspond, respectively, to the first- and second-order Raman-Nath resonances, appear for the perfect periodic structure. They are marked as RN1 and RN2 in the figure, respectively. Increasing σ leads to the weakening of these two emission peaks and at the same time appearance of a few new ones, marked with indices N1, N2, and N3 in **Figure 7(b)–(d)**. These new emitted signals become stronger and stronger with σ, and finally their strengths can exceed those of the original emission resonances.

In **Figure 8**, we display the calculated dependence of the nonlinear Raman-Nath diffractions on the interaction distance. As the Raman-Nath interactions suffer from the phase mismatch in the longitudinal direction, their intensity oscillates with the interaction distance inside the crystal. Obviously the smaller the phase mismatch, the longer the oscillation period. With the parameters used in our calculation (fundamental wavelength λ_1 = 1.545 μm, beam width a = 60 μm, duty cycle D = 0.35), the largest oscillation period takes place at the fifth-order diffraction (m = 5).

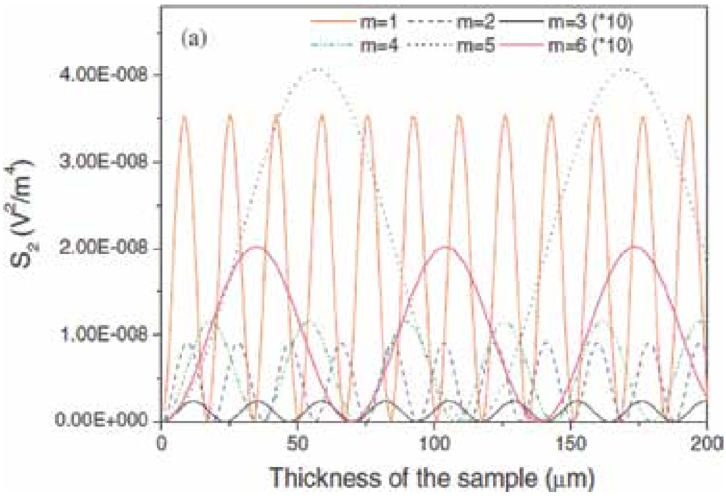

Figure 8. Multi-order nonlinear Raman-Nath SHG as a function of crystal thickness (or interaction distance) [29].

4. Application of Čerenkov harmonic generation to 3D imaging of ferroelectric domain patterns

High-quality visualization of ferroelectric domain structures plays a key role in understanding material property and better control of domain inversion process. However, due to the equality of antiparallel 180° ferroelectric domains in linear optical properties, the common imaging techniques do not apply to the detection of these domains. Currently the selective chemical etching [30] based on the different etching rates of antiparallel domains in hydrofluoric acid is still the most common method used for this purpose. Not only this is a destructive technique, but moreover, it is ineffective in revealing the internal domain structures hidden deep inside the crystals. To overcome some of these drawbacks, a large number of alternative approaches have been adapted to imaging ferroelectric domains, such as advanced electron microscopy [31] and piezo-forced microscopy [32]. However, most of these methods also fail in visualization of deep internal domain structures, which can be diverse and more complex than those on the surface [33]. For example, the inverted domains undergo sidewise expansion with depth [34], transform to preferred shapes depending on the crystallographic symmetry [35, 36], and sometimes merge to form a bigger structures [37]. The details about these domain formation processes such as when, where, and how they occur are very little known due to the lack of reliable techniques for three-dimensional visualization of domain patterns.

It has been shown in Section 2 that when a femtosecond laser beam is tightly focused to produce a focus that is narrow enough to cover a single ferroelectric domain wall, a pair of Čerenkov second harmonic beams will be generated. The Čerenkov signal disappears if the laser beam is moved away from the domain wall. In this way, by recording the second harmonic strengths at different positions inside the crystal, one can obtain a three-dimensional image reflecting the spatial distribution of ferroelectric domain walls (and subsequently domains) inside the crystal. This is a nondestructive imaging method and can offer submicrometer resolution because of its nonlinear optical mechanism [18]. This is a 3D optical method as it also enables one to reveal the details of inverted domains beneath the surface.

Figure 9 displays a schematic illustration of the nonlinear Čerenkov second harmonic imaging system. The fundamental femtosecond laser beam is provided here by a titanium-sapphire laser (Mai Tai, Spectra Physics, 80 MHz repetition rate and up to 12 nJ pulse energy). It is known that in the regime of a tightly focused fundamental beam, the Čerenkov process is insensitive to the wavelength of the fundamental wave. Therefore, this imaging system can operate at a wide range of wavelength limited only by the absorption edge of second harmonic and the total reflection condition. The latter condition means the Čerenkov harmonic emission angle has to be smaller than its total reflection angle so that the Čerenkov signals can get out from the sample for detection. For traditional nonlinear optical ferroelectric materials, such as $LiNbO_3$ and $LiTaO_3$ crystals, the Čerenkov angle becomes larger at shorter wavelength, so the fundamental wavelength used for the visualization cannot be shorter than the critical wavelength.

The main part of this imaging system is a commercial laser scanning confocal microscope (Zeiss, LSM 510 + Axiovert 200). The femtosecond laser beam is coupled into the confocal microscope and then illuminates the sample after being tightly focused by an $100\times$ objective lens (Plan Apochromat, NA = 1.46). A pair of galvanometric mirrors is used to adjust the focus position in the X-Y plane, and a motorized stage is used to move the objective lens in the Z direction. To collect and detect the emitted second harmonic signal, a condenser lens and a

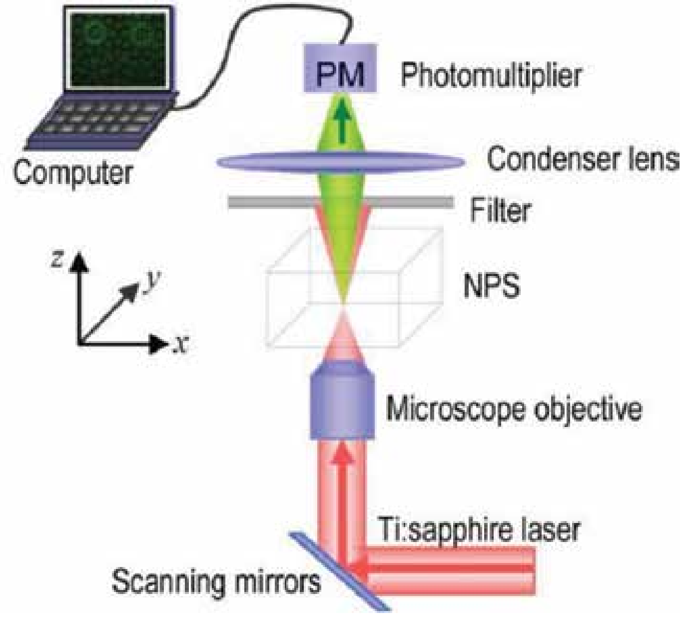

Figure 9. Schematic of the Čerenkov harmonic imaging system for visualization of ferroelectric domain patterns in a nonlinear photonic crystal (NPC) [18].

photomultiplier are employed, respectively. Short-pass filters are used to prevent the transmitted fundamental beam from entering the detectors.

The advantages of this nonlinear Čerenkov imaging system include:

4.1. High contrast and high spatial resolution

A typical two-dimensional image of a ferroelectric domain structure obtained by the Čerenkov second harmonic microscope is shown in **Figure 10(a)**. The quasi-periodic domain patterns, where the bright boundaries represent ferroelectric domain walls which facilitate stronger Čerenkov harmonic emissions, were clearly seen. Obviously the Čerenkov second harmonic microscope is capable of imaging ferroelectric domains with high contrast.

Figure 10(b) depicts the image of ferroelectric domain patterns obtained in an as-grown $Sr_{0.28}Ba_{0.72}Nb_2O_6$ crystal, which process naturally random domain structures in two dimensions. It is seen that the Čerenkov method offers an exceptional spatial resolution and even domain boundaries separated by less than 250 nm can be easily resolved. This is below the diffraction limit for the excitation laser wavelength of 820 nm, owing to the mechanism of nonlinear optical interaction, i.e., the Čerenkov second harmonic signal can only be excited in the very central part of the laser beam's focus.

4.2. Applicability to a wide range of materials

The imaging principle of the Čerenkov SHG microscope lies in the sensitivity of the Čerenkov emission on the existence of the spatial variation of the second-order nonlinearity $\chi^{(2)}$. Therefore, it can apply to any transparent materials with sharp $\chi^{(2)}$ variations. For example, in our experiment we have obtained high-quality images of ferroelectric domain patterns in $LiNbO_3$, $LiTaO_3$, $KTiOPO_4$, and $Sr_{0.28}Ba_{0.72}Nb_2O_6$ crystals, as shown in **Figure 11**.

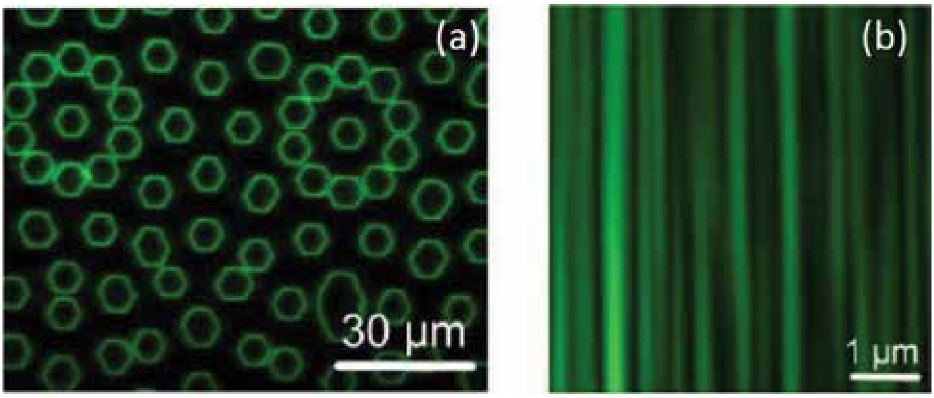

Figure 10. Domain structures imaged by Čerenkov SHG, taken with the focal plane of the fundamental beam located 10 mm inside the corresponding materials: (a) congruent $LiNbO_3$ with 2D quasi-periodic domain structure and (b) as-grown $Sr_{0.28}Ba_{0.72}Nb_2O_6$ crystal.

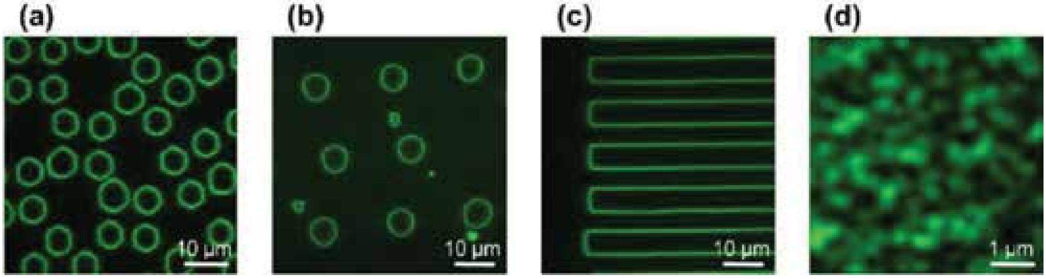

Figure 11. The Čerenkov SHG microscopy applies to a wide range of ferroelectric materials [18]. (a) Congruent $LiNbO_3$ with 2D short-range-ordered domain structure [38]. (b) Stoichiometric $LiTaO_3$ with 2D quasi-periodic domain structure [39]. (c) $KTiOPO_4$ with 1D periodic domain structure [40]. (d) z-cut as-grown $Sr_{0.28}Ba_{0.72}Nb_2O_6$ crystal with naturally random domain structure at X-Y plane [41].

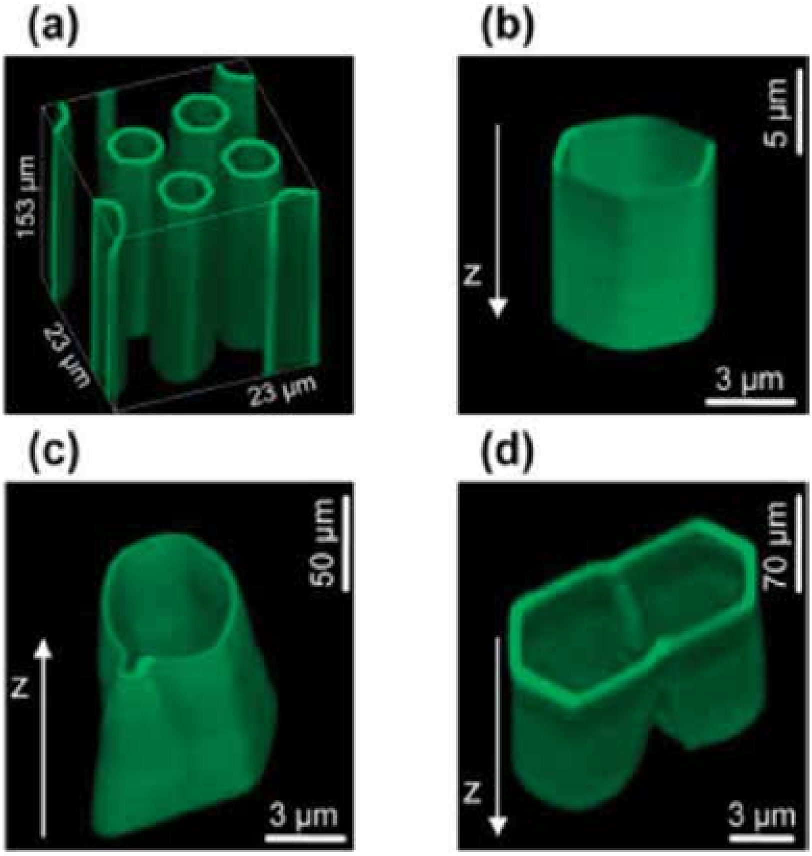

Figure 12. Three-dimensional visualization of inverted ferroelectric domains inside congruent $LiNbO_3$ crystal by Čerenkov-type second harmonic generation laser scanning microscopy. (a) Domain distribution in the nonlinear photonic structure. (b) Transformation from the initially circular to hexagonally shaped domains. (c) Formation of a defect during the domain growth. (d) Merging of two initially separated ferroelectric domains. The ImageJ software was used to create these images.

4.3. Capability for 3D imaging

As we described above, the scanning of laser focus in the X-Y plane enables us to obtain two-dimensional images of ferroelectric domains. Then if we stack a series X-Y plane images recorded at different depths inside the material, we can produce 3D images of domains. This is an advantage that cannot be met by the traditional domain imaging techniques. In **Figure 12** we show a number of 3D images of ferroelectric domain patterns, which are formed in a congruent $LiNbOb_3$ crystal [38]. From these images we can see how the initially circular-shaped domains transform to hexagons with depth [**Figure 12(b)**], how defects were formed during the domain inversion process [**Figure 12(c)**], and how the neighboring domains merge to form a bigger one [**Figure 12(d)**]. Revealing these details is essential for a full understanding of domain inversion and growth processes. This is also very useful for improving the quality of ferroelectric domain patterns, which is critical for a wide range of future applications.

5. Conclusion

We have investigated the nonlinear optical interactions that are strongly dependent on the existence of ferroelectric domain walls, i.e., the spatial variation of the second-order nonlinear coefficient $\chi^{(2)}$ In particular, we have discussed the so-called nonlinear Čerenkov radiation focusing on two special cases including the signal generation from a single and multiple ferroelectric domain wall(s). We have shown that the localized spatial change of nonlinearity $\chi^{(2)}$ constitutes a sufficient condition for strong Čerenkov second harmonic generation. The emitted Čerenkov signals arising from multiple walls can interfere with each other, resulting in the strong dependence of the strength of the overall Čerenkov beams on the wavelengths. Furthermore, the emission from regular periodic domain pattern gives rise to another type of nonlinear interaction, namely, the nonlinear Raman-Nath diffraction. We have derived analytical formulas that govern the emission process and discussed factors that influence the strength of the nonlinear diffraction, including the duty cycle, thickness of the crystal, randomness in domain size, as well as the beam width and wavelength of the fundamental wave. We also utilized the effect of Čerenkov second harmonic generation from a single-domain wall for direct 3D imaging of the antiparallel domains in ferroelectric crystals with sub-diffraction limit resolution. Our studies are important for a better understanding of nonlinear diffraction from ferroelectric domain structures. The nonlinear optical microscopy forms a very powerful tool that will further inspire the design and development of new and sophisticated ferroelectric domain structures for advanced photonic applications.

Acknowledgements

The authors thank the Australian Research Council and Qatar National Research Fund (Grant No. NPRP 8-246-1-060) for financial supports. Mr. Xin Chen thanks China Scholarship Council (PhD Scholarship No. 201306750005). The authors thank Dr. Vito Roppo, Dr. Ksawery

Kalinowski, Dr. Qian Kong, Dr. Wenjie Wang, Prof. Crina Cojocaru, and Prof. Joes Trull for their valued contributions to this work.

Conflict of interest

There is no conflict of interest for this work.

Author details

Xin Chen[1], Wieslaw Krolikowski[1,2] and Yan Sheng[1]*

*Address all correspondence to: yan.sheng@anu.edu.au

1 Laser Physics Centre, Research School of Physics and Engineering, Australian National University, Canberra, Australia

2 Science Program, Texas A&M University at Qatar, Doha, Qatar

References

[1] Valasek J. Piezo-electric and allied phenomena in rochelle salt. Physics Review. 1921;**17**: 475-481. DOI: 10.1103/PhysRev.17.475

[2] Matsumoto S, Lim EJ, Hertz HM, Fejer MM. Quasiphase-matched second harmonic generation of blue light in electrically periodically-poled lithium tantalate waveguides. Electronics Letters. 1991;**27**:2040-2042. DOI: 10.1049/el:19911263

[3] Burns WK, McElhanon W, Goldberg L. Second harmonic generation in field poled, quasi-phase-matched, bulk $LiNbO_3$. IEEE Photonics Technology Letters. 1994;**6**:252-254. DOI: 10.1109/68.275441

[4] Catalan G, Seidel J, Ramesh R, Scott JF. Domain wall nanoelectronics. Reviews of Modern Physics. 2012;**84**:119-156. DOI: 10.1103/RevModPhys.84.119

[5] Seidel J, Fu D, Yang S, Alarcón-Lladó E, Wu J, Ramesh R, Ager JW III. Efficient photovoltaic current generation at ferroelectric domain walls. Physical Review Letters. 2011;**107**: 126805. DOI: 10.1103/PhysRevLett.107.126805

[6] Scott JF, Paz de Araujo CA. Ferroelectric memorie. Science. 1989;**246**:1400-1405. DOI: 10.1126/science.246.4936.1400

[7] Guo R, You L, Zhou Y, Lim ZS, Zou X, Chen L, Ramesh R, Wang J. Non-volatile memory based on the ferroelectric photovoltaic effect. Nature Communications. 2013;**4**:1990. DOI: 10.1038/ncomms2990

[8] Cho Y, Fujimoto K, Hiranaga Y, Wagatsuma Y, Onoe A, Terabe K, Kitamura K. Terabit inch^{-2} ferroelectric data storage using scanning nonlinear dielectric microscopy nano-domain engineering system. Nanotechnology. 2003;**14**:637-642. DOI: 10.1088/0957-4484/14/6/314

[9] Ito H, Takyu C, Inaba H. Fabrication of periodic domain grating in $LiNbO_3$ by electron beam writing for application of nonlinear optical processes. Electronics Letters. 1991;**27**: 1221-1222. DOI: 10.1049/el:19910766

[10] Chen X, Shvedov V, Karpinski P, Sheng Y, Koynov K, Boes A, Mitchell A, Trull J, Cojocaru C, Krolikowski W. Ferroelectric domain patterning with ultrafast light. Optics & Photonics News. 2016;**27**:50

[11] Chen X, Karpinski P, Shvedov V, Koynov K, Wang B, Trull J, Cojocaru C, Krolikowski W, Sheng Y. Ferroelectric domain engineering by focused infrared femtosecond pulses. Applied Physics Letters. 2015;**107**:141102. DOI: 10.1063/1.4932199

[12] Chen X, Karpinski P, Shvedov V, Boes A, Mitchell A, Krolikowski W, Sheng Y. Quasi-phase matching via femtosecond laser-induced domain inversion in lithium niobate waveguides. Optics Letters. 2016;**41**:2410-2413. DOI: 10.1364/OL.41.002410

[13] Ying CYJ, Muir AC, Valdivia CE, Steigerwald H, Sones CL, Eason RW, Soergel E, Mailis S. Light-mediated ferroelectric domain engineering and micro-structuring of lithium niobate crystals. Laser & Photonics Reviews. 2012;**6**:526-548. DOI: 10.1002/lpor.201100022

[14] Sheng Y, Roppo V, Kalinowski K, Krolikowski W. Role of a localized modulation of ($\chi(2)$) in Čerenkov second-harmonic generation in nonlinear bulk medium. Optics Letters. 2012; **37**:3864-3866. DOI: 10.1364/OL.37.003864

[15] Roppo V, Kalinowski K, Sheng Y, Krolikowski W, Cojocaru C, Trull J. Unified approach to Čerenkov second harmonic generation. Optics Express. 2013;**21**:25715. DOI: 10.1364/OE.21.025715

[16] Deng X, Chen X. Domain wall characterization in ferroelectrics by using localized nonlinearitie. Optics Express. 2010;**18**:15597-15602. DOI: 10.1364/OE.21.025715

[17] Saltiel SM, Sheng Y, Voloch-Bloch N, Neshev DN, Krolikowski W, Arie A, Koynov K, Kivshar YS. Cerenkov-type second-harmonic generation in two-dimensional nonlinear photonic structures. IEEE Journal of Quantum Electronics. 2009;**45**:1465-1472. DOI: 10.1109/JQE.2009.2030147

[18] Sheng Y, Best A, Butt H, Krolikowski W, Arie A, Koynov K. Three-dimensional ferroelectric domain visualisation by Čerenkov-type second harmonic generation. Optics Express. 2010;**18**:16539-16545. DOI: 10.1364/OE.18.016539

[19] Karpinski P, Chen X, Shvedov V, Hnatovsky C, Grisard A, Lallier E, Luther-Davies B, Krolikowski W, Sheng Y. Nonlinear diffraction in orientation-patterned semiconductors. Optics Express. 2013;**25**:14903-14912. DOI: 10.1364/OE.23.014903

[20] Wang B, Cojocaru C, Krolikowski W, Sheng Y, Trull J. Transverse single-shot cross-correlation scheme for laser pulse temporal measurement via planar second harmonic generation. Optics Express. 2016;**24**:22210-22218. DOI: 10.1364/OE.24.022210

[21] Chen X, Switkowski K, Hu X, Krolikowski W, Sheng Y. Enhanced fourth harmonic generation via nonlinear erenkov interaction in periodically poled lithium niobate crystal. Optics Express. 2016;**24**:29948-29954. DOI: 10.1364/OE.24.029948

[22] Ayoub M, Futterlieb H, Imbrock J, Denz C. 3D imaging of ferroelectric kinetics during electrically driven switching. Advanced Materials. 2017;**29**:1603325. DOI: 10.1002/adma.201603325

[23] Boyd RW. Nonlinear Optics. New York: Academic Press; 2007

[24] Edwards GJ, Lawrence M. A temperature-dependent dispersion equation for congruently grown lithium niobate. Optical and Quantum Electronics. 1984;**16**:373-375. DOI: 10.1007/BF00620081

[25] Mathieu E. Conditions for quasi Cerenkov radiation, generated by optical second harmonic polarisation in a nonlinear crystal. Zeitschrift für Angewandte Mathematik und Physik. 1969;**20**:433-439. DOI: 10.1007/BF01595035

[26] Wulle T, Herminghaus S. Nonlinear optics of Bessel beams. Physical Review Letters. 1993; **70**:1401-1404. DOI: 10.1103/PhysRevLett.70.1401

[27] Saltiel SM, Neshev DN, Fischer R, Krolikowski W, Arie A, Kivshar YS. Generation of second-harmonic conical waves via nonlinear Bragg diffraction. Physical Review Letters. 2008;**100**:103902. DOI: 10.1103/PhysRevLett.100.103902

[28] Sheng Y, Kong Q, Roppo V, Kalinowski K, Wang Q, Cojocaru C, Krolikowski W. Theoretical study of Čerenkov-type second-harmonic generation in periodically poled ferroelectric crystals. Journal of the Optical Society of America B: Optical Physics. 2012;**29**:312-318. DOI: 10.1364/JOSAB.29.000312

[29] Sheng Y, Kong Q, Wang W, Kalinowski K, Krolikowski W. Theoretical investigations of nonlinear Raman–Nath diffraction in the frequency doubling process. Journal of Physics B: Atomic, Molecular and Optical Physics. 2012;**45**:055401. DOI: 10.1088/0953-4075/45/5/055401

[30] Hooton JA, Merz WJ. Etch patterns and ferroelectric domains in $BaTiO_3$ single crystal. Physical Review. 1955;**98**:409-413. DOI: 10.1103/PhysRev.98.409

[31] Zhu SN, Cao WW. Direct observation of ferroelectric domains in $LiTaO_3$ using environmental scanning electron microscopy. Physical Review Letters. 1997;**79**:2558-2561. DOI: 10.1103/PhysRevLett.79.2558

[32] Jungk T, Hoffmann A, Soergel E. Contrast mechanisms for the detection of ferroelectric domains with scanning force microscopy. New Journal of Physics. 2009;**11**:033092. DOI: 10.1088/1367-2630/11/3/033029

[33] Soergel E. Visualization of ferroelectric domains in bulk single crystals. Applied Physics. 2005;**81**:729-752. DOI: 10.1007/s00340-005-1989-9

[34] Shur VY, Rumyantsev EL, Batchko RG, Miller GD, Fejer MM, Byer RL. Domain kinetics in the formation of a periodic domain structure in lithium niobate. Physics of the Solid State. 1999;**41**:1681-1687. DOI: 10.1134/1.1131068

[35] Rosenman G, Garb K, Skliar A, Oron M, Eger D, Katz M. Domain broadening in quasi-phase-matched nonlinear optical devices. Applied Physics Letters. 1998;**73**:865-867. DOI: 10.1063/1.121969

[36] Sheng Y, Wang T, Ma BQ, Qu E, Cheng B, Zhang D. Anisotropy of domain broadening in periodically poled lithium niobate crystal. Applied Physics Letters. 2006;**88**:041121. DOI: 10.1063/1.2168727

[37] Ni PG, Ma BQ, Wang XH, Cheng B, Zhang D. Second-harmonic generation in two-dimensional periodically poled lithium niobate using second-order quasiphase matching. Applied Physics Letters. 2003;**82**:4230-4232. DOI: 10.1063/1.1579856

[38] Sheng Y, Dou J, Ma B, Cheng B, Zhang D. Broadband efficient second harmonic generation in media with a short-range order. Applied Physics Letters. 2007;**91**:011101. DOI: 10.1063/1.2754365

[39] Bahabad A, Ganany-Padowicz A, Arie A. Engineering two-dimensional nonlinear photonic quasi-crystal. Optics Letters. 2008;**33**:1386-1388. DOI: 10.1364/OL.33.001386

[40] Ni R, Du L, Wu Y, Hu XP, Zou J, Sheng Y, Arie A, Zhang Y, Zhu SN. Nonlinear Cherenkov difference-frequency generation exploiting birefringence of KTP. Applied Physics Letters. 2016;**108**:031104. DOI: 10.1063/1.4940095

[41] Fischer R, Saltiel SM, Neshev DN, Krolikowski W, Kivshar YS. Broadband femtosecond frequency doubling in random media. Applied Physics Letters. 2006;**89**:191105. DOI: 10.1063/1.2374678

Chapter 4

About Mathematical Models of Irreversible Polarization Processes of a Ferroelectric and Ferroelastic Polycrystals

Alexander Skaliukh

Additional information is available at the end of the chapter

http://dx.doi.org/10.5772/intechopen.78262

Abstract

This chapter presents the prevalent mathematical models of irreversible processes in polycrystalline ferroelectric materials when they are subjected to intense electrical and mechanical influences. The main purpose of such models is to describe the dielectric hysteresis loops, with which the models of Rayleigh and Preisach coped well, though they were developed almost a 100 years ago. Nevertheless, in order to describe the whole gamut of material properties in irreversible polarization-depolarization processes, it was required in the last three decades to develop new approaches and methods that take into account the material structure and the physics of the process. In this chapter, we attempted to collect the most common one-dimensional models, with a view to give a brief description of the basics and approaches with the application of working formulas, algorithms and graphs of numerical calculations. On one-dimensional models, the basics of three-dimensional models are worked out, such as evolutionary laws, domains switching criteria, generalizations from “hysteron” to the polarization surface, and so on, so they are a necessary step in modeling. However, some of them proved to be so effective that they obtained the right to independent existence, as happened with the Preisach model, which found application in dynamic systems. This research is based on published articles, monographs, proceedings of conferences, and scientific reports of individual collectives published over the past 20–25 years.

Keywords: mathematical model, hysteresis, domains, polarization, strain, ferroelectric materials, ceramics, constitutive relations

1. Introduction

Polycrystalline ferroelectric materials or ceramics are active materials that, by virtue of their internal structure, have the ability to convert mechanical energy into electrical energy, and vice versa. This means that by acting on the sample an electric field or mechanical stress, we observe a response in the form of an electric displacement and the strain [1]. When the intensity of external electric fields or a mechanical stresses are small, the deformations and electrical displacements caused by them are also small. Such processes are called reversible; they say that there is a linear response. The modeling of such response leads to the construction of constitutive relations in the form of linear algebraic equations, which, like the generalized Hooke law, connect external and internal parameters. We can say that the mathematical model of the behavior of such materials is described by the linear algebraic operators in which the elements of elastic, piezoelectric and dielectric constant tensors are found experimentally. The overwhelming majority of problems concerning the calculation of the physical characteristics of transducers with polarized before saturation piezoceramic elements are solved within the linear response of active materials. In this case, the complete formulation of the problem includes the equations of motion, the equations of electrostatics, geometric relationships, and the constitutive relations. The general solutions obey the corresponding initial and boundary conditions. Such problems in the mathematical plan are linear. In simple cases, they can be solved analytically, and in more complex cases, we have to use numerical methods, for example, the finite element method.

The situation changes dramatically as soon as external loads reach thresholds, and their intensity continues to increase. In this case, irreversible processes begin, expressed in the fact that the response of the material will already be nonlinear. The consequence of this is that under increasing loads we have some nonlinear equations, while for decreasing ones we have other nonlinear equations. The constitutive relations become nonlinear and ambiguous. Mathematically, they can no longer be described by simple algebraic relations, but it is necessary to use operator relations of hysteresis type.

Due to the small volume of the article, we confine ourselves of modeling irreversible polarization-depolarization processes by an electric field and mechanical stresses under isothermal processes. Irreversible processes associated with relaxation properties, with the influence of temperature, with the features of the influence of size the ferroelectric granules, the dynamics of processes, and some others will not be considered here. The main circle of questions will be connected with the analysis of existing mathematical models describing the response of the material to external influences of high intensity for the isothermal process: we will consider the principles of constructing the constitutive relations, analyze them, and formulate some conclusions.

First, we note an interesting regularity: many irreversible processes have a similar response in the sense that the relationships between external and internal parameters are mathematically described by similar relationships. For example, in plasticity media, stresses cause elastic and residual deformations; in ferromagnets, the magnetic field leads to induced and remnant magnetization; in ferroelectrics, the electric field generates induced and residual polarization, etc. In the case of cyclic processes, the responses are described by hysteresis dependences, as shown in **Figures 1–3**. Therefore, it is not surprising that the mathematical methods being developed for the study of certain processes are often used to describe others. Mathematical modeling of nonlinear responses of polycrystalline ferroelectric materials plays a significant role [2], therefore, the creation and use of such models is based on experimental data.

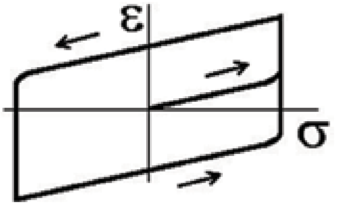

Figure 1. Deformation hysteresis loop.

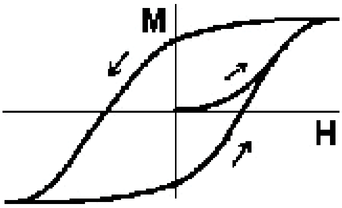

Figure 2. Magnetic hysteresis loop.

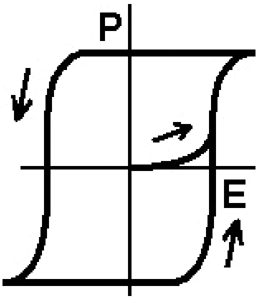

Figure 3. Dielectric hysteresis loop.

2. Some experimental data

The criterion for the correctness and adequacy of the work of any model is the acceptable coincidence of the predicted data with experimental data. It should be noted that a qualitative experiment is a very complex study, so most of them reflect only certain properties with simple effects. We note only those works that reflect the electric and elastic response due to the action of the electric field and mechanical stresses. Basically, these are the works where the properties of ferroelectric ceramics of the perovskite type are investigated: for example, $BaTiO_3$, or a ceramics containing lead: PZT, PLZT 8/65/35. Interesting results [3] on the response of PLZT 8/65/35 on the effect of electric and mechanical fields and similar results [4–10] for complex loads show that the loops of electrical and deformation hysteresis depend significantly on the intensity of the operating fields. Uniaxial mechanical compressive stresses along the electric

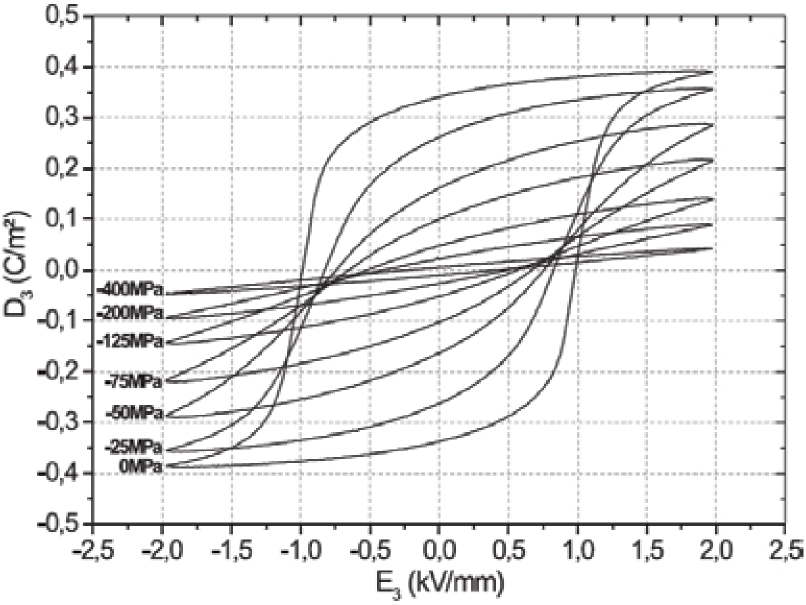

Figure 4. The effect of compressive mechanical stresses on the dielectric hysteresis loops.

field axis affect the ability of domains to rotate: the more intense the mechanical stresses, the fewer domains are able switching along the electric field as it is shown in **Figures 4** and **5**.

The types of considered ceramic materials are full ferroelectrics-ferroelastics, so the response of such materials to the effect of purely mechanical loads is of considerable interest. Some results of

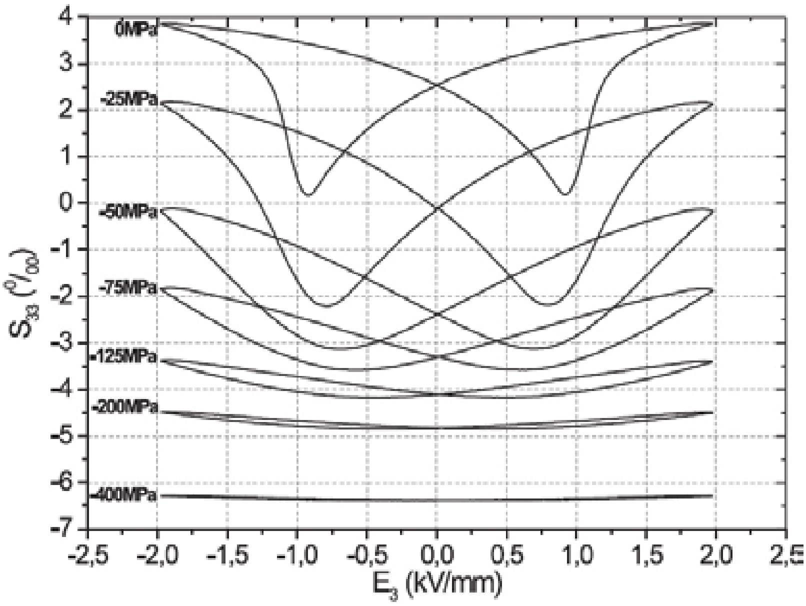

Figure 5. The effect of compressive mechanical stresses on "butterfly" dielectric hysteresis loops.

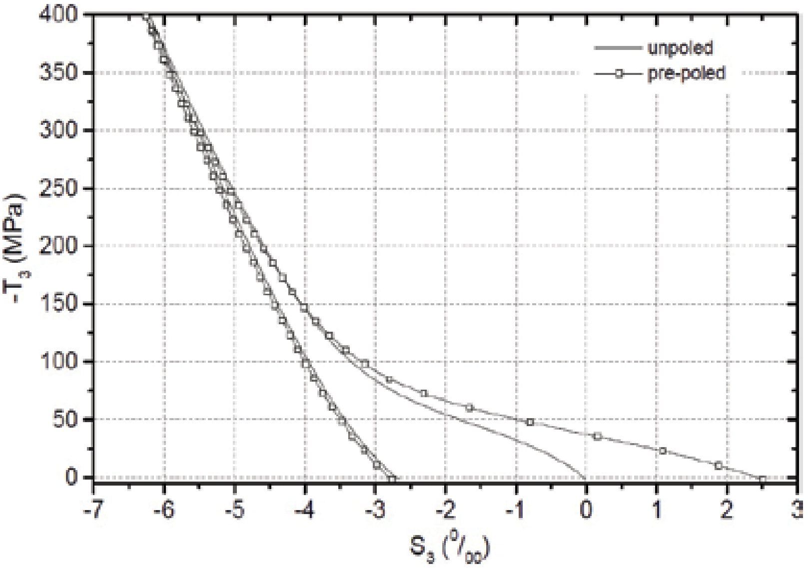

Figure 6. Half-loop "stress-strain" in the case of axial compression.

such tests can be seen in **Figures 6** and **7**. From this it is easy to see that under purely mechanical impacts, the "solid body"—"solid body" phase transition takes place, the material from isotropic (anisotropic) becomes anisotropic, the elastic modules of the material (tangents to the curves) change, residual strains appear that satisfy the property of incompressibility of the material (compare the values of longitudinal and transverse strains).

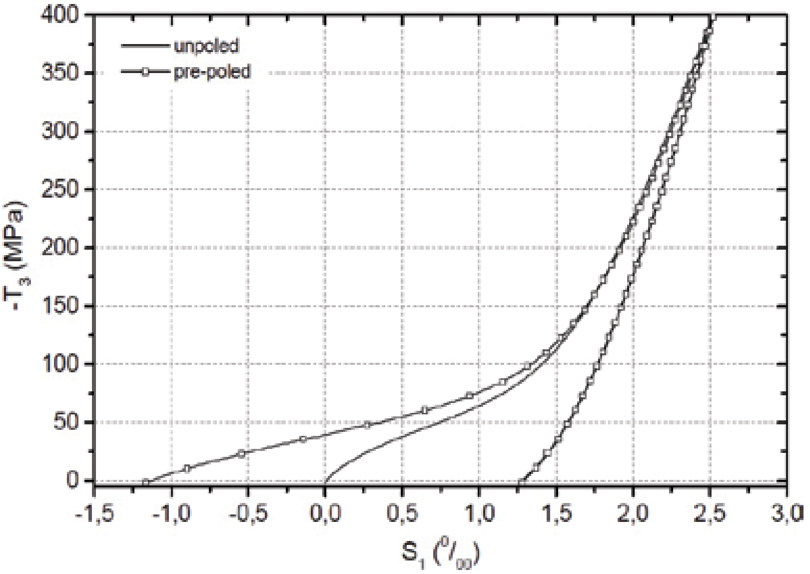

Figure 7. Half-loop "stress-transverse strain" in axial compression.

We note one more interesting property in the response of the material, when small loops of dielectric and strain hysteresis are investigated [9]. Small loops of dielectric and strain hysteresis due to the action of an electric field are shown in **Figures 8** and **9**. Small loops of strain hysteresis due to the action of mechanical stresses are shown in **Figures 10–11**. **Figure 10** reflects the stretching-compressing process, and **Figure 11** reflects only pure compression followed by an increase in intensity.

By behavior of small hysteresis loops, one can judge the change in the elastic, dielectric, and piezoelectric modules of the material. In addition, one can see the property of incompressibility of a material, by estimating the numerical values of strains at zero stresses. Summing up, we can say that the main task of mathematical modeling of irreversible processes is the construction of hysteresis operators taking into account the changing anisotropy of material properties.

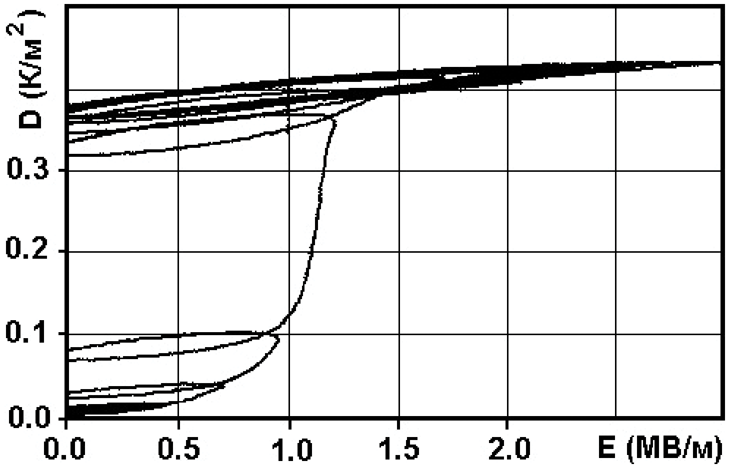

Figure 8. Small loops of dielectric hysteresis.

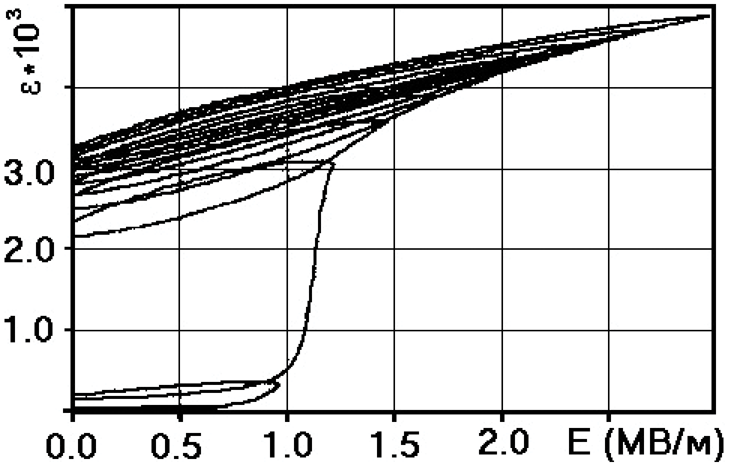

Figure 9. Small loops of deformation hysteresis.

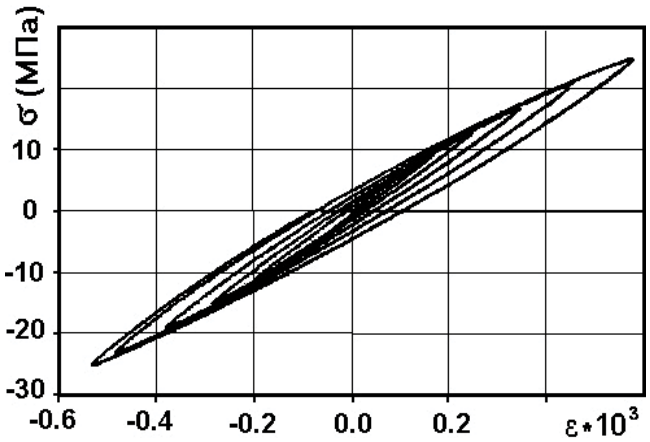

Figure 10. Small loops "stress-strain" at axial stretching-compressing loads.

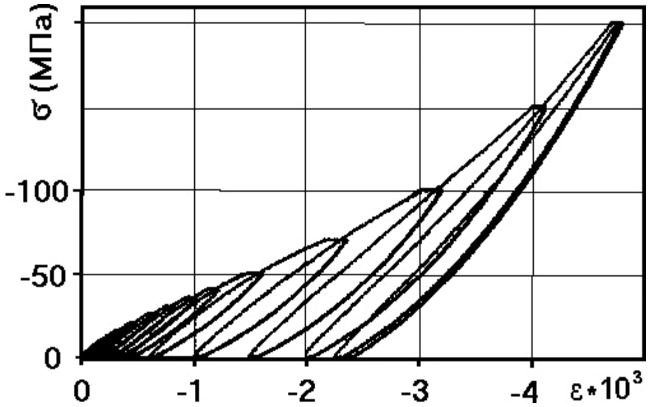

Figure 11. Small loops "stress-strain" at axial compressing loads.

3. Simple models

To compare the efficiency of a particular model, it is needed to have graphic images in the form of hysteresis loops. All the graphs given later were obtained in [2], where the algorithms are also described.

3.1. The Rayleigh model

One of the first models describing hysteresis relationships was the Rayleigh model [11], proposed in 1887 for magnetization processes of iron. Applying it to the polarization processes of polycrystalline ferroelectric continuum, it is necessary to replace the magnetic field by electric field and magnetization by polarization. Mathematically, the branches of the dielectric hysteresis are described by parabolic relationships:

$$P = \begin{cases} \alpha E^2, & \textit{initial polarization curve,} \\ \alpha E_{\max} E \pm \dfrac{\alpha}{2}\left(E_{\max}^2 - E^2\right), & \textit{descending and ascending branches,} \end{cases}$$

where $\alpha = p_s / E_{\max}^2$, p_s—spontaneous polarization, $E_{\max}$—maximum value of the electric field, and the hysteresis loop is shown in **Figure 12**.

Conclusion: a quadratic dependence between the electric field and polarization approximates the dielectric hysteresis for small and medium intensity values of the electric field.

3.2. Evolutionary models

Investigating the nonlinear behavior of ferroelectric materials, the authors [12] assumed that the dielectric displacement D is a function of the electric field E, the dipole moment μ, and the number of dipoles per unit volume N aligned in the direction of the electric displacement. Thus, irreversible parameters μ, N have been introduced into the model, and evolutionary laws are formulated in order to identify them:

$$D = \tilde{D}(E, \mu, N); \quad \dot{N} = g(E, \mu, N), \quad g(0, \mu, N) = 0.$$

Under the assumption of linear functions entering into the previous relations and the linear dependence of the dipole moment on the electric field

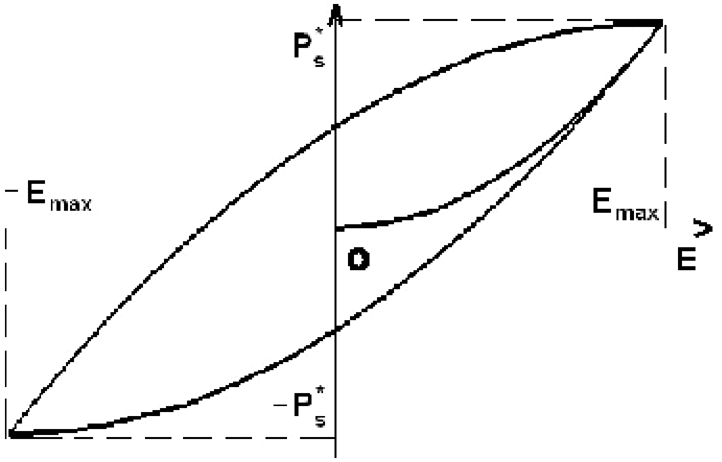

Figure 12. The Rayleigh model.

$$\begin{aligned} &D = \left(\tilde{D}\right)_0 + \left(\tilde{D}_E\right)_0 E + \left(\tilde{D}_\mu\right)_0 (\mu - \mu_0) + \left(\tilde{D}_N\right)_0 (N - N_0); \\ &\dot{N} = (g_E)_0 E + \left(g_\mu\right)_0 (\mu - \mu_0) + (g_N)_0 (N - N_0); \qquad \mu(\tau) - \mu_0 \alpha E(\tau), \end{aligned}$$

a formula for the electric displacement was obtained

$$D = \left(\tilde{D}\right)_0 + \tilde{\varepsilon}(0)E + \int_0^1 \frac{d}{dt} \tilde{\varepsilon}(t - \tau) E(\tau) d\tau; \qquad \tilde{\varepsilon}(t) = \tilde{\tilde{\varepsilon}}(t) + \alpha \tilde{\tilde{\varepsilon}}(t).$$

The creep functions $\tilde{\tilde{\varepsilon}}(t)$, $\tilde{\tilde{\varepsilon}}(t)$ have an exponential form, and because of their cumbersomeness, they are not given here. Similar arguments are also made for the related problem, where the mechanical stress and the electric displacement are presented in the form of similar integral dependences with the same exponential creep functions. To determine the elastic and dielectric properties [13] of the ceramic material PZT 65/35, a connection between the elastic and dielectric constants and the speed of sound in polarized and unpolarized ceramics was established. Similar studies can be found in [14–19].

Conclusion: irreversible parameters were introduced in implicit form, for the find of which evolutionary laws were applied. The constitutive relations were obtained in the form of creep integrals. The creep functions are constructed under the assumption of linear dependences for functions entering into evolutionary dependencies. For the formulation of increasing and falling branches of hysteresis, inequalities for functions describing the load and response of the material were formulated.

3.3. Models of the theory of plasticity

In view of the similarity of the plasticity and polarization phenomena noted earlier, for qualitative description of the polarization effects, use the rheological models of the theory of plasticity. At the basis of our subsequent actions lie analogues of mechanical and electrical quantities: the generalized coordinate—the electric charge; generalized speed—current; coefficient of elastic compliance—capacity; the generalized force is the electromotive force. In the transition to continuous media, forces are replaced by mechanical stresses, displacements by strains, etc. As a result, one can write the following correspondence: $\sigma \leftrightarrow E$, $\varepsilon \leftrightarrow P$, where E is the electric field; P is polarization; σ is mechanical stress; ε is strain. The elastic element is associated with a capacitor and the element of dry friction is a bipolar zener diode (**Figure 13**). The rheological formulas for a capacitor and a zener diode can conveniently be described using differential inclusions [20] which can be represented by the following expressions:

$$E_e = \frac{1}{c} P_e; \quad E_0 \in rS\left(\dot{P}_0\right) \quad (c, r > 0 \ - \ const),$$

where the indices "e" and "0" indicate the induced and residual components, respectively, and $S(v)$ is a function of sets determined by the rule:

$$S(v) := \begin{cases} \{-1\}, & v < 0; \\ [-1,+1], & v = 0; \\ \{+1\}, & v > 0. \end{cases}$$

By connecting these elements in series (**Figure 14a**), according to the conditions $E = E_e + E_0, \quad P = P_e = P_0$, we obtain a differential inclusion $E \in \frac{1}{c} P + rS(\dot{P})$ that determines the "backlash" operator. If these elements are connected in parallel (**Figure 14b**), then from the conditions $E = E_e = E_0, \quad P = P_e + P_0$ it is easy to derive a differential inclusion $\dot{P} \in c\dot{E} + S^{-1}\left(\frac{E}{r}\right)$ that determines the "stop" operator [20]. Next, one can determine the Prager polarization models by adding capacitors to the considered chains, as shown in **Figures 15a**, 15**b**. Not stopping the detailed description of the Prager model, we note only the case shown in **Figure 15b**, which is described by the following rheological formula [2]:

$$\left(1 + \frac{c_1}{c_2}\right)\dot{P} - c_1\dot{E} \in S^{-1}\left(\frac{E - (1/c_2)P}{r}\right).$$

If we collect a battery of one of the chains in parallel, we see that the resulting polarization for such a connection is determined by summing the individual polarization components of each chain, and the electric field is the same for any of them. Let the chains be distributed continuously [2, 21, 22], then there is a distribution density function $f(x): \quad d\mu(x) = f(x)dx$ and three families of positive parameters $\alpha(x), \quad \beta(x), \quad r(x)$. For any $x \in X$ exist a generalized Prager operator $\left(E, \ \left\{E(0) - \alpha P^0(x) \in [-r,+r]\right\}\big|_{x \in X}\right) \ \mapsto \ P$, which is defined by the following system:

Figure 13. Capacitor and bipolar zener diode elements.

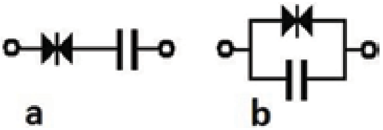

Figure 14. Connected elements: a) in series; b) in parallel.

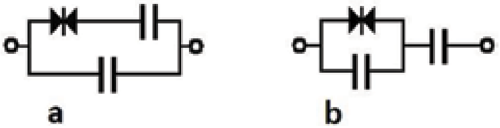

Figure 15. Prager polarization models: a) capacitor in parallel; b) capacitor in series.

$$\dot{P}(x) - \beta(x)\dot{E} \in S^{-1}\left(\frac{E - \alpha(x)P(x)}{r(x)}\right); \quad P = \int_X P(x)d\mu(x);$$
$$E(t) - \alpha P(x,t)|_{t=0} = E(0) - \alpha P^0(x) \quad (\forall x \in X).$$

Taking a battery of continuously distributed chains for a representative volume, we can determine it polarization for any value of the electric field. It is possible to perform calculations using the generalized Prager model if, in addition to the probability function of the distribution density, three functions $\alpha(x), \quad \beta(x), \quad r(x)$ are also given. We give one numerical experiment [2], by selecting appropriately incoming in it functions. Let the electric field vary in time according to the law of the sine. The probability density function is chosen as a function of the normal Gaussian distribution:

$$f(x) = \frac{1}{\sqrt{2\pi}\sigma}\exp\left\{-\frac{(x-b)^2}{2\sigma^2}\right\}.$$

We will assume that the generalized Prager operator is generated by a battery of parallel connected chains with functions of the following form:

$$\alpha(x) = \frac{1}{c_1(x) + c_2(x)}, \quad \beta(x) = c_2(x), \quad c_1(x) = a\frac{2 - \mathrm{th}|x|}{2};$$
$$c_2(x) = b\frac{2 - \mathrm{th}|x|}{2}; \quad r(x) = c\frac{1 + \mathrm{th}|x|}{2} \quad (a, b, c \; - \; const).$$

The result of the calculations is shown in **Figure 16**.

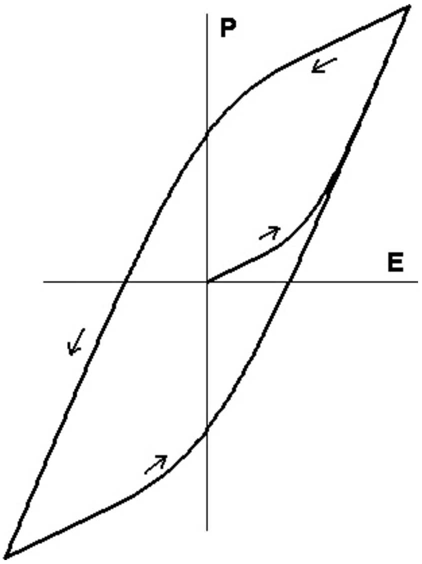

Figure 16. Generalized Prager model.

Conclusion: varying the parameters of the Gaussian distribution, as well as the functions included in the differential inclusions, it is possible to substantially change the shape of the hysteresis loop. This circumstance gives confidence that by the selection of these parameters a good coincidence of the modeled and experimental hysteresis loop in the one-dimensional case can be achieved.

3.4. The Preisach model

This model was proposed in 1935 by Preisach [23]. The model is based on the concept of hysteron [24, 25], which approximates the switching of 180° domain. Simulation of the polarization of ceramics is associated with its representation as a set of a very large number of 180° hysterons with the probability density function $\mu(x, y)$:

$$\iint\limits_{x \geq 0} \mu(x, y) dx dy = 1(x = E_i, \;\; y = E_c),$$

defined on the plane $\{|x| \leq \infty, \;\; y > \infty\}$. The inhomogeneity of physical conditions in different parts of the ceramics generates a large scatter of hysterons at coercive and internal fields, and the switching of each domain is described by a rectangular hysteresis loop with its coercive (E_c) and internal (E_i) fields (**Figure 17**). For each state in the positive half-plane, there is a boundary separating the domains of two opposite directions. For an unpolarized state, it is the abscissa axis (**Figure 18**). When an electric field of definite sign is applied, this boundary moves due to the involvement of new hysterons in the switching process (**Figure 19**). If the electric field changes the growth direction, then the direction of the boundary movement also changes (**Figure 20**).

The distribution function in the vicinity of the coercive fields had to have a pronounced peak, which allows approximating its using known distributions, for example Gauss, with subse-

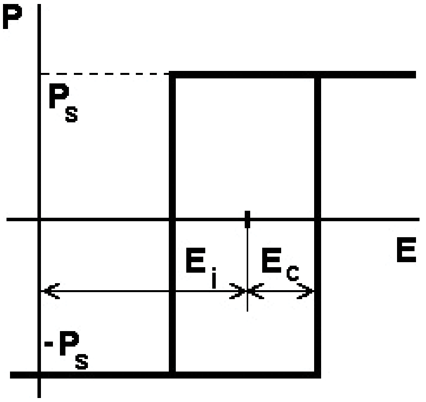

Figure 17. Hysteron.

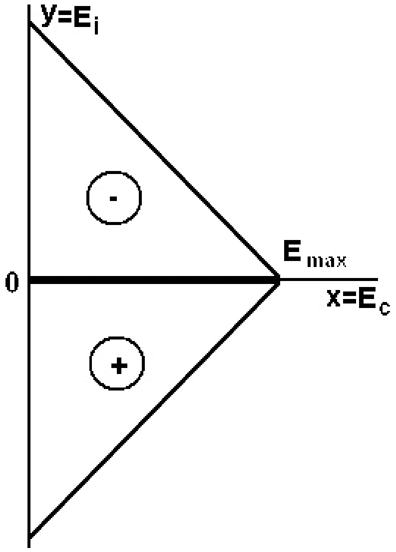

Figure 18. Areas with nonzero density of hysterons for opposite directions of polarization.

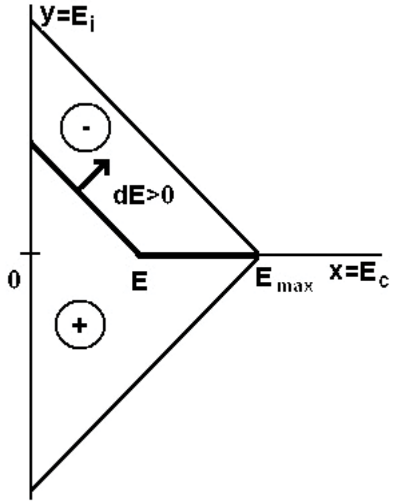

Figure 19. The motion of the separation boundary with increasing field.

quent determination of the parameters entering into it. There are also distribution functions in the form of polynomials degree of intense and coercive fields [26–29]. For a convenient mathematical representation, we introduce the concept of an elementary dipole hysteresis operator (**Figure 21**) or the "relay" operator [22] using the functions of sets. Suppose that for any fixed pair $\alpha, \beta \in R \quad (\alpha < \beta)$, any function $E \in C^0[0, T]$, and any of the values $\xi = -1$, or $\xi = +1$ a function is defined $p: \quad [0, T] \rightarrow \{-1, +1\}$:

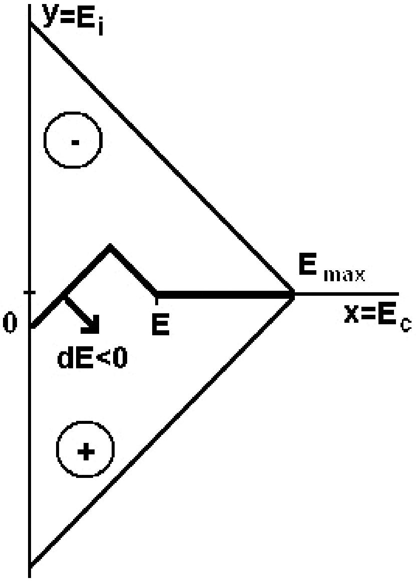

Figure 20. The motion of the separation boundary with decreasing field.

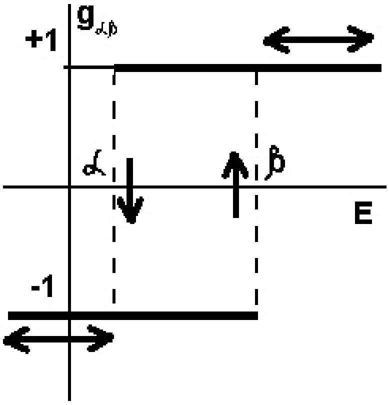

Figure 21. The definition of elementary dipole hysteresis operator.

$$p \in \begin{cases} p(0), & if \quad G_t = 0; \\ -1, & if \quad G_t \neq 0, \ E(\max G_t) = \alpha; \\ +1, & if \quad G_t \neq 0, \ E(\max G_t) = \beta, \end{cases} \quad p(0) \in \begin{cases} -1, & if \quad E(0) \leq \alpha; \\ \xi, & if \quad \alpha \leq E(0) \leq \beta; \\ +1, & if \quad E(0) \geq \beta, \end{cases}$$

and G_t—the set of singular time points, such that for $t \in (0, T]$

$$G_t := \{\tau \in (0, t] : E(\tau) = \alpha \quad or \quad \beta\}.$$

In view of the finiteness of the oscillations of any continuous function between α and β, it follows that $p(t)$ can have a limited number of jumps between $\{+1\},\ \{-1\}$. This allows us to determine the "relay" rate-independent operator

$$\gamma_{\alpha\beta} : C^0[o, T] \times \{-1, +1\} \to \{-1, +1\}.$$

The parameters α, β and x, y for the hysteron are related by the following linear relations: $\alpha = y - x;\quad \beta = y + x$. Using the "relay" operator and the distribution function of the hysterons, the irreversible polarization can be determined by the integral:

$$P(t) = p_s^* \iiint\limits_{x \geq 0} \mu(x, y) \left(\widehat{\gamma}_{\alpha\beta} E\right)(t) dx dy,$$

where p_s^*—the maximum polarization value achievable in the polarization process of ceramic by a homogeneous electric field. In addition, a notation $\gamma_{x-y,\, x+y} = \widehat{\gamma}_{xy}$ is introduced here. It is noteworthy that if we choose an equable distribution function

$$\mu(x, y) = \begin{cases} 1/E_{\max}^2 & at \quad (x, y) \in S_\Delta; \\ 0 & at \quad (x, y) \notin S_\Delta; \end{cases}$$

where S_Δ—the region on the half-plane of the variables x and y, indicated in **Figure 18** by a triangle, then by simple calculations of the integrals we easily find hysteresis dependences of the Rayleigh method.

Various forms of loops of dielectric hysteresis can be found in [2]. For example, if we neglect the correlation coefficient in the Gaussian distribution and use the symmetry condition for the function with respect to the variable y, we obtain

$$\mu(x, y) = \frac{1}{\sqrt{2\pi}\sigma_1} \exp\left[\frac{-(x - a_1)^2}{2\sigma_1^2}\right] \frac{1}{\sqrt{2\pi}\sigma_2} \exp\left(\frac{-y^2}{2\sigma_2^2}\right).$$

To estimate the influence of the parameter a_1 on the behavior of the curves of the hysteresis loop, we set $E_{\max} = 2 \cdot 10^6\ V/m;\ \sigma_1 = \sigma_2 = 2 \cdot 10^2\ V/m;$ and we will increase the parameter a_1 sequentially, assuming $a_1 = 0;\ 1 \cdot 10^6;\ 2 \cdot 10^6;\ 5 \cdot 10^6;\ 7 \cdot 10^6\ V/m$. The resulting hysteresis loops are shown in **Figure 22**, where the cases a, b, c, d, and e correspond to the indicated values of the parameter.

A Preisach model has become widely used not only in the description of magnetic and ferroelectric hysteresis, but it is intensively used in calculating the damping coefficients of many dynamical systems, including the dynamic of dipole switching [30–48]. Two-dimensional models were also developed [49–56].

Conclusion: Preisach model in the simplest case "includes" the domain structure, but operates only 180° domains. In the mathematical plan, the approximation of the real loop is carried out by elementary rectangular hysteresis loops. A model is intended only for finding the residual

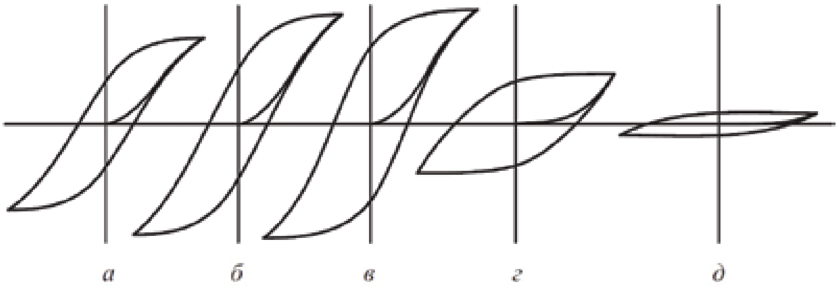

Figure 22. Preisach model: effect of increasing the parameter a_1 on the form of hysteresis loops.

polarization. This model does not include mechanical stresses, which significantly reduces its practical application.

3.5. Model of orientation switching

A representative volume is considered as a set of N domains oriented in space in an arbitrary manner [57]. Here, not only 180°, but also 90° switching are considered. Let the applied electric field has a tension **E** and each domain is characterized by vector of spontaneous polarization $\mathbf{p}_S$ and crystallographic axes **a**, $\mathbf{a}'$, **c** (**Figure 23**). By simple averaging one can determine the vector of residual polarization and the tensor of strain:

$$\mathbf{P}_0 \equiv < \mathbf{p}_S > = \frac{p_S}{N}\sum_k (\mathbf{c})_k; \quad \boldsymbol{\varepsilon}_0 \equiv < \boldsymbol{\varepsilon}_S > = \frac{\varepsilon_S}{N}\sum_k \left(\mathbf{c}\otimes\mathbf{c} - \frac{1}{2}\mathbf{a}\otimes\mathbf{a} - \frac{1}{2}\mathbf{b}\otimes\mathbf{b}\right)_k.$$

Denote the plane perpendicular to the vector **c** through B, and the plane passing through the vectors **E** and **c** by A. We introduce the following angles: the angle γ_c between the direction of the field and the axis **c**; the angle γ_a between the vector **a** and the field **E**; angle ω between the axis **a** and the line of intersection OK. It is obvious that the angles introduced are within

$$0 \le \gamma_c \le \pi; \quad 0 \le \omega \le \pi/4; \quad \omega \le \gamma_a \le \pi/2.$$

Let E_{cc}, E_{ca} be the coercive fields of 180° and 90° switching, respectively. The main conditions of 180° domains switching (turn) are

$$E\cos\gamma_c \ge E_{cc}; \quad \frac{E\cos\gamma_c}{E_{cc}} - \frac{E\cos\gamma_a}{E_{ca}} \ge 0.$$

For 90° domains switching, we have $\frac{E\cos\gamma_a}{E_{ca}} - \frac{E\cos\gamma_c}{E_{cc}} \ge 1$, if $\gamma_c \le \pi/2$ and $E\cos\gamma_a \ge E_{ca}$; $\frac{E\cos\gamma_a}{E_{ca}} - \frac{E\cos\gamma_c}{E_{cc}} \ge 0$, if $\gamma_c > \pi/2$.

A schematic representation of all domains axes **c** before and after polarization can be seen in **Figure 24**. Dielectric hysteresis loop are constructed for quasi-static processes, that is, for a sequence of equilibrium states $\{E_i\}$. With this goal, the process of loading by an electric field

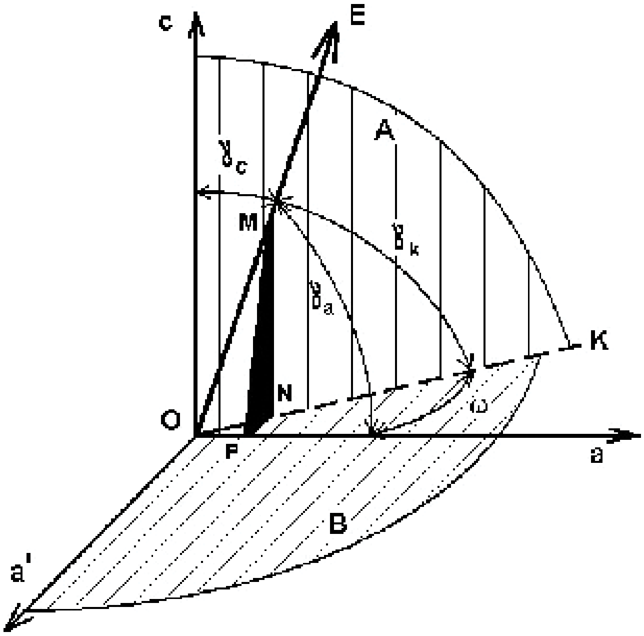

Figure 23. Determination of angles in the model of orientation switching.

$E = E(t)$ is replaced by a sequence of values of the electric field $E \in \{E_i\} : E_i = E(t_i)$, and for each state $E = E_i$, the domain switching conditions are checked, after which the residual polarization and the residual strain are calculated by simple averaging.

As an example [2], a hysteresis loop (**Figure 25**) was calculated for the next set of parameters: $N = 1273248$; $E_{cc} = 2 \cdot 10^6\ V/m$; $E_{ca} = 3 \cdot 10^6\ V/m$; $E_{\max} = 6 \cdot 10^6\ V/m$, where $E_{\max}$—maximum value of the electric field. It is interesting to note that a model makes it possible to determine

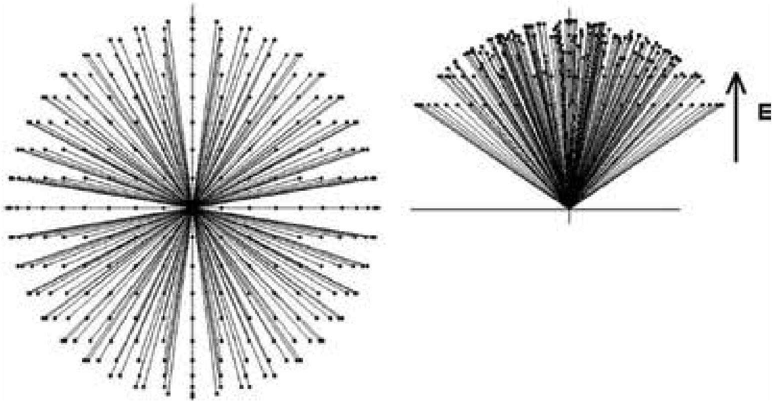

Figure 24. Schematic representation of domains axes **c** before and after polarization.

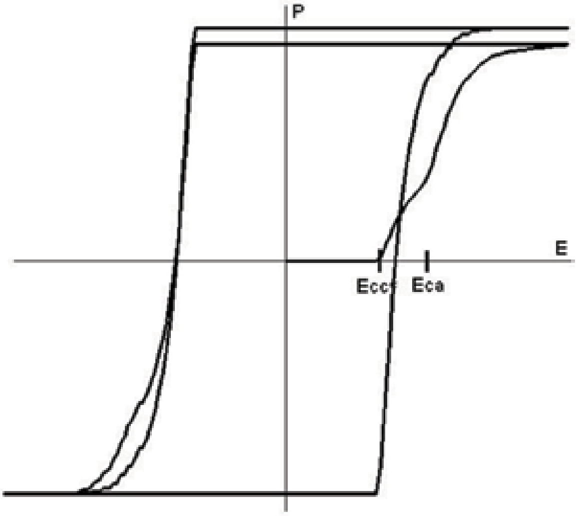

Figure 25. Model of orientation switching.

the value of the angle of cone in which the directions of all vectors of spontaneous polarization are distributed after the removal of the electric field. With the abovementioned numerical values of the parameters, we obtained: $\alpha = 129^0$; $P_{01} = -0.18 \cdot 10^{-4} p_s$; $P_{02} = -0.79 \cdot 10^{-5} p_s$; $P_{03} = 0.81 p_s$.

Conclusion: in physical terms, this model is closer to the physics of the phenomenon of polarization of polycrystalline ferroelectrics, but does not take into account the effect of neighboring domains on each other during the polarization process. Because of this, the loop acquires angular shapes and is not suitable for describing the differential properties of the material. On the other hand, it allows us to find a value of the angle in which the directions of all the spontaneous polarization vectors are located after reaching the saturation polarization. Another drawback of the model is that it does not include mechanical stresses, which does not allow us to investigate ferroelastic phenomena.

3.6. Energy model of switching

In this model, a representative volume is also considered, including a set of domains oriented in space in an arbitrary manner [2] and a residual polarization vector is determined by averaging. The main difference is in describing the orientation of domains and determining the criteria for switching domains. For example, for a ferroelectric of the perovskite type, the axes of the local system are introduced **a**, **b**, **c**, which are the axes of the crystallographic system directed along the ribs of a rectangular parallelepiped, as shown in **Figure 26**. The local system **a**, **b**, **c** with respect to a fixed system $Ox_1x_2x_3$ is determined by three angles φ, ψ, ω. The application of an electric field or mechanical stresses of high intensity causes a process of domain switching. However, the switching is consistent with the crystallographic axes of the ferroelectrics and is possible only in certain directions (**Figure 27**). Each domain in the field of

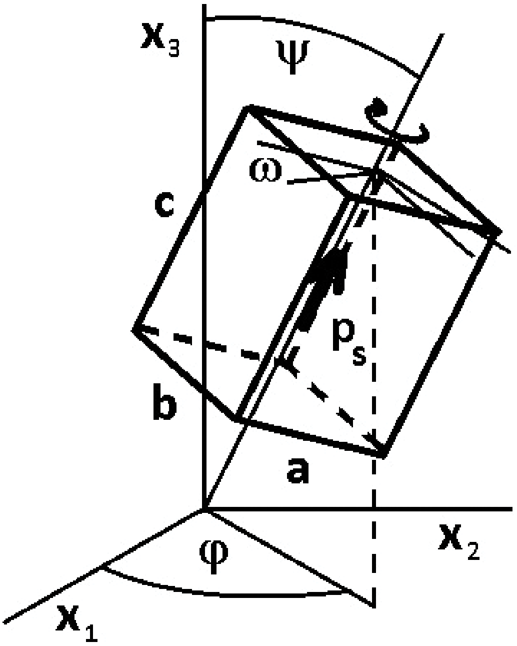

Figure 26. Determination of the angles of the transition from the local to the global coordinate system.

external loads (electric field and mechanical stresses) possesses some energy. When the loading factors change, the energy of each of the domains will change. If a domain has to switch, then that switching will be only in such direction where its energy minimal. The switching process starts only if a difference of domain energy of current state and the state with the minimum energy exceeds the threshold value [1, 58, 59]:

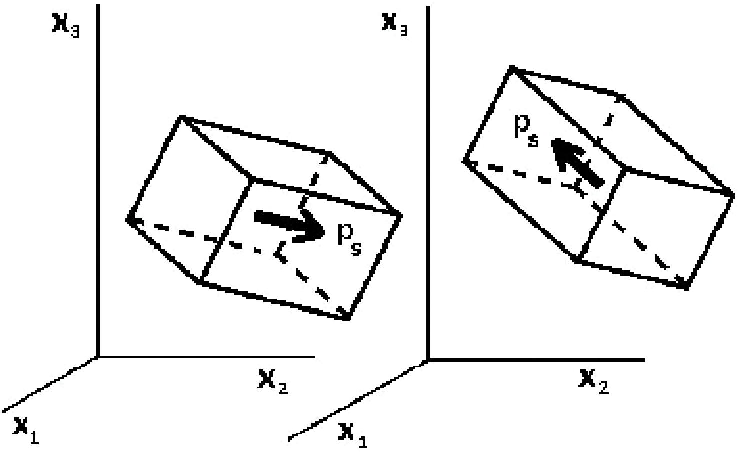

Figure 27. Possible positions of the spontaneous polarization vector and deformation of the unit cell.

$$-\mathbf{p}_\mathbf{S}\cdot\mathbf{E}+\mathbf{p}_\mathbf{S}^{\mathbf{min}}\cdot\mathbf{E}-\boldsymbol{\varepsilon}_\mathbf{S}:\boldsymbol{\sigma}+\boldsymbol{\varepsilon}_\mathbf{S}^{\mathbf{min}}:\boldsymbol{\sigma}\geq U_c,$$

where $\mathbf{E}$ is the electric field vector; $\boldsymbol{\sigma}$ is tensor of mechanical stresses; $\mathbf{p}_\mathbf{S}$ is vector of spontaneous polarization, $\boldsymbol{\varepsilon}_\mathbf{S}$ is tensor of spontaneous strain, and U_c is the threshold value of energy per unit volume. The form of the dielectric hysteresis loop practically coincides with the previous case; therefore, it is not given here.

Conclusion: the energy model of switching at physical essence takes into account the physical phenomena of polarization of polycrystalline ferroelectrics but also does not take into account the effect of neighboring domains on each other during the switching process. The dielectric hysteresis loop has angular shapes and is not suitable for describing the differential properties of a material. In addition, this model operates only with the residual parameters of polarization and strain and does not include induced components. However, this model has an unquestionable advantage because it already includes a mechanical stresses, which allows us to describe not only ferroelectric, but also ferroelastic phenomena.

3.7. The Giles-Atherton model

The model is based on the so-called "limiting" (or anhysteretic) curve, derived analytically on the basis of Weiss theory and Boltzmann statistics [60–67]. If in the polycrystalline ferroelectric material were no mechanisms for locking the walls of the domains, then after the removal of the electric field, the polarization of the representative volume would be zero. With great assumptions, one could say that such a material would behave like polar liquid, where the electric field tries to align dipoles along one direction, and the thermal fields impede it: impacts try to destroy the alignment pattern, and after removing the electric field, the thermal fields neutralize the polarization. Of course, a different domain switching mechanism is observed in polycrystalline ferroelectrics, but the switching model is borrowed from polar liquids.

To determine the dependence connecting the polarization of a representative volume with the strength of the effective electric field [60] let the representative volume of the ferroelectric material contain N domains with a spontaneous vector $\mathbf{p}_\mathbf{s}$. For the averaging operation, a point of reduction is chosen in space, and to each vector of spontaneous polarization is placed in conformity a unit vector parallel to it. The resulting vector of polarization is found by determining the area of the unit sphere onto which the ends of the unit vectors are exit. In an unpolarized state, all unit vectors are distributed uniformly over the entire surface, so that the resulting polarization is zero.

Using the positions of the Weiss theory, we assume that the field of forces acting on the ferroelectric domain is a sum of the electric field $\mathbf{E}$ and some "molecular field" proportional to its polarization: $\mathbf{E}^{ef}=\mathbf{E}+\alpha\mathbf{P}_0$, where α is a certain constant.

The potential energy of a domain that is similar to a dipole depends on the direction of its polarization vector and is expressed by the formula: $U=-\mathbf{p}_s\cdot\mathbf{E}^{ef}V$, where V—domain volume measure.

To determine the distribution of the domain axes in the presence of an effective field orienting them, it is necessary to use the Boltzmann theorem of statistical mechanics. Under the conditions of thermodynamic equilibrium, the distribution law for domains in the presence of a conservative electrostatic field differs from the law of their distribution in the absence of this field by a factor $\exp(-U/k_* T)$, where T is the absolute temperature, $k_* = 1.3807 \cdot 10^{-23}$ J/K is the Boltzmann constant. Therefore, the averaging operation yields the maximum possible polarization

$$\mathbf{P}_\infty = \frac{\int_0^{2\pi} d\varphi \int_0^{\pi} \exp\left(\frac{\mathbf{E}^{ef} \cdot \mathbf{p}_s}{k_* T}\right) \mathbf{p}_s \sin\psi \, d\psi}{\int_0^{2\pi} d\varphi \int_0^{\pi} \exp\left(\frac{\mathbf{E}^{ef} \cdot \mathbf{p}_s}{k_* T}\right) \sin\psi \, d\psi}.$$

In the one-dimensional theory, the direction of the electric field coincides with the direction of the axis Oz of the Cartesian fixed coordinate system, and the residual polarization in this direction is estimated. Taking into account this projection and calculating the integral, we determine the maximum residual polarization P_∞ of the representative volume in the form of a Langevin distribution:

$$P_\infty = p_s \left[\mathrm{cth}\left(\frac{E + \alpha P_0}{a}\right) - \frac{a}{E + \alpha P_0} \right], \qquad a = \frac{k_* T}{p_s V}.$$

In this model, a reversible (induced) part P_e as well as the residual part P_0 of the polarization is taken into account:

$$P = P_e + P_0.$$

The reversible part is the state parameter. It can be defined as:

$$P_e = c(P_\infty - P_0),$$

where c is still an indeterminate factor. The irreversible part of the polarization is the parameter of the process. Therefore, to determine it, we can use the evolutionary law, which can be written in differentials:

$$dP_0 = \frac{1}{k\delta}(P_\infty - P_0)\, dE^{ef},$$

where $\delta = \mathrm{sign}(dE)$, and k is a positive constant, also subjecting to determination. Passing from the effective to the applied field, we obtain an ordinary differential equation:

$$\frac{dP_0}{dE} = \frac{P_\infty - P_0}{k\delta - \alpha(P_\infty - P_0)}.$$

To solve the equation, we need use numerical methods, for example, the fourth-order Runge-Kutta method. When the electric field varies according to the harmonic law, we obtain dielectric hysteresis loops. The model includes five parameters: p_s, α, c, a, k, which are found from the condition of coincidence of calculated and experimental data. Numerous experiments were carried out in [2], and the effect of the model parameters on the shape of loops was investigated. It is shown that the coefficient α is responsible for the amplitude of the loop, the coefficient a—for its slope, the coefficient k for the loop area, the coefficient *c* for the flatness of the loop. Varying the values of the coefficients, one can achieve not only a qualitative but also a quantitative coincidence with the experimental data. It is shown that it is possible to start up the procedure for determining the model coefficients by the coincidence of the calculated values with the experimental data in the set of points.

Some examples of numerical calculations in which the influence of the coefficient k on the form of the hysteresis curves is studied are shown in **Figures 28–30**.

Conclusion: Giles-Atherton model deals with a huge number of distributed domains in a representative volume. Using of Boltzmann statistics made it possible, first, to construct an extremely possible polarization in the form of a Langevin distribution; second, to obtain the density of distribution of domains as a function of exponential type; third, to use the switching criterion. In this case, the switching is reduced to the energy rotations of the domains in dependency of the intensity of the electric field. The model contains both a reversible and a residual part of the polarization. The model contains a set of five parameters, which are chosen from the condition of coincidence of the calculated large hysteresis loop and experimental data. Due to shortcomings of the model, one can be attributed include a very rough approximation in the description of domain rotations in ferroelectrics, where this process is replaced by the process of rotation of dipoles in polar liquids in the construction of limiting polarization. This immediately affects when trying to build small hysteresis loops, where the results of calculations lead to large discrepancies.

3.8. Modeling of ferroelastics

It is interesting to note that, despite its shortcomings, the Giles-Atherton model can be used to describe deformation of ferroelastics [68]. Repeating the main contents of the previous model, we

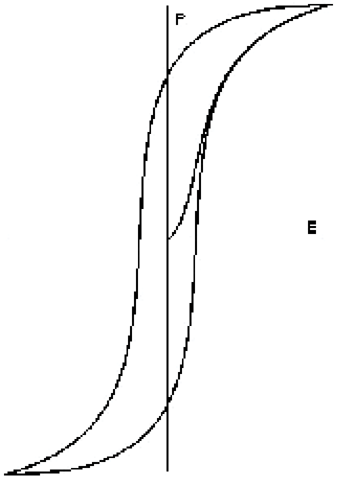

Figure 28. The Giles-Atherton model: the smaller the coefficient *k*, the narrower the hysteresis loop.

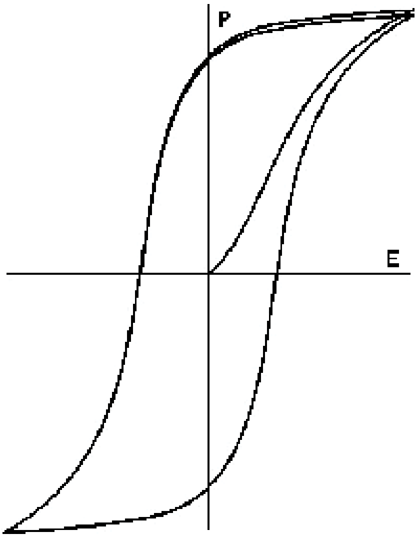

Figure 29. Model Giles-Atherton: with increasing coefficient *k*, the slope of the hysteresis loop changes.

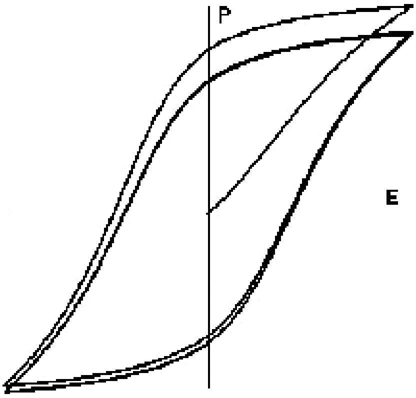

Figure 30. The Giles-Atherton model: with increasing coefficient *k*, the amplitude of the hysteresis loop changes.

can introduce the limiting strain, which in the one-dimensional case of stretching-compression reduces to calculating the probability integral of the imaginary argument:

$$\varepsilon_\infty = \frac{\varepsilon_s}{2}\frac{\int\limits_{-1}^{1}\exp\left[\frac{3(\sigma+\beta\varepsilon)}{2a}t^2\right]t^2\,dt}{\int\limits_{-1}^{1}\exp\left[\frac{3(\sigma+\beta\varepsilon)}{2a}t^2\right]dt},\qquad a = k_*T/\varepsilon_s V.$$

The total deformation consists of the reversible ε_e and irreversible ε_0 parts: $\varepsilon = \varepsilon_e + \varepsilon_0$, and to determine the irreversible part, we obtain an ordinary differential equation

$$\frac{d\varepsilon_0}{d\sigma} = \frac{\varepsilon_\infty - \varepsilon_0}{k\delta - \alpha(\varepsilon_\infty - \varepsilon_0)}.$$

The large and small loops of strain hysteresis, calculated from this model, can be seen in **Figures 31**, **32**.

In [68, 69], two modifications were made for these models in order to obtain small hysteresis loops. First, to the induced component of polarization and strain was added a summand proportional to the loading field. Second, restrictions on the process of domain switching during the construction of small cycles are introduced. The results of this modernization are shown in **Figures 33**, **34**. The obtained results are in good agreement with the experimental data shown in **Figures 8** and **11**, not only qualitatively, but also quantitatively.

Conclusion: the dignities and drawbacks of the model for ferroelastics are the same as those of the Giles-Atherton model.

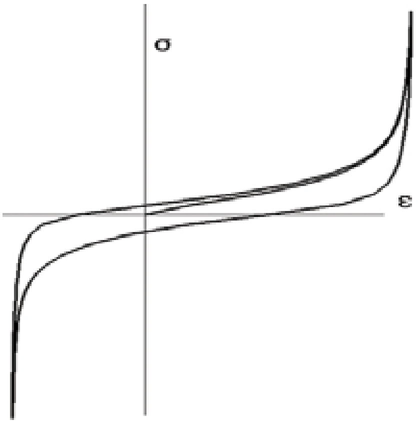

Figure 31. Modeling of ferroelastics: large hysteresis loop.

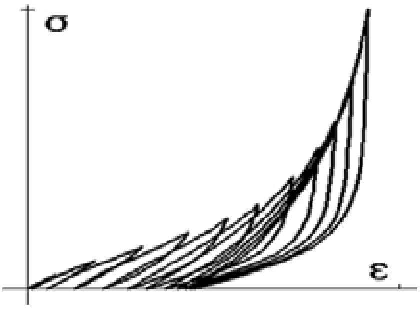

Figure 32. Modeling of ferroelastics: small hysteresis loops.

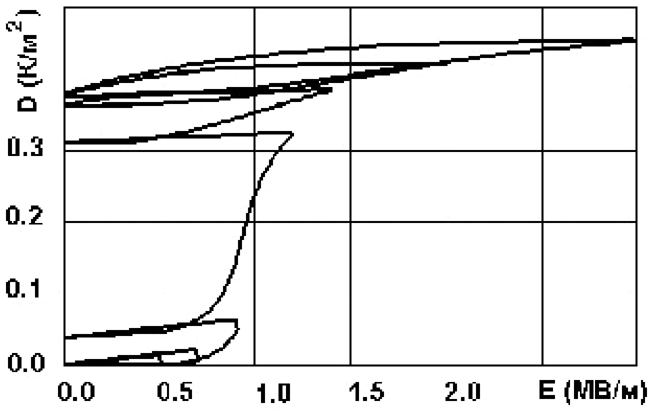

Figure 33. Improved Giles-Atherton model: small loops of dielectric hysteresis.

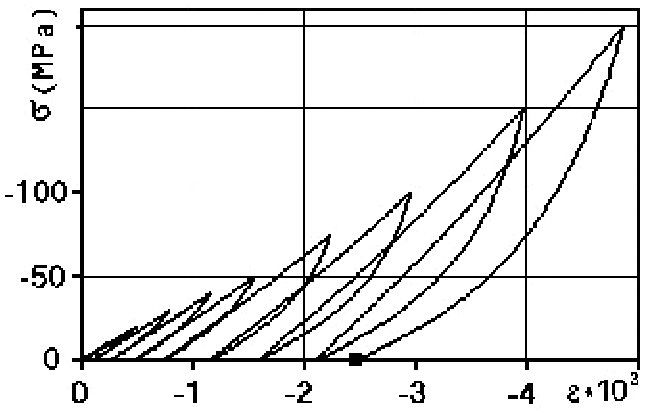

Figure 34. Improved Giles-Atherton model: small loops of deformation hysteresis.

4. Discussion

Each of the presented models performs the basic function related to the description of hysteresis dependencies. However, each of them is based on different prerequisites. Therefore, the results of the work of a particular model differ from the corresponding experimental data. The Rayleigh model gives a coincidence with the experimental data for small and medium fields. The Preisach model is widely used in areas where the integral properties of hysteresis are important. The model of orientation switching and model of the energy switching allow us to determine the cone of the angles all domains for which the directions of the vectors of the spontaneous polarization lined up inside this cone after the polarization to saturation, but the hysteresis loops have angular shapes. The Giles-Atherton model, taking into account the modernization, allows describing not only large but also small hysteresis loops.

Advantages and disadvantages of each of the considered models were presented earlier. Each of the models has a number of parameters that influence on the shape of the hysteresis loops. To determine these parameters, it is necessary to compare the calculated and experimental data. However, in the mathematical plan, this model belongs to the class of inverse problems and has a number of specific difficulties.

To sum up, it can be noted that the one-dimensional models allow describing hysteresis dependences of irreversible polarization processes. The more accurate the model is based on the physics of the phenomenon, the more accurate the results of its work. For example, those models that include lot of domains are more accurate in describing quantitative dependencies. However, analysis shows that at the present moment a universal mathematical model of the polarization and deformation of polycrystalline ferroelectric materials has not yet been developed, which would accurately reflect the data of the experimental dependences. Many problems that are importance remain unresolved. Unresolved problems include the following:

- small loops of dielectric and strain hysteresis have been poorly investigated;
- existing models do not reflect functional dependencies on the effects of any loading components with simultaneous exposure to electric fields and mechanical loads;
- the question of the validity of the application of the developed models to thin films remains open;
- there are no studies of how the anisotropy of the material changes with the simultaneous action of an electric field and mechanical stresses;
- very poorly represented models, which take into account the effect of neighboring domains on current switching;
- there are practically no studies related to the analysis of the similarity and differences in the existing models of Preisach, Rayleigh, Giles-Atherton, plasticity materials, except for [70, 71];
- in fact there is no mathematical analysis of the effect of model parameters on the final result, there is no formulation of a minimum set of parameters;
- very poorly represented models, which use the functions of the density of the distribution of domains.

5. Conclusions

One-dimensional models that reflect the hysteretic properties of polycrystalline ferroelectric media on the external effects of high-intensity electric and mechanical fields are considered. The bases of construction of each model are disassembled. The fundamentals of the construction of each of the well-known Rayleigh models, evolution models, models of plasticity theory, Preisach models, models of orientation switching, energy switching models, the Giles-Atherton model are analyzed and the results of their work in the form of hysteresis loops are presented. The main advantages and disadvantages of each model are noted; in particular, the differential and integral properties of hysteresis dependences are marked. It is noted that each of the models has a number of parameters, the choice of which affects the shape of the hysteresis loop. However, in the mathematical sense, such a choice generates additional difficulties, which are connected with the solution of inverse problems. Unresolved problems in the general problem of modeling the polarization of polycrystalline ferroelectric materials are noted. A list of works is given in which the main ideas and results of each of the earlier models are reflected.

Acknowledgements

This work was supported by the Russian Foundation for Basic Research (Grant 17-08-00860-a).

Author details

Alexander Skaliukh

Address all correspondence to: a.s.skaliukh@gmail.com

Southern Federal University, Rostov on Don, Russia

References

[1] Hall DA. Review. Nonlinearity in piezoelectric ceramics. Journal of Materials Science. 2001;**36**:4575-4601

[2] Belokon AV, Skaliukh AS. Mathematical Modeling of Irreversible Processes of Polarization. Moscow:Fizmatlit; 2010. 328 p. (In Russian)

[3] Lynch CS. The effect of uniaxial stress on the electro-mechanical response of 8/65/35 PLZT. Acta Metallurgica et Materialia. 1996;**44**(10):4137-4148

[4] Zhou D. Experimental Investigation of Non-linear Constitutive Behavior of PZT Piezoceramics. Dissertation, Institut für Materialforschung II Von der Fakultät für Maschinenbau der Universität Karlsruhe; 2003 (TH). 141 p

[5] Kamlah M, Wang Z. A Thermodynamically and Microscopically Motivated Constitutive Model for Piezoceramics. Wissenschaftliche Berichte FZKA 6880, Forschungszentrum Karlsruhe in der Helmgoltz-Gemeinschaft; 2003. 99 p

[6] Di Chen. Experimental Investigation of Strain Distributions and Polarization in Lead-based and Lead-free Ferroelectrics. Dissertation Doktors der Ingenieurwissenschaften, des Karlsruher Instituts für Technologie; 2017. 96 p

[7] Zareian Jahromi SA. Nonlinear Constitutive Modeling of Piezoelectric Materials. A thesis submitted to the faculty of graduate studies in partial fulfilment of the requirements for the degree of doctor of Philosophy. Department of Mechanical and Manufacturing Engineering, Calgary; 2013. 165 p

[8] Zhou D, Kamlah M, Munz D. Effects of bias electric fields on the non-linear ferro-elastic behavior of soft lead zirconate titanate piezoceramics. Journal of the American Ceramic Society. 2005;**88**(4):867-874

[9] Zhou DY, Kamlah M, Munz D. Uniaxial compressive stress dependence of the high-field dielectric and piezoelectric performance of soft PZT piezoceramics. Journal of Materials Research and Technology. 2004;**19**(3). pp. 834-842

[10] Zhou D, Kamlah M, Munz D. Effects of uniaxial prestress on the ferroelectric hysteretic response of soft PZT. Journal of the European Ceramic Society. 2005;**25**:425-432

[11] Rayleigh L. The behaviour of iron and steel under the operation of feeble magnetic forces. Philosophical Magazine. 1887;**23**:225-245

[12] Chen PJ, Peercy PS. One dimensional dynamic electromechanical constitutive relations of ferroelectric materials. Acta Mechanica. 1979;**31**:231-241

[13] Chen PJ, Tucker TJ. Determination of the polar equilibrium properties of the ferroelectric ceramic PZT 65/35. Acta Mechanica. 1981;**38**:209-218

[14] Chen PJ, Montgomery ST. A macroscopic theory for the existence of the hysteresis and butterfly loops in ferroelectricity. Ferroelectrics. 1980;**23**:199-208

[15] Chen PJ, Tucker TJ. One dimensional polar mechanical and dielectric responses of the ferroelectric ceramic PZT 65/35 due to domain switching. International Journal of Engineering Science. 1981;**19**:147-158

[16] Bailey PB, Chen PJ. Transient electromechanical responses of ferroelectric ceramics to impulsive electric fields. International Journal of Solids and Structures. 1981;**17**:471-478

[17] Chen PJ, Madsen MM. One dimensional polar responses of the electrooptic ceramic PLZT 7/65/35 due to domain switching. Acta Mechanica. 1981;**41**:255-264

[18] Chen PJ. Hysteresis effects in deformable ceramics. In: Maugin GA, editor. The Mechanical Behavior of Electromagnetic Solid Continua (IUTAM). North-Holland, Amsterdam: Elsevier Science Publishers; 1984. pp. 137-143

[19] Chen PJ. Three dimensional dynamic electromechanical constitutive relations of ferroelectric materials. International Journal of Solids and Structures. 1980;**31**:1059-1067

[20] Filatov OP, Khapaev MM. Averaging of Systems of Differential Inclusions: Textbook. Moscow: Publishing House of Moscow University; 1998. 160 p. (In Russian)

[21] Palmov VA. Oscillations of Elastic-plastic Bodies. Moscow: Nauka; 1976. 328 p. (in Russia)

[22] Visintin A. On hysteresis in elasto-plasticity and in ferromagnetism. International Journal of Non-Linear Mechanics. 2002;**37**:1283-1298

[23] Preisach F. Uber die magnetische nachwirkung. Zeitschrift fur Physik. 1935;**94**:277-302

[24] Visintin A. Quasilinear first-order PDEs with hysteresis. Journal of Mathematical Analysis and Applications. 2005;**312**:401-419

[25] Visintin A. Quasilinear hyperbolic equations with hysteresis. Annales de l'Institut Henri Poincaré–AN. 2002;**19**(4):451-476

[26] Robert G, Damjanovic D, Setter N. Preisach distribution function approach to piezoelectric nonlinearity and hysteresis. Journal of Applied Physics. 2001;**90**(5):2459-2464

[27] Robert G, Damjanovic D, Setter N. Preisach modelling of ferroelectric pinched loops. Applied Physics Letters. 2000;**77**(26):4413-4415

[28] Robert G, Damjanovic D, Setter N, Turik AV. Preisach modeling of piezoelectric nonlinearity in ferroelectric ceramics. Journal of Applied Physics. 2001;**89**(9):5067-5074

[29] Turik AV. To the theory of polarization and hysteresis of ferroelectrics. Solid State Physics. 1963;**5**(4):1213-1215

[30] Zs S, Tugyi I, Gy K, Fuzi J. Identification procedures for scalar Preisach model. Physica, B. 2004;**343**:142-147

[31] Azzerboni B, Cardelli E, Finocchio G. A comparative study of Preisach scalar hysteresis models. Physica B. 2004;**343**:164-170

[32] Ragusa C. An analytical method for the identification of the Preisach distribution function. Journal of Magnetism and Magnetic Materials. 2003;**254-255**:259-261

[33] Fuzi J. Strong coupling in electromechanical computation. Journal of Magnetism and Magnetic Materials. 2000;**215-216**:746-748

[34] Kadar G. On the product Preisach model of hysteresis. Physica B. 2000;**275**:40-44

[35] Hu H, Mrad RB. On the classical Preisach model for hysteresis in piezoceramic actuators. Mechatronics. 2003;**13**:85-94

[36] Liu J, Sh Z, Chen F, Ch Y, Zhou X. Measurements and simulation of hysteresis loops of donor-doped strontium bismuth tantalate ceramics. Physics Letters A. 2004;**321**:199-204

[37] Meyer V, Sallese J-M, Fazan P, Bard D, Pecheux F. Modeling the polarization in ferroelectric materials: a novel analytical approach. Solid-State Electronics. 2003;**47**:1479-1486

[38] Yu Y, Naganathan N, Dukkipati R. Preisach modelling of hysteresis for piezoceramic actuator system. Mechanism and machin theory. 2002;**37**:49-59

[39] Chuntao L, Yonghong T. A neural networks model for hysteresis nonlinearity. Sensors and Actuators A. 2004;**112**:49-54

[40] Sjostrom M. Differentiation and power loss computation of classical Preisach model. Physica B. 2004;**343**:96-100

[41] Pasco Y, Berry A. Consideration of piezoceramic actuator nonlinearity in the active isolation of deterministic vibration. Journal of Sound and Vibration. 2006;**289**:481-508

[42] Kadar G, Szabo G. Hysteresis modeling. Journal of Magnetism and Magnetic Materials. 2000;**215-216**:592-596

[43] Fuzi J. Experimental verification of a dynamic hysteresis model. Physica B. 2004;**343**:80-84

[44] Zirka SE, Moroz YI, Marketos P, Moses AJ. Properties of dynamic Preisach models. Physica B. 2004;**343**:85-89

[45] Morentin FJ, Alejos O, Francisco C, Munoz JM, Hernandez-Gomez P, Torres C. Simple standard problem for the Preisach moving model. Physica B. 2004;**343**:107-111

[46] Cardelli E, Bertoncini F, Di Fraia S, Tellini B. Implementation of the modified Preisach scalar model in the finite difference - time - domain numerical modeling. Physica B. 2001; **306**:126-131

[47] Belbas SA, Mayergoyz ID. Optimal control of dynamical systems with Preisach hysteresis. International Journal of Non-Linear Mechanics. 2002;**37**:1351-1361

[48] Cross R, Krasnoselskii AM, Pokrovskii AV. A time-dependent Preisach model. Physica B. 2001;**306**:206-210

[49] Visintin A. Vector Preisach model and Maxwell's equations. Physica B. 2001;**306**:21-25

[50] d'Aquino M, Serpico C. A new Preisach-type vector model of hysteresis. Journal of Magnetism and Magnetic Materials. 2004;**272-276**:731-733

[51] Fuzi J. Two Preisach type vector hysteresis models. Physica B. 2004;**343**:159-163

[52] Kedous-Lebouc A, Vernescu C, Cornut B. A two-dimensional Preisach particle for vectorial hysteresis modeling. Journal of Magnetism and Magnetic Materials. 2003;**254-255**:321-323

[53] Fuzi J. Anisotropic vector Preisach particle. Journal of Magnetism and Magnetic Materials. 2000;**215-216**:597-600

[54] Kahler G, Torre ED. Application of simplified vector Preisach model to vector magnetizing process. Physica B. 2000;**275**:114-119

[55] Torre ED, Pinzaglia E, Cardelli E. Vector modeling-Part I: Generalized hysteresis model. Physica B. 2006;**372**:111-114

[56] Serpico C, d'Aquino M, Visone C, Davino D. A new class of Preisach-type isotropic vector model of hysteresis. Physica B. 2004;**343**:117-120

[57] Fesenko EG, Danziger AYa, Kramarov OP, and Others. Polarization of Ceramics–Rostov on Don, Publishing House of Rostov State University, 1968. 136 p. (in Russia)

[58] Skaliukh A. About hysteretic operators arising in the modelling of the polarization of ferroelectric materials. Proceedings of the International Conference on Mathematical Sciences, July 17-19, 2014, Chennai, India, Sathyabama University, Published By Elsevier, a division of Reed Elsevier India Private Limited, New Delhi; 2014. pp. 635-638

[59] Shindo Y, Narita F, Horiguchi K, Magara Y, Yoshida M. Electric fracture and polarization switching properties of piezoelectric ceramic PZT studied by the modified small punch test. Acta Materialia. 2003;**51**:4773-4782

[60] Tamm IE. Fundamentals of the Theory of Electricity: Textbook for high schools. 11th ed. Moscow: FIZMATLIT; 2003. 616 p. (in Russia)

[61] Jiles DC, Atherton DL. Theory of magnetic hysteresis. Journal of Magnetism and Magnetic Materials. 1986;**61**:48-60

[62] Sadowski N, Batistela NJ, Bastos JPA, Lajoie-Mazenc M. An inverse Jiles - Atherton model to take into account hysteresis in time-stepping finite-element calculations. IEEE Transactions on Magnetics. 2002;**38**(2):797-800

[63] Jiles DC. Introduction to Magnetism and Magnetic Materials. New York: Chapman and Hall; 1991

[64] Smith RC. A nonlinear optimal control method for magnetostrictive actuators. Journal of Intelligent Material Systems and Structures. 1998;**9**(6):468-486

[65] Smith RC, Hom CL. A domain wall model for ferroelectric hysteresis. SPIE Conference on Mathematics and control in Smart Structures, SPIE Vol. 3667, Newport Beach, CA, March 1-4, 1999. pp. 150-161

[66] Smith RC, Hom CL. Domain wall theory for ferroelectric hysteresis. Journal of Intelligent Material Systems and Structures. 1999;**10**(3):195-213

[67] Smith RC, Ounaies Z. A domain wall model for hysteresis in piezoelectric materials. Journal of Intelligent Material Systems and Structures. 2000;**11**(1):62-79

[68] Skaliukh A, Belokon A. Modeling strain and dielectric hysteretic type dependences in polycrystalline ferroelectrics by methods of two-level continuum. 1st International Conference on Rheology and Modeling of Materials (IC-RMM1). Journal of Physics: IOP Conference Series. 2015;**602**:012025

[69] Parinov IA, editor. Piezoceramic Materials and Devices. Chapter 2. N.-Y.: NOVA Publishers; 2012. pp. 55-104

[70] Benabou A, Clenet S, Piriou F. Comparison of Preisach and Jiles–Atherton models to take into account hysteresis phenomenon for finite element analysis. Journal of Magnetism and Magnetic Materials. 2003;**261**:139-160

[71] Suzuki T, Matsumoto E. Comparison of Jiles–Atherton and Preisach models extended to stress dependence in magnetoelastic behaviors of a ferromagnetic material. Journal of Materials Processing Technology. 2005;**161**:141-145

Section 2

Ferroelectrics Applications

Chapter 5

On the Mechanical and Dielectric Properties of Biocomposites Containing Strontium Titanate Particles

Amarilis Declet-Vega, Nelson Sepúlveda-Ramos and
Oscar Marcelo Suárez

Additional information is available at the end of the chapter

http://dx.doi.org/10.5772/intechopen.76858

Abstract

In recent years, scientists advanced the study of bio-ferroelectric composites to develop new environmentally friendly and inexpensive electronic elements such as capacitors, actuators, and transistors. Accordingly, the present research relates to composites made of chitosan-cellulose polymeric matrix and strontium titanate (STO) nanoparticles. The variables considered include different percentages of cellulose (15 and 25 v%) and strontium titanate nanoparticles (10 and 20 wt%). The electrical characterization of the composites included measuring their dielectric constant, current density, and conductivity. The results suggest that the addition of STO nanoparticles raised the dielectric constant while lowering the current density and the conductivity of the nanocomposites. Moreover, although the cellulose addition increased the current density and the conductivity of the composites, it lowered their dielectric constant. Also, the resulting biocomposite capacitors could withstand up to 60 V without any detectable dielectric breakdown. The other two properties measured were the ultimate tensile strength (UTS) and the degradation temperature (Tdeg). Higher percentages of cellulose decreased the UTS and the Tdeg of the chitosan-cellulose composites while the addition of cellulose slightly raised these properties of the composites made of chitosan-cellulose and STO nanoparticles. The results proved that these types of biocomposites are apt as capacitors with adequate strength to withstand aggressive environments. This work was fully conducted in the facilities of the Nanotechnology Center hosted by the University of Puerto Rico – Mayagüez, from December 2014 to January 2017.

Keywords: ferroelectric nanoparticles, dielectric constant, biopolymers, chitosan, biocomposites, strontium titanate

1. Introduction

Biopolymers have attained significant market potential due to their numerous applications in diverse fields such as "bio-ceramic, bio-sensing, bio-encapsulation, and bio-inorganic nanoparticles" [1]. The main motivation for studying these biopolymers rises from their unique characteristics: bio-compatibility, low environmental impact, and nontoxicity (for human use) [2, 3]. Since these materials are biodegradable, they can be recycled, which translates into waste reduction and smaller recycling cost. An additional appealing feature is the low fabrication cost of these biopolymers when compared to petroleum-based ones.

Researchers have been using these biopolymers as matrices for composites containing ferroelectric particles, i.e., $BaTiO_3$, $SrTiO_3$, $CaTiO_3$, and $PbTiO_3$. In particular, they have been seeking for an alternative for processable high permittivity materials with high dielectric constant, moderate dielectric strength, low dielectric loss, high electrical resistivity, among other properties [4, 5]. These electrical characteristics made these composites particularly suitable for capacitors, transistors, and actuators.

For instance, Neagu et al. studied dielectric properties of bio-composites made of chitosan with different percentages of $BaTiO_3$ particles: 0, 1 and 10% [6]. Among the different fabrication methods available to produce the polymeric films, the authors selected the dry phase inversion casting process. This research demonstrated that higher $BaTiO_3$ concentrations in the polymeric matrix raised the dielectric constant while lowering the dielectric loss. This led to a simple approach to create flexible electronic devices made of polymeric and ferroelectric constituents.

Moreover, Elimat evaluated the electrical properties of composites made of epoxy with various zinc oxide (ZnO) concentrations and reinforced with 1.0 wt% of conductive carbon black nanoparticles to dissipate any potential electrostatic charges [7]. The results revealed an increase in higher dielectric constant values as the temperature and the ZnO concentration heightened. However, that dielectric constant diminished for higher frequencies, namely from 0.1 to 1 MHz; this was attributed to the dipoles' lack of time to align with the electrical field. In addition, the authors demonstrated that higher concentrations of ZnO nanoparticles increased the electrical conductivity of the composites. Such higher electrical conductivity is due to the increase of the charge carriers' density in the polymeric matrix.

Petrov et al. studied the electrical properties of chitosan and hydroxyapatite (HA) biocomposites. In their study, they implemented an innovative approach via a corona discharge treatment to increase the charge surface of the polymeric matrix. The researchers tested the dielectric permittivity of the composites using dielectric spectroscopy and by employing a parallel plate capacitor for the electrical measurements. Their results evinced no difference in dielectric permittivity between the composites made of 6 and 10 g/L of chitosan solution. However, a notable difference was observed in the dielectric permittivity as a function of temperature and frequency. Although higher temperatures increased the dielectric permittivity of the composites, such permittivity decreased at higher frequencies [8].

Hosokawa et al. fabricated composites made of chitosan and cellulose to study their mechanical properties [9]. To fabricate the composites, chitosan was dissolved in a water/acetic acid while cellulose fibers were diluted in an aqueous solution. Then, a small amount of chitosan was added into the cellulose solution containing glycerol. The ensuing solution was mechanically stirred and degassed before the drying process. Their results suggest that the tensile strength decreased as the swelling degree increased in the composites. The authors attributed this to the crosslinking between the carbonyl groups (C═O) and the carbonyl groups (C–OH) in the cellulose structure with the amine groups of the chitosan.

Another pertinent study was conducted by Ibrahim et al., who fabricated polyester-oil palm ash composites [10]. The specimens were prepared at different volume fraction of oil palm ash (0, 10, 20 and 30%) in unsaturated polyester matrix. All samples were mechanically characterized with a universal testing machine with a 10 kN load capacity, operated at a 5 mm/min strain rate. The measured tensile strength of the composites decreased from 26.8 to 13 MPa with the tensile modulus rising from 375 to 499 MPa as the content of nanofillers increased from 0 to 30%. The smaller tensile strength was attributed to the interaction of the nanofiller with the polymer matrix. Conversely, the fillers imparted greater stiffness to the composite. In addition, when the authors analyzed the composites' thermal properties, they discovered that the particles enhanced the thermal stability of the composites from 293.55°C without oil palm ash to 401.72°C with 30% oil palm ash.

Aware of such trend and in an effort to propose an alternative material suitable for capacitors, in the present research we engineered a composite with a chitosan-cellulose matrix, reinforced with strontium titanate ($SrTiO_3$) nanoparticles. The polymeric matrix provides flexibility, which is adjustable with the relative amount of cellulose, while the $SrTiO_3$ (STO) nanoparticles helped tune the dielectric constant, the current density, and the electrical conductivity. The control of the capacitance dependency on the frequency would allow devices to vary their capacitance depending on the application in which they would be deployed. Hence, this work brings about a novel perspective on the tunable properties of the chitosan-based composite for flexible electronics and bio-compatible properties.

2. Experimental procedure

The present research encompassed two stages. In the first one, the composites were synthesized to produce enough material for the second stage. Upon this stage, the composites underwent both mechanical and electrical characterization. This experimental section was completed in the facilities of the Nanotechnology Center hosted by the University of Puerto Rico – Mayagüez, from August 2013 to August 2015.

2.1. Materials selection

All samples were fabricated using poly (D-glucosamine) deacetylated chitosan ($(C_6H_{11}O_4N)_n$, 75% deacetylation, Sigma Aldrich), cellulose powder (cotton linens, Sigma Aldrich) and strontium titanium oxide ($(SrTiO_3)$, 99 + %, Fisher). A chitosan solution was dissolved in acetic acid solution (CH_3CO_2H, 99.7 + %, Alfa Aesar) while 4-methylmorpholine N-oxide solvent (CH_3CO_2H, 99.7 + %, Alfa Aesar) was needed to dissolve the cellulose powder. The fabrication of the composites consisted of two subsequent stages: (1) fabrication of chitosan-cellulose films, and (2) synthesis of chitosan-cellulose composites containing $SrTiO_3$ nanoparticles.

2.2. Sample preparation

To prepare the specimens, one must considered their adequate size for the ensuing characterization. In particular, special care was taken to better the uniform distribution of the particles in the matrix.

2.2.1. Biopolymeric films

The biopolymeric films consisted of a mixture of chitosan and cellulose, prepared by means of the solution casting technique. To prepare the chitosan solution, a fixed concentration of the polymer (1.5 v%) was dissolved in an acetic acid aqueous solution and mechanically stirred. Furthermore, the cellulose solution was made by adding the polymer into a 4-Methylmorpholine N-oxide (NMMO) solvent, followed by mechanical stirring at 65°C to enhance the polymer solubility. A fixed concentration of cellulose, i.e., 0.5 v%, was used for the preparation of the composites. A higher concentration of cellulose would have raised the water content, which could have been detrimental for the resulting electrical, mechanical, and thermal properties.

After the stock solutions of chitosan and cellulose were prepared separately, we readied smaller stock solutions with different volume percentages of chitosan and cellulose: 85 v%Ch-15 v%Cel and 75 v%Ch-25 v%Cel. After mixing the components, we mechanically stirred the solutions, poured them into petri dishes, and let them dry in an oven at 40°C. Afterwards, we removed the films from the petri dishes using a basic solution and dried them in an oven once again [7].

2.2.2. Bio-ferroelectric nanocomposites

The double layered bio-ferroelectric composites were fabricated layer-by-layer via the solution casting method. The first layer consisted of chitosan-cellulose bio-polymers and the second layer consisted of the bio-polymers mixed with strontium titanate (STO) particles. To fabricate the said first layer, small solutions of chitosan and cellulose (i.e., 85 v%Ch-15 v%Cel and 75 v%Ch-25 v%Cel) were synthesized and transferred in the petri dishes for the dry process. The purpose of the second layer was to prevent the nanoparticles from settling and passing through the still soft first polymeric film. Hence, for the second layer, the same amount of small solutions was synthesized, this time with different STO amounts, i.e., 10 and 20 wt%; the goal was to analyze their effect in the electrical properties of the resulting bio-composites. Thereafter, these solutions were transferred onto their corresponding first layer of chitosan-cellulose followed by a second drying process to remove any residual water from the polymeric matrix.

The dispersion of nanoparticles within a given matrix has always been an issue, as proven in a prior research [11]. Therefore, to enhance such dispersion in the matrix we reduced the size of the particles using a varioplanetary high energy ball mill. To find the optimal time in which we could reduce the particle size to the smallest possible, the particle size was determined at different milling times using the Scherrer equation [12, 13]. Afterwards, the particle size was computed at different milling times to select the most time-efficient operation, i.e., maximum size reduction at minimal time. The overall technique had been successfully implemented to reduce the size of compound particles in previously published works [14, 15].

2.3. Characterization

2.3.1. Structure analysis

All samples were characterized with a Rigaku ULTIMA III diffractometer operated at 40 kV and 44 mA. The characterization of the composites was conducted at 25°C with a 2θ step of 0.02° and a 1 s dwelling time. The target used was copper with a $K\alpha$ wavelength of 0.154178 nm.

2.3.2. Electrical analysis

To measure the capacitance of the composites, we utilized a QuadTech 2200 automatic transformer system (with an AC supply). The frequency range was set from 1 to 10 kHz. Once the capacitance readings as a function of the frequency were recorded, the dielectric constant was determined for the biocomposites using Eq. (1).

$$K = \frac{C.d}{A.\varepsilon_0} \quad (1)$$

where K is the dielectric constant; C, the capacitance of the dielectric material; A, the area of the plates; d, the distance between the plates; and ε_o, the permittivity of vacuum [16].

To study dielectric breakdown in the composite, a GW INSTEK GPS-3303 DC power supply provided the current passing through the material when the applied voltage changed from 5 to 60 V. A GW-INSTEK GDM-8246 power meter connected in series was used to register the current values by following the guidelines of the ASTM D-149 standard [17]. According to this standard, the current flow must be recorded at equal increments of voltage and after a specific time. For our research, 5 V increments were applied to the dielectric material and then, after 10 s, the current flow was recorded at each of those increments. The current allowed us to determine the conductivity of the dielectric material.

To construct the capacitor, an AJA ATC Orion magnetron sputtering unit permitted to apply a titanium coating on both sides of the biocomposite film for 20 min at 200 W. All these capacitors were characterized using a Caframo™ stirrer clamp made of cast zinc-aluminum alloy and coated with epoxy as shown in **Figure 1**. The stirrer clamp also included a hold chuck key to ensure a close circuit between the capacitor and the copper electrodes. One electrode was placed at the base of the chuck key while another electrode was placed at the base of the Calframo™ stirrer clamp. In addition, a small weight of 1.27 N was placed on top of the chuck key to ensure proper contact between the capacitor and the electrodes. The ASTM D-150 standard provided guidelines to select the dimensions of the capacitors, i.e., 10 mm in length and 10 mm in width [18, 19].

Figure 1. Calframo™ stirrer clamp utilized in the measurement of the dielectric properties.

2.3.3. Thermal analysis

A Mettler Toledo TGA/SDTA thermogravimetric / differential thermal analyzer (operated at a 5°C/min. Temperature ramp from 25 to 500°C) allowed determining the degradation temperature (T_{deg}) of the composites in a nitrogen atmosphere. The samples were placed on a weight scale, which detects the mass loss of the samples as a function of temperature. To determine the said T_{deg}, the first derivate was applied to the heating rate curve obtained from the thermal analyzer.

2.3.4. Mechanical characterization

The samples' ultimate tensile strength was measured at room temperature (25°C) using a low force Instron® model 5944 universal testing machine. The deformation velocity was set at 1 mm/min. Also, the dimensions of the samples followed the ASTM D-1708, which specifies a 22 mm gauge length, a 5 mm width, and a 5 mm radius fillet.

3. Results and discussion

3.1. $SrTiO_3$ Nanoparticles

Previous research showed that the particle size affects electrical, mechanical, and thermal properties of similar composites [20]. As aforementioned, to improve the dispersion of the particles in the polymeric matrix, the particle size was reduced using the high energy ball mill.

Furthermore, reducing the size of the particles can create impurities upon ball milling and to confirm that the crystalline structure of the strontium titanate remained without changes, the powder was analyzed by x-ray diffraction. **Figure 2** displays the resulting diffractogram that matched with the expected STO pattern; the presence of impurities was not detected.

As aforementioned, from the diffractograms, Scherrer equation allowed estimating the particle size of the STO powder at different milling times. The equation takes into consideration the width of the largest XRD peak in the diffractogram [21, 22], which in our case (**Figure 2**) lies at $\theta = 32.5°$. The Miller indexes were identified by comparison with a prior publication by Trepakov et al. [23].

Figure 3 presents the milling time effect on the particle size. Two stages can be observed in the reduction (by fragmentation) of the particle size. The first stage occurs between 0 to 5 h of milling and presents a rapid reduction in the particle size from 46 to 18 nm. The rapid reduction in the particle size may be attributed to the fragmentation of large agglomerates into individual aggregates and therefore, the fracture of aggregates into individual primary particles and small aggregates [24]. In the second stage (5–20 h) of milling, the change in size was negligible. This was attributed to the increasing agglomeration of the fractured particles that impedes further fragmentation and, hence, size reduction; further, formation of surface cracks between the small aggregates or at the surface of individual particles could also have occurred [24].

As indicated previously, the relevance of adjusting the particle size lies on its effect on the electrical and mechanical properties of the nanocomposites. According to the literature, the nanoparticles agglomeration could adversely affect the electrical and mechanical properties of the nanocomposites [21, 22]. As the particle size decreases, the dispersion of the nanoparticles increases in the polymeric matrix and, therefore, improves the electrical and mechanical properties.

Scanning electron microscopy (SEM) images in **Figure 4** allow observing the dispersion of the nanoparticles in the polymer matrix. At low magnification, the presence of STO aggregates

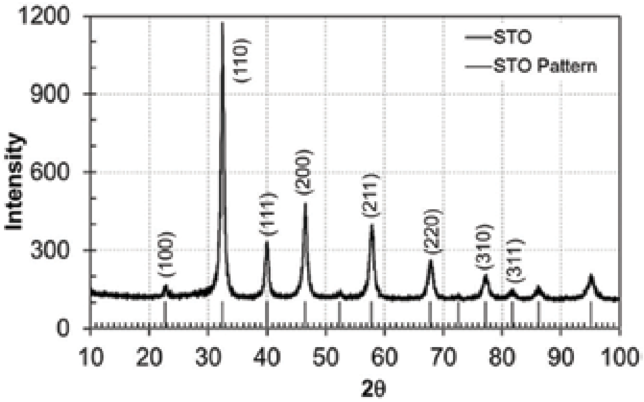

Figure 2. X-ray diffraction pattern of STO after 10 h of milling and powder diffraction line pattern.

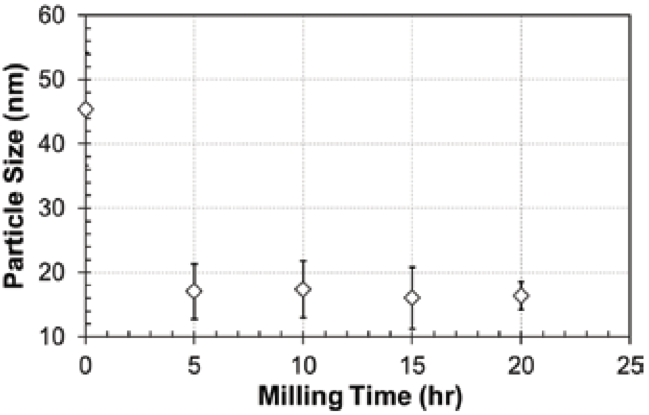

Figure 3. Particle size of STO nanoparticles at different milling times.

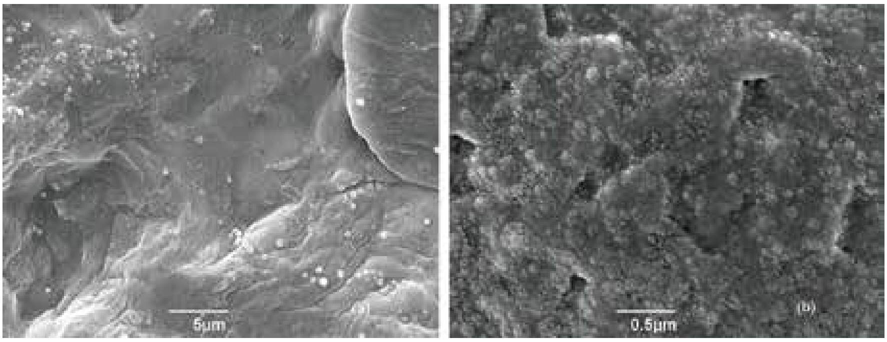

Figure 4. Secondary electron images obtained from the biocomposite with 20 wt% STO particles: (a) low magnification; (b) high magnification.

is apparent on the polymer surface. However, a significant dispersion of STO aggregates becomes visible on the polymer surface at high magnification.

3.2. Electrical properties

The dielectric constant was computed from the experimental results by using the capacitance equation for a parallel plate capacitor (Eq. (1)) at different frequencies. In a previous study, the addition of cellulose was detrimental to the capacitance of the nanocomposites while larger amounts of STO nanoparticles raised it [11]. Since the capacitance and the dielectric constant are directly proportional, higher amount of cellulose decreased the dielectric constant while the addition of the STO nanoparticles raised the dielectric constant of the nanocomposites (**Figure 5**). In addition, the dielectric constant of the nanocomposites diminished at high frequencies [25]. We expect that this finding will not only increase the capacity of energy storage devices but also control their capacitance values at different frequencies.

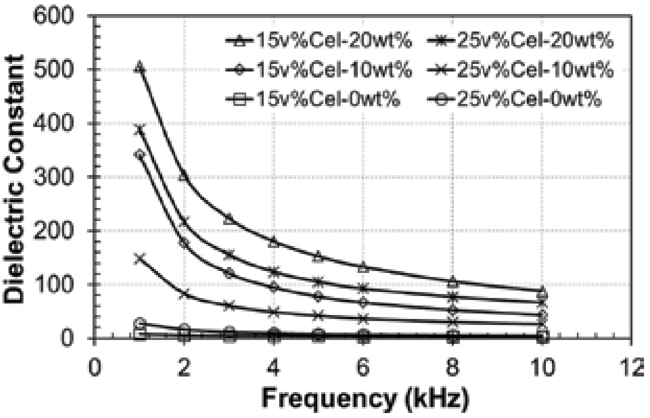

Figure 5. Calculated dielectric constant of the nanocomposites as a function of frequency.

As aforementioned, chitosan was dissolved in a water/acetic acid solution, enhancing the interaction between cellulose and water molecules in the solution. Such molecular interactions can be: (a) water molecules linked to cellulose hydroxyl (–OH) groups, or (b) water molecules confined between the polymer chains due to intermolecular hydrogen bonds. These interactions heightened the water content in the nanocomposites and, hence, raised the current flow through the capacitor [11, 26].

Moreover, higher amounts of STO nanoparticles increased the dielectric constant of the material [11]. The main characteristic of these ferroelectric nanoparticles consists of their ability to raise the material's stored energy. However, these ferroelectric nanoparticles are difficult to disperse in a polymeric matrix due to their high internal energy. It has also been reported that particle size reduction, by expanding the polymer-particles interface, enhanced the electrical properties of nanocomposites [11, 14].

Furthermore, the literature demonstrates how frequency alters the dipoles orientation of the STO nanoparticles [4–7]. When those nanoparticles are aligned with the applied electrical field, the dielectric material becomes polarized. However, the dipoles cannot remain aligned to the electrical field at higher frequencies [11]. In as much as the dielectric constant dwindles at those high frequencies, the polarization mechanism cannot contribute effectively to the dielectric properties. This represents a limitation because for higher frequencies applications this will cause decrease in the dielectric properties.

After analyzing the dielectric constant of the composites, we gaged the current density, i.e., charge transported through the cross-sectional area (**Figure 6**). Thus, we discovered that the current density raised for higher amounts of cellulose in the composites, as well as for voltages from 5 to 60 V. As explained previously, the water content of in the nanocomposites swells with the addition of cellulose, resulting in higher current densities through the dielectric material. Moreover, the STO nanoparticles addition improves the capacitor's ability to store more energy by lowering the current flow through the dielectric material. As shown in **Figure 6**, the current density for the composites with STO nanoparticles increased

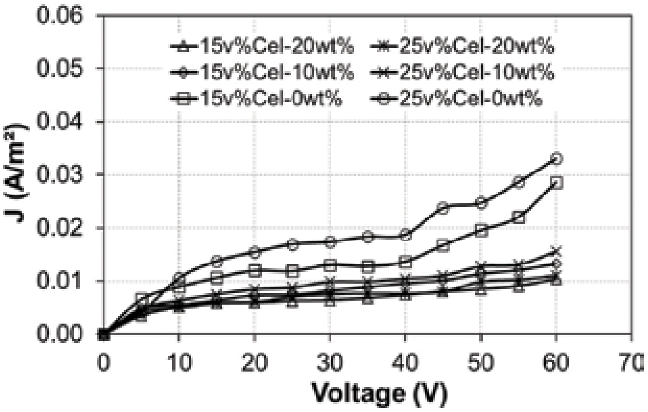

Figure 6. Effects of the applied electrical field, cellulose and STO nanoparticles content in the current density passing through the capacitors.

slightly [27]. Additionally, due to the fact that for safety reasons our instrumentation could only apply 60 V, we could not observe any breakdown in the composites up to that voltage. Not finding that breakdown voltage proves to be one limitation of the present research that could be overcome with a more energetic testing system. Yet, we strongly believe that the capacitors could withstand higher voltages with the addition of STO nanoparticles.

Furthermore, the electrical conductivity of the dielectric material was computed from the current density. For this calculation, a linear regression analysis was applied to the curves of current density as a function of voltage. The slope of the curve represented the conductivity divided by the thickness of the capacitor (σ_t). According to the results, higher content of cellulose heightened the conductivity of the dielectric material while the addition of STO nanoparticles lowered it (**Figure** 7). This is an important finding, since one can design capacitors by tuning the levels of cellulose and STO particles present in the biocomposite which are also in agreement with a recent study by Wang et al. [28].

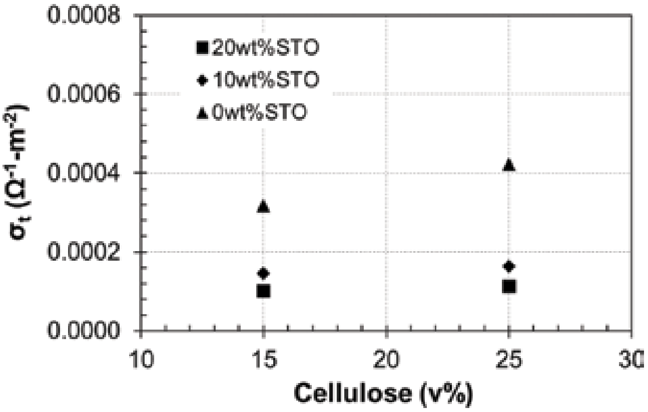

Figure 7. Effects of the cellulose and STO nanoparticles content in the electrical conductivity of the capacitors.

3.3. Thermal and tensile analysis

In this section, the thermal and mechanical properties of the composites were studied as a function of the cellulose percent, i.e., 15 and 25 v%, and the amount of strontium titanate nanoparticles, i.e., 0, 10 and 20 wt%.

As presented previously, the degradation temperature of the nanocomposites was analyzed via thermogravimetric analysis. Our results suggest that higher degradation temperature resulted from increasing the amount of cellulose in the composites bearing STO nanoparticles, which is opposite to the observed behavior for the composites without STO nanoparticles (**Figure 8**). In other words, the higher stability of the STO phase prevents early degradation (low T_{deg}) of the biocomposites. This outcome suggests that higher levels of both cellulose and STO could render these composites suitable for high temperature applications as in instrumentation operating in tropical regions.

In terms of mechanical behavior, the ultimate tensile strength (UTS) was determined using a uniaxial testing machine, as mentioned before. **Figure 9** reveals that higher UTS values were obtained in composites bearing more cellulose: from 15 to 25 v% for the composites containing STO nanoparticles, which is contrary to the behavior observed in composites without nanoparticles. When the UTS values for the composites are compared, the UTS values increased as the percentages of STO nanoparticles decreased from 20 to 0 wt%. We deem this an important finding as it enables the design of devices that can withstand minor loads without being mechanically ruptured upon service.

The addition of cellulose lowered slightly the T_{deg} and UTS for the composites without STO nanoparticles, an outcome attributed to the pH value of the solution. As shown in **Table 1**, the pH value for the composites without STO nanoparticles increased from 4.78 to 5.08. At higher pH values, the amino groups are protonated causing electrostatic repulsion between the polymer's chains [27]. Therefore, the electrostatic repulsions better the swelling degree of the polymer, as the water content heightens in the polymer [29]. Because of this apparent

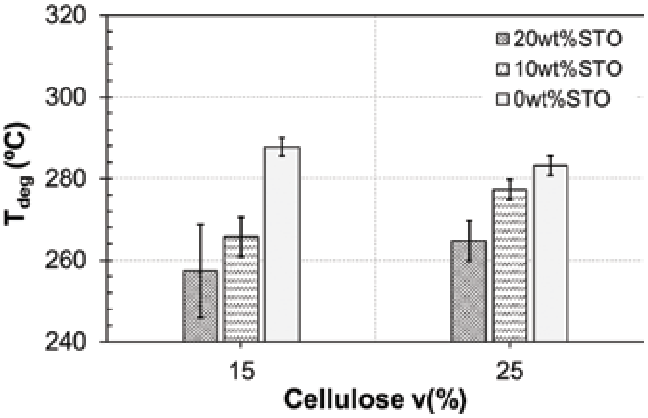

Figure 8. TGA analysis for composites made of 1.5v% chitosan/0.5v% cellulose considering 20, 10, and 0 wt% of strontium titanate nanoparticles.

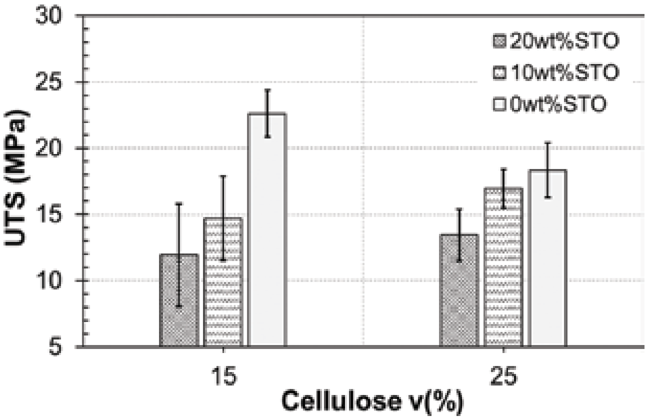

Figure 9. Tensile analysis for composites made of 1.5 v% chitosan/0.5 v% cellulose considering 20, 10 and 0 wt% of STO nanoparticles.

Percentage of cellulose (v%)	Percentage of STO nanoparticles (wt%)	pH value
15	0	4.78
15	10	4.78
15	20	5.00
25	0	5.08
25	10	5.08
25	20	5.20

Table 1. Measurements of pH value for the solutions containing different percentages of cellulose and STO nanoparticles.

shortcoming, when designing a device with these composites, one must consider this finding. Further testing of these composites under high humidity environment could shed light on the potential water absorption leading to swelling.

A different behavior was observed in the composites with STO nanoparticles where the T_{deg} and UTS increased. The polymer-polymer interaction and the polymer-particle interaction can be responsible of these results. The addition of STO nanoparticles could have furthered the entanglement of the polymer's chains and, consequently, the free volume. However, the water present in these free spaces can be removed during the drying process because the molecules of water are not confined between the polymer's chains.

In addition, the presence of more nanoparticles heightens the polymer-nanoparticles interfacial energy, which could cause cracks through the nanoparticles in the polymeric matrix. Besides, any agglomeration of nanoparticles can be detrimental for the polymer-nanoparticle interfacial bonding. Such agglomerates can favor the presence of pores and nucleate microspaces through the nanoparticles, raising the brittleness of the composites. All these are factors that require further experimentation, which falls beyond the scope of the present research.

All in all, we were able to establish a characterization baseline that can serve as design platform for capacitors intended to sustain high load at relatively elevated temperatures by adjusting the cellulose level and nanoparticles content. In closing, we are confident that this research would lead to the creation of organic and inexpensive tunable capacitors for RF applications like antennas or MEMS-based tunable filters.

4. Conclusions

The present work aimed at studying the electrical, thermal, and mechanical properties of composites made of chitosan, cellulose and strontium titanate nanoparticles. The compositional variables considered encompassed: cellulose content (15 and 25 v%) and amount of strontium titanate nanoparticles (10 and 20 wt%).

The chitosan-cellulose and polymer-nanoparticles composites were successfully fabricated via sol gel casting method. Strontium titanate nanoparticles were dispersed in the polymeric matrix using a double-layered technique. To achieve a better dispersion of the nanoparticles, the particles size was reduced from 43 to 18 nm using the high ball mill technique. As a result, a high dispersion of the nanoparticles in the polymeric matrix was achieved.

With respect to the measured electrical properties, the addition of the strontium titanate nanoparticles raised the dielectric constant, capacitance, and electrical resistivity of the composites, as expected from a dispersed dielectric material. Similarly, the addition of the nanoparticles decreased the current density passing through the biocomposite. In addition, the dielectric rupture of the composites was not observed up to a maximum applied voltage of 60 V.

Furthermore, mechanical and thermal analysis tests of the composites revealed that the addition of cellulose adversely affected the ultimate tensile strength and the degradation temperature of the composites without strontium titanate due to the high content of water. However, an opposing behavior was observed on the composites with strontium titanate nanoparticles, in which higher content of cellulose raised both the ultimate tensile strength and the degradation temperature while the addition of titanate nanoparticles lowered it.

Acknowledgements

Preliminary work on strontium titanate-containing biocomposites was published in an international journal [11]. This work is supported by the National Science Foundation under research Grant Nos. 0833112 and 1345156 (CREST program) and under instrumentation Grant Nos. 0619349 and 0922994. The authors would like to thank the invaluable assistance of the undergraduate student Javier Martínez and the technical personnel of the Materials Laboratories and Power Electronics Laboratories of the University of Puerto Rico-Mayagüez.: Dr. Eduardo I. Ortiz Rivera, and the students Daniel A. Merced Cirino and Alexander Collazo Irizarry.

Conflict of interest

The authors declare that there is no conflict of interest regarding the publication of this manuscript.

Author details

Amarilis Declet-Vega, Nelson Sepúlveda-Ramos and Oscar Marcelo Suárez*

*Address all correspondence to: oscarmarcelo.suarez@upr.edu

Nanotechnology Center for Biomedical, Environmental and Sustainability Applications,
College of Engineering, University of Puerto Rico-Mayagüez, USA

References

[1] Dujardin BE, Mann S. Bio-inspired materials chemistry. Advanced Materials. 2002; **14**:775-788

[2] Shukla SK, Mishra AK, Arotiba OA, et al. Chitosan-based nanomaterials: A state-of-the-art review. International Journal of Biological Macromolecules. 2013;**59**:46-58

[3] Rinaudo M. Chitin and chitosan: Properties and applications. Progress in Polymer Science. 2006;**31**:603-632

[4] Kingery WD. Introduction to ceramics. Journal of the Electrochemical Society. 1977;**124**: 152C

[5] Carter CB, Norton MG. Ceramic Materials. 2nd ed. New York, USA: Springer-Verlag; 2013. Epub ahead of print 2013. DOI: 10.1016/S0026-0657(01)80220-4

[6] Neagu AM, Petronela L, Cazacu A, et al. Impedance analysis and tunability of $BaTiO_3$–chitosan composites: Towards active dielectrics for flexible electronics. Composites: Part B. 2014;**66**:109-116

[7] Elimat Z. AC-impedance and dielectric properties of hybrid polymer composites. Journal of Composite Materials. 2013;**49**:3-15

[8] Petrov I, Kalinkevich O, Pogorielov M, et al. Dielectric and electric properties of new chitosan-hydroxyapatite materials for biomedical application: Dielectric spectroscopy and corona treatment. Carbohydrate Polymers. 2016;**151**:770-778

[9] Hosokawa J, Nishiyama M, Yoshihara K, et al. Biodegradable film derived from chitosan and homogenized cellulose. Industrial and Engineering Chemistry Research. 1990;**29**:800-805

[10] Ibrahim MS, Sapuan SM, Faieza AA. Mechanical and thermal properties of composites from unsaturated polyester filled with oil palm ash. Journal of Mechanical Engineering Science. 2012;**2**:2231-8380

[11] Declet-Vega A, Sepúlveda-Ramos N, Martínez-Santos J, et al. Study of electrical properties of biocomposites containing ferroelectric nanoparticles. Journal of Composite Materials. 2017;**51**:1979-1985

[12] Holzwarth U, Gibson N. The Scherrer equation versus the 'Debye-Scherrer equation'. Nature Nanotechnology. 2011;**6**:534

[13] Alexander L, Klug HP. Determination of crystallite size with the X-ray spectrometer. Journal of Applied Physics. 1950;**21**:137-142

[14] Suárez OM, Vazquez J, Reyes-Russi L. Synthesis and characterization of mechanically alloyed $Al/Al_xMg_{1-x}B_2$ composites. Science and Engineering of Composite Materials. 2009;**16**:267-276

[15] Florián-Algarín D, Padilla A, Suárez OM, et al. Strengthening of Al and Al-Mg alloy wires by melt inoculation with Al/MgB_2 nanocomposite. Journal of the Mechanical Behavior of Materials. 2015;**24**:207-212

[16] Minteer TM. The many capacitance terms of two parallel discs in free space. European Journal of Physics. 2014;**35**:15

[17] ASTM-D-149. Standard test method for dielectric breakdown voltage and dielectric strength of solid electrical insulating materials at commercial power. ASTM International - Standards. 2013;**9**:1-13

[18] ASTM D150-11, Standard Test Methods for AC Loss Characteristics and Permittivity (Dielectric Constant) of Solid Electrical Insulation, ASTM International, West Conshohocken, PA, 2011. DOI: 10.1520/D0150-11

[19] Yang K, Huang X, Xie L, et al. Core-shell structured polystyrene/$BaTiO_3$ hybrid nanodielectrics prepared by in situ RAFT polymerization: A route to high dielectric constant and low loss materials with weak frequency dependence. Macromolecular Rapid Communications. 2012;**33**:1921-1926

[20] Barber P, Balasubramanian S, Anguchamy Y, et al. Polymer Composite and Nanocomposite Dielectric Materials for Pulse Power Energy Storage. 2009;**2**:1697-1733

[21] Burton AW, Ong K, Rea T, et al. On the estimation of average crystallite size of Zeolites from the Scherrer equation: A critical evaluation of its application to Zeolites with one-dimensional pore systems. Microporous and Mesoporous Materials. 2009;**117**:75-90

[22] Uvarov V, Popov I. Metrological characterization of X-ray diffraction methods for determination of crystallite size in nano-scale materials. Materials Characterization. 2007;**58**:883-891

[23] Trepakov VA, Potůček Z, Makarova MV, et al. $SrTiO_3$:Cr nanocrystalline powders: Size effects and optical properties. Journal of Physics. Condensed Matter. 2009;**21**:1-5

[24] Kelleher MC, Hashmi MSJ. The effect of vibratory milling on the powder properties of zinc oxide Varistors. Journal of Materials Processing Technology. 2008;**201**:645-650

[25] Wu Y, Guan K, Wang Z, et al. Isolation, Identification and Characterization of an Electrogenic Microalgae Strain. PLoS One. 2013;**8**:1-7

[26] Mazeau K. The hygroscopic power of amorphous cellulose: A modeling study. Carbohydrate Polymers. 2015;**117**:585-591

[27] Karthika R, Gopinath LR, Archaya S, et al. Isolation of diesel degrading bacteria, identification of catechol gene and its biogas production. IOSR Journal of Environmental Science, Toxicology and Food Technology. 2014;**8**:76-82

[28] Wang H, Fu Q, Luo J, et al. Three-phase Fe_3O_4 /MWNT/PVDF nanocomposites with high dielectric constant for embedded capacitor. Applied Physics Letters. 2017;**110**:242902

[29] Szymańska E, Winnicka K. Stability of chitosan—A challenge for pharmaceutical and biomedical applications. Marine Drugs. 2015;**13**:1819-1846

Chapter 6

Lead Zirconium Titanate Films and Devices Made by a Low-Temperature Solution-Based Process

Phan Trong Tue and Yuzuru Takamura

Additional information is available at the end of the chapter

http://dx.doi.org/10.5772/intechopen.79378

Abstract

As the most important multifunctional oxide material, lead zirconium titanate (PZT) has a diverse range of applications such as piezo actuators, ferroelectric nonvolatile memories, sensors, and transducers due to its excellent structural and electrical properties. However, it generally requires a high annealing temperature (above 600°C) to attain the desired properties, which hinders the integration of PZT with silicon-based Complementary Metal Oxide Semiconductor (CMOS). Therefore, the fabrication of PZT films by a chemical solution deposition (CSD) at temperatures compatible with Si-CMOS technology or even with polymeric substrate for flexible electronics would be of high technological interest. So far, different strategies to decrease the crystallization temperature of CSD-derived PZT films have been studied. This chapter presents a critical review on the low-temperature solution-processed PZT films and devices, and addresses challenges for fundamental understanding and practical integration of multifunctional PZT in devices. In the first part, recent advances in fabrication of CSD-derived PZT films at a low temperature are thoroughly reviewed. The second part discusses various techniques for patterning PZT into micro-nano-sized patterns. Lastly, some potential applications of the low-temperature CSD-derived PZT films and devices are demonstrated.

Keywords: lead zirconium titanate (PZT), ferroelectric, ferroelectric nonvolatile memory, piezoelectric actuator, solution process, low-temperature deposition

1. Introduction

Highly integrated nano-ferroelectric/piezoelectric devices with Si-CMOS technology require a low-processing temperature (≤450°C) of ferroelectric/piezoelectric films [1]. Among ferroelectric/piezoelectric materials, lead zirconium titanate (PZT) [2] appears as the most promising candidate because of its excellent structural and electrical properties, in addition to its relatively low processing temperature (~600°C) compared to organic, lead-free, and the other inorganic materials [3, 4].

Many efforts have been done for lowering the process temperature of device-quality PZT films to below 450°C such as the chemical vapor deposition [5], pulse laser deposition [6], and sputtering [7]. However, most of these technologies are costly and complicated, which are not suitable for practical applications. On the other hand, the chemical solution deposition (CSD) technique offers many advantages such as simplicity, low-cost, large area deposition, and feasibility of material compositional control. Many low-temperature CSD methods, including tailoring precursor solution [8, 9], seeding the film [10], hydrothermal annealing [11], and better lattice matching [12], have been investigated, but all provide insufficient film quality and compromised properties. Hitherto, the relatively successful approaches have been microwave annealing [13], localized heating by pulse laser [14], and ultraviolet-assisted annealing [15]. Nevertheless, microwave heating results in damage of CMOS circuits, while the costly pulse laser processing is unfavorable for industrial application.

This chapter presents a critical review on the low-temperature solution-processed PZT films and devices since last 15 years, and addresses challenges for fundamental understanding and practical integration of multifunctional PZT films in devices. Database collection was performed using major searching engines such as ISI Web of Science (Thomson Reuters) and Google Scholar. In the first part, recent advances in fabrication of CSD-derived PZT films at a low temperature (≤450°C) using chemical and physical approaches are thoroughly reviewed. The second part discusses various techniques such as wet/dry-etching, lift-off, and imprinting for patterning PZT into micro-nano-sized patterns. Lastly, some potential applications of the low-temperature CSD-derived PZT films and devices for sensor/actuator and energy harvesting are demonstrated.

2. Recent progress of low-temperature PZT films fabricated by a chemical solution deposition (CSD) method

2.1. Chemical pathway

2.1.1. Seeded diphasic sol-gel (SDSG) precursors

It is evident from literatures that there have been few studies of the phase evolution of PZT films at temperature normally considered suitable for pyrolysis (350–450°C) rather than crystallization (600°C). The reaction pathway from nucleation to full growth of perovskite PZT phase plays an important role in optimizing and lowering process-temperature of sol-gel derived films.

To understand the mechanism of transformation from the nucleation to the growth of perovskite PZT, microstructural development, crystallinity and electrical properties of low-temperature pyrolyzed PZT films (<400°C) were systematically investigated. The films were prepared on Pt-coated Si substrates by a sol-gel route, in which different concentrations of nanometric PZT powders were dispersed in the sol (seeded precursor) [10, 16, 17]. It was found that the formation of perovskite phase was facilitated by the seeds as a result of the reduced activation

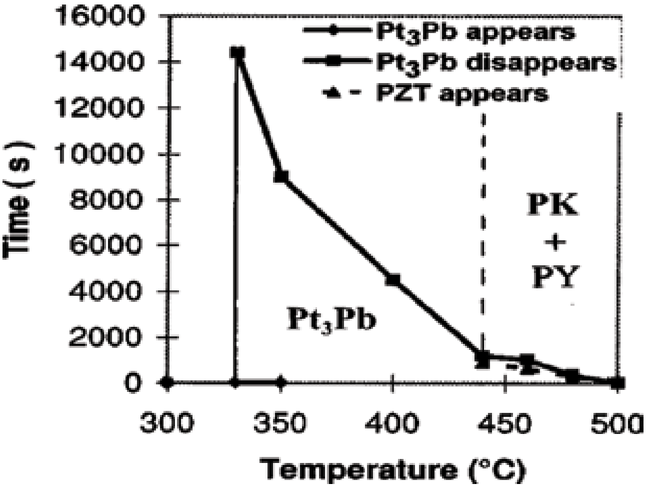

Figure 1. Temperature-time-texture diagram for the metastable $PbPt_3$ phase and perovskite PZT for the three-layer films dried at 200°C [19].

energy [17]. The seeded PZT films showed a lesser (111)-preferential orientation, greater nucleation density, and a better ferroelectricity. The formation of the metastable intermetallic Pt_xPb interlayer, between the film and the Pt electrode layer, was also observed. However, the local random perovskite nucleation might result in the decreased (111) orientation of the seeded films [18]. The obtained dielectric permittivity (ε), remnant polarization (P_r), and coercive field (E_c) of the 430°C-pyrolyzed seed-PZT film were 500, 6.71 μC/cm², and 80 kV/cm, respectively.

2.1.2. Formation of an early stage seeded PbPtx layer

It has been reported that an intermetallic $PbPt_3$ phase is formed in the early stages of pyrolysis for PZT thin films deposited on a platinized substrate, which greatly influences on crystallization temperature, microstructure, and electrical properties of resulting films [18, 19]. This metastable phase forms at around 330°C and disappears as elevated heating (**Figure 1**). The pyrolysis and annealing conditions as well as the film thickness determine the formation of this intermetallic phase. These conditions impact on the reduction of Pb^{2+} into Pb, which drives the formation of the $PbPt_3$ phase. The perovskite nucleation was found on top of the intermetallic phase rather than directly on Pt. This explains why the formation of PZT(111) phase is facilitated by the intermediate ones (**Figure 2**) [20]. Due to very small lattice mismatch (0.4%) between the $PbPt_3$ and PZT phases, the nucleation activation energy might be reduced. As a result, well (111)-oriented perovskite PZT was able to be fabricated at 440–480°C. The PZT film exhibited a good quality with a pyroelectric coefficient of 1.8×10^{-4} Cm^{-2} K^{-1} and a P_r of 24 μC/cm² [20].

2.1.3. Solvothermal synthesis

Solvothermal synthesis is a method of crystallizing solution-derived materials under a high pressure and at a temperature higher than boiling temperatures of used solvents. The method

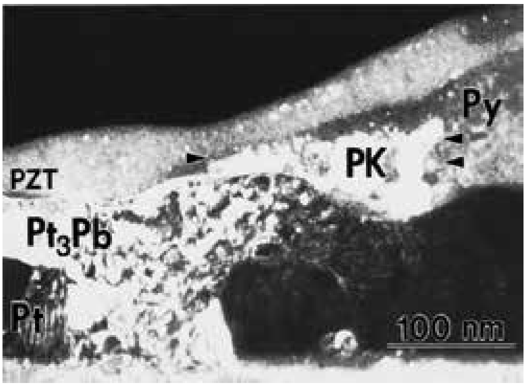

Figure 2. Dark-filed cross-section TEM for a film PZT/Pt/Ti/SiO_2/Si after annealing at 440°C [20].

has been widely used for the synthesis and growth of various materials and thin films such as metal oxides [21, 22].

The advantage of the solvothermal method is low reaction temperature, generally below 200°C. It is important to note that this temperature is lower than the Curie temperature of PZT (~200–350°C), and more than 400°C below the reaction temperature required by the other methods. When PZT is used as a transducer, the output force is proportional to the applied voltage, which increases as the film thickness increases. In this regard, the hydrothermal method is advantageous of making micrometer-thick film; consequently, it is a promising feature for developing a microactuator driver. In addition, since the material is synthesized in solution, the film is deposited on all surfaces of the substrate making it a three-dimensional (3D) structure. Such a 3D structure is advantageous not only for actuators but also for FeRAM applications.

The hydrothermal growth of polycrystalline PZT films on Ti-substrates in a two-step process (nucleation and growth) showed that alkaline medium such as KOH was important for the formation of the PZT solid solution [23, 24]. By slightly changing the reaction conditions, PZT films could be grown in a single step [25].

Hetero-epitaxial growth of PZT films on (001) $SrTiO_3$ (STO) was achieved at 90-150°C (**Figure 3(a)**) [26]. The growth proceeded with the formation of (100)-faceted islands and their coalescence. Full coverage was obtained upon hydrothermal treatment at 150°C for 24 h. However, both the (001) and (100) orientations were detected. In addition, ferroelectric properties were not able to be evaluated due to the lack of conductivity of the STO substrate and the peel-off morphology of the film [27]. Later, these issues were resolved by adjusting the position at which the substrate was suspended in the solution, and by the use a highly conductive $SrRuO_3$ film as a bottom electrode [28]. The $2P_r$ and E_c for PZT film on $SrRuO_3$/STO (001) were 17.1 μC/cm^2 and 36 kV/cm, respectively, and those of PZT on $SrRuO_3$/STO (111) were 32.7 μC/cm^2 and 59 kV/cm, respectively (**Figure 3(b)**).

2.1.4. Excluding pyrochlore phase formation

It is well known that PZT pyrochlore phase is formed at 300–400°C. Once this stable phase is developed, a high annealing temperature (>600°C) is required to transform it from the

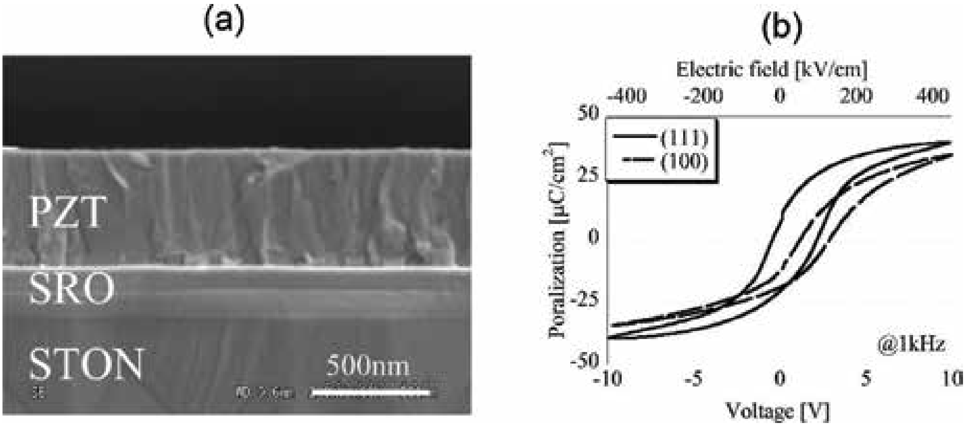

Figure 3. (a) Cross section of SEM image of the deposited PZT thin film on the $SrRuO_3$//STO (100) substrate. (b) Hysteresis curves for PZT thin films on $SrRuO_3$//STO (100) [26].

pyrochlore to a perovskite structure. A simple method for the crystallization of solution-processed PZT films at 400–450°C by intrinsic change in the crystallization path via circumventing the pyrochlore phase formation was reported [29]. The approach does not need any modification of the precursors nor special facilities. Conventionally, the spin-coated films are normally pyrolyzed at over 300°C for a complete removal of solvent and organic ingredients. However, by this pyrolysis step, the pyrochlore phase is subsequently formed. In this work, by lowering the pyrolysis temperature to a well-below pyrochlore temperature (i.e., 210°C), it was able to retain a proper amount of carbon atoms in the gel film as shown in **Figure 4(a)**. The remaining carbon acted as a reagent to reduce Pb^{2+} to Pb^0 when heated up to 400°C in subsequent annealing (**Figure 4(b)** and **(c)**). A significantly enhanced intensity of the $PbPt_x$ peak for the 210°C-pyrolyzed sample compared to the others indicated that larger amount of Pb^o was produced (**Figure 4(b)** and **(c)**). In the presence of sufficient organic carbon, Pb^{2+} was reduced to Pb^0, which spontaneously reacted with Pt to form the intermediate $PbPt_x$ phase at temperatures as low as 200°C. As a result, the lack of Pb^{2+} prevented the formation of this intermediate phase (**Figure 4(b)** and **(d)**) that accounts for the high-temperature crystallization of the perovskite phase in the conventional processes. The process was successfully demonstrated on several representative electrode materials (Au, stacked Pt/RuO_2, and RuO_2) in addition to Pt.

2.2. Physical pathway

2.2.1. Ultraviolet-assisted annealing

Recently, ultraviolet (UV)-assisted annealing has been applied for fabrication of various functional oxide thin films since the process is capable of facilitating organic decomposition and condensation of oxide network. Consequently, high-quality oxide thin films can be realized at a low temperature [30, 31].

Shimura et al. reported a low-temperature fabrication of PZT films using a thermal UV/O_3 annealing process [15]. A spin-coated PZT gel film was placed on a heated stage (200°C) and

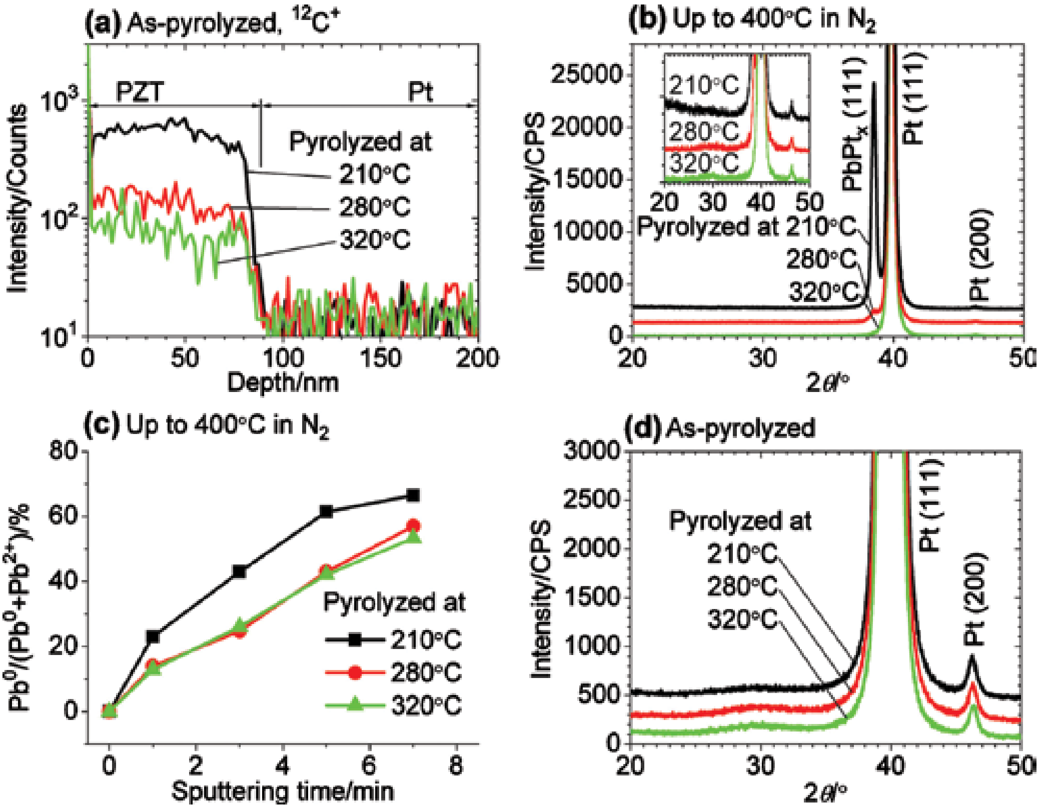

Figure 4. Effects of pyrolysis temperature on carbon content, valence state of Pb, and phase composition before perovskite crystallization. (a) SIMS analysis for carbon of the as-pyrolyzed samples. (b) XRD patterns for samples further heated to 400°C. (c) Percentages of reduced Pb. (d) XRD patterns for the as-pyrolyzed samples [29].

irradiated with UV light (185 and 254 nm) in O_3 ambient before crystallization (**Figure 5**). The thermal UV irradiation facilitated the decomposition of organic components. At a proper temperature, the organic residue such as carbon and hydrogen atoms created a reducing environment within the gel film, which prevented the pyrochlore structure development. As a result, the ferroelectric perovskite structure with (111)-preferential orientation was able to be achieved at 450°C (**Figure 6(a)**). The P_r, E_c, and leakage current of the PZT film were 23.6 μC/cm², 109.6 kV/cm (**Figure 6(b)**), and 10^{-6} A/cm², respectively [15]. Similarly, ferroelectric PZT films were fabricated on $LaNiO_3$ electrode at a low temperature of 450–480°C by a method assisted with UV irradiation [32]. The obtained film annealed at 480°C showed a P_r of 21 μC/cm² and leakage current of 9.71×10^{-8} A/cm² at 100 kV/cm, with good retention and high stability of photocurrent.

In order to enhance absorption in the UV-range, UV-absorber additives are normally added to precursor solutions such as "*photoactive sol*" (*Ph*) [33]. The dip-coated thin gel layer was irradiated under the UV-light, followed by rapid thermal annealing in O_2 atmosphere. Formation of highly reactive oxygen radical from ozonolysis facilitated the decomposition of organic components via breaking of the alkyl group-O bonds, resulting in a subsequent formation of the metal–O–metal bonds. As a result, ferroelectric perovskite structure can be obtained at 400°C. Furthermore, incorporation of nanoseeds into the *Ph* sol (*PhS*) increased

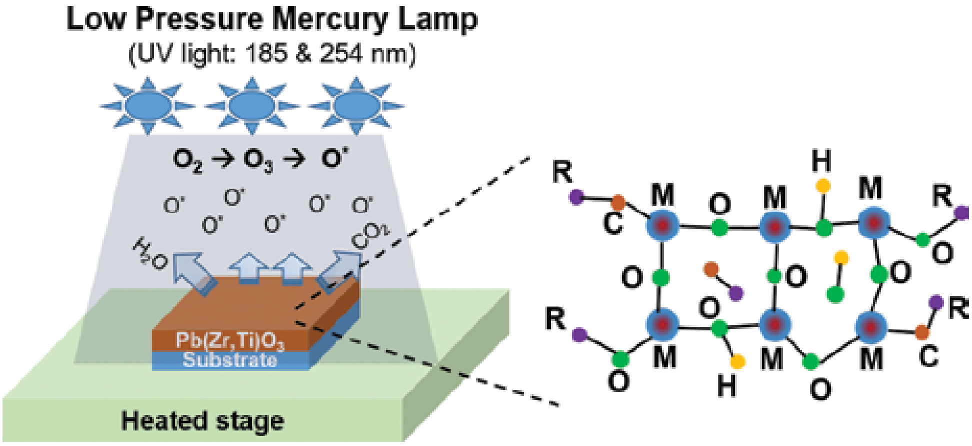

Figure 5. An illustration of UV treatment process for PZT films.

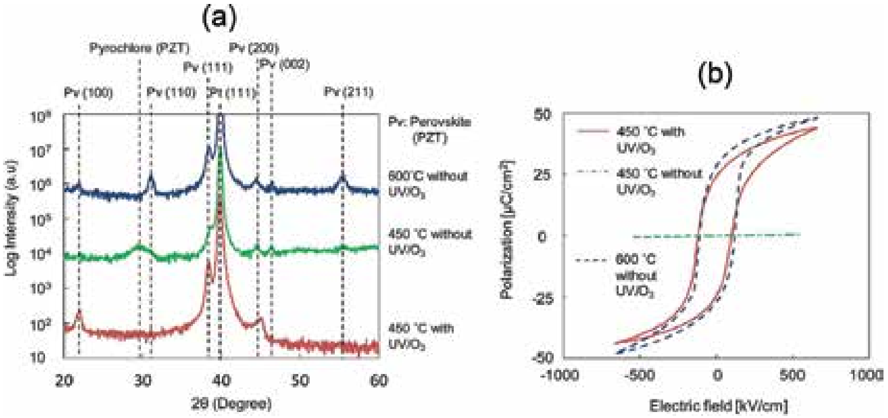

Figure 6. (a) XRD patterns and (b) hysteresis loop characteristics of PZT films prepared by conventional 600°C process and 450°C process with and without the UV/O_3 treatment [15].

the number of nucleation sites in the resulting film, which produced a further reduction of crystallization temperature [34]. The mechanism proposed for the low-temperature processing of *PhS*-PZT thin films is described in **Figure 7**. Combination of the enhanced UV-absorbance and internal nanocrystalline seeds led to a significant improvement in the formation of the PZT perovskite structure at a low temperature, which originated from a decrease of the Gibbs free energy barrier. The 350°C-PZT film deposited on a flexible PI substrate with a thickness of 190 nm, showed value of P_r ~ 15 μC/cm². This value is close to those reported for PZT films processed at temperature over 600°C, P_r ~ 20 μC/cm², and are higher than those reported for organic ferroelectric films, P_r ~ 10 μC/cm², both on rigid Si substrates.

2.2.2. *Laser-assisted annealing*

Laser annealing (LA) is an alternative technique for fast and low-temperature fabrication of PZT films. This technique uses focused high-energy laser beam in continuous or pulse mode

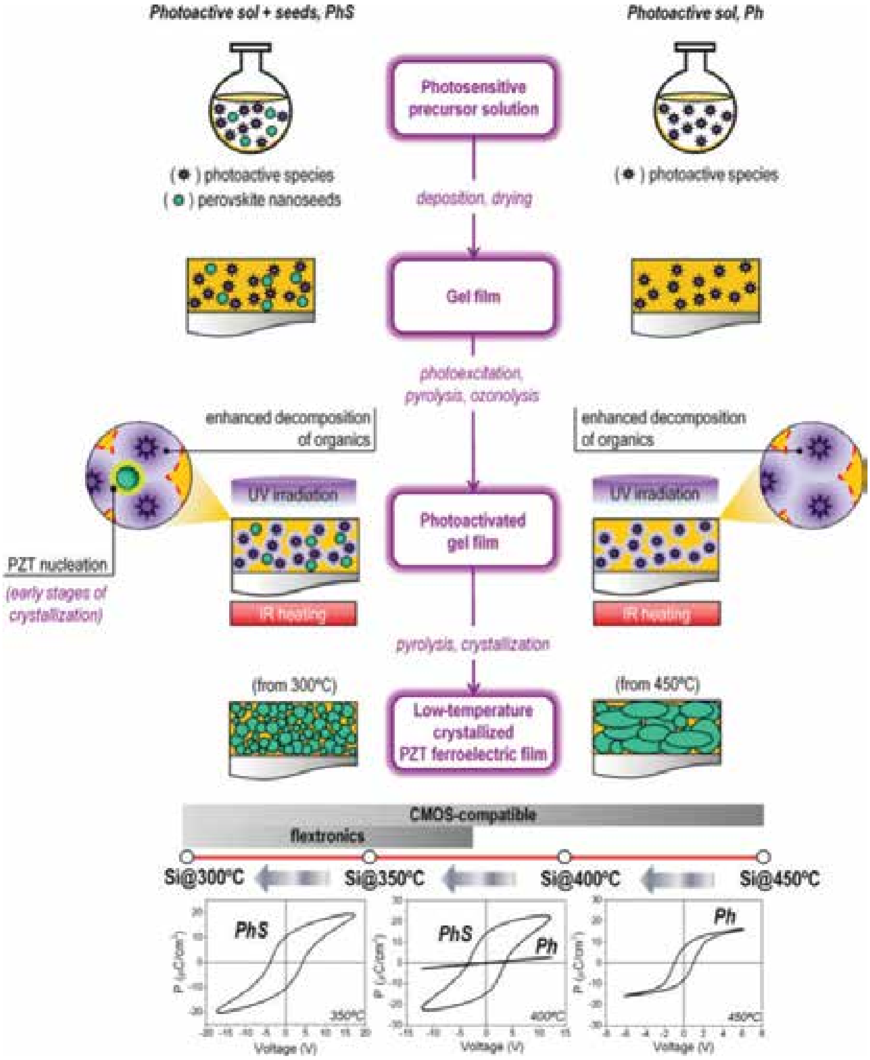

Figure 7. Mechanisms for the low-temperature processing of inorganic ferroelectric thin films using the activated *PhS* solutions [34].

to scan the desired film's areas to fuse and bond the powders into a layer of solid mass, and has been used in manufacture of solar cells and power devices. The advantages of LA include the flexibility in manufacturing composites with different geometries with assistance of computer, controllable sintering thickness depending on the laser energy and scanning speed, low influence on the substrate to create the possibility of processing PZT on low melting point substrates. However, LA technique is not suitable for a large area PZT sample due to the limitation of laser spot size (generally ~50 μm in diameter). Many researchers have attempted to apply this technique to PZT crystallization since three decades ago. Bharadwaja et al. [14] reported highly textured (001) and (111) $Pb(Zr_{0.52}Ti_{0.48})O_3$ thin films (300–350 nm thick) fabricated via excimer laser annealing (248 nm KrF pulsed excimer laser) on (111)Pt/Ti/SiO_2/Si

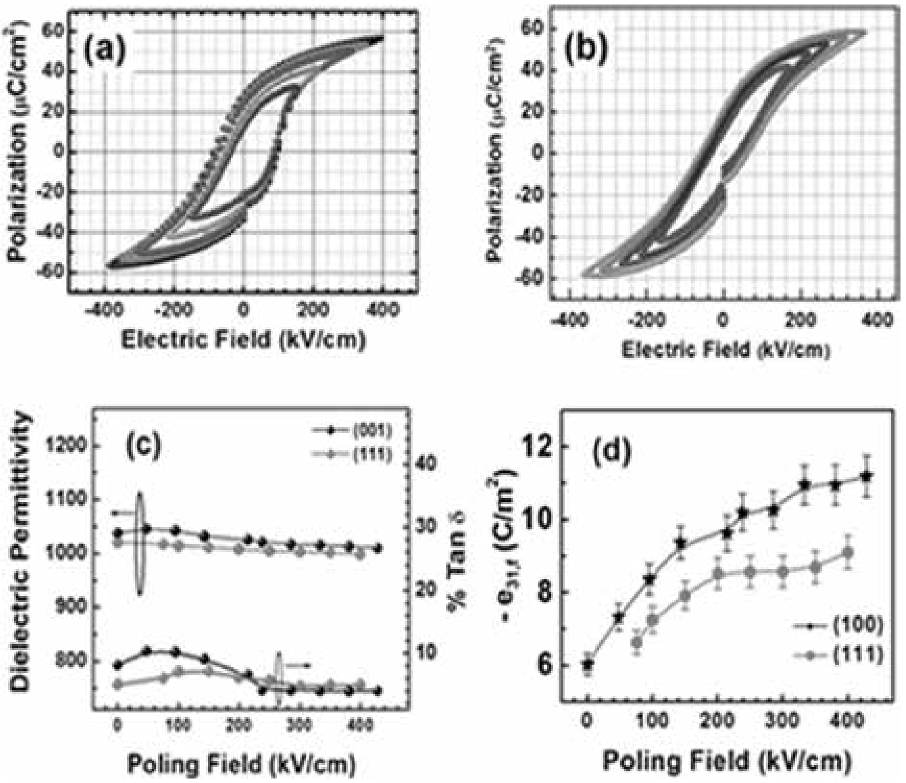

Figure 8. Polarization hysteresis of laser annealed (a) (001) and (b) (111) PZT thin films. (c) Dielectric permittivity and loss tangents and (d) piezoelectric $e_{31,f}$ results as a function of poling field for laser annealed (001) and (111) textured PZT thin films [14].

and (001)$PbTiO_3$/Pt/ Ti/SiO_2/Si substrates. It was shown that by minimizing nucleation energy with suitable buffer layers, PZT films can be grown in preferred orientation at relatively low temperatures (350–375°C) with good functional properties for thin-film MEMS applications (**Figure 8**). Both (001) and (111) oriented PZT films exhibited relatively good ferroelectricity with large P_r (31 and 24 μC/cm^2 for (001) and (111) PZT, respectively) and small E_c (86 and 64 kV/cm for (001) and (111) PZT, respectively). The maximum $e_{31,f}$ piezoelectric charge coefficients are ~11 and 9 C/m^2 for (001) and (111) PZT thin films, respectively. However, in this case, particular sputtered amorphous PZT films were needed.

Considering productivity, a semiconductor diode laser is preferred because of its low cost, small size, and low energy consumption, compared with conventional solid state, CO_2 or excimer lasers. Chen et al. recently reported a method that can be used to crystallize PZT films derived from sol-gel solution on either Pt or Li-Nb-O-coated Si substrate by LA treatment using a 980 nm continuous wave semiconductor laser [35, 36]. From dielectric constant measurement, it is found that one LA process generates 45-nm-thick crystallized PZT layer. The dielectric constant of the PZT film is about 1200, which is comparable to that of PZT films prepared by conventional RTA technique. However, the substrate temperature required for LA-crystallized PZT film by this method is relatively high (~500°C).

2.2.3. *Microwave-assisted annealing (MV)*

Microwave is an electromagnetic wave with wavelength ranging between 1 and 1 mm and frequency ranging from 1 to 300 GHz [37]. The difference between conventional furnace thermal annealing and MV annealing is the mechanism of these two methods. The thermal approach sinters samples by transferring heat through objects via thermal conduction. Thus, the heating source of this technique is the furnace. However, the MV annealing is different. The materials absorb the electromagnetic energy and transform it into heat to increase the temperature. Therefore, the heating source is materials themselves.

Recently, the MV processing has been gaining great attention for various types of materials including ceramics and metal-oxide thin films. Compared to the conventional thermal annealing technique, the MV heating offers more thermal uniformity, lower annealing temperature, shorter processing time with extremely high rate, and reduced grain growth [38]. MW-annealing techniques were applied for crystallization of PZT films at relatively low temperatures (<500°C) [13, 39–42]. For instance, Wang et al. reported a crystallization study of sol-gel $Pb(Zr_{0.45}Ti_{0.55})O_3$ films on platinized Si substrates, pyrolyzed at 400°C, and heated at 430–450°C for 30 min, using a single-mode 2.45 GHz microwave irradiation system in a magnetic field. Good ferroelectric response was obtained upon heating the films at/above 450°C [13] (**Figure 9**). It was found that the MV-annealed PZT films first crystallized into an intermediate pseudo-perovskite phase at 430°C, and then mostly crystallized into the perovskite phase at 450°C. This phenomenon was not observed in PZT films prepared by conventional thermal processing. The crystallization of amorphous PZT films by MV annealing is due to the heat originated from the substrate together with direct MV irradiation onto the films.

Although, the densification of the MV-annealed films is much higher than the conventional thermal process with the same temperature and duration, some fundamental issues limit wide usage of the MV-annealed PZT films. That is because the PZT can only absorb waves with a specific range of frequency, which limits the tools to high frequency (>25 GHz). However, most commercialized MV tools are at approximately 2.4 GHz, which lead to low MV absorption of PZT. Therefore, either preheating is used or absorption aids are added to increase the efficiency of sintering. For example, Sharma et al. added carbon powder in the PZT film to enhance the absorption [43]. Additionally, because the heat is generated internally, the

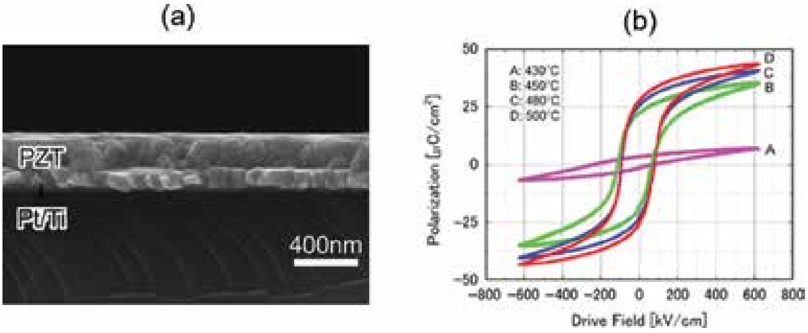

Figure 9. (a) SEM image of PZT film crystallized by MV at 450°C. (b) Hysteresis loops of PZT films crystallized by MV at different temperatures [13].

volume of material is determining the heat generation. For a nonuniform film, the heat would generate nonuniformly and result in nonuniform property, and even cracks in the films.

2.2.4. Flash-lamp annealing

The photonic sintering is a technique that uses a broadband (UV to IR), short (<ms) and high-intensity pulse generated from a xenon gas-filled flash-lamp to heat the films. The thermal budget transferred to the film and substrate can be controlled by the pulse duration allowing PZT sintering while minimizing substrate heating. This unique annealing technique enables a direct formation of perovskite PZT film on low melting point substrates. Amorphous PZT films were successfully transformed to perovskite phase by a flash lamp annealing technique (energy of 27 J/cm^2) with a crystallization time of 1.2 ms at a substrate temperature of 350°C [44]. Granular

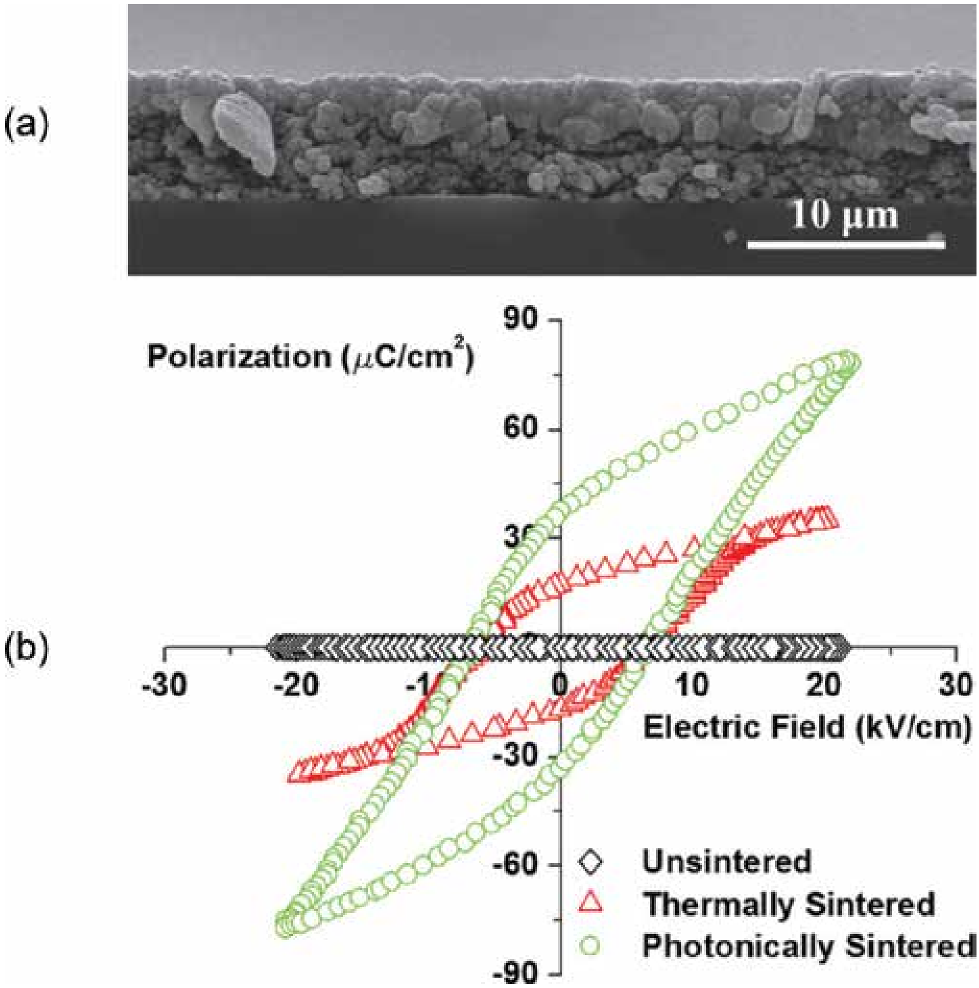

Figure 10. (a) Cross-sectional SEM image of photonically sintered PZT film on stainless steel substrate. (b) Low-frequency hysteresis loop shows that photonically sintered (green) PZT film has superior remanent polarization (32.4 µC/cm^2) than the thermally sintered (red) film (17.1 µC/cm^2) [45].

PZT grains were observed on various kinds of electrodes (Pt, Ru, RuO_2), which indicates that crystal growth begins from the film surfaces. However, the small local sintering area (μm to mm scale) precludes applications with large feature sizes.

Recently, Borkholder et al. demonstrated a new method of printing and sintering microscale PZT films with low substrate temperature increase [45]. PZT ink was aerosol-jet printed on either stainless steel or PET substrates. After drying at 200°C for 2 h in vacuum, the printed PZT gel was photonically sintered using repetitive sub-ms pulses of high-intensity broad spectrum light in an atmospheric environment. The highest measured substrate temperature was 170°C. The obtained P_r and E_c were 32.4 μC/cm^2 and 6.7 kV/cm, respectively (**Figure 10**).

3. Micro/nanoscale patterning of PZT films

3.1. Etching process

3.1.1. Physical dry etching

Dry-etching process with a high etch rate, high selectivity to electrode material, and vertical etch profile is preferable for patterning PZT films. Recently, many researchers have studied the etching of PZT films using halogen gases with various etching systems such as reactive ion etching (RIE) [46, 47] and inductively coupled plasma (ICP) [48, 49]. The main problem in the dry etching of PZT films is that the vapor pressures of the etch by-product (mainly metal halogen compounds) are low. Furthermore, the metal halogen compounds have different vapor pressures, which cause compositional variation in the multicomponent PZT films [50]. The etching of PZT films has been studied more widely in chlorinated plasma than in fluorinated plasma because of high vapor pressure of metal chlorides compared with fluoride counterparts. Lee et al. [49] studied the dry-etching mechanism of PZT films in high-density CF_4 and Cl_2/CF_4 ICP. The etching of PZT films in CF_4-based plasma is chemically assisted sputter etching, and the dominant step of the overall etching process is either the formation or the removal of the etch by-products, depending on the etching conditions. The etching of PZT films in Cl_2/CF_4 mixed plasma is mainly dominated by the formation of metal chlorides, which depends on the concentration of the atomic Cl and the bombarding ion energy. The PZT film showed a maximum etch rate in 90% $Cl_2/(Cl_2/CF_4)$ plasma where the concentration of atomic Cl was maximum (**Figure 11(a)**). The amount of sidewall residue was greatly reduced in Cl_2/CF_4 mixed plasma compared with in CF_4 plasma. A more vertical etch profile of PZT films was obtained by lowering the process pressure and increasing the substrate bias voltage (**Figure 11(b)**). However, the plasma etch process degrades the structural and electrical properties because of physical damage and chemical residue contamination. The physical damage caused by the bombardment of energetic charged ions to the film surface, which alters the near-surface region and changes its electrical properties. The surface contamination by the etch by-products and penetration of mobile ions into the bulk may also degrade film's quality. Later, Kim et al. reported both a reduction in the etching damage to PZT films during etching in a Cl_2/CF_4 plasma with Ar or O_2 added and the recovery of etching damage by using O_2 annealing [51].

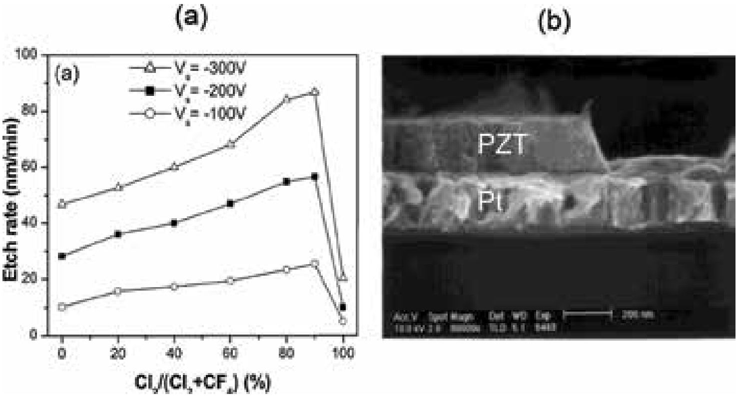

Figure 11. (a) The etching rate of PZT films as a function of $Cl_2/(Cl_2 + CF_4)$ concentration. (b) Cross-sectional SEM image of PZT pattern [49].

3.1.2. Chemical wet etching

Wet etching is an effectively alternative technique for PZT film's patterning due to its high etching rate, low cost, and high selectivity. Since, PZT can be regarded as a compound of PbO, ZrO_2 and TiO_2, etchants containing several compositions are demanded for PZT thin film etching. In recent years, many studies have been performed on wet etching of PZT films using mixtures of various acids, following single-or two-step processes [39, 52–56]. However, problems such as fast etch rate (>400 nm/min), severe undercut, and formation of higher etch residue were encountered. Wang et al. introduced a two-step wet-etching process, using buffered HF acid (BHF) in the first step, and $2HCl:H_2O$ at 45°C in the second step, to etch PZT films [54]. However, significant undercutting and brim damage were observed in the achieved pattern. Later, a novel wet-etching process was proposed using $1BHF:2HCl:4NH_4Cl:4H_2O$ solution as the etchant, where NH_4 was used as an additive to decrease the undercutting of the obtained PZT pattern. Using this technique, PZT patterns with acceptable undercutting (1.5:1) can be obtained.

Ezhilvalavan et al. proposed a wet-etch recipe using 25% [$BOE:HCl:CH_3COOH:HNO_3:NH_4Cl$:EDTA ethylenediamine tetra acetate trihydrate]:75% H_2O to pattern PZT films [39]. The etch recipe provided a high etch rate (200 nm/min) and high selectivity with respect to photoresist, limited undercutting (1.5:1, lateral:thickness), and effectively removed the residues on the etched surfaces. Using this recipe, a high-quality patterned PZT film was obtained with a large P_r of 30 μC/cm^2, a E_c of 150 kV/cm (**Figure 12**), fatigue-free characteristics, and a low leakage current density of 10^{-6} A/cm^2 at 200 × 10^5 kV/cm. Although various wet-etching procedures have been attempted, the details of the etching mechanism and residue stripping are not properly explained, and more importantly, the ferroelectric/piezoelectric characteristics of the etched PZT structures and its electrical reliability tests have not been studied in details.

3.2. Lift-off process

Compared to the etching technique, lift-off process is preferable since it has not suffered from the physical and chemical damages caused by etch plasma. The pattern ability of PZT films

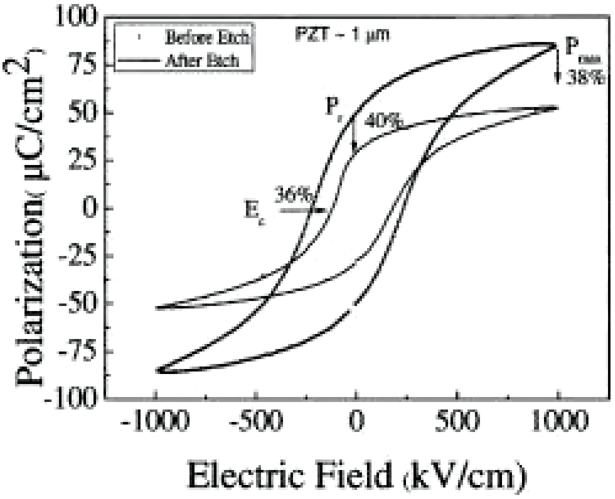

Figure 12. Hysteresis loop of the 1-μm-thick PZT film patterned by a wet-etch process [39].

by lift-off process using thick photoresist [57], hydrophobic self-assembly-monolayer, or thin ZnO film [58] as a sacrificial layer was already proved. However, the feature size was mostly limited above 50 μm, and also PZT films exhibited random crystalline structure, large leakage current, and rather poor ferroelectric properties. Recently, Tue et al. demonstrated sub-5 μm pattern of sol-gel-derived PZT films with a thickness of 80–390 nm by a novel lift-off process using solution-processed amorphous metal oxides as a sacrificial layer (**Figure 13**) [59]. The process includes three steps as follows: (1) deposition and patterning of the sacrificial lift-off layer (In-Zn-O), (2) PZT spin coating, and (3) etching of the sacrificial layer for PZT lift-off. It was found that the amorphous In-Zn-O layer acted as a good barrier between the Pt substrate and PZT film, inhibiting the crystallization of PZT film. In addition, the In-Zn-O film can be easily removed by a wet etching leading to a clean and smooth surface. As a result, the lift-off PZT film exhibited better ferroelectric properties, higher breakdown endurance, and more well-defined shape compared with the wet-etched ones.

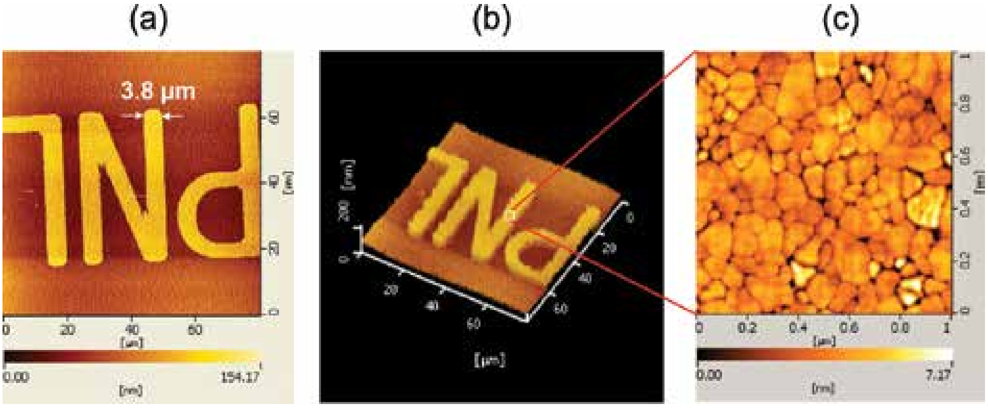

Figure 13. AFM image of fine PZT pattern: (a) 2D morphology, (b) 3D morphology, and (c) local surface morphology [59].

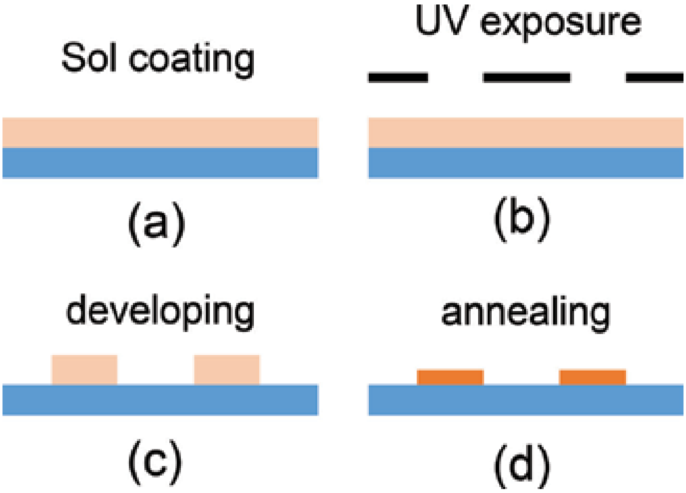

Figure 14. Scheme for patterning of PZT thin film by ultraviolet (UV) light.

3.3. Direct UV-patterning

A general scheme for patterning of PZT thin film by a UV light is shown in **Figure 14**, which is similar to a photoresist patterning process. An UV-sensitive PZT sol is first synthesized, and then spin-coated on a substrate without thermal drying step. After that, the gel film is irradiated under the UV light through a mask for photolysis step. The pattern on the mask will be transferred to PZT film according to the exposed and unexposed area. After the photolysis, the PZT film is placed in a nonionic surfactant solution to remove the unexposed area and is sintered for crystallization.

Many studies have reported the use of UV light for direct patterning PZT thin films using photo-sensitive PZT sol solutions [60–64]. Calzada et al. synthesized photo-sensitive $PbTiO_3$ solutions, which have a maximum of absorption in UV between 200 and 300 nm [60]. Weihua et al obtained an UV photosensitive PZT sol using chemical modification in acetylacetone [61]. Marson et al. developed a highly concentrated solution for producing photo-patternable layers of PZT by dissolving an amorphous PZT powder into acrylic acid [62]. Although ferroelectric/piezoelectric properties of PZT films patterned by the UV-light are comparable to those of conventional PZT thin films, they normally require complicated modification of the precursor solution, and also feature sizes of PZT patterns are relatively large (in the order of tens of micrometers).

3.4. Direct nanoimprinting lithography (NIL)

Since the first development in 1995, the nanoimprint lithography (NIL) has become one of the advanced patterning methods for nanofabrication. The idea of NIL is to transfer patterns by pressing a designed master mold into resist [65]. NIL overwhelms other lithographic processes by its low cost, high throughput, and high resolution. Various kinds of functional materials can be textured by NIL, and functional devices are obtained accordingly.

Li et al. reported pattern transfer of nanoscale ferroelectric PZT gratings on a platinized substrate by a reversal NIL without any chemical etch processes [66]. PZT sol was spin coated onto

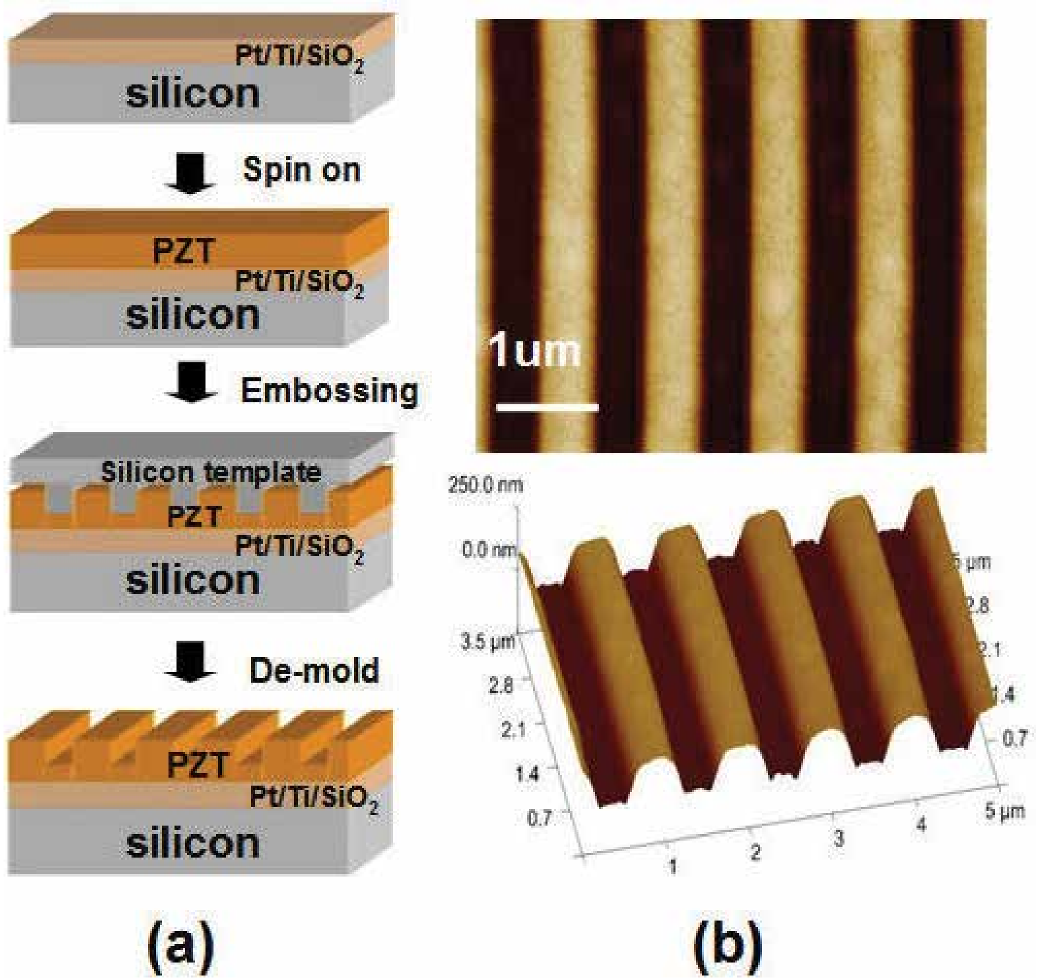

Figure 15. PZT films nanoembossing process and results of embossed profiles. (a) A schematic diagram illustrating a one-step embossing process to form a stagger shape in a PZT film with two different thicknesses and (b) AFM images of embossed stagger like profiles of PZT film [67].

a template with an antistick layer. The template with PZT was then placed onto the substrate and applied a pressure. After that, the substrate was separated from template directly. The transferred sample was then crystallized by thermal annealing in air at 650°C for 15 min. The patterned lines appeared to be reasonably straight and well ordered with few defects. The height of the gratings was in the range between 125 and 250 nm depending on the template mold.

Shen et al applied a nanoembossing technique to form a stagger structure in PZT film [67]. **Figure 15(a)** illustrates the nanoembossing process of PZT film. **Figure 15(b)** displays the embossed PZT film profiles measured by AFM; showing an embossed depth of about 160 on a 450-nm thick PZT film with well-quadrate-patterned profiles. After crystallization, the PZT films exhibited a tetragonal structure with (111) preferred orientation. In addition, the morphology of the embossed region remained stable. Chen group demonstrated a low-press, low-temperature direct NIL method for patterning PZT films [68, 69]. In general, conventional direct NIL utilizes ultrahigh pressure or temperature to form patterns on the film. The use of a sharp-tip mold combined with an underlying soft gel film may overcome issues of the conventional NIL. This approach is more favorable because of its simplicity and reduced temperature as well as imprinting pressure. Besides, imprinting on the gel film instead of on the bulk film makes the NIL much easily to be carried out. It was also successfully demonstrated that the NIL on the metal/ferroelectric bilayer structure would help to overcome the flattened problem of pattern in a gel film. Moreover, the metal film prevents the mold from directly contacting with the PZT gel. Therefore, no residual or contaminant will be observed on the mold.

4. Applications of low-temperature-processed PZT films

Thanks to multifunctional properties, PZT films can be utilized for various applications in sensor, actuator, nonvolatile memory, and energy harvesting as well. Once PZT films can be deposited at a low temperature, which is compatible with Si technology, direct integration of PZT films to other active control element, i.e., Si-CMOS, becomes possible. Further lowering of PZT process temperature to be compatible with flexible substrates enables flexible PZT-based electronics. This part briefly summarizes emerging applications of low-temperature PZT films.

4.1. Piezoelectric actuator

A diaphragm-type piezo actuator was demonstrated using a low-temperature (450°C) solution-processed PZT film [15]. Cross-sectional structure and SEM image of the fabricated actuator is given in **Figure 16(a)** and **(b)**. The observed experimental data agreed well with simulation result in which the actuator displacement linearly increased as the increase of applied voltage (**Figure 16(c)**). The maximum displacement was approximately 130 nm at 10 V. These results verify that the low-temperature-processed PZT film can be applied for actuator applications.

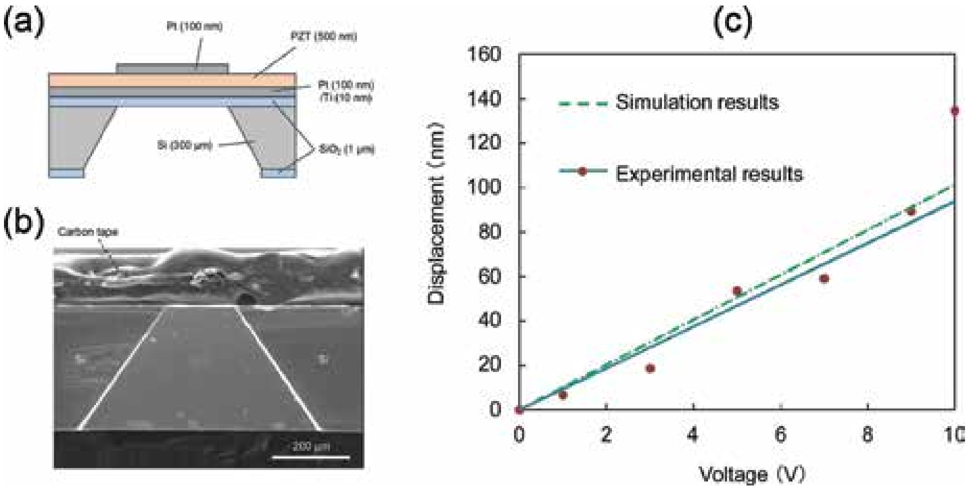

Figure 16. (a) Cross-sectional structure and (b) SEM image of the fabricated PZT actuator. (c) Comparison of the displacement between experiment and simulation results [15].

4.2. Piezoelectric energy harvester

Energy harvesting, which collects useful energy from wasted energy sources, is the most promising technology to provide solutions for the shortage of a fossil fuel, various environmental problems, and the improvement of energy efficiency in smart grids. Piezoelectric energy harvesters have been actively studied due to their easy integration with MEMS and integrated circuit technologies [70–74]. The cantilever type is the most typical structure of a piezoelectric energy harvester, in which a piezoelectric material is deposited onto a rigid Si cantilever, and a proof mass is located at the free end of the cantilever. The electricity can be generated by a conversion of kinetic energy from the mechanically stimulated proof mass via the piezoelectric material. However, the typical rigid-body-based cantilever type energy harvester has a large resonance frequency due to its high spring constant. Thus, it is not for harvesting energy from human activity or low-frequency ambient vibration. In this regard, flexible PZT appears as a promising candidate for flexible energy harvesting applications.

Cho et al. presented a microfabricated flexible and curled PZT cantilever using d_{33} piezoelectric mode for vibration-based energy harvesting applications [70]. The proposed energy harvester consists of PI layer, PZT thin film, and interdigitated IrO_x electrodes. The PZT thin film on PI layer showed $2P_r$ and $2E_c$ of approximately 47.9 μC/cm^2 and 78.8 kV/cm, respectively. At optimal conditions of resistive load (6.6 MΩ) and resonant frequency (97.8 Hz), the fabricated

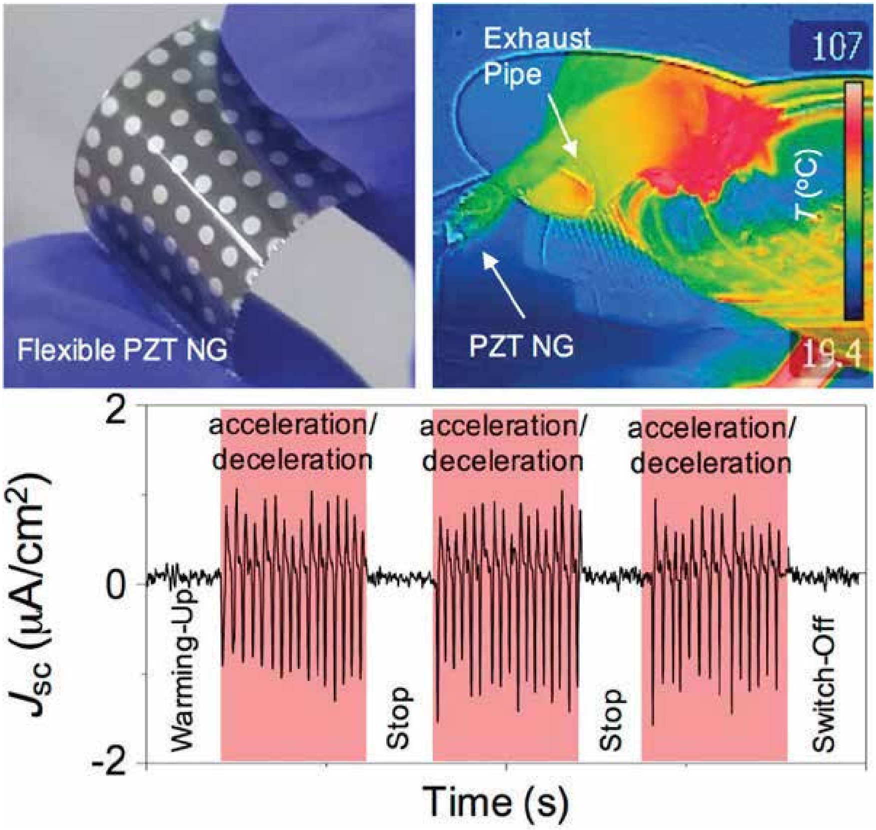

Figure 17. Illustration of flexible PZT film-based NG [74].

device was able to generate output voltage and power of 1.2 V and 117 nW, respectively. Through the introduction of indium-tin-oxide (ITO) and polyethylene terephthalate (PET) substrates to laser lift-off PZT-based energy harvester, a transparent flexible device (TFD) was implemented [71]. The TFDs based on PZT films generated an AC-type output signal and output power of 8.4 nW/cm^2, at periodically bending and releasing motion.

Recently, single-cell hybrid nanogenerators (NGs) that can simultaneously harvest mechanical and thermal energies have received great attention [72–74]. Jung group reported the development of a hybrid piezoelectric-pyroelectric NG using PZT material to simultaneously harvest mechanical and thermal energies from extreme resources [74]. By the combination of perovskite $LaNiO_3$ and Ni-Cr metal foil as a bottom electrode and a flexible substrate, they have successfully grown a PZT film with a large P_r (28 μC/cm^2), high piezoelectric constant (140 pC/N), and high pyroelectric coefficient (50 nC/cm^{2}K). The PZT-based NG was proven to stably generate electric power in harsh environment, and at elevated temperatures (**Figure 17**).

The success of flexible piezoelectric energy harvesters lies in its packaging density, output voltage and power, resonance bandwidth, lifetime, and cost. Among these, the two biggest challenges are wider bandwidth and higher power density. Advances in novel piezoelectric materials such as giant coefficient and lead-free piezoelectric as well as harvester structural design are expected to bring us closer to battery-free autonomous systems.

5. Conclusion

This review on low-temperature processing of solution-derived PZT films summarized major approaches to decrease the crystallization temperature below 450°C. The success would mitigate the integration of PZT films in electronics devices and diminish a possible loss of stoichiometry and consequent worsened functional properties due to either evaporation of volatile species (lead-, alkali-oxides) or possible interface reactions. The approaches described here include chemical and physical treatments for the precursor solutions, as-deposited, and as-pyrolyzed films by solvothermal synthesis, UV-light treatment, laser, microwave, and flash-lamp-assisted annealing. It reveals that design of functional precursor solutions, which are photo-sensitive and possibly decomposable at a low temperature, is critical to the production of high-quality PZT films.

Combination of low-temperature solution-processed PZT films with facile micro-/nano-patterning techniques would open new opportunities for low-cost, large-area transparent, flexible ferroelectric/piezoelectric devices such as nonvolatile memory, piezoelectric sensor/actuator/transducer, and energy harvesters.

Acknowledgements

The authors would like to thank JST, ERATO Shimoda Nano-Liquid Process project and JST-CREST project for financial support. Members of the Center for Single Nanoscale Innovative Devices, Japan Advanced Institute of Science and Technology are acknowledged for their technical assistance.

Conflict of interest

The authors declare that they have no competing interests.

Author details

Phan Trong Tue* and Yuzuru Takamura

*Address all correspondence to: phan-tt@jaist.ac.jp

School of Materials Science, Japan Advanced Institute of Science and Technology, Nomi-shi, Ishikawa, Japan

References

[1] Muralt P, Polcawich RG, Trolier-McKinstry S. Piezoelectric thin films for sensors, actuators, and energy harvesting. MRS Bulletin. 2009;**34**(9):658-664

[2] Setter N et al. Ferroelectric thin films: Review of materials, properties, and applications. Journal of Applied Physics. 2006;**100**(5):051606

[3] de Araujo CAP et al. Fatigue-free ferroelectric capacitors with platinum electrodes. Nature. 1995;**374**:627

[4] Park BH et al. Lanthanum-substituted bismuth titanate for use in non-volatile memories. Nature. 1999;**401**:682

[5] Aratani M et al. Epitaxial-grade polycrystalline $Pb(Zr,Ti)O_3$ film deposited at low temperature by pulsed-metalorganic chemical vapor deposition. Applied Physics Letters. 2001;**79**(7):1000-1002

[6] Schatz A, Pantel D, Hanemann T. Pulsed laser deposition of piezoelectric lead zirconate titanate thin films maintaining a post-CMOS compatible thermal budget. Journal of Applied Physics. 2017;**122**(11):114502

[7] Tsuchiya K, Kitagawa T, Nakamachi E. Development of RF magnetron sputtering method to fabricate PZT thin film actuator. Precision Engineering. 2003;**27**(3):258-264

[8] Maki K et al. Lowering of crystallization temperature of sol-gel derived $Pb(Zr, Ti)O_3$ thin films. Integrated Ferroelectrics. 2000;**30**(1-4):193-202

[9] Perez J, Vilarinho PM, Kholkin AL. High-quality $PbZr_{0.52}Ti_{0.48}O_3$ films prepared by modified sol–gel route at low temperature. Thin Solid Films. 2004;**449**(1):20-24

[10] Wu A et al. Early stages of crystallization of sol−gel-derived lead zirconate titanate thin films. Chemistry of Materials. 2003;**15**(5):1147-1155

[11] Morita T et al. Ferroelectric properties of an epitaxial lead zirconate titanate thin film deposited by a hydrothermal method below the Curie temperature. Applied Physics Letters. 2004;**84**(25):5094-5096

[12] Il DK, Ho GK. Characterization of highly preferred $Pb(Zr,Ti)O_3$ thin films on $La_{0.5}Sr_{0.5}CoO_3$ and $LaNi_{0.6}$ $Co_{0.4}O_3$ electrodes prepared at low temperature. Japanese Journal of Applied Physics. 2001;**40**(4R):2357

[13] Wang Z et al. Crystallization of ferroelectric lead zirconate titanate thin films by microwave annealing at low temperatures. Journal of the American Ceramic Society. 2011; **94**(2):404-409

[14] Bharadwaja SSN et al. Highly textured laser annealed $Pb(Zr_{0.52}Ti_{0.48})O_3$ thin films. Applied Physics Letters. 2011;**99**(4):042903

[15] Shimura R et al. Solution-based process with thermal UV treatment for fabrication of piezoelectric PZT films for an actuator array at temperatures under 450°C. Sensors and Actuators A: Physical. 2017;**267**:287-292

[16] Wu A et al. Effect of lead zirconate titanate seeds on Pt_xPb formation during the pyrolysis of lead zirconate titanate thin films. Journal of the American Ceramic Society. 2002; **85**(3):641-646

[17] Wu A et al. Characterization of seeded sol–gel lead zirconate titanate thin films. Journal of the European Ceramic Society. 1999;**19**(6):1403-1407

[18] Chen S-Y, Chen IW. Temperature–time texture transition of $Pb(Zr_{1-x}Ti_x)O_3$ thin films: I, role of Pb-rich intermediate phases. Journal of the American Ceramic Society. 1994;**77**(9):2332-2336

[19] Huang Z, Zhang Q, Whatmore RW. The role of an intermetallic phase on the crystallization of lead zirconate titanate in sol–gel process. Journal of Materials Science Letters. 1998;**17**(14):1157-1159

[20] Huang Z, Zhang Q, Whatmore RW. Low temperature crystallization of lead zirconate titanate thin films by a sol-gel method. Journal of Applied Physics. 1999;**85**(10):7355-7361

[21] Guozhang Cao and Ying Wang. Nanostructures and nanomaterials: Synthesis, properties and applications. World Scientific. 2011. ISBN 978-981-4322-50-8

[22] Yoshimura M, Byrappa K. Hydrothermal processing of materials: Past, present and future. Journal of Materials Science. 2008;**43**(7):2085-2103

[23] Katsuhiko S et al. Preparation of lead zirconate titanate thin film by hydrothermal method. Japanese Journal of Applied Physics. 1991;**30**(9S):2174

[24] Takayuki K et al. Bending actuator using lead zirconate titanate thin film fabricated by hydrothermal method. Japanese Journal of Applied Physics. 1992;**31**(9S):3090

[25] Morita T, Kanda T, Yamagata Y, Kurosawa M, Higuchi T. Single process to deposit lead zirconate titanate (PZT) thin film by a hydrothermal method. Japanese Journal of Applied Physics. 1997;**36**:2998-2999

[26] Chien AT, Speck JS, Lange FF. Hydrothermal synthesis of heteroepitaxial Pb(Zr_xTi_{1-x})O_3 thin films at 90-150°C. Journal of Materials Research. 1997;**12**(5):1176-1178

[27] Oledzka M et al. Influence of precursor on microstructure and phase composition of epitaxial hydrothermal $PbZr_{0.7}Ti_{0.3}O_3$ films. Chemistry of Materials. 2003;**15**(5):1090-1098

[28] Morita T et al. Ferroelectric property of an epitaxial lead zirconate titanate thin film deposited by a hydrothermal method. Journal of Materials Research. 2004;**19**(6):1862-1868

[29] Li J et al. A low-temperature crystallization path for device-quality ferroelectric films. Applied Physics Letters. 2010;**97**(10):102905

[30] Kim YH et al. Flexible metal-oxide devices made by room-temperature photochemical activation of sol–gel films. Nature. 2012;**489**:128-132

[31] Umeda K et al. Impact of UV/O_3 treatment on solution-processed amorphous $InGaZnO_4$ thin-film transistors. Journal of Applied Physics. 2013;**113**(18):184509

[32] Yue J et al. UV-assisted low-temperature sol–gel deposition of Pb($Zr_{0.4}Ti_{0.6}$)O_3 film and its photoelectrical properties. Journal of Sol-Gel Science and Technology. 2017;**83**(3):647-652

[33] Bretos I et al. Activated solutions enabling low-temperature processing of functional ferroelectric oxides for flexible electronics. Advanced Materials. 2014;**26**(9):1405-1409

[34] Bretos I et al. Active layers of high-performance lead zirconate titanate at temperatures compatible with silicon nano- and microelectronic devices. Scientific Reports. 2016;**6**: 20143

[35] Yagi XCAM. Development of crystallization of PZT films by laser annealing. Ricoh Technical Report. 2014;**39**:06

[36] Miyazaki T et al. Low-temperature crystallization of CSD-derived PZT thin film with laser annealing. Materials Science and Engineering B. 2010;**173**(1):89-93

[37] Katz JD. Microwave sintering of ceramics. Annual Review of Materials Science. 1992; **22**(1):153-170

[38] Agrawal DK. Microwave processing of ceramics. Current Opinion in Solid State and Materials Science. 1998;**3**(5):480-485

[39] Wang ZJ et al. Low-temperature growth of high-quality lead zirconate titanate thin films by 28 GHz microwave irradiation. Applied Physics Letters. 2005;**86**(21):212903

[40] Bhaskar A et al. Low-temperature crystallization of sol–gel-derived lead zirconate titanate thin films using 2.45 GHz microwaves. Thin Solid Films. 2007;**515**(5):2891-2896

[41] Ankam B et al. Effect of microwave annealing temperatures on lead zirconate titanate thin films. Nanotechnology. 2007;**18**(39):395704

[42] Wang ZJ et al. Low-temperature growth of ferroelectric lead zirconate titanate thin films using the magnetic field of low power 2.45 GHz microwave irradiation. Applied Physics Letters. 2008;**92**(22):222905

[43] Pramod KS et al. Dielectric and piezoelectric properties of microwave sintered PZT. Smart Materials and Structures. 2001;**10**(5):878

[44] Koji Y et al. Novel Pb(Ti, Zr)O_3 (PZT) crystallization technique using flash lamp for ferroelectric RAM (FeRAM) embedded LSIs and one transistor type FeRAM devices. Japanese Journal of Applied Physics. 2002;**41**(4S):2630

[45] Ouyang J et al. Photonic sintering of aerosol jet printed lead zirconate titanate (PZT) thick films. Journal of the American Ceramic Society. 2016;**99**(8):2569-2577

[46] Bale M, Palmer RE. Reactive ion etching of piezoelectric $Pb(Zr_xTi_{1-x})O_3$ in a SF_6 plasma. Journal of Vacuum Science & Technology, A: Vacuum, Surfaces, and Films. 1999;**17**(5):2467-2469

[47] Wang S et al. Deep reactive ion etching of lead zirconate titanate using sulfur hexafluoride gas. Journal of the American Ceramic Society. 1999;**82**(5):1339-1641

[48] Chee Won C, Chang Jung K. Etching effects on ferroelectric capacitors with multilayered electrodes. Japanese Journal of Applied Physics. 1997;**36**(5R):2747

[49] Jin-Ki J, Won-Jong L. Dry etching characteristics of Pb(Zr,Ti)O_3 films in CF_4 and Cl_2/CF_4 inductively coupled plasmas. Japanese Journal of Applied Physics. 2001;**40**(3R):1408

[50] Masaru O et al. Metalorganic chemical vapor deposition of c-axis oriented PZT thin films. Japanese Journal of Applied Physics. 1990;**29**(4R):718

[51] Kang M-G, Kim K-T, Kim D-P, Kim C-I. Reduction of dry etching damage to PZT films etched with a Cl-based plasma and the recovery behavior. Journal of the Korean Physical Society. 2002;**41**(4):6

[52] Mancha S. Chemical etching of thin film PLZT. Ferroelectrics. 1992;**135**(1):131-137

[53] Miller RA, Berwnstein JJ. A novel wet etch for patterning lead zirconate-titanate (PZT) thin-films. Integrated Ferroelectrics. 2000;**29**(3-4):225-231

[54] Wang LP et al. Wet-etch patterning of lead zirconate titanate (PZT) thick films for microelectromechanical systems (MEMS) applications. MRS Proceedings. 2000;**657**:EE5.39

[55] Kelu Z, Jian L, Jiaru C. A novel wet etching process of Pb(Zr,Ti)O_3 thin films for applications in microelectromechanical system. Japanese Journal of Applied Physics. 2004;**43**(6S):3934

[56] Che L, Halvorsen E, Chen X. An optimized one-step wet etching process of $Pb(Zr_{0.52}Ti_{0.48})O_3$ thin films for microelectromechanical system applications. Journal of Micromechanics and Microengineering. 2011;**21**(10):105008

[57] Zhao HJ, Ren TL, Liu JS, Liu LT, Li ZJ. Fabrication of high quality PZT thick film using lift-off technique. In: Technical Proceedings of the 2003 Nanotechnology Conference and Trade Show, Vol. 1; 2003. p. 4

[58] Li J et al. Micro-patterning of PZT thick film by lift-off using ZnO as a sacrificial layer. Ceramics International. 2015;**41**(6):7325-7328

[59] Tue PT, Shimoda T, Takamura Y. Fine-patterning of sol-gel derived PZT film by a novel lift-off process using solution-processed metal oxide as a sacrificial layer. Ceramics International. 2016;**42**(16):18431-18435

[60] Calzada ML et al. Photo-sensitive sol-gel solutions for the low-temperature UV-assisted processing of $PbTiO_3$ based ferroelectric thin films. Journal of Materials Chemistry. 2003;**13**(6):1451-1457

[61] Weihua Z, Gaoyang Z, Zhiming C. Photosensitive PZT gel films and their preparation for fine patterning. Materials Science and Engineering B. 2003;**99**(1):168-172

[62] Marson S et al. Direct patterning of photosensitive chemical solution deposition PZT layers. Journal of the European Ceramic Society. 2004;**24**(6):1925-1928

[63] Kang GY et al. Fabrication and electromechanical properties of a self-actuating $Pb(Zr_{0.52}Ti_{0.48})O_3$ microcantilever using a direct patternable sol-gel method. Applied Physics Letters. 2006;**88**(4):042904

[64] Kumar SR et al. Control of microstructure and functional properties of PZT thin films via UV assisted pyrolysis. Journal of Sol-Gel Science and Technology. 2007;**42**(3):309-314

[65] Chou SY, Krauss PR, Renstrom PJ. Imprint of sub-25 nm vias and trenches in polymers. Applied Physics Letters. 1995;**67**(21):3114-3116

[66] Li Z-D et al. Pattern transfer of nano-scale ferroelectric PZT gratings by a reversal nanoimprint lithography. Microelectronic Engineering. 2011;**88**(8):2037-2040

[67] Shen Z et al. Nano-embossing technology on ferroelectric thin film $Pb(Zr_{0.3},Ti_{0.7})O_3$ for multi-bit storage application. Nanoscale Research Letters. 2011;**6**(1):474

[68] Hsieh KC et al. Directly patterning ferroelectric films by nanoimprint lithography with low temperature and low pressure. Journal of Vacuum Science & Technology, B: Microelectronics and Nanometer Structures--Processing, Measurement, and Phenomena. 2006;**24**(6):3234-3238

[69] Chen HL et al. Using direct nanoimprinting of ferroelectric films to prepare devices exhibiting bi-directionally tunable surface plasmon resonances. Nanotechnology. 2008; **19**(43):435304

[70] Cho H, Park J, Park JY. Micro-fabricated flexible PZT cantilever using d33 mode for energy harvesting. Micro and Nano Systems Letters. 2017;**5**(1):20

[71] Do YH et al. Preparation on transparent flexible piezoelectric energy harvester based on PZT films by laser lift-off process. Sensors and Actuators A: Physical. 2013;**200**:51-55

[72] Lee JH et al. Highly stretchable piezoelectric-pyroelectric hybrid nanogenerator. Advanced Materials. 2014;**26**(5):765-769

[73] Yang Y et al. Flexible hybrid energy cell for simultaneously harvesting thermal, mechanical, and solar energies. ACS Nano. 2013;**7**(1):785-790

[74] Ko YJ et al. Flexible $Pb(Zr_{0.52}Ti_{0.48})O_3$ films for a hybrid piezoelectric-pyroelectric nanogenerator under harsh environments. ACS Applied Materials & Interfaces. 2016;**8**(10): 6504-6511

Chapter 7

$BaTiO_3$-Based Lead-Free Electroceramics with Their Ferroelectric and Piezoelectric Properties Tuned by Ca^{2+}, Sn^{4+} and Zr^{4+} Substitution Useful for Electrostrictive Device Application

Bharat G. Baraskar, Pravin S. Kadhane,
Tulshidas C. Darvade, Ajit R. James and
Rahul C. Kambale

Additional information is available at the end of the chapter

http://dx.doi.org/10.5772/intechopen.77388

Abstract

Dense microstructure $BaTiO_3$ (BT) ceramic with *c*/*a* ~1.0144 and average grain size ~7.8 μm is developed by achieving the ferroelectric parameters Psat. = 24.13 μC/cm^2 and Pr = 10.42 μC/cm^2 with lower coercive field of Ec = 2.047 kV/cm. For BT ceramic, the “sprout” shape nature is observed for strain-electric field measurements with remnant strain ~ 0.212%, converse piezoelectric constant ~376.35 pm/V and electrostrictive coefficient Q_{33}~ 0.03493 m^4/C^2. To tune the piezoelectric properties of BT ceramic, the substitutions of Ca^{2+} and Sn^{4+}, Zr^{4+} are done for Ba^{2+} and Ti^{4+} sites respectively. The $Ba_{0.7}Ca_{0.3}Ti_{1-x}Sn_xO_3$ (x = 0.00, 0.025, 0.050, 0.075, and 0.1, BCST) system was studied with ferroelectric, piezoelectric and electrostrictive properties. The electrostrictive coefficient (Q_{33}) ~ 0.0667 m^4/C^2 was observed for x = 0.075 and it is higher than the lead-based electrostrictive materials. Another (1-X) $Ba_{0.95}Ca_{0.05}Ti_{0.92}Sn_{0.08}O_3$ (BCST) – (X) $Ba_{0.95}Ca_{0.05}Ti_{0.92}Zr_{0.08}O_3$ (BCZT), ceramics (x = 0.00, 0.25, 0.50, 0.75, and 1) is studied. The BCST-BCZT ceramic system shows the increase of polymorphic phase transition temperatures toward the room temperature by Ca^{2+}, Sn^{4+} and Zr^{4+} substitution. For BCST-BCZT system the composition x = 0.75 exhibits the d_{33}, and Q_{33} values of 310 pC/N, 385 pm/V and 0.089 m^4/C^2 respectively which is greater than BT ceramics.

Keywords: lead-free piezoelectric, $BaTiO_3$, ferroelectric, curie temperature, electrostrictive coefficient

1. Introduction

Currently, most of the electronic devices and naval departments use the materials that are based on interconversion of mechanical and electrical energies i.e. piezoelectric effect for actuator/transducer/energy harvester applications. The examples of these devices include ink-jet printers, fuel injection actuators in cars, transducers for ultrasonic imaging and therapy in medicine, sensors and actuators for vibration control, and sonars. In many of devices, ($PbZr_{1-x}Ti_xO_3$, PZT) based piezoelectric materials are mainly employed due to its excellent piezoelectric properties viz. piezoelectric charge coefficient (d_{33} ~ *250–600 pC/N*), electromechanical coupling factor (*Kp ~ > 0.50*), mechanical quality factor (Q_m ~ 10–1000), high dielectric constant (ε_r ~ > 700), low dielectric loss (t*anδ ~ < 1%*) and high Curie temperatures (Tc ~ > 300°C). However, lead oxide (PbO), main component of PZT, is highly toxic and its toxicity is further enhanced due to its volatilization at higher temperature, particularly during calcination/ sintering and thus causing environmental pollution. Today, with increasing level of electronic equipments being manufactured, used and discarded, it has been well recognized that the level of hazardous substances (in the environment) has been rising day- to- day life. Further, Pb causes severe chronic poisoning and pain with long-term exposure (years-to-decades), even when accumulated in small traces. Therefore, to reduce environmental damage during the waste disposal of piezoelectric products as well as health hazard issues, many countries have adopted the waste from electrical and electronic equipment (WEEE), restriction of hazardous substances (RoHS) and end-of life vehicles (ELV) legislations coined by the European Union and banned the use of Pb/ PbO based materials for electronic and automobile industries. Thus, there is an open challenge to search and invent the lead-free piezoelectric ceramics and transfer them into applications in place of PZT ceramics [1]. Among the lead-free piezoelectric ceramics, perovskite-structured ferroelectrics such as $BaTiO_3$ [BT], $(Bi_{1/2}Na_{1/2})TiO_3$ [BNT], $(Bi_{1/2}K_{1/2})TiO_3$ [BKT], $KNbO_3$ [KN], $(K,Na)NbO_3$ [KNN], and their solid solutions have drawn great interest of researchers. However, there are some general problems associated with these lead-free piezoceramics such as lower Curie temperatures (T_c), or low depolarization temperatures (T_d), difficulties in poling treatments, low relative densities. For example, a) The processing of KNN ceramic has some critical issues such as volatility of alkali-oxides, compositional inhomogeneity, poor densification, and phase stability; b) $BaTiO_3$ (BT) based piezoelectric shows stable piezoelectric properties, but the main issue is of lower Curie temperature (T_c) ~ < 100°C and lower coercive field which results in more temperature dependent properties and less polarization stability as well as difficulties in poling treatments; c) BNT and BKT based ceramics have suffered from its poor sinterability and hence densification.

Barium titanate, $BaTiO_3$ (BT) is the first polycrystalline ceramic ever discovered that exhibits the stable piezoelectric and dielectric properties; hence considered as a promising lead-free ferroelectric ceramic with perovskite ABO_3 structure [2]. BT is one of the promising ferroelectric materials specifically known for its wide range of applications from dielectric capacitor to non-linear optic devices. For BT ceramic, below Curie temperature (120°C), the vector of the spontaneous polarization points in the [001] direction (tetragonal phase), below 5°C it reorients in the [011] (orthorhombic phase), and below −90°C in [111] direction (rhombohedral phase) [3–5]. The present scenario of BT based electroceramics is to bring the polymorphic phase transition (PPT) i.e. Rhombohedral to orthorhombic (T_{R-O}) and Orthorhombic to Tetragonal (T_{O-T}) close to room temperature to achieve the phase coexistence at 300 K and hence shows the enhanced piezoelectric properties [6]. For Zr^{4+}, Sn^{4+}, and Hf^{4+} substitution at Ti^{4+} site in $BaTiO_3$ increases PPT temperatures from low temperatures (0°C and −90°C) to room temperature [6]. Recently, high performance BT-based ceramics such as $(Ba,Ca)(Ti,Zr)O_3$ (BCZT) and $(Ba,Ca)(Ti,Sn)O_3$ (BCST) prepared by substitution of Ca^{2+} at A-site and Zr^{4+}/Sn^{4+} at B-site showed the properties comparable to that of soft PZT materials [7–12]. Furthermore, the substitution of Ca^{2+}at Ba^{2+} in $BaTiO_3$-$CaTiO_3$ system (i.e. to form $Ba_{1-x}Ca_xTiO_3$ (BCT) ceramics) results in a slight increase in the Curie temperature (T_C) and on the other hand suppresses the orthorhombic to tetragonal (T_{O-T}) transition temperature. This is one of the important considerations in developing the temperature stability of piezoelectric properties for various practical applications [13]. Many research groups have reported the dielectric, diffused phase transition, ferroelectric and piezoelectric properties of BCZT and BCST ceramics [6, 7, 13–22]. However, there is a need of detailed investigation of electrostrictive properties of BT based lead free electroceramics which are correlated with the structure–property-composition having the phase coexistence of orthorhombic-tetragonal (O-T), Rhombohedral-Orthorhombic (R-O) and Rhombohedral-Tetragonal (R-T) lattice symmetries, at room temperature. Thus, in view of the above, we have investigated the ferroelectric, piezoelectric and electrostrictive properties of Ca^{2+}, Sn^{4+} and Zr^{4+} modified $BaTiO_3$ ceramics and tried to correlate the observed results with the phase coexistence of noncentrosymmetric lattice symmetries achieved at room temperature.

2. Experimental details

2.1. Synthesis

2.1.1. $BaTiO_3$ (BT) synthesis

Barium titanate, $BaTiO_3$ polycrystalline electroceramic was synthesized by conventional solid-state reaction method. Staring raw materials barium carbonate ($BaCO_3$, ≥ 99%) and titanium dioxide (TiO_2, ≥ 99%) (from Sigma Aldrich) were weighted and mixed in stoichiometric proportions and ball-milled for 15 h in the ethanol medium. After ball milling slurry were dried at 100°C overnight and dried powder grounded well. Then the powder pressed into pellets of 2 cm in diameter and 4–5 mm in thickness and calcined at 1260°C for 5 h. The calcined pellets were crushed and grounded well to form the fine powder. Thereafter, pellets with 10 mm diameter and 0.6–1 mm in thickness were prepared from calcined powder by using poly vinyl alcohol (PVA) as a binder. Finally, the prepared pellets were sintered at 1300°C for 5 h.

2.1.2. $Ba_{0.7}Ca_{0.3}Ti_{1-x}Sn_xO_3$ (BCST) synthesis

$Ba_{0.7}Ca_{0.3}Ti_{1-x}Sn_xO_3$ (BCST) ceramics with x = 0.00, 0.025, 0.050, 0.075, 0.1 were prepared by solid state reaction method. Stoichiometric amounts of AR grade raw materials of $BaCO_3$ (99%), $CaCO_3$ (99%), TiO_2 (99%) and SnO_2 (99.9%) (all are from Sigma Aldrich) were mixed with the addition of ethanol, and dried, then calcined at 1130°C for 10 h. Thereafter, they were remixed and pressed into pellets having 10 mm diameter and 0.6–1 mm in thickness and sintered for two times first at 1260°C for 10 h and secondly at 1400°C for 5 h in an air atmosphere. The post-calcination at 1260°C for 10 h was carried out to achieve proper diffusion to assist the homogenization and avoid the phase segregation of $CaTiO_3$.

2.1.3. (1−x) $Ba_{0.95}Ca_{0.05}Ti_{0.92}Sn_{0.08}O_3$-$xBa_{0.95}Ca_{0.05}Ti_{0.92}Zr_{0.08}O_3$ [(1−x)BCST-xBCZT] synthesis

The (1−x) $Ba_{0.95}Ca_{0.05}Ti_{0.92}Sn_{0.08}O_3$-$xBa_{0.95}Ca_{0.05}Ti_{0.92}Zr_{0.08}O_3$ [(1−x)BCST-xBCZT] lead-free piezoelectric ceramics with x = 0, 0.25, 0.50, 0.75, 1 were prepared by mixed oxide solid state reaction. High purity analytical grade $BaCO_3$, $CaCO_3$, TiO_2, SnO_2, and ZrO_2 (Hi Media; purity ≥99%) chemicals were mixed in stoichiometric proportion and ball milled for 24 h using ethanol medium. Thereafter solutions were dried and calcined at 1200°C for 10 h in air. Calcined powders were grounded well and pressed into pellets of 1 cm in diameter and ~ 0.7–0.8 mm in thickness using 5 wt% polyvinyl alcohol (PVA) as a binder. After burning out PVA at 600°C the samples were sintered at 1350°C for 10 h.

All ferroelectric materials system investigated in this book chapter was prepared and characterized for structural information at functional ceramics laboratory, Savitribai Phule Pune University.

2.2. Characterizations

The phase formation, crystal lattice symmetry and microstructural features of the samples were examined using the X-ray diffraction (XRD) with a CuKα radiation (λ = 1.5406 Å; D8 Advance, Bruker Inc., Germany) and the scanning electron microscopy (JEOL-JSM 6306A, Japan). The relative density of sintered pellets was estimated from the ratio of the apparent density measured by Archimedes' principle and the theoretical density calculated using crystal cell parameters. For electrical property measurements, silver paste was applied on both sides of the polished surfaces of pellet and then the sample was cured at 200°C for overnight to dry out the moisture prior to any measurements. Dielectric constant (ε_r) and loss tangent (tanδ) were measured as a function of temperature from −100 to 150°C at 100 kHz using inductance-capacitance-resistance (LCR) meter (HIOKI- 3532-50, Japan), connected to a computer-controlled furnace. Polarization (P) versus electric field (E) i.e. P-E hysteresis loops and the electric field induced strain i.e. S-E curves for ceramics were recorded at Ceramics and Composites Group, DMRL, Hyderabad on virgin (unpoled) samples at an applied electric field of ~ 50–60 kV/cm at 0.1 Hz, using a ferroelectric test system (TF Analyzer 2000 of M/s. aixAcct Systems, GmbH, Germany). The piezoelectric constant d_{33} for poled ceramics was measured using piezoelectric coefficient d_{33} meter (YE2730A d_{33} meter, USA).

3. Results and discussion

3.1. High dense $BaTiO_3$ ceramic with their ferroelectric and piezoelectric properties

X-ray diffraction study confirmed the tetragonal crystal structure having c/a ~ 1.0144. The dense microstructure was evidenced from morphological studies with an average grain size ~ 7.8 μm as shown in **Figure 1(a)**. **Figure 1(b)** shows the temperature dependent variation of the dielectric permittivity (ε_r) in the range of 25–160°C at fixed frequencies viz. 1, 25, 50, 75 and100 kHz for BT ceramic sintered at 1300°C. The phase transition from ferroelectric to paraelectric was observed at Curie temperature (T_c ~ 125°C) with ε_r = 5617 [23]. **Figure 1(c)** shows the polarization-electric field (P-E) hysteresis loops for BaTiO$_3$ ceramic measured at 0.1 Hz and room temperature. Typical hysteresis loop confirms the ferroelectric nature of the sample at room temperature. The hysteresis loop is well saturated and fully developed, indicate that external field has enough energy to switch and rotate the ferroelectric domain of BT ceramic. The saturation and remnant polarization, P_{sat} = 24.13 μC/cm^2 and P_r = 10.42 μC/cm^2 was observed at the electric field strength of 57.14 kV/cm having lower coercive field of E_c = 2.047 kV/cm. The reason for achieving improved ferroelectric properties in the present work may be attributed to the high value of c/a ratio ~1.014 and dense microstructure with average grain size 7.8 μm. The lower Ec indicate that low energy loss during electric field sweep having low energy barriers for polarization rotation i.e. soft ferroelectric nature. Low energy barrier can greatly promote the polarization rotation and effectively enhance the piezoelectric properties [3]. **Figure 1(d)** shows variation of polarization current density with respect to applied electric field. Current density exhibits the peaking behavior for both positive and negative cycle of applied electric field. The peaking behavior is a characteristic feature of the good ferroelectric ceramic having saturation polarization. Therefore, in present work we are successful to obtain the high-quality BT ceramic having saturated polarization states [23]. Thus, the observed ferroelectric properties are promising for ferroelectric memory device applications with larger P_r and P_s having low E_c. The estimated value of electric dipole moment for BT is 0.6689 × 10^{-27} C.cm by using Pr and lattice constant values.

Figure 1(e) shows the bipolar electric field induced strain curves measured for BT sample at frequency of 0.1 Hz with respect to bipolar electric fields. Sample revealed the "sprout"

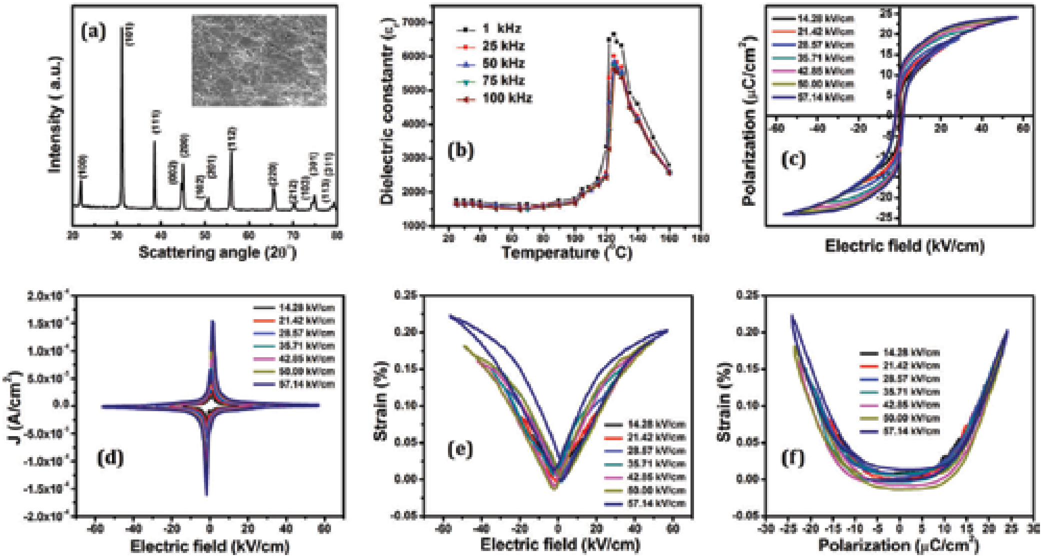

Figure 1. (a-f). (a) X- ray diffraction pattern, inset SEM, (b) relative permittivity verses temperature, (c) P-E hysteresis loop (d) J-E loop, (e) S-E loop, (f) S-P curve, of BaTiO$_3$ ceramics. (reprinted figure from ref. 23. Copyright (2016) by the AIP publishing.).

shape loop instead of "butterfly" loop which confirms the improved piezoelectric behavior [4]. Which indicates that the BT ceramic is not showing negative strain behavior, therefore here we should note that the enhancement of strain (S) is due to the sprout shape of bipolar electric field induced strain curve [4]. For electric field E = 57.14 kV/cm, better value of remnant strain 0.212% and higher value of the converse piezoelectric coefficient d^*_{33} = 376 pm/V were observed. Unfortunately, practical implementations of BT-based ceramics for commercial actuator applications are still limited by their inferior electromechanical properties as compare to those of their conventional PZT counterparts. In the present study, it is worth pointing out that the strain reaches 0.212% at E = 57.14 kV/cm which is a promising value for lead-free piezoelectric ceramic. Large value of strain output of $BaTiO_3$ is accompanied by small strain hysteresis which enabling the materials to be a promising potential for actuator applications. It is well known that domain switching and domain wall motion of $BaTiO_3$ ceramic could contribute to field-induced strain as an extrinsic effect. Since the extrinsic contribution is sensitive to external excitation, the large electric field in strain measurement may be responsible for a larger d^*_{33} = 376 pm/V [23]. Here for $BaTiO_3$ ceramic the strain-electric field hysteresis loop, which resembles the "sprout" shape loop, is may be due to the three types of effects; one is the normal converse piezoelectric effect of the lattice and other two are due to switching and movement of domain walls of $BaTiO_3$ [24]. The electrostriction coefficients Q is a four-rank tensor property that describes the relationship between polarization-induced strain (S) which proportional to the square of polarization (P) and is given by $S = QP^2$ [25]. **Figure 1(f)** shows the variation of strain with respect to polarization for $BaTiO_3$ ceramic; using this graph of strain vs. polarization we can find value of electrostriction coefficient. The relationship between field-induced strain S and polarization P satisfied equation; $Q_{33} = (S_3)/(P_3)^2$, where Q_{33} is electrostrictive coefficient, S_3 is the strain and P_3 is the polarization [4]. In our case for $BaTiO_3$ the observed value of the electrostrictive coefficient was Q_{33} = 0.035 m^4/C^2 this is larger than that of PZT (0.018–0.025 m^4/C^2) based ceramic [4]. The high Q_{33} of the BT ceramic is an important factor accounting for their high piezoelectric constant [4]. The high Q_{33} of the present BT ceramic means that it would be valuable to investigate the possible electrostrictive applications of BT ceramic.

3.2. Tune the ferroelectric and piezoelectric properties of $BaTiO_3$ by Ca^{2+} and Sn^{4+} substitution

The phase formation, microstructural aspects and dielectric properties for $Ba_{0.7}Ca_{0.3}Ti_{1-x}Sn_xO_3$ (BCST) ceramics with x = 0.00, 0.025, 0.05, 0.075 and 0.1 compositions are investigated and concluded that the compositions with x = 0.00, 0.025 and 0.05 reveals the tetragonal lattice symmetry *P4mm*, while the composition x = 0.075 shows the phase coexistence of tetragonal and orthorhombic lattice symmetries i.e. *P4mm* + *Amm2*. However, the composition x = 0.10 shows the combination *P4mm* (60%) and cubic $Pm\bar{3}m$ (40%) (ICSD# 99736) lattice symmetries which is called the pseudo-cubic (PC) lattice symmetry [26]. Thus, to invoke the improved ferroelectric and piezoelectric behavior of the material system an attempt to be made to achieve phase coexistence of noncentrosymmetric lattice symmetries near room temperature. The average grain size of BCST ceramics is found to be decreased from 8.56 to 2.36 μm with increasing Sn^{4+} content from x = 0.00 to 0.1 [26]. This is due to the lower grain-growth rates of slowly diffusing Sn^{4+} due to its higher ionic radii compared to Ti^{4+}. Thus, incorporation of Sn^{4+} inhibits the grain growth of $BaTiO_3$ based electroceramics. To evident the phase coexistence of noncentrosymmetric lattice symmetries near room temperature the temperature dependent dielectric constant measurements were performed in the range of −150 to 150°C . Based on the dielectric anomaly observed at different temperatures with Sn^{4+} content in BCST ceramics, a phase diagram has been constructed and is shown in **Figure 2**. Thus, the observed dielectric results support the XRD results about the phase coexistence of orthorhombic-tetragonal lattice symmetry for x = 0.075 of BCST ceramics. All the BCST ceramics exhibits low dielectric loss (tanδ) < 4% in the measured temperature range.

Figure 3 (a-e), shows the polarization-electric field (*P-E*) hysteresis loop and displacement current density - electric field (*J-E*) curves measured with an applied electric field up to 50–60 kV/cm at 0.1 Hz. Both the P-E and J-E measurements were performed on virgin (unpoled) composition. All BCST ceramics exhibit a typical electric-field induced ferroelectric polarization hysteresis loop, which confirms the ferroelectric nature of investigated samples. In the present work, the compositions with $x = 0.00$ and 0.1 do not show the well-saturated P-E hysteresis loops. Because to achieve the saturation state of polarization in electroceramics is rather quite difficult due to the dielectric strength of the electroceramics which limits the electric field value. Moreover, the saturation state of polarization as well as the proper values of coercive field (E_c) and remnant polarization (P_r) can be reported by measuring the electric field induced displacement current density that reveals the sharp peaking behavior during positive and negative cycles [27, 28]. The presence of J-E peak corresponds to the E_c value i.e. a field responsible for domain switching for a saturated loop [27–29]. It is important to note that, most of the time, the reported values of P_r and E_c values are estimated from the observed P-E hysteresis loop which is not well saturated; thus, in principles they are not proper values as they are measured from the pre-saturated P-E loops [27, 28]. Therefore, the peak value of displacement current density (*J*) shown in **Figure 3(a-e)** for the forward and reverse cycles indicate the presence of a cyclic and uniform in both the directions, a typical characteristic of ferroelectric materials.

An observation made from **Figure 3(a-e)** reveals that the compositions with $x = 0.00$ and 0.1 does not exhibit the sharp peaking behavior hence they are said to be not the completely saturated, whereas the compositions with $x = 0.025$, 0.05 and 0.075 show the sharp peaking behavior of displacement current density. Thus, the compositions with $x = 0.025$, 0.05 and 0.075 are said to be completely saturated with respect to an applied electric field. Another important observation is made from **Figure 3** that for compositions with $x = 0.025$, 0.05 and 0.075, both the P-E and J-E curves are intersecting at a value of electric field which is approximately corresponds to the coercive field E_c. On the other hand, the compositions with $x = 0.00$ and 0.1 does not show any intersection of P-E and J-E plots. Furthermore, the compositions with x = 0.025, 0.05 and 0.075 exhibit the symmetric nature during positive and negative cycle of an applied electric field i.e. there is no imprint behavior of polarization state. This means that the compositions with $x = 0.025$, 0.05 and 0.075 may be useful for piezoelectric Ac device i.e. vibrational energy harvesting applications. The ferroelectric parameters namely remnant polarization (P_r), maximum polarization (P_{max}) and coercive electric field (E_c), with Sn^{4+} content is presented in **Figure 3(f)**. For $x = 0.00$ the observed values of P_r, P_{max} and E_c are 5.75 μC/cm², 12.70 μC/cm²

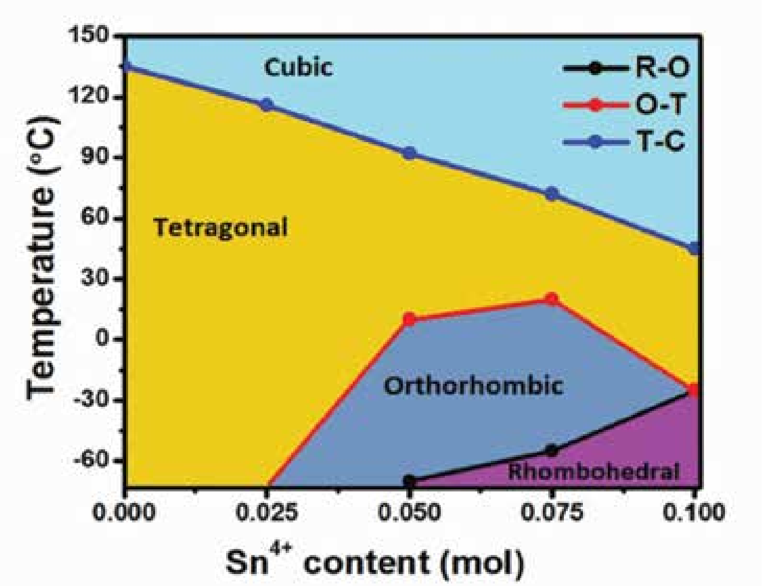

Figure 2. Phase diagram for $Ba_{0.7}Ca_{0.3}Ti_{1-x}Sn_xO_3$ ceramics. (reprinted figure from ref. 26. Copyright (2017) by the American ceramic society.).

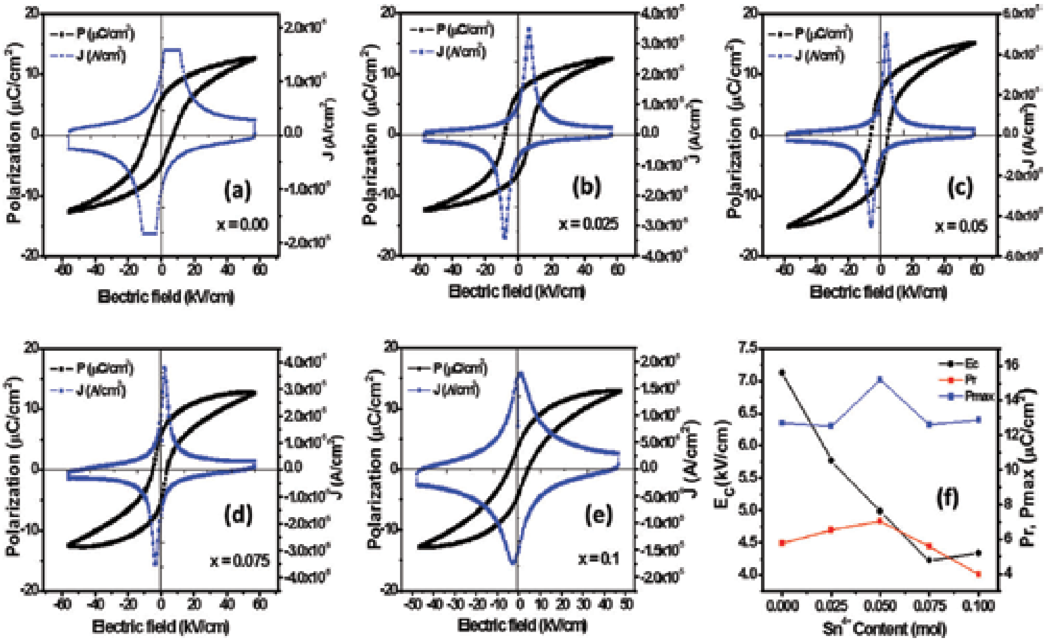

Figure 3. (a-f) (a-e) variation of polarization and displacement current density with applied electric field at 0.1 Hz for BCST ceramics, (f) variation of coercive field (E_c), remnant polarization (P_r) and maximum polarization (P_{max}) with Sn^{4+} content in BCST ceramics. (reprinted figure from ref. 26. Copyright (2017) by the American ceramic society.).

and 7.12 kV/cm, respectively. Here, the BCT showed high value of E_c which indicates that the ferroelectric domains are stabilized and thus the larger electric field is required to reverse the domains [13]. Further, as Sn^{4+} content increases from $x = 0.025$ to 0.1, the observed E_c values are in the range, 5.77–4.34 kV/cm, which indicates that these ceramics are relatively easy to pole and hence it may be possible to achieve better piezoelectric and electrostrictive properties. The possible reason for decrease of E_c with Sn^{4+} is ascribed to the decrease of c/a ratio with Sn^{4+} content, because the stress resulted from the domain switching gets reduced with decrease of c/a ratio; hence the domain switches easily under a lower electric field [30]. With Sn^{4+} content increases, the P_r increases up to 7.05 μC/cm^2 (for $x = 0.05$) and then decreases to 3.97 μC/cm^2, for $x = 0.1$. This increase of P_r values with increasing Sn^{4+} content is quite reliable, as it is known that the Sn^{4+} are not ferroelectric active whereas Ti^{4+} are ferroelectric active [16, 17, 19]. Thus, the incorporation of Sn^{4+} into $BaTiO_3$ may dilute the ferroelectricity and suppresses the piezoelectric/electrostrictive properties. However, in the present study, we have noticed the increasing trend of P_r with Sn^{4+} content up to $x = 0.05$ which could show the promising piezoelectric/electrostrictive properties. The increase in P_r and P_{max} for $x = 0.05$ may be attributed to the tetragonal crystal lattice symmetry retained in the composition. However, the compositions $x = 0.075$ and 0.1 exhibit the crystallographic phase coexistence of orthorhombic-tetragonal and pseudo-cubic lattice symmetries respectively which gives rise to the instability of ferroelectric domain and thus the P_r and P_{max} decreases [31]. Furthermore, by using remnant polarization and lattice constant values we have estimated the electric dipole moment for BCST ceramics and are found to be (0.3618, 0.4119, 0.4460, 0.3542, 0.2464) x 10^{-27} C.cm namely for x = 0.00, 0.025,0.050,0.075 and 0.1 respectively.

The bipolar strain (S) versus electric field (E) behavior was investigated for all the BCST samples and is shown in **Figure 4(a-e)**. They exhibit a typical butterfly loop, which is a feature of piezoelectric system for biaxial field. It is well-known that the butterfly loop is observed due to the normal converse piezoelectric effect of the lattice along with the switching and movement of domain walls. Here, all the BCST ceramics show the hysteretic strain behavior which may be associated with the domain reorientation. The converse piezoelectric constant is defined as $d_{33}^* = S_{max}/E_{max}$, where S_{max} is the maximum strain at maximum electric field (E_{max}); accordingly, it is calculated and shown in **Figure 4(f)**. A careful observation made on S-E plots reveals that the butterfly shape for $x = 0.00$ is not symmetric for positive and negative electric field cycle. This type of asymmetric strain behavior is not suitable for AC applications where the electric field cycles get continuously changed and hence will not work properly as desired. Therefore, an effort should be made to tailor the materials composition to get the symmetric butterfly loop with as small as deviation in d_{33}^* values for positive and negative cycles. Interestingly, in the present work, we have observed that, with Sn^{4+} content increases, the asymmetric butterfly observed for $x = 0.00$, tends to transform towards the symmetric butterfly loop for $x = 0.1$ having small deviations in d_{33}^* values for positive and negative cycles.

The average value of d_{33}^* i.e. $(d_{33}^*)_{ave}$, is calculated and plotted as a function of Sn^{4+} content for BCST ceramics as shown in **Figure 4(f)**. It is observed that, as Sn^{4+} content increases the $(d_{33}^*)_{ave}$ value increases linearly from 133 pm/V (for $x = 0.00$) to 199 pm/V (for $x = 0.075$) and thereafter decreases to 185 pm/V (for $x = 0.1$). The observed values of $(d_{33}^*)_{ave}$ are lower compared to the reported values for Sn^{4+} modified $BaTiO_3$-$CaTiO_3$ and $BaTiO_3$ ceramics [10, 16–19, 32–34] but

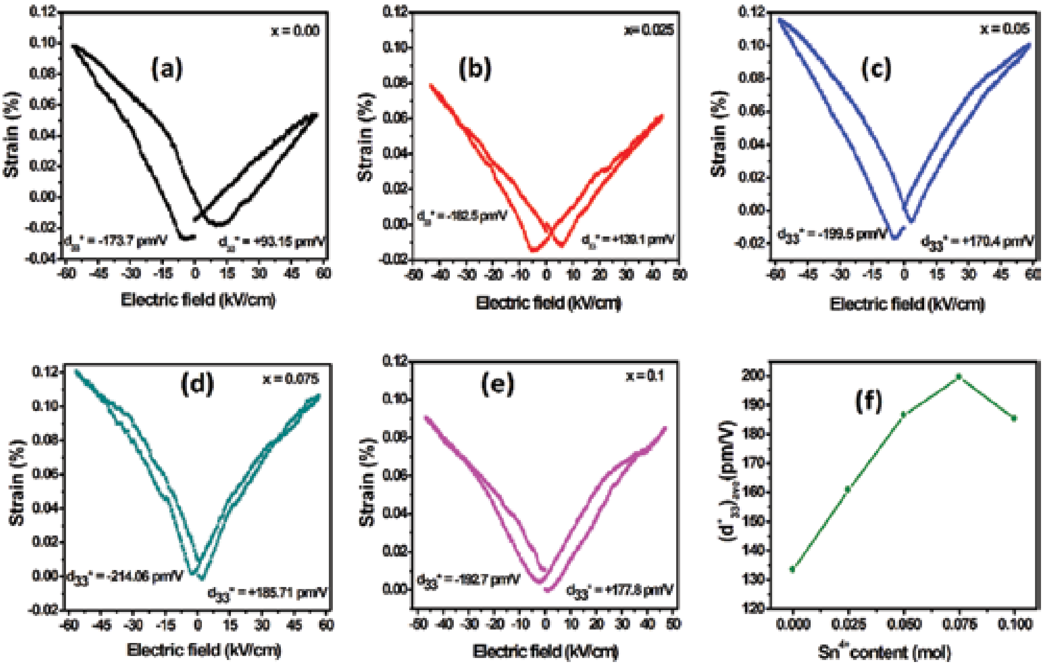

Figure 4. (a-f) (a-e) variation of bipolar electric field induced strain hysteresis loops measured at 0.1 Hz for BCST ceramics (f) variation of effective piezoelectric coefficient$(d^*_{33})ave.$ with respect to Sn^{4+} content in BCST ceramics. (reprinted figure from ref. 26. Copyright (2017) by the American ceramic society.).

it is remarkable to understand the observed symmetric and asymmetric nature of S-E butterfly loop having smaller hysteresis area. Furthermore, it can be seen from **Figure 4(a-e)** that the bipolar strain level increases from 0.097 at −56 kV/cm, 0.052% at +56 kV/cm (for x = 0.00) to 0.12 at −56 kV/cm, 0.105% at +56 kV/cm (for x = 0.075). The observed values of strain 0.115 at 56 kV/cm and 0.1% at 56 kV/cm for x = 0.075 and x = 0.05, respectively, are quite remarkable and comparable to the lead-based piezoelectric materials [35]. Thus, the present BCST ceramics with x = 0.05 and 0.075 possess the reasonably high strain level ~ 0.10 (with sprout shape rather than the usual butterfly loop) and consistently smaller area of hysteresis loop, suitable candidate for piezoelectric Ac devices [36]. The higher value of strain observed for x = 0.075 may be attributed to the ferroelectric orthorhombic-tetragonal phase coexistence at room temperature as evidenced from XRD and dielectric measurements. The strain as well as $(d^*_{33})_{ave}$ values observed to be decreases for x = 0.1 and this may be because at this composition, the system gets transformed from non-centrosymmetric to less symmetric crystal structure i.e. pseudo-cubic structure as confirmed from XRD data. The results of electromechanical investigations for BCST ceramics obtained at an applied electric field up to 50–60 kV/cm at a frequency of 0.1 Hz. The strain curves follow the square of the polarization i.e. $S\text{-}P^2$ as shown in **Figure 5(a-e)**, and the corresponding averaged $(Q_{33})_{ave}$ value was calculated and shown in **Figure 5(f)**. The observed $S\text{-}P^2$ hysteresis loop suggests that the strain and polarization are not in phase. The $(Q_{33})_{ave}$ value of lead-based electrostrictive material, such as $Pb(Mg_{1/3}Nb_{2/3})O_3\text{-}PbTiO_3$(PMN-PT), is reported to be about 0.017 m^4/C^2 [37]. This means that the $(Q_{33})_{ave}$

values of BCST materials are notably larger than that of the lead-based and other known lead-free electrostrictors [38–40]. Thus, the Sn^{4+} modified BCT ceramics with x = 0.05, 0.075 and 0.1 having $(Q_{33})_{ave}$ ~ 0.0469, 0.0667 and 0.0543 m^4/C^2, respectively, exhibiting the non-linear strain-polarization relation, can be registered as a promising candidate for electrostrictive actuator applications.

3.3. Tune the ferroelectric and piezoelectric properties of $BaTiO_3$ by Ca^{2+}, Sn^{4+} and Zr^{4+} substitution

Figure 6(a) shows the XRD patterns of the (1−x) $Ba_{0.95}Ca_{0.05}Ti_{0.92}Sn_{0.08}O_3$ (BCST) – (X) $Ba_{0.95}Ca_{0.05}Ti_{0.92}Zr_{0.08}O_3$ (BCZT) i.e. (1−x) BCST-xBCZT ceramics with x = 0.00, 0.25, 0.50, 0.75, and 1 measured at room temperature. All the ceramics possess the single-phase perovskite structure, and no secondary phases are detected, showing the formation of a stable solid solution between BCST and BCZT. The standard diffraction peaks cited from the tetragonal (T) $BaTiO_3$ (PDF#81-2205), the orthorhombic (O) (PDF#81–2200) and rhombohedral (R) (PDF#85–0368) are indicated by vertical lines for comparison. Sample with x = 0.00, shows the phase coexistence of O and T phases [34]. The diffraction peaks for 0.25 ≤ x ≥ 0.5 well matches with PDF#81–2200, suggesting that the crystalline structure of samples is of orthorhombic symmetry. The composition x = 1 reveals the rhombohedral phase according to PDF#85–0368. The composition x = 0.75 showed the phase coexistence of orthorhombic and rhombohedral lattice

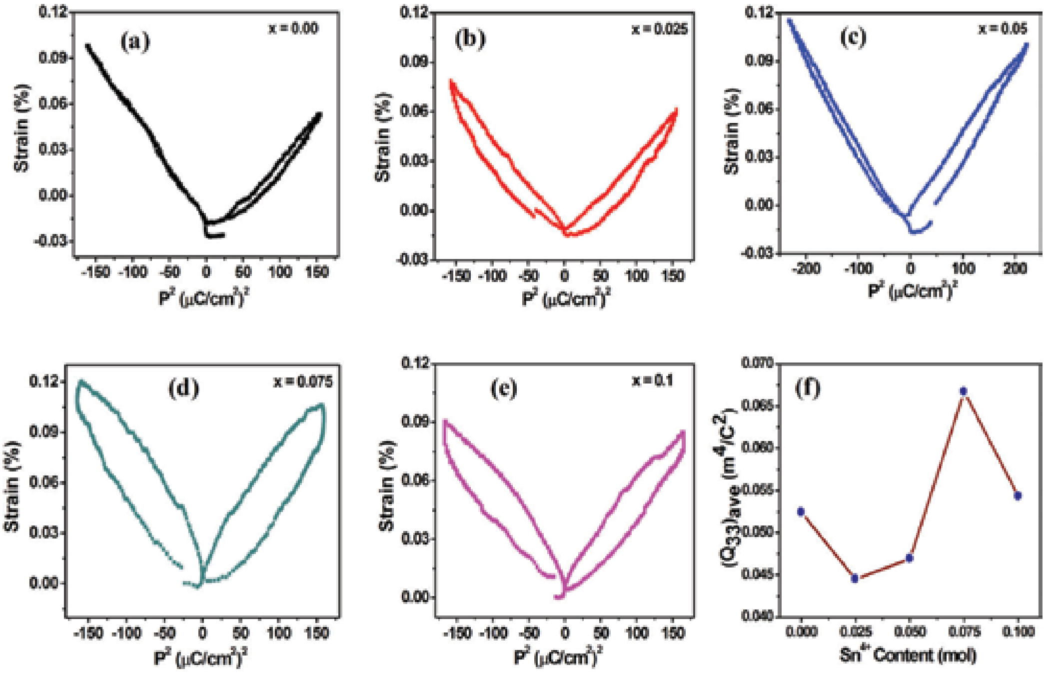

Figure 5. (a-f) (a-e) strain-polarization loops measured at 0.1 Hz for BCST ceramics (f) variation of electrostrictive coefficient$(Q_{33})_{ave}$ with Sn^{4+} content in BCST ceramics. (reprinted figure from ref. 26. Copyright (2017) by the American ceramic society.).

symmetries. The change in diffraction peak around 45° as shown in **Figure 6(b)** the gradual transitions from orthorhombic to mixed phase to rhombohedral symmetry of the unit cell at room temperature, due to the increase of x content that can be favorable to enhance the piezoelectric properties. **Figure 7** shows the temperature dependence of dielectric constant (ε_r) and dielectric loss (*tanδ*) of (1−x) BCST-xBCZT ceramics with different x, which measured at 100 kHz between −100 and 180°C. Effect of change of composition on the ferroelectric phase transitions are observed. As can be seen, (1−x) BCST-xBCZT ceramics exhibits three obvious polymorphic phase transitions corresponding to the rhombohedral to orthorhombic ($T_{R\text{-}O}$), orthorhombic to tetragonal ($T_{O\text{-}T}$) and tetragonal to cubic (T_c) respectively. The Curie temperature (T_c) is about 74°C for x = 0.00 and displays linear increasing trend up to 106°C for x = 1.00 with increasing x. This observation indicates that the Curie temperature is higher for the substitution of Ti^{4+} with Zr^{4+} than the substitution of Ti^{4+} with Sn^{4+}. It is observed that all three transitions $T_{R\text{-}O}$, $T_{O\text{-}T}$ and T_c shift to higher temperature with increase in BCZT content. Interestingly this improves Curie temperature as well as at x = 0.75 the $T_{R\text{-}O}$ observed at room temperature, provides the phase coexistence. The multiphase coexistence boundary, which has hardly any energy barrier for polarization rotation between different ferroelectric phases, is in favor of both polarization rotation and extension contributing to enhancement of piezoelectricity [41]. The observed results are in analogues to the structural analysis of (1−x) BCST-xBCZT ceramics. The dielectric constants are found in the order of 8269–9877 with lower dielectric loss in the range of 0.033–0.046, also the room temperature dielectric constant values are observed in the range of 1300–2700.

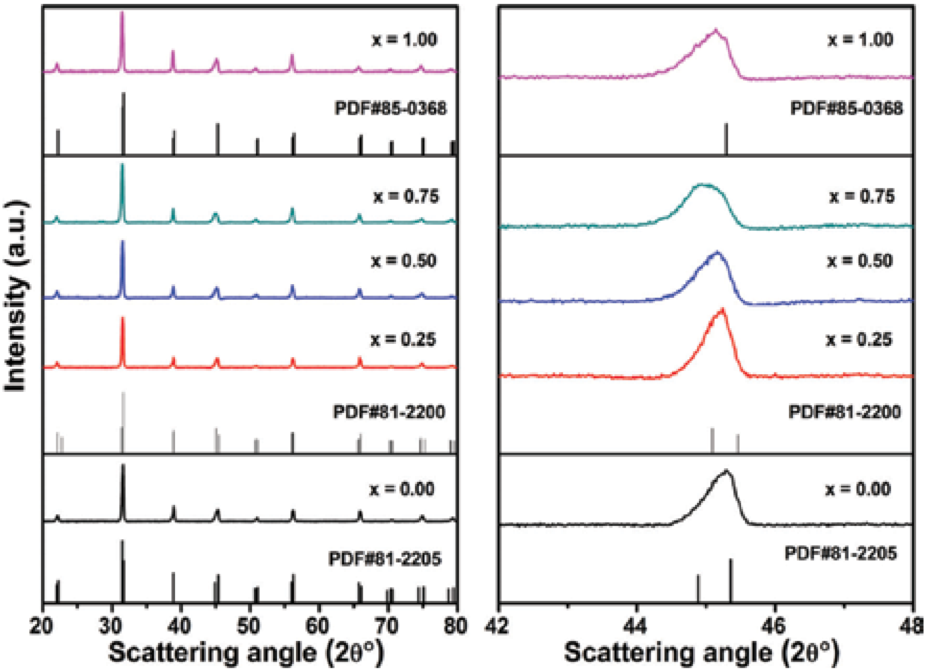

Figure 6. (a-b) (a) combined x- ray diffraction pattern between 2θ = 20 to 80° and (b) enlarged x-ray diffraction pattern between 2θ = 42 to 48°.

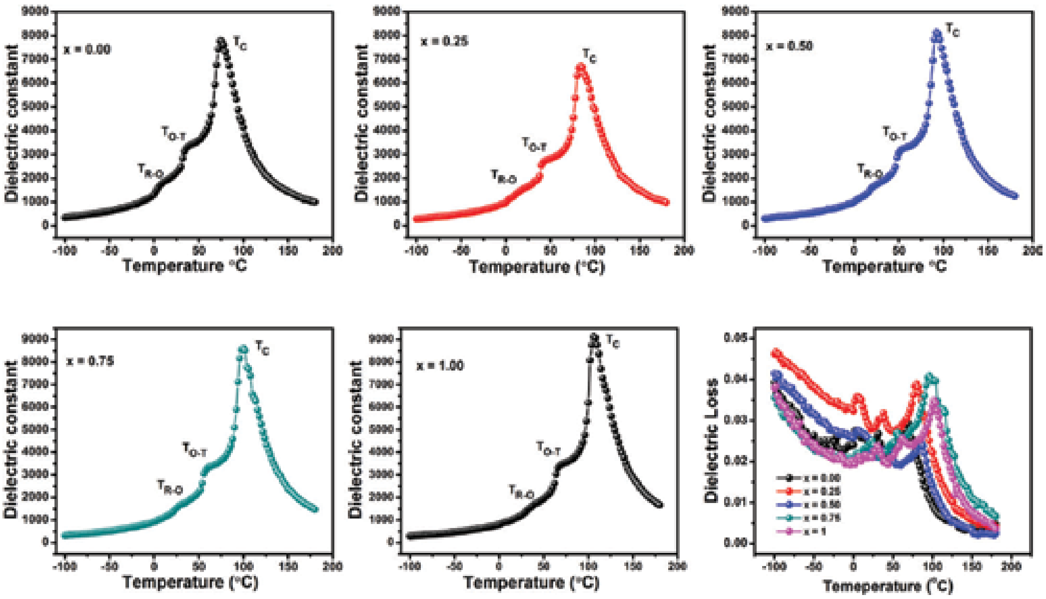

Figure 7. Temperature dependence of dielectric constant (ε_r) and dielectric loss ($tan\delta$) of (1−x) BCST-xBCZT ceramics with x = 0.00, 0.25, 0.50, 0.75, and 1.

The micrograph images for (1−x) BCST-xBCZT system is shown in **Figure 8**, well densified and pore-free microstructure, consisting of irregular grains in which the large one is approximately 35 μm and the small is only about 6 μm with well-defined grain boundaries were observed. Clear grain boundary observed for ceramics samples could enhance the density and helps to improve the electrical properties of the $BaTiO_3$ based ceramics [42, 43]. All the obtained ceramics are well sintered and acquires the relative densities in the range of 93–95% with average grain size 19.4–25 μm. **Figure 9** shows the polarization versus electric field hysteresis loops of (1−x) BCST-xBCZT ceramics with different x content measured with an applied electric field up to 30–40 kV/cm at 0.1 Hz. All samples possess a typical ferroelectric polarization hysteresis loop with remnant polarization (P_r), saturation polarization (P_s) and coercive field (E_c). The ferroelectric properties, i.e. the P_r and the coercive field E_c are observed in the range of 4.7–6.6 μC/cm^2 and 2.6–3.6 kV/cm respectively. Remnant polarization increases with increase in BCZT content. Sample with x = 0.75 shows superior value of remnant polarization 6.3 μC/cm^2 with lower value of Ec = 2.9 kV/cm this can be attributed to the dipole moments of the compositions near the R-O phase coexistence being able to reorient dipoles more completely [34]. The decrease of E_c reveals that, the sample become "softer" with increase of x [10, 44]. The sample of "soft" indicates that the free energy profile for polarization rotation is anisotropically flattened at the two phases and multiphase coexistence [10]. However, Lower value of Ec indicates that the lower energy barriers are needed for polarization rotation. This lower energy barrier can greatly facilitate the polarization rotation and effectively enhance the piezoelectric properties [10, 44]. **Figure 9** shows displacement current density-electric field (J-E) curves measured for (1−x) BCST-xBCZT ceramics with an applied electric field up to 30–40 kV/cm at 0.1 Hz. All samples show sharp-peaking behavior which reveals that

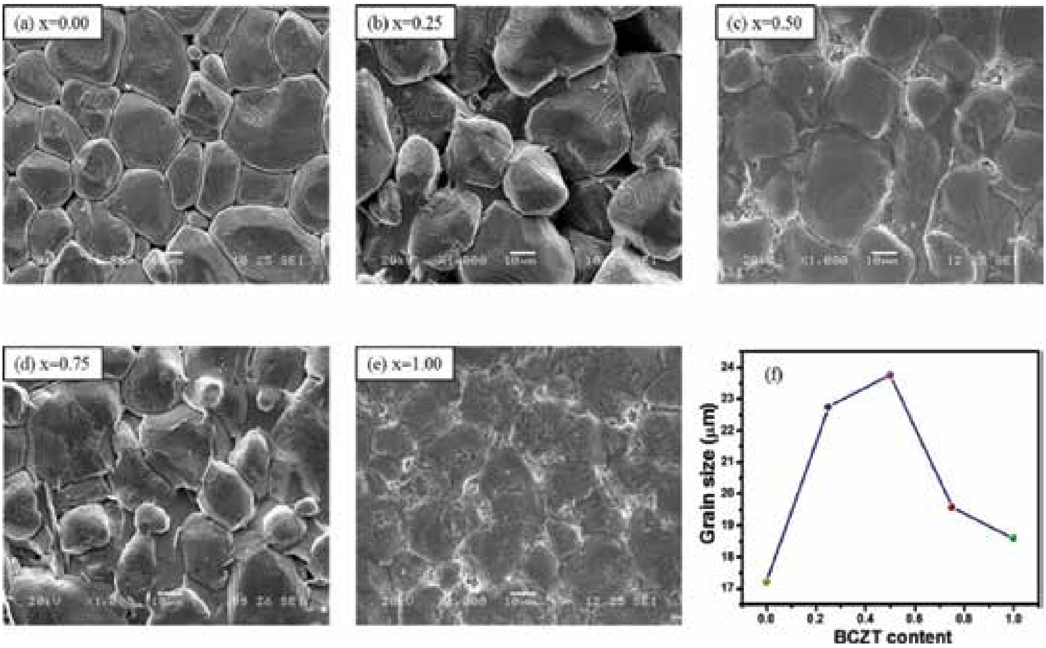

Figure 8. (a-e) SEM micrographs of (1−x)BCST-xBCZT ceramic pellets sintered at 1350°C for 10 h (f) variation of average grain size with respect to BCZT content.

samples are completely saturated with respect to applied electric field [26]. Furthermore, by using remnant polarization and lattice constant values we have estimated the electric dipole moment for (1−x) BCST-xBCZT ceramics and are found to be (0.3045, 0.3500, 0.3505, 0.4090, 0.4132) × 10^{-27} C.cm namely for x = 0.00, 0.25,0.50,0.75 and 1.0 respectively.

Figure 10 shows the bipolar field-induced strain (S-E) curves for (1−x) BCST-xBCZT ceramics measured with an applied electric field up to 30–40 kV/cm at 0.1 Hz. All samples reveal the butterfly shaped S-E loops that are typical feature of ferroelectric materials. A prominent enhancement in the maximum positive strain response from 0.086% at x = 0.00 to 0.122% at x = 0.75 is observed. In ferroelectric, electric field induced butterfly like hysteresis strain loops are occurs fundamentally due to the intrinsic and extrinsic contribution [41]. By modifying the chemical composition of $BaTiO_3$ based masteries one can achieve phase coexistence that facilitated the polarization rotation and enhance the intrinsic contribution (lattice strain) [10, 34, 41]. In ferroelectric materials the domain switching provides the extrinsic contribution, it happens when ferroelectric materials change the spontaneous polarized state along the applied electric field direction. Therefore, the higher strain S = 0.122 observed for x = 0.75 is attributed to the R-O phase coexistence. However, the extrinsic contribution is attributed to the lower value of E_c which supports to easy domain switching and contributes to achieve the superior piezoelectric properties. **Figure 10** shows variation of direct piezoelectric coefficient $(d_{33})_{ave}$ and converse piezoelectric coefficient $(d^{*}_{33})_{ave}$ for (1−x)BCST-xBCZT ceramics as a function of BCZT content. It can be observed that both of d_{33} and d^{*}_{33} curves possess a peak with increasing BCZT content. At x = 0.75, the

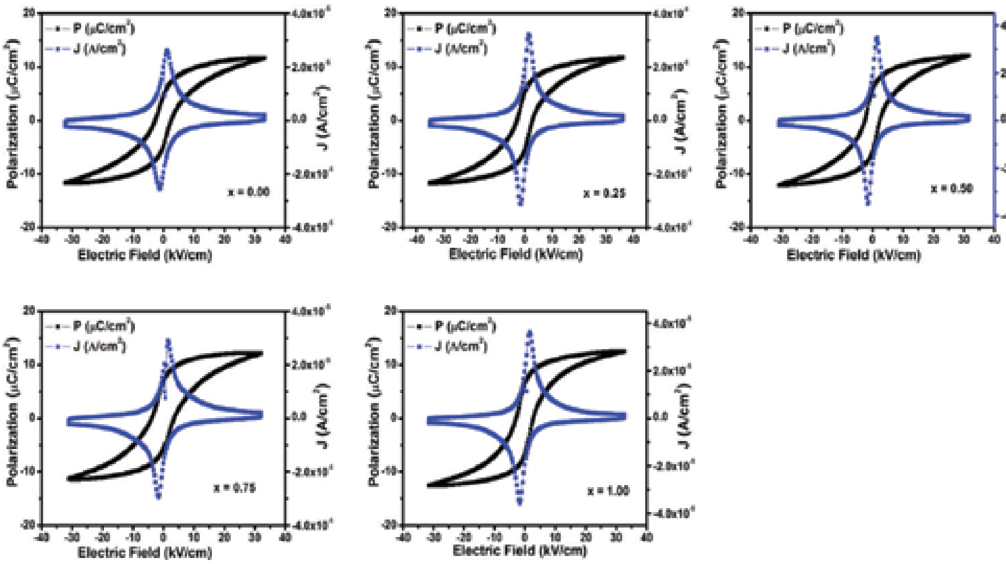

Figure 9. Variation of polarization and displacement current density with applied electric field at 0.1 Hz for (1−x)BCST-xBCZT ceramics.

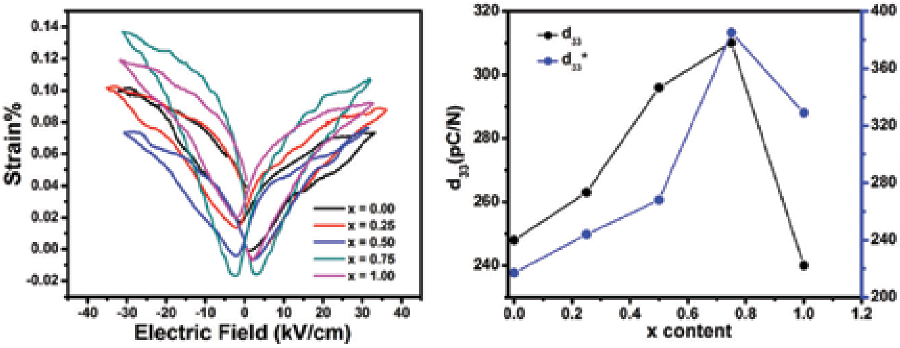

Figure 10. Variation of bipolar electric field induced strain hysteresis loops measured at 0.1 Hz, variation of direct piezoelectric coefficient *(d_{33})ave.* and converse piezoelectric coefficient *(d^*_{33})ave.* for (1−x)BCST-xBCZT ceramics.

higher d_{33} and d^*_{33} of the (1−x) BCST-xBCZT ceramics are 310 pC/N and 385 pm/V respectively with Q_{33} of 0.089 m^4/C^2. It is believed that the observed high piezoelectric properties should be ascribed to the phase coexistence. The O-T phase coexistence causes instability of the polarization state; therefore, the polarization direction can be easily rotated by external stress or electric field, resulting in a high piezoelectricity [10, 34, 41]. Therefore, to achieve high piezoelectric properties for lead free ceramics one has prepare samples having PPT or MPB phase compositions. The 0.25BCST-0.75BCZT ceramic sample shows the superior piezoelectric properties having moderate Curie temperature ~ 100°C can be a potential lead-free piezoelectric material to further study to replace the toxic lead based piezoelectric materials.

4. Future scope and implications

The search of lead-free piezoelectric ceramics has significantly improved over the last two decades. The deep research in ferroelectric materials can develop better ferroelectric and electrostrictive ceramics. It is necessary to develop lead free ceramic materials having morphotropic phase boundary like PZT and improve the temperature dependence of piezoelectric properties of lead free ceramics. Lower Curie temperature of BT based ceramics hinders their use in practical applications. Improvement in this regime is most welcome in the future. The improvement in piezoelectric properties of BT based ceramics has done in last few years which are attractive for various applications; though need to improve other basic properties such as Curie temperature and temperature dependent piezoelectric properties to accelerate the use of BT based materials in piezoelectric applications. It is difficult to replace the PZT by single lead free piezoelectric material. Therefore, need to develop different lead-free materials which can fulfill the different challenges and can useful for various piezoelectric applications. The BT based polycrystalline electroceramics possess inferior properties than BT based single crystal materials. In future this gap can be fulfilled by textured piezoceramics. The textured piezoelectric ceramics have potential to fulfill the gap between polycrystalline and single crystal piezoelectric ceramics. In conventional polycrystalline ceramics grains are randomly oriented while in the textured polycrystalline ceramics grain structure is oriented along one of the crystallographic direction. Due to the orientation of grain structure in specific crystallographic direction, the textured piezoelectric materials give higher performance characteristics close to single crystal materials. Also, as compare to single crystal materials the textured polycrystalline ceramics do not suffer from fracture toughness issues. In future textured BT based piezoelectric materials can become potential materials to replace the lead based piezoelectric materials.

5. Conclusions

We have successfully developed the superior quality high dense microstructure $BaTiO_3$ (BT) electroceramic material with c/a axial ratio of ~1.0144 having an average grain size ~7.8 μm. The BT exhibits the saturation and remnant polarization of $P_{sat.} = 24.13$ μC/cm^2 and $P_r = 10.42$ μC/cm^2 respectively with lower coercive field of $E_c = 2.047$ kV/cm, which is good for ferroelectric memory device applications. The concept of peaking characteristics of the polarization current density-electric field measurement is introduced to evidences the saturation state of polarization for most of the ferroelectric materials. The pure BT ceramics possesses the "sprout" shape nature instead of typical "butterfly loop" for strain-electric field measurements with remnant strain ~ 0.212%, converse piezoelectric constant d^*_{33} ~376.35 pm/V and electrostrictive coefficient Q_{33}~ 0.03493 m^4/C^2. The lead-free $Ba_{0.7}Ca_{0.3}Ti_{1-x}Sn_xO_3$ ($x = 0.00$, 0.025, 0.050, 0.075, and 0.1, abbreviated as BCST) electroceramic system showed the maximum electrostrictive coefficient (Q_{33}) value of 0.0667 m^4/C^2 for $x = 0.075$ and it is higher than some of the significant lead based electrostrictive materials. From BCST system the compositions $x = 0.05$ and 0.075 showed the notable electrostrictive properties that may be useful for piezoelectric Ac device applications. For (1−x) BCST-xBCZT ceramics with x = 0.00, 0.25, 0.50, 0.75, and 1 we are successful to push the polymorphic phase transition temperatures (PPT) close to room temperature by Ca^{2+}, Sn^{4+} and Zr^{4+} substitution for BT system. For BCST-BCZT system the composition x = 0.75 exhibits the d_{33}, d^*_{33} and Q_{33} values of 310 pC/N, 385 pm/V and 0.089 m^4/C^2 respectively which is greater than BT ceramics. Thus, the piezoelectric and ferroelectric properties of BT ceramic can significantly tune by Ca^{2+} and Sn^{4+}, Zr^{4+} substitutions useful for electromechanical device application in future. Still there is a scope for BT based ceramics with Ca^{2+} and Sn^{4+}, Zr^{4+} substitutions to achieve the morphotropic phase boundary composition having giant piezoelectric properties.

Acknowledgements

RCK thankfully acknowledge the Science and Engineering Research Board (SERB)-DST, Government of India (File No. EMR/2016/001750) for providing the research funds under Extra Mural Research Funding (Individual Centric) scheme.

Conflict of interest

The authors declare that they have no conflict of interest.

Author details

Bharat G. Baraskar[1], Pravin S. Kadhane[1], Tulshidas C. Darvade[1], Ajit R. James[2] and
Rahul C. Kambale[1]*

*Address all correspondence to: rckambale@gmail.com

1 Functional Ceramics Laboratory, Department of Physics, Savitribai Phule Pune University, Pune, Maharashtra, India

2 Ceramics and Composites Group, Defense Metallurgical Research Laboratory, (Ministry of Defence), Hyderabad, Telangana, India

References

[1] Rödel J, Webber KG, Dittmer R, Jo W, Kimura M, Damjanovic D. Transferring lead-free piezoelectric ceramics into application. Journal of the European Ceramic Society. 2015;**35**:1659-1681

[2] Mahesh MLV, Bhanu Prasad VV, James AR. Effect of sintering temperature on the microstructure and electrical properties of zirconium doped barium titanate ceramics. Journal of Materials Science: Materials in Electronics. 2013;**24**:4684-4692

[3] Acosta M, Novak N, Rojas V, Patel S, Vaish R, Koruza J, Rossetti GA, Rödel J. BaTiO3-based piezoelectrics: Fundamentals, current status, and perspectives. Applied Physics Reviews. 2017;**4**:041305

[4] Wang JJ, Meng FY, Ma XQ, Xu MX, Chen LQ. Lattice, elastic, polarization, and electrostrictive properties of $BaTiO_3$ from first-principles. Journal of Applied Physics. 2010; **108**:034107

[5] Li YL, Cross LE, Chen LQ. A phenomenological thermodynamic potential for single crystals. Journal of Applied Physics. 2005;**98**:064101

[6] Kalyani AK, Brajesh K, Senyshyn A, et al. Orthorhombic-tetragonal phase coexistence and enhanced piezo-response at room temperature in Zr, Sn, and Hf modified $BaTiO_3$. Applied Physics Letters. 2014;**104**:252906

[7] Liu W, Ren X. Large piezoelectric effect in Pb-free ceramics. Physical Review Letters. 2009;**103**:257602

[8] Deluca M, Stoleriu L, Curecheriu LP, et al. High-field dielectric properties and Raman spectroscopic investigation of the ferroelectric-to-relaxor crossover in $BaSn_xTi_{1-x}O_3$ ceramics. Journal of Applied Physics. 2012;**111**:084102

[9] Zhao L, Zhang BP, Zhou PF, et al. Phase structure and property evaluation of (Ba,Ca)(Ti,Sn)O3 sintered with Li_2CO_3 addition at low temperature. Journal of the American Ceramic Society. 2014;**97**:2164-2169

[10] Zhu LF, Zhang BP, Zhao L, et al. High piezoelectricity of $BaTiO_3$-$CaTiO_3$- $BaSnO_3$ lead-free ceramics. Journal of Materials Chemistry C. 2014;**2**:4764

[11] Mahesh MLV, Bhanu Prasad VV, James AR. Enhanced dielectric and ferroelectric properties of lead-free $Ba(Zr_{0.15}Ti_{0.85})O_3$ ceramics compacted by cold isostatic pressing. Journal of Alloys and Compounds. 2014;**611**:43-49

[12] Shen ZY, Li JF. Enhancement of piezoelectric constant d_{33} in $BaTiO_3$ ceramics due to nano-domain structure. Journal of the Ceramic Society of Japan. 2010;**118**:940-943

[13] Zhu XN, Zhang W, Chen XM. Enhanced dielectric and ferroelectric characteristics in Ca-modified $BaTiO_3$ ceramics. AIP Advances. 2013;**3**. DOI: 082125

[14] Wei XY, Feng YJ, Yao X. Dielectric relaxation behavior in barium stannate titanate ferroelectric ceramics with diffused phase transition. Applied Physics Letters. 2003; **83**:2031-2033

[15] Lu SG, Xu ZK, Chen H. Tunability and relaxor properties of ferroelectric barium stannate titanate ceramics. Applied Physics Letters. 2004;**85**:5319-5321

[16] Singh KC, Nath AK, Thakur OP. Structural, electrical and piezoelectric properties of nanocrystalline tin-substituted barium titanate ceramics. Journal of Alloys and Compounds. 2011;**509**:2597-2601

[17] Cai W, Fan Y, Gao J, et al. Microstructure, dielectric properties and diffuse phase transition of barium stannate titanate ceramics. Journal of Materials Science: Materials in Electronics. 2011;**22**:265-272

[18] Horchidan N, Ianculescu AC, Vasilescu CA, et al. Multiscale study of ferroelectric-relaxor crossover in $BaSn_xTi_{1-x}O_3$ ceramics. Journal of the European Ceramic Society. 2014;**34**:3661-3674

[19] Yasuda N, Ohwa H, Asano SH. Dielectric properties and phase transitions of $Ba(Ti_{1-x}Sn_x)O_3$ solid solution. Japanese Journal of Applied Physics. 1996;**35**:5099

[20] Jonker GH. Philips Technical Review. 1955;**17**:129

[21] Smolenskii GA, Isupov VA. Phase transitions in some solid solutions with ferroelectric properties. Doklady Akademii Nauk SSSR. 1954;**97**:653

[22] Shvartsman VV, Kleemann W, Dec J, et al. Diffuse phase transition in $BaTi_{1-x}Sn_xO_3$ ceramics: An intermediate state between ferroelectric and relaxor behavior. Journal of Applied Physics. 2006;**99**:124111

[23] Baraskar BG, Kakade SG, James AR, Kambale RC, Kolekar YD. Improved ferroelectric, piezoelectric and electrostrictive properties of dense $BaTiO_3$ ceramic. AIP Conference Proceedings. 2016;**1731**:140066

[24] Weaver PM, Cain MG, Stewart M. Temperature dependence of strain-polarization coupling in ferroelectric ceramics. Applied Physics Letters. 2010;**96**:142905

[25] Uchino K, Nomura S, Cross LE, Newnham RE, Jang SJ. Electrostrictive effect in perovskites and its transducer applications. Journal of Materials Science. 1981;**16**:569-578

[26] Baraskar BG, Kambale RC, James AR, Mahesh MLV, Ramana CV, Kokelar YD. Ferroelectric, piezoelectric and electrostrictive properties of Sn^{4+}-modified $Ba_{0.7}Ca_{0.3}TiO_3$ lead-free electroceramics. Journal of the American Ceramic Society. 2017;**100**:5755-5765

[27] Viola G, Saunders T, Wei X, et al. Contribution of piezoelectric effect, electrostriction and ferroelectric/ferroelastic switching to strain-electric field response of dielectrics. Journal of Advanced Dielectrics. 2013;**3**:1350007

[28] Yan H, Inam F, Viola G, et al. The contribution of electrical conductivity, dielectric permittivity and domain switching in ferroelectric hysteresis loops. Journal of Advanced Dielectrics. 2011;**1**:107-118

[29] Kumar A, Prasad VVB, Raju KCJ, et al. Poling electric field dependent domain switching and piezoelectric properties of mechanically activated $(Pb_{0.92}La_{0.08})(Zr_{0.60}Ti_{0.40})O_3$ ceramics. Journal of Materials Science: Materials in Electronics. 2015;**26**:3757-3765

[30] Fan L, Chen J, Li S, et al. Enhanced piezoelectric and ferroelectric properties in the $BaZrO_3$ substituted $BiFeO_3$-$PbTiO_3$. Applied Physics Letters 2013;**102**:022905

[31] Fu D, Itoh M, Koshihara S. Invariant lattice strain and polarization in $BaTiO_3$-$CaTiO_3$ ferroelectric alloys. Journal of Physics. Condensed Matter 2010;**22**:052204

[32] Horchidan N, Ianculescu AC, Curecheriu LP, et al. Preparation and characterization of barium titanate stannate solid solutions. Journal of Alloys and Compounds. 2011; **509**:4731-4737

[33] Xue DZ, Zhou YM, Bao HX, et al. Large piezoelectric effect in Pb-free Ba(Ti,Sn)O_3-x(Ba,ca)TiO_3 ceramics. Applied Physics Letters. 2011;**99**:122901

[34] Zhu LF, Zhang BP, Zhao XK, et al. Enhanced piezoelectric properties of $(Ba_{1-x}Ca_x)(Ti_{0.92}Sn_{0.08})O_3$ lead-free ceramics. Journal of the American Ceramic Society. 2013;**96**:241-245

[35] Lupascu DC. Fatigue in Ferroelectric Ceramics and Related Issues. New York: Springer; 2004

[36] Nath AK, Medhi N. Density variation and piezoelectric properties of $Ba(Ti_{1-x}Sn_x)O_3$ ceramics prepared from nanocrystalline powders. Bulletin of Materials Science. 2012;**35**:847-852

[37] Furuta A, Uchino K. Dynamic observation of crack propagation in piezoelectric multilayer actuators. Journal of the American Ceramic Society. 1993;**76**:1615

[38] Li F, Jin L, Xu Z, et al. Electrostrictive effect in ferroelectrics: An alternative approach to improve piezoelectricity. Applied Physics Reviews. 2014;**1**:011103

[39] Ang C, Yu Z. High, purely electrostrictive strain in lead-free dielectrics. Advanced Materials. 2006;**18**:103

[40] Zhang ST, Kounga AB, Jo W, et al. High-strain lead-free antiferroelectric electrostrictors. Advanced Materials. 2009;**21**:4716

[41] Zhu L-F, Zhang B-P, Zhao X-K, Zhao L, Yao F-Z, Han X, Zhou P-F, Li J-F. Phase transition and high piezoelectricity in (Ba,ca)$(Ti_{1-x}Sn_x)O_3$ lead-free ceramics. Applied Physics Letters. 2013;**103**:072905

[42] Li W, Xu Z, Chu R, Fu P, Zang G. Enhanced ferroelectric properties in $(Ba_{1-x}Ca_x)(Ti_{0.94}Sn_{0.06})O_3$ lead-free ceramics. Journal of European Ceramic Society. 2012;**32**:517-520

[43] Wu J, Xiao D, Wu B, Wu W, Zhu J, Yang Z, Wang J. Sintering temperature-induced electrical properties of $(Ba_{0.90}Ca_{0.10})(Ti_{0.85}Zr_{0.15})O_3$ lead-free ceramics. Materials Research Bulletin. 2012;**47**:1281-1284

[44] Xu C, Yao Z, Lu K, Hao H, Yu Z, Cao M, Liu H. Enhanced piezoelectric properties and thermal stability in tetragonal-structured (Ba,ca)(Zr,Ti)O_3 piezoelectrics substituted with trace amount of Mn. Ceramics International. 2016;**42**:16109-16115

Chapter 8

Preparation and Device Applications of Ferroelectric β-PVDF Films

Liuxia Ruan, Donghai Zhang, Junwei Tong,
Jianli Kang, Yufang Chang, Lianqun Zhou,
Gaowu Qin and Xianmin Zhang

Additional information is available at the end of the chapter

http://dx.doi.org/10.5772/intechopen.77167

Abstract

Organic ferroelectric materials have unique characters comparing to their inorganic counterparts in electronics because they show the advantages such as low cost, lightweight, small thermal budget, flexible and nontoxic characteristics. The ferroelectric poly(vinylidene fluoride) (PVDF) is mostly desired for memory devices due to its polar phase. To obtain the ferroelectric memory devices for data storage, ultrathin PVDF films are required to allow for low operation voltages with both small roughness and free of pin-holes. Micron-meter thick films of ferroelectric phase PVDF can be easily achieved by many preparation methods. But the nanofilms could be mainly fabricated by coating method and Langmuir–Blodgett deposition technique. Meanwhile, according to the structure of devices, four types of organic memory cells using ferroelectric phase PVDF films were introduced, such as memory based on metal/organic semiconductor/metal ferroelectric tunnel junctions, organic capacitors, field effect transistor and organic diodes. The research has been mainly done in Zhang's laboratory from September 2016 to explore the preparation and potential applications of ferroelectric PVDF films. In this chapter, we summarize several device investigations and show the PVDF films have the promising memory applications.

Keywords: PVDF films, memory devices, spin coating, Langmuir–Blodgett method, ferroelectric tunnel junctions, organic capacitors, field effect transistor, organic diodes

1. Introduction

Poly(vinylidene fluoride) (PVDF) exists five crystalline structures, α, ε, β, δ, and γ phases. Both α and ε phases are nonpolarized. The polar β, δ, and γ phases are very interesting in various applications [1, 2]. In particular, the β-phase PVDF (expressed in TTTT conformation) is mostly desired for ferroelectric memories in the data storage fields. The dipole moments in the molecule stem from the strongly electronegative fluorine atoms predominantly, inducing the ferroelectricity of β-phase PVDF [3, 4].

A number of methods have been proposed to prepare the PVDF films with the thickness up to several microns such as electric poling, hygroscopic salts, mechanical stretching, epitaxy with KBr, and solvent evaporation [5–7]. In contrast, the spin coating and Langmuir–Blodgett deposition techniques are two main methods to obtain the ferroelectric β-phase PVDF films with the thickness down to 300 nm or more less [8, 9]. Furthermore, spin coating can be used to fabricate the large area uniform films from the industrial point of view [10]. Langmuir–Blodgett (LB) deposition technique can prepare the ultra-thin PVDF films with the thickness of several nanometers [11]. In this chapter, we firstly report the main results about the fabrications of β-phase PVDF films by spin coating method and Langmuir–Blodgett deposition techniques. Then, the typical applications of β-phase PVDF films in several organic devices are introduced.

2. Preparation

Microelectronic devices using β-phase PVDF film generally require nanoscale thickness and pin hole-free to avoid the electrical shorts [12]. Many works have been done to discuss the preparation and application of PVDF thin films. The purpose of these studies is preparation of smooth thin films or achieving a ferroelectric phase (β, δ, or γ phase) [13–15].

The high coercive field is one drawback for PVDF and its copolymers used in the devices, which determines the minimum electric field that needed to reverse the polarization state. With the coercive fields of 50 MV/m and higher [16], the thickness of β-phase PVDF films must be less than 100 nm to allow for low operation voltage. The early devices based on β phase PVDF [17], required an operation voltage up to 200 V, while the more recent reports still need 30 V or more to operate [18–20]. The ultrathin films of P(VDF-TrFE) obtained by Langmuir–Blodgett deposition on silicon wafers has produced one nanometer ferroelectric films [21] and operation voltage less than 10 V for nonvolatile memory devices [22]. The β-phase PVDF nanofilms are mainly prepared by spin coating and LB deposition.

2.1. Spin coating

Spin coating is a desirable method to achieve the large area uniform nanofilms. However, the surface of traditional spin coating PVDF film is too rough for the application in microelectronics. The acquisition homogeneous and smooth PVDF nanofilms with small roughness is a major breakthrough for spin coating and electron device [10, 23, 24]. Smooth PVDF films have been obtained by humidity-controlled spin coating, dimethyl formamide (DMF), N-methylpyrrolidone (NMP), dimethyl sulfoxide (DMSO), or dimethylacetamide (DMAc) used as polar solvents to dissolve PVDF [10, 12, 23]. The micrographs were obtained using the JEOL JSM-IT100 of thin films SEM were under different relative humidity by spin coating were evaluated, as shown in **Figure 1** [25].

The percentage of β-phase PVDF (β%) in films fabricated by spin coating method is mainly studied by Fourier transform infrared (FTIR) (BRUKER) spectroscopy and X-ray diffraction (XRD) (RIGAKU) techniques. It is found that the processing conditions such as solution concentration, spin rotation speed (rpm) and annealing temperature obviously affect the percentage of β-phase PVDF [26]. The value of β% was calculated and the different percentages for the corresponding films at different annealing temperatures were plotted in **Figure 2**.

Meanwhile, Cardoso et al. successfully prepare thin PVDF films with high β-phase content by thermally annealing at 70°C [27]. A 160 nm thick PVDF film mainly consists of the ferroelectric β phase was prepared by rapid thermal annealing and humidity controlled spin coating method [10]. Ramasundaram et al. reported the fabrication of PVDF films dominantly with β phase using a heat-controlled setup of spin coating [9].

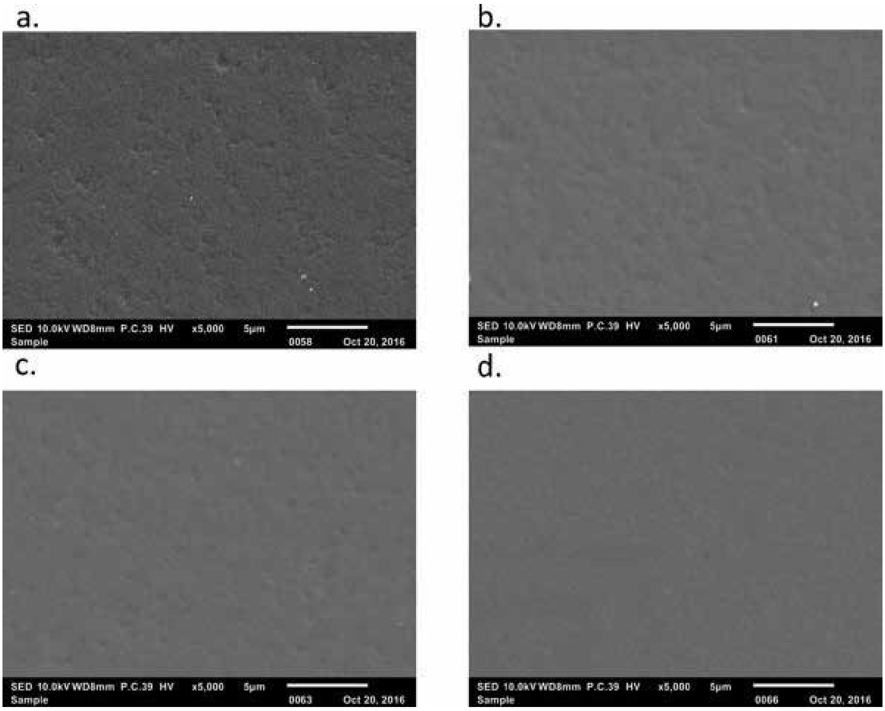

Figure 1. Scanning electron microscopy (SEM) micrographs of PVDF films prepared by spin coating with the relative humidity at (a) 20%, (b) 40%, (c) 60%, and (d) 80% [25]. This research was conducted at Center of High Technology Materials New Mexico in 2017.

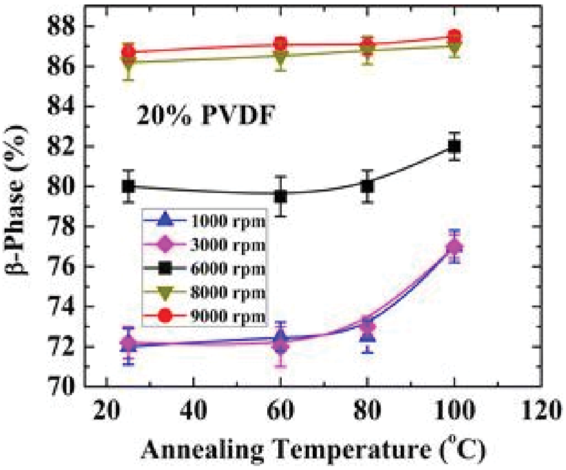

Figure 2. β-phase dependence of 20% PVDF films on annealing temperatures [26]. This research was conducted at Center of High Technology Materials New Mexico in 2017.

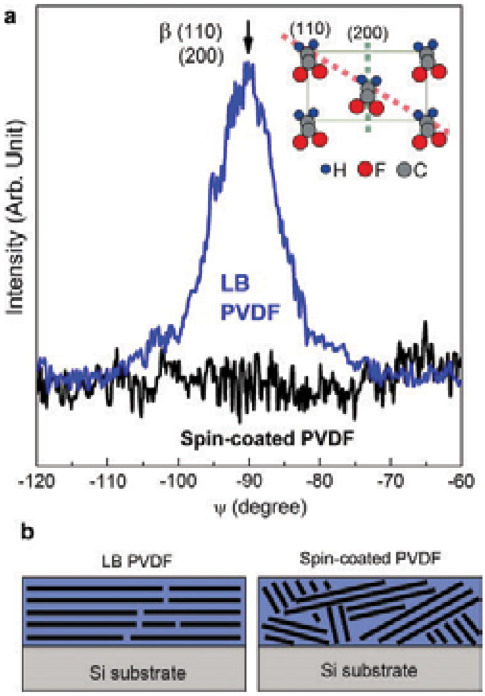

Figure 3. (a) The ψ dependence of the XRD peak β (110) (200) of the PVDF LB film and a spin-coated PVDF film. (b) Cross-sectional view to compare the molecular chain orientation of the LB PVDF film and spin-coated PVDF film. The black bars are used to denote the PVDF molecular chains [8]. This research was conducted at Agency for Science, Technology and Research of Singapore in 2012.

2.2. Langmuir-Blodgett method

As an effective technique, LB deposition was usually used to fabricate nanoscale films, in which the interaction of water with PVDF molecules is involved [8, 28]. This could deposit PVDF films at room temperature on any substrate material because the films were grown layer-by-layer [29].

The orientation of dipoles of the PVDF LB film was analyzed by the XRD peak intensity (β (200) (110)) compared with a spin-coated PVDF film using an XRD system (D8-ADVANCE, Bruker AXS GmbH, Karlsruhe, Germany) as shown in **Figure 3a**. It was found that LB deposition process can directly format β crystalline phase of PVDF, with the molecular chains parallel and the dipoles aligned perpendicular to the substrate. The results of ψ-scan XRD indicated that the molecular chains in the LB films were parallel with the substrates, but chains in the spin-coated film are randomly oriented, as schematically illustrated in **Figure 3b** [8].

Zhu et al. reported that the 5–35 layers PVDF nanofilms could be prepared by the LB method at 20°C [30]. The dependence of root-mean square (RMS) surface roughness on the thickness of PVDF nanofilms is shown in **Figure 4**. The high surface roughness of 35 and 81 nm thick films is expected to be related to a sudden decrease of polarization. A Pr of 6.6 μC cm^{-2} was acquired for 81 nm thick PVDF homopolymer film with no post-treatment. They also firstly achieved the ferroelectricity in a 12 nm thick PVDF film, indicating a potential low-voltage application of PVDF nanofilms [11]. The thickness of each PVDF layer could be thin as 2 nm. Therefore, an ultra-thin PVDF film can be expected through layer-by-layer growth using LB method. Recently, the β-phase PVDF films was reported with the thickness around five nanometers [31].

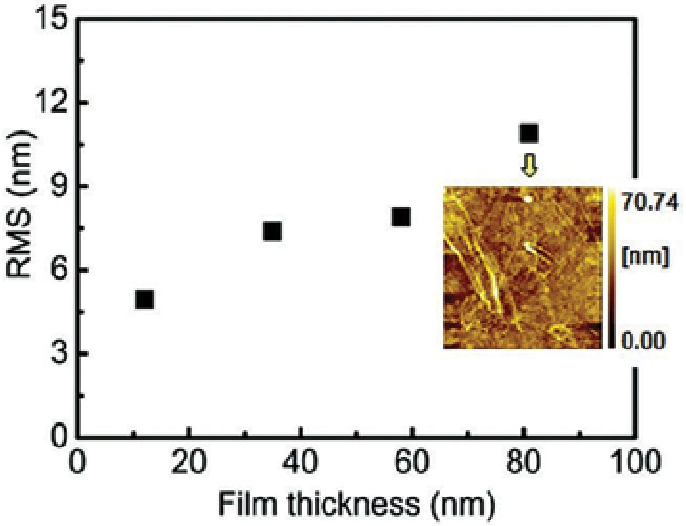

Figure 4. The dependence of root-mean square (RMS) surface roughness on different thickness of PVDF LB nanofilms. The inset is an atomic force micropy image of PVDF film at 81 nm thickness [11]. This research was conducted at Tohoku University of Japan in 2014.

3. Application in organic memory devices

In modern society, more and more electronic products are studied in both inorganic and organic electronics. Organic memory cells develop at a slow pace, but researches of organic memory devices based on PVDF and its copolymers will become extremely important to develop the future organic electronic products. In the case of copolymers including poly(vinylidene fluoride-trifluoroethylene) (P(VDF-TrFE)), the addition of one more fluorine atom provides the delicate configuration balance and always results in the polar ferroelectric β structure [32]. However, PVDF possesses higher ferroelectric transition temperature and thermal stability of remnant polarization in comparison with its copolymers [33, 34]. PVDF has a high Curie temperature of 167°C compared to the P(VDF-TrFE) copolymers with Curie temperatures from 60 to 100°C related with the TrFE content [10]. The higher Curie temperature of PVDF as a ferroelectric layer potentially allows the higher temperature operation of polymer memory than that of its copolymers. In addition, the copolymers are unlikely suitable for mass production because their synthesis is extremely complicated and thus ineffective cost [35].

In the following report, four types of PVDF memory cells will be introduced according to the structure of memory devices. They are ferroelectric tunnel junctions, organic capacitors, field effect transistor and organic diodes [36, 37].

3.1. Ferroelectric tunnel junctions

The idea of ferroelectric tunnel junctions (FTJs) was derived from the observation of spin-dependent tunneling phenomenon. FTJ is a device with two ferromagnetic metal layers separated by insulating barrier [38]. Perovskite-type ABO_3 metal oxides (e.g., $BaTiO_3$ or $KNbO_3$) are widely known as ferroelectric materials for their excellent piezoelectric response and strong polarization [39, 40]. However, their applications are limited by brittleness, heavy weight, high cost, and large thermal budget [41]. The electric polarization of ferroelectric PVDF is comparable to that of perovskite oxides. The use of organic ferroelectrics PVDF could solve the problem of thermal budget because PVDF can be processed at 200°C or lower temperature [19]. Furthermore, PVDF films are very appealing due to their flexible, light weight, low cost, and nontoxic characteristics [41–43]. PVDF thin films are very promising and used as barriers in FTJs for these properties [44]. Ferroelectric tunnel barriers allow switching of the tunneling conductance between two stable states because their spontaneous polarization can be reversed under a bias voltage. This phenomenon is known as tunneling electro resistance (TER). In the past years, extensive studies in theory have confirmed the possibility to fabricate PVDF FTJs [45–55]. By contrast, the progress in experimental investigations is not so good owing to the challenges in the fabrication of PVDF ultra-thin films with high purity of ferroelectric active phase.

On the basis of first principles calculations, simultaneous TER and TMR effects and multiple resistance states were demonstrated [51, 56, 57]. The TMR is defined as:

$$\mathrm{TMR} = \frac{G_P - G_{AP}}{G_P + G_{AP}} \times 100\% \qquad (1)$$

where $G_P = G_{\uparrow\uparrow} + G_{\downarrow\downarrow}$ and $G_{AP} = G_{\uparrow\downarrow} + G_{\downarrow\uparrow}$ are the junction conductance, when the magnetizations of two electrodes are parallel and antiparallel, respectively.

The TER is defined as:

$$\mathrm{TER} = \frac{G_{\leftarrow} - G_{\rightarrow}}{G_{\leftarrow} + G_{\rightarrow}} \times 100\% \tag{2}$$

where $G_{\leftarrow}$ is the conductance for the PVDF polarization pointing to the left, and $G_{\rightarrow}$ the conductance for the PVDF polarization pointing to the right, and horizontal arrows indicate the polarization direction. The conductance of the Co/PVDF/O/Co(0001) MFTJ was calculated by Velev et al. using the first principles electronic structure [51]. The results are shown in **Table 1**, where also the conductance of Co/PVDF/Co MFTJ with clean interfaces is given for comparison.

3.1.1. *Au/PVDF/W tunnel junctions*

Tian et al. report a robust room temperature TER of ~300% and ~1000% in organic FTJs using ultrathin PVDF films (1 and 2 layers (Ls) with the thickness of 2.2 and 4.4 nm, respectively) [58]. Three-dimensional sketch of the PVDF FTJs is shown in **Figure 5a**, and the junction sizes are defined by the bottom electrode isolated by a SiO_2 matrix. The deposition of PVDF ultra-thin films were performed prior to the deposition of micron-size Au as top electrodes. The typical I–V characteristics of the PVDF FTJs are shown in **Figure 5b**. A Keithley 6430 sub-femtoampere source meter with a remote preamplifier was used to perform the I–V measurements [58].

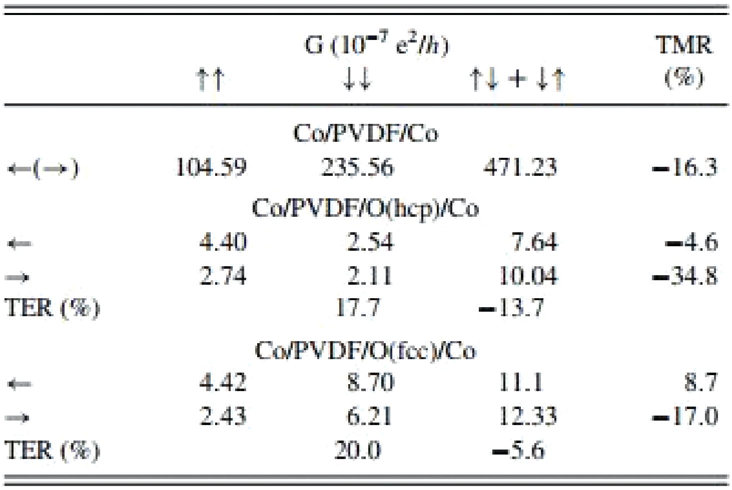

	G (10^{-7} e^2/h)			TMR
	↑↑	↓↓	↑↓ + ↓↑	(%)
		Co/PVDF/Co		
←(→)	104.59	235.56	471.23	−16.3
		Co/PVDF/O(hcp)/Co		
←	4.40	2.54	7.64	−4.6
→	2.74	2.11	10.04	−34.8
TER (%)		17.7	−13.7	
		Co/PVDF/O(fcc)/Co		
←	4.42	8.70	11.1	8.7
→	2.43	6.21	12.33	−17.0
TER (%)		20.0	−5.6	

Table 1. Conductance per unit cell area, TER, and TMR for Co/PVDF/O/Co tunneling junction. ↑↑ and ↓↓ are used to represent the conductance for parallel magnetization of the electrodes. ↑↓ + ↓↑ is the total conductance for the antiparallel magnetization. ← and → are the left and right polarization orientation of PVDF, respectively [51]. This research was conducted at University of Puerto Rico of USA in 2012.

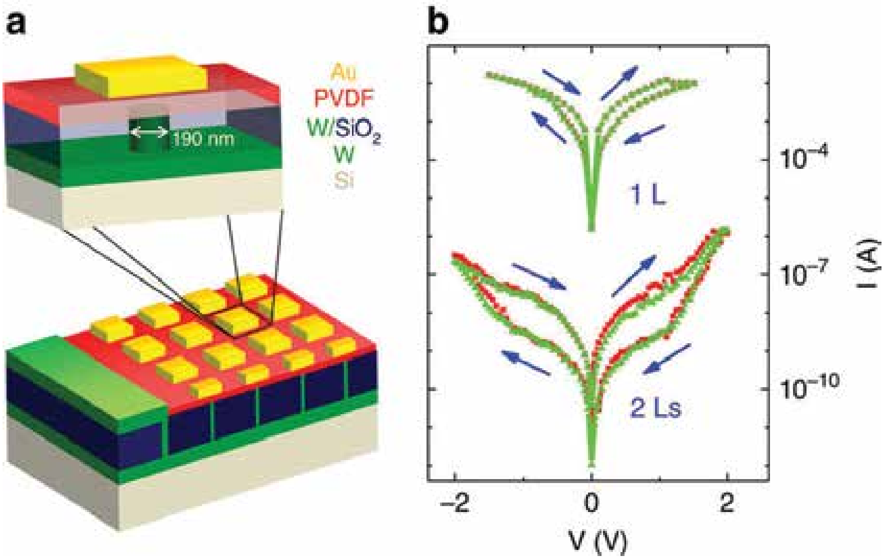

Figure 5. TER in submicron Au/PVDF/W tunnel junctions. (a) Three-dimensional sketch of PVDF FTJs. (b) I–V curves in the 1 L and 2Ls PVDF FTJs. The arrows show the direction of the voltage sweeps [58]. This research was conducted at Chinese Academy of Sciences in 2016.

The transport mechanisms and electro resistive effects in the FTJs with a 5 nm thick barrier can be divided into Fowler-Nordheim tunneling, direct tunneling, and thermionic injection currents [59]. The larger TER response for thicker barriers agrees with electrostatics models based on a direct tunneling process [60, 61]. The devices show a room temperature TER effect as high as 1000%, which will open a new route for low cost, silicon-compatible, or potentially rollable organic devices.

3.1.2. $La_{0.6}Sr_{0.4}MnO_3$/PVDF/Co structures

The observation of a large 300% TMR in $La_{0.7}Sr_{0.3}MnO_3/Alq_3$/Co tunnel junctions is a particularly interesting result, where the interfaces of ferromagnetic metal/organic hybrid play a key role for spin injection in spintronics [62]. Liang et al. fabricated $La_{0.6}Sr_{0.4}MnO_3$(LSMO)/PVDF/Co FTJ organic structures with PVDF as a tunneling barrier to study the ferroelectric control of the spin-polarization of the spacer interfaces [57]. **Figure 6a** shows the device structure. The surface morphology of PVDF barrier investigated by AFM (Asylum Research, MFP-3D, USA) in **Figure 6b** reveals a smooth surface with 3.12 nm RMS roughness in the range of 1 × 1 μm^2. Amplitude hysteresis loops and representative local piezoresponse force microscopy (PFM) phase are shown in **Figure 6c**. **Figure 6d** shows the PFM phase image recorded on the PVDF surface.

It has been demonstrated that tuning the ferroelectric polarization of PVDF can control the spin-polarization of the PVDF/Co spinterface actively at low temperatures. Two polarization states are possibly related to either F-C-H/Co or H-C-F/Co interface (see the inset of **Figure 6e**). **Figure 6e** shows the magneto-response of the LSMO/PVDF/Co device for two different

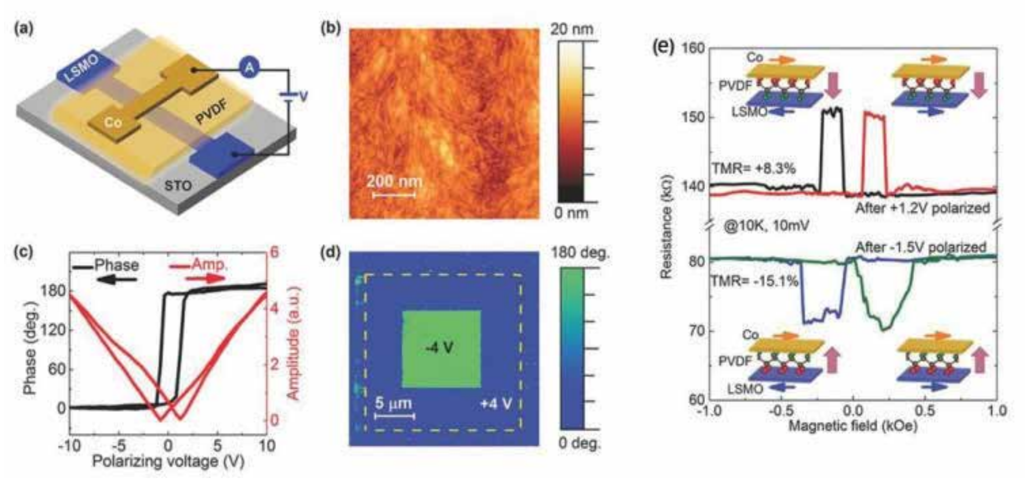

Figure 6. Morphology and characterization of LSMO/PVDF/Co. (a) Schematics of the LSMO/PVDF/Co device. (b) AFM topography of the PVDF barrier surface. (c) Amplitude hysteresis loops and representative local PFM phase measured on the PVDF surface. (d) PFM phase image recorded on the PVDF surface. (e) Tunneling magneto-resistance of the device measured after +1.2 V and − 1.5 V polarized. The insert graphs denote four different resistance states associated with the orientations of magnetization and polarization [57]. This research was conducted at CNRS-Université de Lorraine of France in 2016.

ferroelectric polarizations under 10 mV at 10 K. The positive TMR will vanish with increasing temperature up to 120 K. The negative TMR effect can survive over 250 K.

Ferroelectric PVDF was also introduced to control the magneto transport and the spin transport through the spinterface of ferromagnet/organic is studied. A LSMO/PVDF/MgO (0.5 nm)/Co device shows a much higher junction resistance in comparison with the devices without MgO layer indicating the insertion of MgO likely suppresses the diffusion of Co top layer. There is no coupling for PVDF/Co spinterface with MgO insertion layer, and the MgO/Co interface totally modifies the spin polarization [57]. The TMR sign with the MgO insertion layer is consistent with the reports of Co/MgO/Co magnetic tunnel junctions [63].

3.1.3. *Fe_3O_4/AlO/PVDF/Co/Al stacking structure*

Fe_3O_4 is one potential electrode because of its high spin polarization efficiency (100%) and high Curie temperature (~850 K) in theory [64, 65]. The PVDF spin devices with Fe_3O_4/AlO/PVDF/Co/Al stacking structure shown in **Figure 7a** was successfully fabricated very recently [31]. The magnetoresistance (MR) ratio at room temperature can achieve approximately 2.6% for the FTJs with 3-layer PVDF barrier (~7 nm thick). In **Figure 7b**, it is noted that the MR ratios increase with reducing measurement temperature. This is attributed to the reduction in spin scattering. The standard four-probe method is used to measure MR curves. The I–V curves were measured by A nanovoltmeter (model 2182A, Keithley Inst. Inc.) and an AC and DC current source (model 6221, Keithley Inst. Inc.). In addition, the MR response decreases with increasing PVDF layer numbers likely owing to the change of spin transport mechanism

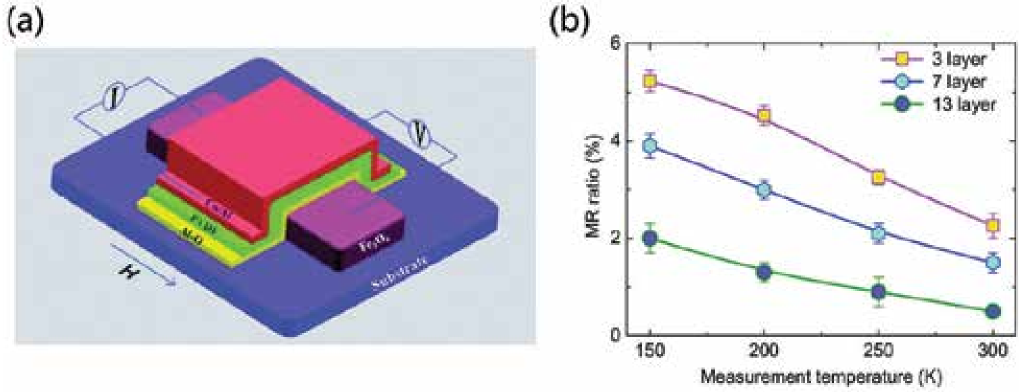

Figure 7. (a) Diagrammatic sketch of the Fe_3O_4/AlO/PVDF/Co/Al FTJs structure. The magnetic field along the long direction of the Fe_3O_4 strip was applied to measurement the magnetoresistance. (b) Magnetoresistance ratio dependence on different measurement temperature and various layer PVDF for spin valves [31]. This research was conducted at Northeastern University of China in 2017.

from tunneling to hopping transport. This study is valuable to realize the design of flexible spin devices using PVDF barriers operated at room temperature.

3.2. Field effect transistor

Recently, ferroelectric field effect transistor (FeFET) device architectures have been formed by using ferroelectric thin films as gate insulators because of the various advantages such as easily integrated structure, small cell sizes, low operating voltages, and nondestructive readout capability [14, 36]. The high ON/OFF ratio at zero gate voltage must be ensured to distinguish the different data recognition for nonvolatile ferroelectric memory. In generally, both ON and OFF source–drain current are strongly dependent on the charge density of semi-conducting layer, and the operating voltage of FeFET depends on the thickness and dielectric constant of the gate dielectric [66].

The composition of organic transistor has three main components: three electrodes including source, drain and gate; an active semiconductor layer; and a dielectric layer [37]. A FeFET was successfully fabricated utilizing 100 nm thick PVDF/PMMA (80:20) films as a gate insulator [14]. The capacitor with a 160 nm thick β-phase PVDF film exhibited the fairly large remanent polarization (Pr) of 7 $\mu C\ cm^{-2}$ with the coercive voltage (V_c) of 8 V corresponding to coercive electric field (Ec) of ~50MV/m (as shown in **Figure 8a**). A typical ferroelectric hysteresis with the drain current bistability at zero gate bias was shown in **Figure 8b** for a FeFET with the PVDF as gate dielectric and Agilient technologies E5270B parameter analyzer was used to characterize this transistor in a dark environment [10].

The Au/PVDF/SiO_2/p-Si stack is successfully prepared by Gerber et al., and the various dimension Au gate electrodes were deposited by vacuum evaporation. The inset diagram denotes the cross-section of the device in **Figure 9**. The FeFET exhibited excellent current-voltage characteristics for the various gate voltage V_g from 0 to +3.5 V [67]. The FeFET measurements were accomplished using a semiconductor parameter analyzer in a shielded metal box at room temperature.

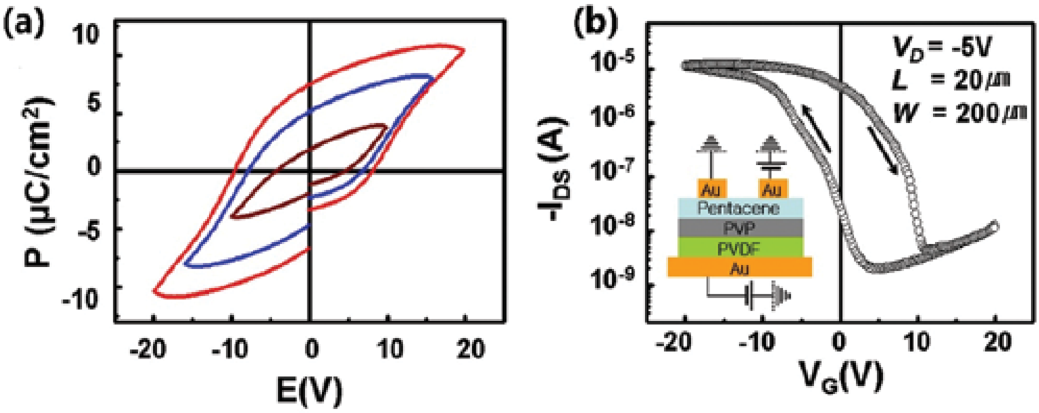

Figure 8. (a) Polarization vs. applied voltage (P-V) hysteresis loops of a PVDF film with thickness of 160 nm. (b) I_D–V_G transfer curve of organic thin film transistors (OTFTs) with PVDF–PVP as the bilayer gate dielectric. The hysteresis direction is denoted by arrows. The inset is the diagrammatic sketch of FeFET device structure [10]. This research was conducted at Yonsei University of Korea in 2008.

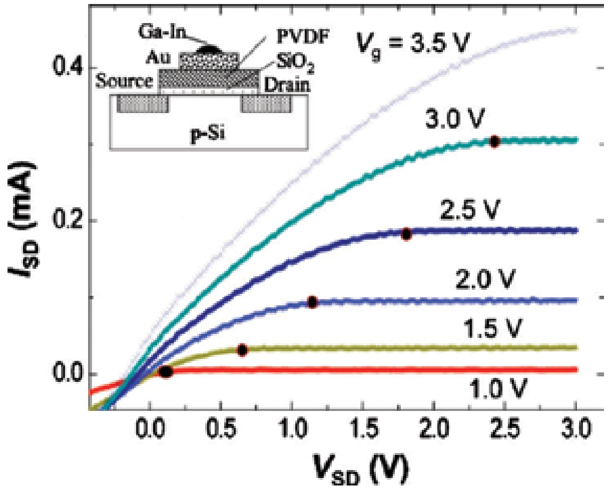

Figure 9. Source–drain current ISD curves depend on the gate voltage values for an Au/PVDF/SiO_2/p-Si FeFET. Inset: The cross-section of FeFET device [67]. This research was conducted at Research Center Jülich of Germany in 2010.

The high performance TFT device with a PVDF/GOnP nanocomposite as insulator has been found to have an ON/OFF current ratio of 10^5, and a field effect mobility of 1.1 $cm^2 V^{-1}$ s, which can make the OTFTs operated successfully at voltages below 2 V [68].

3.3. Organic capacitors

The metal/ferroelectric polymer/metal (MFM) capacitor is a basic ferroelectric polarization storage component in memory storage devices, in which a ferroelectric polymer film is sandwiched between metal electrodes. Organic ferroelectric material PVDF has attracted much interest recently for its applications in low operating voltage, nonvolatile memory storage devices. Many researches are focused on MFM capacitors [69].

The structure of ferroelectric device has been shown in **Figure 10a**, in which a PEDOT:PSS layer as a hole-only (electron blocking) transport layer is inserted between the Al top electrode and the PVDF LB nanofilm. The chemical structure of PEDOT:PSS is shown in **Figure 10b**. Ferroelectricity was characterized at different voltage amplitudes (**Figure 5c**), which shows asymmetric displacement-electric field hysteresis loops. The hysteresis loops were characterized by a traditional Sawyer–Tower method. The Pr values depend on the electric field (**Figure 10d**) [70]. The Pr values increase with the increasing electric field, which is accordance with reference report [13]. The dipole moments of PVDF in the films are slightly oriented at a low electric field, and the dipole moments are highly oriented at a high electric field, thereby leading to the increase of Pr.

The asymmetric hysteresis loops for the capacitor with the PEDOT:PSS layer are different from that of the Al/PVDF LB nanofilms/Al device, which shows symmetric hysteresis loops [11]. Memory devices utilize the hysteresis by associating the positive remanent polarization (+Pr) and negative remanent polarization (−Pr) with a Boolean 1 and 0 [4]. Asadi et al. reported a diode with a Ag/PVDF:P3HT/LiF/Au capacitor, which possesses asymmetric hole accumulation properties under positive or negative polarization [22].

The low-density storage capability and slow switching speed are the major problems for most organic memory devices [71–73]. The performance of these devices can be greatly enhanced by several methods such as forming hybrid organic structures, [74] organic/inorganic

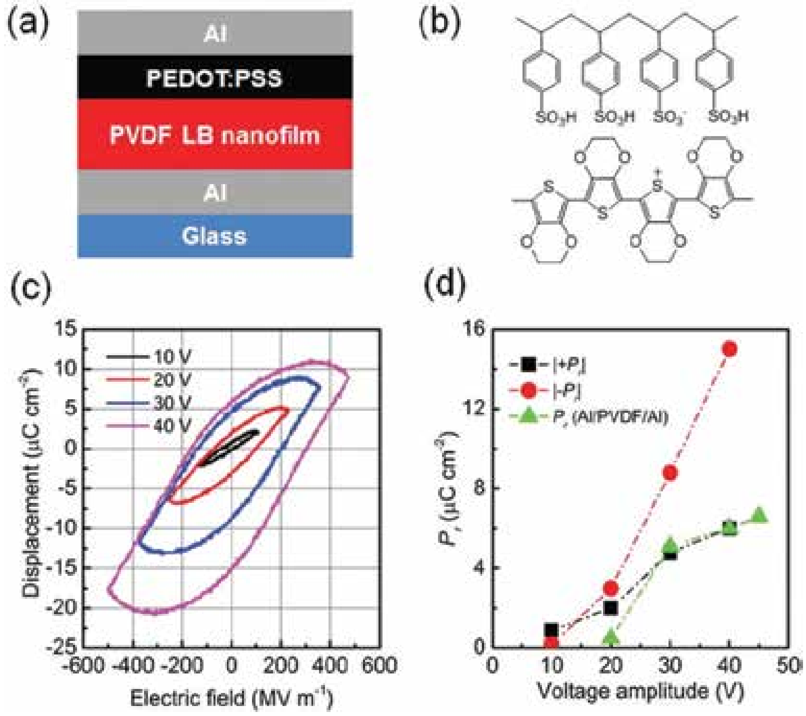

Figure 10. (a) Layer structure of the PEDOT:PSS ferroelectric device, (b) The chemical structure of PEDOT:PSS, (c) The hysteresis loops of the device at different applied voltage amplitudes, and (d) Pr values dependence of the electric field [70]. This research was conducted at Tohoku University of Japan in 2015.

composites, [75] or by dispersing nanomaterials [76]. The simple metal-insulator-metal (MIM) structure is shown in **Figure 11a**, in which the insulator part composed of graphene nano flakes (GR) embedded in PVDF layer was sandwiched between Platinum (Pt) top electrode and ITO bottom electrode. The nonvolatile resistive memory switching was investigated using this structure. The I–V characteristic curves under various compliance current of 1, 10 and 100 μA are shown in **Figure 11b**. The I–V curves were measured by a Keithley 2401 in top–bottom configuration.

The I–V characteristics of the Hg/PVDF/Au device were obtained by DC voltage sweep program (**Figure 12a**). The quick transition from high resistance state to low resistance state was realized at the set voltage. The resistance versus voltage (R-V) curves are shown in **Figure 12b**. A maximum resistance ratio of 25 may be practical for application in nonvolatile memory devices [34]. Several phenomena in capacitor structures exist in the literature used to explain the bistability using the filamentary conduction along with Schottky emission, trap charging and discharging, space charge limited current and Poole-Frenkel emission [78]. The I–V cycles were performed using a Keithley 238 SMU unit.

3.4. Organic diodes

The device structure of FeFETs would complicate the construction of a larger integrated memory technology. In addition, ferroelectric capacitors with relatively simple device structure have a limited scaling capability. Ferroelectric diodes can combine the advantages of FeFETs and capacitors. Therefore, there is an ongoing research activity in a diode structure to realize the resistive switching [4].

The semilogarithmic forward and reverse I–V characteristics of the Au/n-InP and Au/PVDF/n-InP Schottky diodes are shown in **Figure 13**. The I–V was measured using a Keithley source measuring unit 2400. The reverse leakage current of the Au/n-InP diode (6.809×10^{-5} A at −1 V)

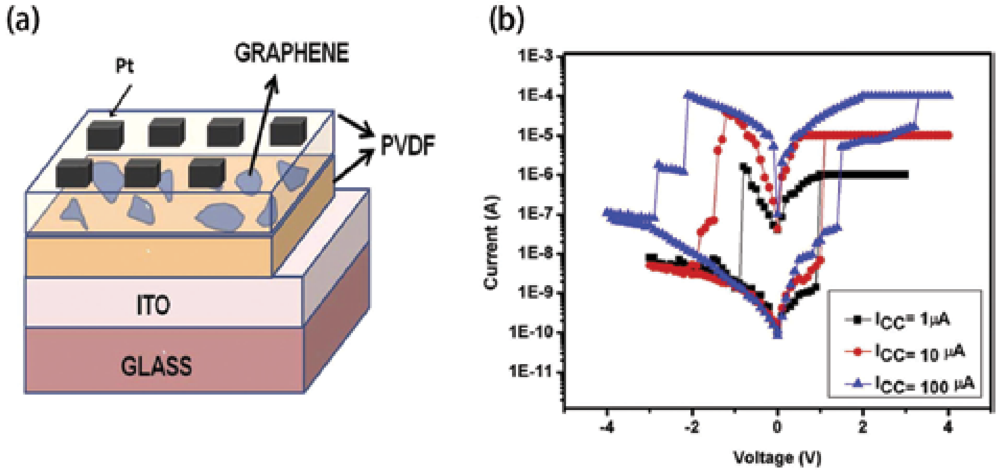

Figure 11. (a) Schematic diagram of the Pt/PVDF/GR/PVDF/ITO memory device fabricated layer by layer. (b) Typical I–V characteristic curves of the device under different compliance currents varying from 1 to 100 μA [77]. This research was conducted at University of Puerto Rico of USA in 2014.

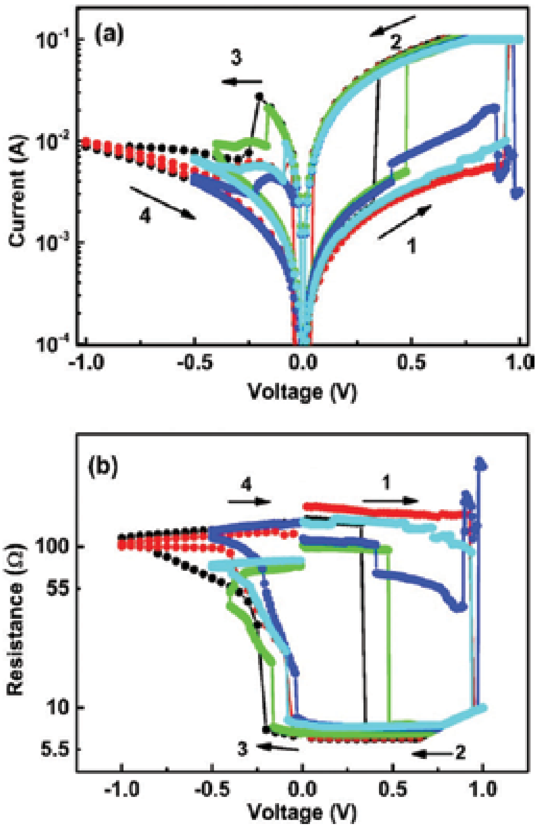

Figure 12. (a) I–V curves of the Hg/PVDF/Au device (b) R–V curves of the Hg/PVDF/Au device [34]. This research was conducted at Pondicherry University of India in 2017.

is higher than that of the Au/PVDF/n-InP diode (2.387×10^{-7} A at −1 V). This proves that the PVDF as an organic interlayer can improve the electrical characteristics of the Schottky diodes. The diode parameters are confirmed from the forward bias I–V curves, which can be described by the thermionic emission theory. The calculated barrier heights based on I–V measurements are 0.57 eV for Au/n-InP and 0.73 eV for Au/PVDF/n-InP. The increased barrier height indicated that the PVDF films can influence the space charge region of n-InP [79]. The Au/PVDF/Si structure fabricated by Kim et al. showed good ferroelectric properties. The current density and memory window width for the PVDF film were about 10^{-6} A/cm^2 and 1.8 V under a bias voltage of 5 V, respectively [80].

The interfacial electrical properties will become very poor due to the diffusion of constituent atoms into the Si substrate, if a ferroelectric film is directly deposited on a Si substrate. In order to solve this problem, a metal-ferroelectric-insulator-semiconductor (MFIS) structure is formed with a buffer layer inserted between Si substrate and the ferroelectric film, as shown in **Figure 14** [81]. The MFIS diodes with low-voltage operation has attracted great interest because they can be used as one-transistor type nonvolatile memories [20, 82, 83]. The MFIS

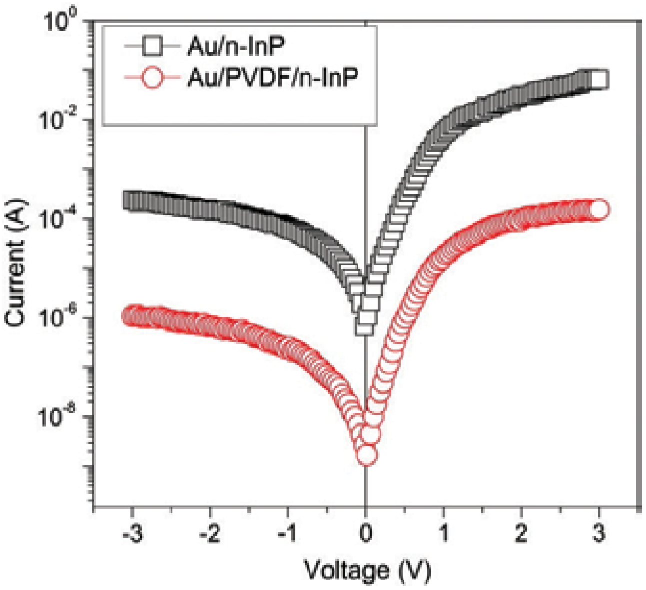

Figure 13. The forward and reverse bias I–V characteristics of Au/PVDF/n-InP and the Au/n-InP Schottky diodes at room temperature [79]. This research was conducted at Sri Venkateswara University of India in 2014.

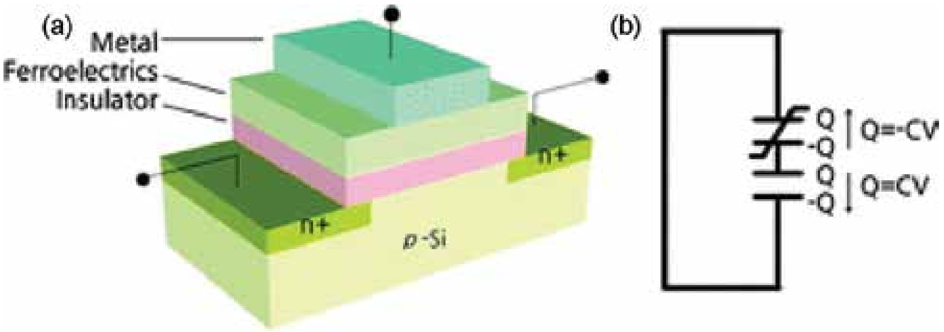

Figure 14. (a) Schematic drawings for the MFIS diodes and (b) The equivalent circuit of the MFIS structure [81]. This research was conducted at Waseda University of Japan in 2016.

diodes seem to have solved the problems of the MFS structure, but the retention characteristics of MFIS diodes are unreliable for commercialization in spite of considerable advancement in data retention time in recent reports [84, 85].

The metal-insulator-metal diode is composed of the thin layers of an n-type polymer such as PGSt as the dielectric material, and a p-type polymer such as PTMA, PVDF. The retention cycles of the ON and OFF states under open-circuit conditions persisted for more than 10^4 times [86].

4. Conclusion

Although there are still some crucial problems for PVDF applications, such as memory times, density storage, low operating voltage and so on, these are being solved. With more and more research done in this field, the more advanced fabrication method of PVDF films could be developed, and ferroelectric β-phase PVDF should have a promising future to build up the information storage units.

Acknowledgements

This work was supported by the National Natural Science Foundations of China (No. 51471046, 51525101) and the Research Funds for the Central Universities (No. N170205001). The authors declare no competing financial interest.

Author details

Liuxia Ruan[1], Donghai Zhang[1], Junwei Tong[1], Jianli Kang[2], Yufang Chang[3], Lianqun Zhou[4], Gaowu Qin[1] and Xianmin Zhang[1]*

*Address all correspondence to: zhangxm@atm.neu.edu.cn

1 Key Laboratory for Anisotropy and Texture of Materials (Ministry of Education), School of Material Science and Engineering, Northeastern University, Shenyang, China

2 State Key Laboratory of Separation Membranes and Membrane Processes, Tianjin Polytechnic University, Tianjin, China

3 Computer Teaching and Researching Section, Shenyang Conservatory of Music, Shenyang, China

4 Suzhou Institute of Biomedical, Engineering and Technology, Chinese Academy of Sciences, Suzhou, China

References

[1] Prest W Jr, Luca D. The formation of the γ phase from the α and β polymorphs of polyvinylidene fluoride. Journal of Applied Physics. 1978;**49**(10):5042-5047

[2] Lovinger AJ. Annealing of poly (vinylidene fluoride) and formation of a fifth phase. Macromolecules. 1982;**15**(1):40-44

[3] Kepler RG, Anderson R. Ferroelectric polymers. Advances in Physics. 1992;**41**(1):1-57

[4] Naber RC, Asadi K, Blom PW, de Leeuw DM, de Boer B. Organic nonvolatile memory devices based on ferroelectricity. Advanced Materials. 2010;**22**(9):933-945

[5] Sencadas V, Moreira MV, Lanceros-Méndez S, Pouzada AS, Gregório Filho R. α to β Transformation on PVDF films obtained by uniaxial stretch. Materials Science Forum, Trans Tech Publ. 2006:872-876

[6] Yang D, Chen Y. β-phase formation of poly (vinylidene fluoride) from the melt induced by quenching. Journal of Materials Science Letters. 1987;**6**(5):599-603

[7] Branciforti MC, Sencadas V, Lanceros-Mendez S, Gregorio R. New technique of processing highly oriented poly (vinylidene fluoride) films exclusively in the β phase. Journal of Polymer Science Part B: Polymer Physics. 2007;**45**(19):2793-2801

[8] Chen S, Li X, Yao K, Tay FEH, Kumar A, Zeng K. Self-polarized ferroelectric PVDF homopolymer ultra-thin films derived from Langmuir–Blodgett deposition. Polymer. 2012;**53**(6):1404-1408

[9] Ramasundaram S, Yoon S, Kim KJ, Lee JS. Direct Preparation of Nanoscale Thin Films of Poly (vinylidene fluoride) Containing β-Crystalline Phase by Heat-Controlled Spin Coating. Macromolecular Chemistry and Physics. 2008;**209**(24):2516-2526

[10] Kang SJ, Park YJ, Sung J, Jo PS, Park C, Kim KJ, Cho BO. Spin cast ferroelectric beta poly (vinylidene fluoride) thin films via rapid thermal annealing. Applied Physics Letters. 2008;**92**(1):012921

[11] Zhu H, Yamamoto S, Matsui J, Miyashita T, Mitsuishi M. Ferroelectricity of poly (vinylidene fluoride) homopolymer Langmuir–Blodgett nanofilms. Journal of Materials Chemistry C. 2014;**2**(33):6727-6731

[12] Li M, Katsouras I, Piliego C, Glasser G, Lieberwirth I, Blom PW, de Leeuw DM. Controlling the microstructure of poly (vinylidene-fluoride)(PVDF) thin films for microelectronics. Journal of Materials Chemistry C. 2013;**1**(46):7695-7702

[13] Li M, Wondergem HJ, Spijkman M-J, Asadi K, Katsouras I, Blom PW, De Leeuw DM. Revisiting the δ-phase of poly (vinylidene fluoride) for solution-processed ferroelectric thin films. Nature Materials. 2013;**12**(5):433

[14] Kang SJ, Park YJ, Bae I, Kim KJ, Kim HC, Bauer S, Thomas EL, Park C. Printable ferroelectric PVDF/PMMA blend films with ultralow roughness for low voltage non-volatile polymer memory. Advanced Functional Materials. 2009;**19**(17):2812-2818

[15] Park JH, Kurra N, AlMadhoun M, Odeh IN, Alshareef HN. A two-step annealing process for enhancing the ferroelectric properties of poly (vinylidene fluoride)(PVDF) devices. Journal of Materials Chemis-try C. 2015;**3**(10):2366-2370

[16] Ducharme S, Fridkin V, Bune A, Palto S, Blinov L, Petukhova N, Yudin S. Intrinsic ferroelectric coercive field. Physical Review Letters. 2000;**84**(1):175

[17] Yamauchi N. A metal-insulator-semiconductor (MIS) device using a ferroelectric polymer thin film in the gate insulator. Japanese Journal of Applied Physics. 1986;**25**(4R):590

[18] Nguyen CA, Wang J, Chen L, Mhaisalkar SG, Lee PS. Low-voltage organic ferroelectric field effect transistors using Langmuir–Schaefer films of poly (vinylidene fluoride-trifluororethylene). Organic Electronics. 2009;**10**(1):145-151

[19] Fujisaki S, Ishiwara H, Fujisaki Y. Low-voltage operation of ferroelectric poly (vinylidene fluoride-trifluoroethylene) copolymer capacitors and metal-ferroelectric-insulator-semiconductor diodes. Applied Physics Letters. 2007;**90**(16):162902

[20] Gerber A, Kohlstedt H, Fitsilis M, Waser R, Reece T, Ducharme S, Rije E. Low-voltage operation of metal-ferroelectric-insulator-semiconductor diodes incorporating a ferroelectric polyvinylidene fluoride copolymer Langmuir-Blodgett film. Journal of Applied Physics. 2006;**100**(2):024110

[21] Bune AV, Fridkin VM, Ducharme S, Blinov LM, Palto SP, Sorokin AV, Yudin S, Zlatkin A. Two-dimensional ferroelectric films. Nature. 1998;**391**(6670):874

[22] Asadi K, De Leeuw DM, De Boer B, Blom PW. Organic non-volatile memories from ferroelectric phase-separated blends. Nature Materials. 2008;**7**(7):547

[23] Benz M, Euler WB, Gregory OJ. The influence of preparation conditions on the surface morphology of poly (vinylidene fluoride) films. Langmuir. 2001;**17**(1):239-243

[24] Ruan L, Yao X, Chang Y, Zhou L, Qin G, Zhang X. Properties and Applications of the β Phase Poly (vinylidene fluoride). Polymer. 2018;**10**(3):228

[25] Dawson NM, Atencio PM, Malloy KJ. Facile deposition of high quality ferroelectric poly (vinylidene fluoride) thin films by thermally modulated spin coating. Journal of Polymer Science Part B: Polymer Physics. 2017;**55**(3):221-227

[26] Shaik H, Rachith S, Rudresh K, Sheik AS, Raman KT, Kondaiah P, Rao GM. Towards β-phase formation probability in spin coated PVDF thin films. Journal of Polymer Research. 2017;**24**(3):35

[27] Cardoso V, Minas G, Costa CM, Tavares C, Lanceros-Mendez S. Micro and nanofilms of poly (vinylidene fluoride) with controlled thickness, morphology and electroactive crystalline phase for sensor and actuator applications. Smart Materials and Structures. 2011;**20**(8):087002

[28] Burda C, Chen X, Narayanan R, El-Sayed MA. Chemistry and properties of nanocrystals of different shapes. Chemical Reviews. 2005;**105**(4):1025-1102

[29] Losurdo M, Hingerl K. Ellipsometry at the Nanoscale. Springer; 2013

[30] Zhu H, Mitsuishi M, Miyashita T. Facile Preparation of Highly Oriented Poly (vinylidene fluoride) Langmuir–Blodgett Nanofilms Assisted by Amphiphilic Polymer Nanosheets. Macromolecules. 2012;**45**(22):9076-9084

[31] Zhang X, Tong J, Zhu H, Wang Z, Zhou L, Wang S, Miyashita T, Mitsuishi M, Qin G. Room temperature magnetoresistance effects in ferroelectric poly (vinylidene fluoride) spin valves. Journal of Materials Chemistry C. 2017;**5**(21):5055-5062

[32] Tajitsu Y, Chiba A, Furukawa T, Date M, Fukada E. Crystalline phase transition in the copolymer of vinylidenefluoride and trifluoroethylene. Applied Physics Letters. 1980;**36**(4):286-288

[33] Li M, Stingelin N, Michels JJ, Spijkman M-J, Asadi K, Feldman K, Blom PW, de Leeuw DM. Ferroelectric phase diagram of PVDF: PMMA. Macromolecules. 2012;**45**(18):7477-7485

[34] Pramod K, Gangineni R. Low voltage bipolar resistive switching in self-assembled PVDF nanodot network in capacitor like structures on Au/Cr/Si with Hg as a top electrode. Organic Electronics. 2017;**42**:47-51

[35] Kang SJ, Park YJ, Hwang J, Jeong HJ, Lee JS, Kim KJ, Kim HC, Huh J, Park C. Localized pressure-induced ferroelectric pattern arrays of semicrystalline poly (vinylidene fluoride) by microimprinting. Advanced Materials. 2007;**19**(4):581-586

[36] Guo Y, Yu G, Liu Y. Functional Organic Field-Effect Transistors. Advanced Materials. 2010;**22**(40):4427-4447

[37] Ling Q-D, Liaw D-J, Zhu C, Chan DS-H, Kang E-T, Neoh K-G. Polymer electronic memories: Materials, devices and mechanisms. Progress in Polymer Science. 2008;**33**(10):917-978

[38] Tsymbal EY, Gruverman A, Garcia V, Bibes M, Barthélémy A. Ferroelectric and multiferroic tunnel junctions. MRS Bulletin. 2012;**37**(2):138-143

[39] Garcia V, Bibes M, Bocher L, Valencia S, Kronast F, Crassous A, Moya X, Enouz-Vedrenne S, Gloter A, Imhoff D. Ferroelectric control of spin polarization. Science. 2010;**327**(5969):1106-1110

[40] Pantel D, Goetze S, Hesse D, Alexe M. Reversible electrical switching of spin polarization in multiferroic tunnel junctions. Nature Materials. 2012;**11**(4):289

[41] Nakhmanson S, Nardelli MB, Bernholc J. Collective polarization effects in β-polyvinylidene fluoride and its copolymers with tri-and tetrafluoroethylene. Physical Review B. 2005;**72**(11):115210

[42] Dediu VA, Hueso LE, Bergenti I, Taliani C. Spin routes in organic semiconductors. Nature Materials. 2009;**8**(9):707

[43] Szulczewski G, Sanvito S, Coey M. A spin of their own. Nature Materials. 2009;**8**(9):693

[44] Tsymbal EY, Kohlstedt H. Tunneling across a ferroelectric. Evgeny Tsymbal Publications. 2006:22

[45] Dang ZM, Lin YH, Nan CW. Novel ferroelectric polymer composites with high dielectric constants. Advanced Materials. 2003;**15**(19):1625-1629

[46] Naber RC, Tanase C, Blom PW, Gelinck GH, Marsman AW, Touwslager FJ, Setayesh S, De Leeuw DM. High-performance solution-processed polymer ferroelectric field-effect transistors. Nature Materials. 2005;**4**(3):243

[47] Hu Z, Tian M, Nysten B, Jonas AM. Regular arrays of highly ordered ferroelectric polymer nanostructures for non-volatile low-voltage memories. Nature Materials. 2009;**8**(1):62

[48] Lee KH, Lee G, Lee K, Oh MS, Im S. Flexible low voltage nonvolatile memory transistors with pentacene channel and ferroelectric polymer. Applied Physics Letters. 2009;**94**(9):69

[49] Shin YJ, Kang SJ, Jung HJ, Park YJ, Bae I, Choi DH, Park C. Chemically cross-linked thin poly (vinylidene fluoride-co-trifluoroethylene) films for nonvolatile ferroelectric polymer memory. ACS Applied Materials & Interfaces. 2011;**3**(2):582-589

[50] Liu Y-L, Li Y, Xu J-T, Fan Z-Q. Cooperative effect of electrospinning and nanoclay on formation of polar crystalline phases in poly (vinylidene fluoride). ACS Applied Materials & Interfaces. 2010;**2**(6):1759-1768

[51] Velev JP, López-Encarnación JM, Burton JD, Tsymbal EY. Tsymbal, Multiferroic tunnel junctions with poly (vinylidene fluoride). Physical Review B. 2012;**85**(12):125103

[52] Jayakumar O, Mandal B, Majeed J, Lawes G, Naik R, Tyagi A. Inorganic–organic multiferroic hybrid films of Fe_3O_4 and PVDF with significant magneto-dielectric coupling. Journal of Materials Chemistry C. 2013;**1**(23):3710-3715

[53] Li W, Jiang L, Zhang X, Shen Y, Nan C. High-energy-density dielectric films based on polyvinylidene fluoride and aromatic polythiourea for capacitors. Journal of Materials Chemistry A. 2014;**2**(38):15803-15807

[54] Liu Y, Wang B, Zhan Q, Tang Z, Yang H, Liu G, Zuo Z, Zhang X, Xie Y, Zhu X. Positive temperature coefficient of magnetic anisotropy in polyvinylidene fluoride (PVDF)-based magnetic composites. Scientific Reports. 2014;**4**:6615

[55] Georgakopoulos S, Del Pozo F, Mas-Torrent M. Flexible organic transistors based on a solution-sheared PVDF insulator. Journal of Materials Chemistry C. 2015;**3**(47):12199-12202

[56] Velev JP, Duan C-G, Burton J, Smogunov A, Niranjan MK, Tosatti E, Jaswal S, Tsymbal EY. Magnetic tunnel junctions with ferroelectric barriers: prediction of four resistance states from first principles. Nano Letters. 2008;**9**(1):427-432

[57] Liang S, Yang H, Yang H, Tao B, Djeffal A, Chshiev M, Huang W, Li X, Ferri A, Desfeux R. Ferroelectric control of organic/ferromagnetic spinterface. Advanced Materials. 2016; **28**(46):10204-10210

[58] Tian B, Wang J, Fusil S, Liu Y, Zhao X, Sun S, Shen H, Lin T, Sun J, Duan C. Tunnel electroresistance through organic ferroelectrics. Nature Communications. 2016;**7**:11502

[59] Pantel D, Alexe M. Electroresistance effects in ferroelectric tunnel barriers. Physical Review B. 2010;**82**(13):134105

[60] Gruverman A, Wu D, Lu H, Wang Y, Jang H, Folkman C, Zhuravlev MY, Felker D, Rzchowski M, Eom C-B. Tunneling electroresistance effect in ferroelectric tunnel junctions at the nanoscale. Nano Letters. 2009;**9**(10):3539-3543

[61] Zhuravlev MY, Sabirianov RF, Jaswal S, Tsymbal EY. Giant electroresistance in ferroelectric tunnel junctions. Physical Review Letters. 2005;**94**(24):246802

[62] Barraud C, Seneor P, Mattana R, Fusil S, Bouzehouane K, Deranlot C, Graziosi P, Hueso L, Bergenti I, Dediu V. Unravelling the role of the interface for spin injection into organic semiconductors. Nature Physics. 2010;**6**(8):615

[63] Yuasa S, Fukushima A, Kubota H, Suzuki Y, Ando K. Giant tunneling magnetoresistance up to 410% at room temperature in fully epitaxial Co/MgO/Co magnetic tunnel junctions with bcc Co (001) electrodes. Applied Physics Letters. 2006;**89**(4):042505

[64] Yanase A, Siratori K. Band structure in the high temperature phase of Fe_3O_4. Journal of the Physical Society of Japan. 1984;**53**(1):312-317

[65] Zhao L, Mi W, Jiang E, Bai H. Spin-polarized transport of electrons from polycrystalline Fe_3O_4 to amorphous Si. Applied Physics Letters. 2007;**91**(5):052113

[66] Jung S-W, Yoon S-M, Kang SY, You I-K, Koo JB, Baeg K-J, Noh Y-Y. Low-voltage-operated top-gate polymer thin-film transistors with high-capacitance P (VDF-TrFE)/PVDF-blended dielectrics. Current Applied Physics. 2011;**11**(3):S213-S218

[67] Gerber A, Fitsilis M, Waser R, Reece TJ, Rije E, Ducharme S, Kohlstedt H. Ferroelectric field effect transistors using very thin ferroelectric polyvinylidene fluoride copolymer films as gate dielectrics. Journal of Applied Physics. 2010;**107**(12):124119

[68] Sannigrahi J, Bhadra D, Chaudhuri B. Crystalline graphite oxide/PVDF nanocomposite gate dielectric: Low-voltage and high field effect mobility thin-film transistor. Physica Status Solidi A. 2013;**210**(3):546-552

[69] Knotts G, Bhaumik A, Ghosh K, Guha S. Enhanced performance of ferroelectric-based all organic capacitors and transistors through choice of solvent. Applied Physics Letters. 2014;**104**(23):84_1

[70] Zhu H, Yamamoto S, Matsui J, Miyashita T, Mitsuishi M. Asymmetric Ferroelectric Switching Based on an Al/PVDF Langmuir-Blodgett Nanofilm/PEDOT: PSS/Al Device. Molecular Crystals and Liquid Crystals. 2015;**618**(1):89-94

[71] Ma L, Liu J, Yang Y. Organic electrical bistable devices and rewritable memory cells. Applied Physics Letters. 2002;**80**(16):2997-2999

[72] Kim T-W, Oh S-H, Lee J, Choi H, Wang G, Park J, Kim D-Y, Hwang H, Lee T. Effect of metal ions on the switching performance of polyfluorene-based organic non-volatile memory devices. Organic Electronics. 2010;**11**(1):109-114

[73] Ramana CV, Moodley M, Kannan V, Maity A. Solution based-spin cast processed organic bistable memory device. Solid-State Electronics. 2013;**81**:45-50

[74] Braun S, Salaneck WR, Fahlman M. Energy-level alignment at organic/metal and organic/organic interfaces. Advanced Materials. 2009;**21**(14-15):1450-1472

[75] Kim TW, Yang Y, Li F, Kwan WL. Electrical memory devices based on inorganic/organic nanocomposites. NPG Asia Materials. 2012;**4**(6):e18

[76] Kim SS, Cho W-J, Ahn C-G, Im K, Yang J-H, Baek I-B, Lee S, Lim KS. Fabrication of fin field-effect transistor silicon nanocrystal floating gate memory using photochemical vapor deposition. Applied Physics Letters. 2006;**88**(22):223502

[77] Khurana G, Misra P, Katiyar RS. Multilevel resistive memory switching in graphene sandwiched organic polymer heterostructure. Carbon. 2014;**76**:341-347

[78] Lim EW, Ismail R. Conduction mechanism of valence change resistive switching memory: a survey. Electronics. 2015;**4**(3):586-613

[79] Reddy VR. Electrical properties of Au/polyvinylidene fluoride/n-InP Schottky diode with polymer interlayer. Thin Solid Films. 2014;**556**:300-306

[80] Kim JH, Kim DW, Jeon HS, Park BE. Electrical Characteristics of Metal–Ferroelectric–Semiconductor Structures Based on Poly (vinylidene fluoride). Japanese Journal of Applied Physics. 2007;**46**(10S):6976

[81] Park B-E. Non-volatile Ferroelectric Memory Transistors Using PVDF and P (VDF-TrFE) Thin Films. Ferroelectric-Gate Field Effect Transistor Memories. Dordrecht: Springer 2016. pp. 141-155

[82] Park B-E, Ishiwara H. Electrical properties of $LaAlO_3$/Si and $Sr_{0\cdot8}Bi_{2\cdot2}Ta_2O_9/LaAlO_3$/Si structures. Applied Physics Letters. 2001;**79**(6):806-808

[83] Park B-E, Takahashi K, Ishiwara H. Five-day-long ferroelectric memory effect in Pt/(Bi, $La)_4Ti_3O_{12}/HfO_2$/Si structures. Applied Physics Letters. 2004;**85**(19):4448-4450

[84] Takahashi M, Sakai S. Self-aligned-gate metal/ferroelectric/insulator/semiconductor field-effect transistors with long memory retention. Japanese Journal of Applied Physics. 2005;**44**(6L):L800

[85] Takahashi K, Aizawa K, Park B-E, Ishiwara H. Thirty-day-long data retention in ferroelectric-gate field-effect transistors with HfO_2 buffer layers. Japanese Journal of Applied Physics. 2005;**44**(8R):6218

[86] Oyaizu K, Nishide H. Radical polymers for organic electronic devices: A radical departure from conjugated polymers? Advanced Materials. 2009;**21**(22):2339-2344

Edited by Husein Irzaman

Ferroelectricity is a symptom of inevitable electrical polarization changes in materials without external electric field interference. Ferroelectricity is a phenomenon exhibited by crystals with a spontaneous polarization and hysteresis effects associated with dielectric changes when an electric field is given. Our fascination with ferroelectricity is in recognition of a beautiful article by Itskovsky, in which he explains the kinetics of a ferroelectric phase transition in a thin ferroelectric layer (film). We have been researching ferroelectric materials since 2001. There are several materials known for their ferroelectric properties. Barium titanate and barium strontium titanate are the most well known. Several others include tantalum oxide, lead zirconium titanate, gallium nitride, lithium tantalate, aluminium, copper oxide, and lithium niobate. There is still a blue ocean of ferroelectric applications yet to be expounded. It is and hopefully always will be a bright future.

Published in London, UK

IntechOpen

ISBN 978-1-83881-714-5
9 781838 817145